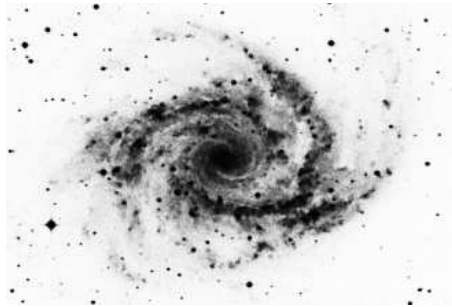


A new model of spiral galaxies based on propagating star formation



John Paul Sleath
Queens' College

A dissertation submitted for the degree of Doctor of
Philosophy in the University of Cambridge

September 1995

TRADEMARKS

The photographs appearing in Fig. 6.3 and chapter headings were extracted from the Digitized Sky Survey using the WWW Skyview Virtual Observatory (<http://skview.gsfc.nasa.gov/skyview.html>). The southern sky images are based on photographic data obtained using The UK Schmidt Telescope. The UK Schmidt Telescope was operated by the Royal Observatory Edinburgh, with funding from the UK Science and Engineering Research Council, until June 1988, and thereafter by the Anglo-Australian Observatory. Original plate material is copyright © the Royal Observatory Edinburgh and the Anglo-Australian Observatory. The northern sky images are based on photographic data obtained using the Oschin Schmidt Telescope on Palomar Mountain. The Palomar Observatory Sky Survey was funded by the National Geographic Society. The Oschin Schmidt Telescope is operated by the California Institute of Technology and Palomar Observatory. The plates were processed into the present compressed digital form with their permission. The Digitized Sky Survey was produced at the Space Telescope Science Institute (STScI) under U.S. Government grant NAG W-2166.

Sun is a trademark of Sun Microsystems, Inc. SPARC is a registered trademark of SPARC International, Inc. Products bearing the SPARC trademark are based on an architecture developed by Sun Microsystems, Inc. SPARCstation is a trademark of SPARC International Inc., licensed exclusively to Sun Microsystems Inc.

UNIX is a registered trademark of Novell, Inc.

The galaxies shown in chapter headings are as follows:

- Chapter 1 – NGC 2997,
- Chapter 2 – NGC 4321,
- Chapter 3 – NGC 1566,
- Chapter 4 – NGC 1232,
- Chapter 5 – NGC 6946,
- Chapter 6 – NGC 5194,
- Chapter 7 – NGC 628,
- Chapter 8 – simulation.

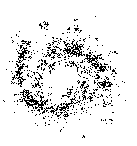
From the intrinsic evidence of his creation, the Great Architect of the Universe now seems to appear as a pure mathematician.

Sir James Jeans, "The Mysterious Universe"

Felix qui potuit rerum cognoscere causas.

Lucky is he who has been able to understand the causes of things.

Virgil, Georgics, no. 2 (of Lucretius)



Preface

This dissertation is the result of work undertaken at the Mullard Radio Astronomy Observatory, Cambridge between October 1992 and September 1995, and includes nothing which is the outcome of work done in collaboration. It has not, nor has any similar dissertation been submitted for a degree, diploma or other qualification at this, or any other, university. This dissertation does not exceed 60 000 words in length.

The “without whom”s. First, thanks to Paul Alexander, my supervisor, for his inspirational, but non-interfering guidance and advice. It was good to be allowed to do things my own way, knowing that help was available when direction was lost. I’d also like to acknowledge David Titterington for keeping the MRAO cluster running and not moaning when I was using every processor. Many other people in RA have made a huge contribution to my enjoyment of the last three years; in particular of course my fellow students and officemates. Memories of the trip to Leiden will remain with me for many years! Those that have availed themselves of the services of ‘Sleath & Jenness, Computer Consultants’ can rest assured that the COFFEE program will continue to be supported.

Away from the lab, I’d have gone quite mad without the support of my friends, especially in the archery and hillwalking clubs. If I mentioned everyone in the detail that they all deserve, this preface would be longer than the rest of the dissertation! Particular mention must however go to Tracey and Jo, very special friends who, in their different ways, were always there when it mattered most.

And of course, I wouldn’t have made it this far without the encouragement of Mum, Dad and Martin, to whom I dedicate this dissertation.

Contents

1	Introduction	1
2	Review of galactic models	5
2.1	Propagating star formation	5
2.1.1	Observational evidence	5
2.1.2	Computer models	7
2.1.3	Percolation theory – a digression	9
2.2	Other galaxy models	12
2.2.1	N-body codes	12
2.2.2	SPH and hybrid schemes	15
3	The model	19
3.1	The physics of propagating star formation	19
3.2	The implementation	21
3.2.1	The star formation mechanism	21
3.2.2	The galactic potential and the SDW	23
3.2.3	The kinetic temperature of the cloud particles	27
3.3	Computational considerations	28
3.3.1	Calculation of near neighbours	28
3.3.2	The rotation integration scheme	29
3.3.3	Particle dynamics	31
3.3.4	Random number generation	32
3.3.5	The initialisation of the model	33
3.4	Running a simulation	34
4	The star formation rate	37
4.1	The effect of the input parameters on the CFR	37
4.1.1	Star forming parameters	39



4.1.2	Cloud dynamics parameters	41
4.2	The Galactic cluster formation rate	41
4.3	The Schmidt law	42
4.3.1	The Schmidt Law for the new model	44
4.3.2	Observational determinations of the SFR	45
4.3.3	The observed Schmidt Law	47
4.4	A magnetic origin for M_{st} ?	49
5	Spiral density waves and galactic structure	55
5.1	The effect of the SDW on the cluster formation rate	55
5.1.1	Amplitude of the SDW	56
5.1.2	Spiral pattern speed	57
5.1.3	SDW pitch angle	58
5.1.4	Number of spiral arms	59
5.1.5	Comparison with observations	59
5.2	Structure as a function of the input parameters	60
5.3	Resonances and the radial distribution of star formation	69
6	The observational sample	73
6.1	Tracers of star formation	73
6.2	Galaxy orientation	76
7	Quantitative measures of galactic structure	87
7.1	Description of the techniques	87
7.1.1	Fourier analysis	88
7.1.2	Minimal spanning tree spectra	89
7.1.3	Multi-fractals	91
7.2	Application of the techniques	94
7.2.1	Fourier spectra of galaxies	94
7.2.2	Experiments with MST edge-length spectra	104
7.2.3	Multi-fractal techniques	110
8	Concluding remarks	123
8.1	Summary of work to date	123
8.2	Future studies with the current model	125
8.3	Developing the model	125
A	Running a simulation	129
A.1	Input parameter file	129
A.2	Useful UNIX scripts	131

CONTENTS	ix
B Simulation source code	135
C Classification of galaxies	185
Abbreviations used in the text	189
Symbols used in the text	191
List of publications	193
Bibliography	195



List of Figures

2.1	Typical output from the SSPSF gas-model	9
2.2	The percolation phase transition	11
2.3	Phase transition of the SSPSF stellar model	11
2.4	Construction of the hierarchical tree for N-body calculations	14
3.1	The Galactic rotation curve	25
3.2	The gravitational potential	25
3.3	The position of the crest of the SDW	26
3.4	The radial force perturbation due to a spiral density wave	27
3.5	Grid for determining which clouds are within a shock	28
3.6	Richardson extrapolation	29
3.7	Orbital path for an isolated particle	30
3.8	Cloud–supershell collision geometry	31
3.9	The initial oscillations of the star formation rate	33
4.1	Variation of CFR with star forming parameters	40
4.2	Correlation of cloud mass with M_{st}	40
4.3	Cluster formation rate versus cloud velocity dispersion	41
4.4	Typical distribution of cloud masses	43
4.5	Observational determination of Schmidt Law	45
4.6	The minimum energy condition for magnetic fields	50
4.7	Average magnetic field for different galactic types	50
4.8	Correlation of FIR luminosity with galactic magnetic field	51
5.1	The cluster formation rate as a function of spiral amplitude A	56
5.2	Variation of the cluster formation rate with Ω_p	57
5.3	Variation of cluster formation rate with SDW pitch angle	58
5.4	Variation of galactic structure with propagation scaling mass	61
5.5	Variation of galactic structure with cloud velocity dispersion	63



5.6	Variation of galactic structure with SDW amplitude	65
5.7	Variation of galactic structure with SDW pitch angle	67
5.8	Resonance curves arising from the model potential	69
5.9	Galactic (and model) gas distribution	70
6.1	Distribution of morphological types in the observational sample	75
6.2	Discrepancies between PA and inclination values for the observational sample	75
6.3	The observational sample	78
7.1	Example of a minimal spanning tree	89
7.2	Illustration of the KS and Kuiper tests	90
7.3	Effect of varying A on Fourier spectra of model galaxies	95
7.4	Effect of varying M_{st} on Fourier spectra of model galaxies	96
7.5	Average Fourier transform amplitude as a function of SDW strength	97
7.6	Relationship between pattern and SDW pitch angles	97
7.7	Fourier transform, now including old clusters	98
7.8	Fourier spectra of the observational sample	99
7.9	Fourier transforms of non-standard simulations	103
7.10	Example MST edge-length spectrum for a standard simulation	105
7.11	Distribution of clusters younger than 10^7 yr for ensemble of standard simulations	107
7.12	Distribution of clusters younger than 10^8 yr for ensemble of standard simulations	108
7.13	Sample MST spectra – NGC 3031 and two simulations	109
7.14	The Hénon attractor	111
7.15	Multifractal dimension as a function of M_{st} (MST method)	112
7.16	Multifractal dimensions for selection of observed galaxies	113
7.17	Effect of pixellation on fractal dimensions	114
7.18	Comparison of multifractal dimensions calculated with the two different methods	116
7.19	Multifractal dimension for three values of M_{st} (Correlation–Sum method)	117
7.20	Correlation–Sum dimensions as a function of model input parameters	119
7.21	Correlation of Fourier transform peak amplitude with multifractal dimension	120
7.22	Correlation–Sum multifractal dimensions of NGC 3031	120
7.23	Multifractal dimensions as a function of Hubble morphological class	121
C.1	The Hubble sequence of galactic morphologies	185
C.2	The DDO system of galaxy classification	187

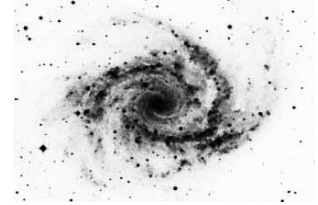
List of Tables

2.1	Applications of percolation theory	10
3.1	Constants defining the Galactic potential	24
4.1	Standard input parameters	38
6.1	Observations of H II regions	74
7.1	Comparing MST spectra – identical parameters, youngest clusters only	105
7.2	Comparing MST spectra – identical parameters, older clusters included	106
7.3	Comparing MST spectra for different values of M_{st}	106
7.4	Comparing MST spectra with different lower cutoffs	110
A.1	Model input parameters	130
A.2	Model units	130
C.1	Revised Hubble sequence	186
C.2	Conversion of Hubble types to Revised System	187



Chapter 1

Introduction



Understanding the physical basis of star formation is one of the major challenges still facing astrophysics. On the scale of individual stars much progress has been made since the advent of telescopes capable of working in the sub-millimetre band. Such studies have concentrated on single, isolated, stars where the physics of the outflows, stellar winds, accretion discs etc. can be more easily investigated. Most stars are however, born in clusters and associations, and it is in these dense environments, enveloped by the still collapsing and fragmenting molecular cloud, that the interaction between cloud material and newly-forming stars becomes an important consideration. Supernova explosions, arising from the death of super-massive stars which have already raced through their life whilst lower mass stars are still forming, also play a major role by heating and shocking the interstellar material, creating expanding cavities of ionised gas. It is this complexity which makes a detailed understanding of star formation such a formidable goal.

On larger scales, we know that the galactic star formation rate varies with certain global characteristics of the galaxy concerned, for example, the total mass and the gas fraction. Detailed studies of star forming regions generally take little account of such considerations – for example we might consider the proximity of a collapsing molecular cloud to a spiral arm to be an important factor controlling the overall properties of the star clusters formed. Unfortunately it is not possible to model a whole galaxy with sufficient resolution (both spatial and temporal) such that the creation of individual stars can be followed in a global context. On the largest scales of whole galaxies, modelling has concentrated on the dynamics and resulting overall structures, with star formation being added in an often *ad hoc* manner.

The model described in this dissertation occupies a half-way position, both in the scale ranges of the physics considered and also the computational techniques used to model the galaxies. Star formation is considered at the level of giant molecular cloud complexes – the same clouds are followed dynamically as they orbit in the overall galactic potential and collide both with each other and supershells (resulting from supernovae explosions), but without having recourse to a full self-gravitating model. The star formation process is based on the theory of ‘propagating star formation’ (PSF), a stochastic approach which allows the detailed physics controlling the creation of



new stars (e.g. the presence of magnetic fields, turbulence etc.) to be subsumed into a single parameter which determines the probability of star formation occurring. The model is described in much greater detail in Chapter 3.

The observational evidence for the reality of triggered star formation is wide and varied – a brief overview is provided in §2.1.1 below. The history of models based upon propagating star formation is considered in §2.1.2, whilst in §2.2 I review some alternative galactic models based on other schemes and ideas.

The principle outputs from the new model consist of the star formation rate and the physical structures produced. I will show in Chapter 4 how the star formation rate varies as function of the input parameters. Importantly this will permit a prediction of the star formation rate of our Galaxy to be made; a forecast which is shown to be extremely accurate (§4.2). Furthermore, from similar considerations, it will be shown that the model predicts a simple power-law relationship between the star formation rate and the average gas density; such a dependency is commonly known as a Schmidt–Law (see §4.3). The spatial distribution of star-forming regions will be considered in Chapter 5, where it will be shown that unlike many simulations of galactic star formation, the new model can reproduce the whole family of disc galaxies.

No computer model, however elegant, is worth anything if it is unable to be compared with observational data. I have taken catalogues of H II regions from the literature for a sample of spiral galaxies (Chapter 6), since such regions trace the location of current star formation. To compare with the results obtained from the model, we require a way in which to classify the morphology of the galaxy. Many such schemes already exist – I provide a brief summary as Appendix C. These are all somewhat subjective however, ultimately coming down to the decision of the observer, and perusing a catalogue compiled from the results of many authors, it is clear that a consensus often cannot be reached. It would therefore be useful if a more quantitative method for classifying galaxies existed. I have adopted a number of approaches in an attempt to come up with, ideally, a single index with which to specify a galaxy. More importantly still this would hopefully permit a direct comparison of observational with simulated data in a way which treated each sort equally. The results of these trials are reported in Chapter 7.

The model as described within this dissertation was designed with two main criteria in mind: that the physics should be as realistic as possible and that the resulting computer code would be sufficiently fast and compact such that it would run on the workstations available at that time (1992–93). Propagating star formation provides a natural framework which satisfies these requirements – however, even within the duration of the project, the speed of workstations has improved dramatically, and hence in Chapter 8, I provide some ideas for ways in which the model could be extended and developed. There of course also remain many things that could be done with the current version, and these, together with a summary of the studies performed to date, are also discussed in this chapter.

Finally, for reference purposes I include further information on the code, including an example input parameter file, details of the internal system of units, some UNIX scripts to assist in running

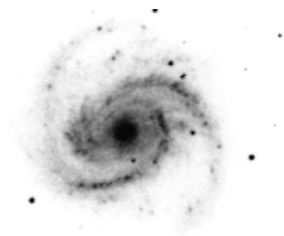
the program (all as Appendix A) and a complete source code listing (Appendix B). These are intended to provide any future user of the model with sufficient information to be able to achieve results with the minimum of difficulties, and also constitute a convenient reference source for those developing the code further.

This dissertation is concerned with a dynamical, evolving galaxy model. Clearly this is difficult to show in a book such as this, but in an attempt to illustrate the sort of results obtained, when the pages are flicked through from the back to the front then the small images in the bottom corner will form a short animated sequence. Each frame is separated by a simulated 2 Myr, and hence the total duration of the animation is 214 Myr. The galaxy was computed using the ‘standard’ parameters (§4.1), and only star clusters younger than 20 Myr have been shown for clarity.



Chapter 2

Review of galactic models



By combining aspects of both propagating star formation and N-body simulations, the new model is able to describe both the small scale dynamics of molecular clouds and the larger scale galactic structures that arise due to the star formation process. In this chapter I review other models of galactic star formation that have used one or either of these approaches and also consider some of the observational evidence for propagating star formation.

2.1 Propagating star formation

The concept of propagating star formation is based on the idea that the collapse of molecular clouds and subsequent star formation can be triggered by the interaction of the cloud with a supernova shock wave. The shock wave arises from the explosive death of a massive member of a previous generation of stars. The idea, originally proposed by Öpik (1953), has since been the basis of many computer simulations. First we must consider the observational evidence for propagating star formation.

2.1.1 Observational evidence

Observations of star formation triggered by expanding shocks from nearby OB associations were first remarked upon by Baade (1963) from his studies of star formation in irregular galaxies:

“... when star formation is going on in an area it spreads in some way like a disease; that is the definite impression one gets.”

More recently, efforts to determine the reality of propagating star formation have concentrated on the Large Magellanic Cloud (LMC) and our own Galaxy, for it is only in studies of these systems that sufficient angular resolution is available to determine age progressions and propagating structures. Many examples of old dispersed clusters surrounded by much younger H II regions and compact OB associations have been found. One particularly good case is DEM 34 (N11) in the



LMC, a large filamentary shell surrounding a central OB association (LH9). The periphery of the shell contains three OB associations (LH 10, LH 13 and LH 14) together with associated H II regions connected by ionised filaments. The kinematics of DEM 34 have been studied by Meaburn *et al.* (1989) – they find that the object is best described as several radially expanding shells, which are ascribed to be the result of a combination of stellar winds and multiple supernova explosions arising from the most massive stars. Particularly interesting in the context of propagating star formation is the work of Heydari-Malayeri & Testor (1983) and Heydari-Malayeri *et al.* (1987; 1988) on this object who show that the central OB association LH 9 is in fact older than the others around the periphery. This contradicts earlier work due to their re-classification of a number of objects, previously identified as extremely massive stars as compact clusters of more moderate mass OB stars, indicative of the problems associated with these sort of observations.

The LMC is a non-rotating system, and we might expect differential galactic rotation to have an important affect on any star formation mechanism. Thus we need, in addition, to consider Galactic examples of propagating star formation. On the smallest scales the OB association and molecular cloud complex Cepheus OB3 shows the formation of one cluster triggered by a nearby association. The scenario envisaged for this molecular cloud (Elmegreen 1991) is of a cluster which formed 8 Myr ago pushing on a neighbouring cloud through the interaction of stellar winds and supernova explosions. After some 4 million years this resulted in the formation of a new cluster moving with a radial speed of $\sim 5 \text{ km s}^{-1}$ relative to the cloud towards us. The embedding gas of the new cluster shares its radial velocity whereas the rest of the cloud is at the original velocity of the earlier cluster. Other good examples of similar structures include W4/W3 (Elmegreen & Wang 1988) and M17 (Hobson *et al.* 1993).

Looking at larger scales there are again a number of Galactic systems which provide strong evidence for propagating star formation. In the nearby Orion Arm we find the old OB association Tau-Gem which is surrounded by, and would appear to have provided the energy required to accelerate, the Lindblad ring, a slowly expanding shell of both atomic and molecular gas. On the periphery of the Ring we find a second generation of star formation concentrated in the Ori OB1, Per OB2 and Sco-Cen-Oph associations (Elmegreen 1985). Blaauw (1984) has considered these regions in conjunction with all the OB associations which are judged to be members of the Orion Arm within a distance of 1.5 kpc from the Sun. He finds that the triggered star formation has propagated in many different directions within the arm, consistent with a stochastic picture, but not what would be expected if the star formation arose from the passage of a spiral density wave. In this latter case there should be a systematic progression of association ages across the arm which is not found.

At greater distances from the Sun (2–3 kpc) we find the Sagittarius-Carina spiral arm. Avedisova (1988) has studied the star-forming regions along the arm between $l = 280^\circ - 025^\circ$ and finds that they naturally group into three segments. Two of the complexes (labelled A and B) contain most of the extremely young clusters and the most luminous H II regions. Sandwiched between them, the third segment (C) contains only older clusters (estimated to be older than $10^{7.5}$ yr) and

a small number of faint H II regions excited by the B stars in the clusters, despite it covering an approximately equal area on the sky to each of areas A and B. The hypothesis is that shells and shocks powered by stellar winds and supernovae explosions from the O stars which must originally have been present in segment C, resulted in the triggering of star formation in the neighbouring areas A and B. Again note that in this case the age progression is not *across* the arm as would be expected if the star formation was triggered by a spiral density wave, but rather *along* it, consistent with the hypothesis of stochastic propagating star formation.

Although limited by the spatial resolution available, further evidence can be gleaned from external galaxies as well. Radio observations of the irregular galaxy NGC 1569 at 1.5 GHz and 8.4 GHz (Wilding *et al.* 1993) suggest that the two extremely luminous clusters seen optically in the centre of the galaxy have ceased to form stars – however two adjacent regions do show up as thermal continuum radio sources, including some areas which are optically thick at 1.5 GHz suggesting that in these areas we see current star formation which is propagating outwards from the bright clusters.

Many reviews of the observational evidence for propagating star formation are available – see for example Elmegreen (1992) and references therein.

2.1.2 Computer models

The first computer simulations based on this idea (which they named Self-Propagating Star Formation, SPSF) were performed by Mueller & Arnett (1976). Galaxies were modelled on a two-dimensional polar grid, consisting of approximately 2500 cells which rotated differentially. Each cell was labelled to indicate whether star formation was currently occurring within it, and if not, how long it had been since the previous star formation episode. At the next discrete timestep (25 Myr), all cells which bordered a cell containing a newly formed star cluster would themselves undergo star formation, provided that the time elapsed since the last creation event was greater than some regeneration time (chosen to be between 3 and 10 timesteps). The cell containing the star cluster doing the triggering was then re-labelled as not undergoing current star formation, and its elapsed time counter reset. Star formation could also occur spontaneously, modelled by randomly choosing cells at each timestep to be considered as undergoing star formation, normally at the level of 1% of the total number of cells. The simulation was initiated by sprinkling new stars at random across the grid. Spiral density waves could also be incorporated in a primitive way by simply reducing the regeneration time along the arms.

The results showed ragged, flocculent structures with no realistic spiral structures reproduced. If a strong spiral density wave was imposed (i.e. a large difference in the arm and inter-arm regeneration times) then the images improved, although it was still not possible to reproduce a classic two-armed grand-design spiral. But most importantly, no quantitative link between the model and its input parameters with observational data was established.

The work of Mueller & Arnett was developed and much enhanced by Gerola & Seiden (1978). They introduced the idea of Stochastic Self-Propagating Star Formation (SSPSF), that is the pres-



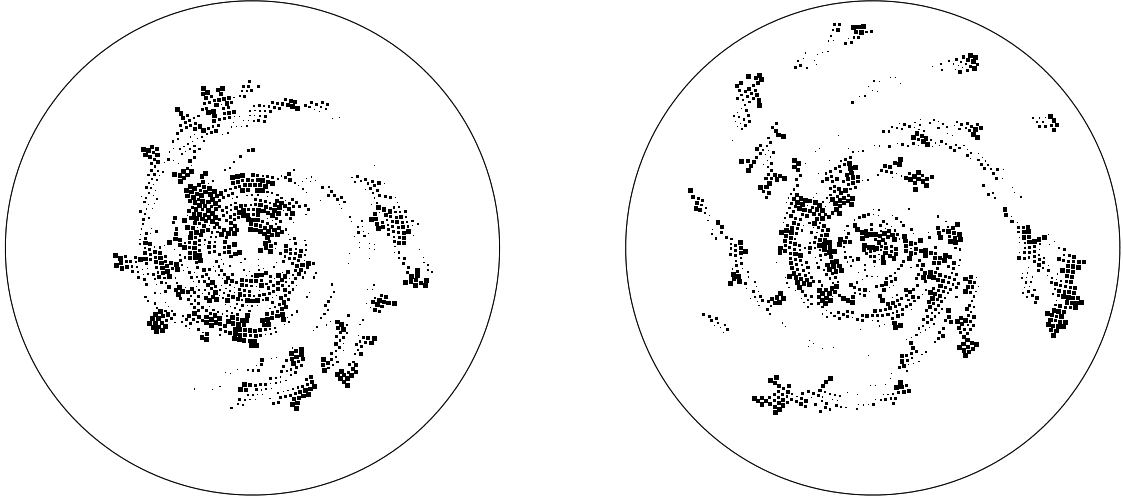
ence of a newly formed star no longer implied that star formation would *definitely* occur in neighbouring clouds. Rather, star formation was a stochastic process with a well defined probability that star formation would occur in a cell, given that there existed a nearby, new star cluster, of the form $P = P_{\text{st}} t / \tau$ where P_{st} was an input parameter to the model, t was the time elapsed since the previous star formation episode and τ was now known as the ‘refractory time’ rather than the ‘regeneration time’. In addition the number of cells used was much larger (7350) to reduce the influence of edge effects. In all other respects this new model was basically the same as its predecessor. This so called ‘stellar-model’ produced spiral structures which looked far more realistic than those of Mueller & Arnett: however, the same criticisms apply – only flocculent spirals could be modelled and there was no attempt to compare with observations in a quantitative manner. Interestingly, as a consequence of its stochastic nature it demonstrated the usual properties associated with a percolating system (see §2.1.3 and Schulman & Seiden 1983).

The next development was the incorporation of interstellar gas into an SSPSF model. Stars result from the gravitational collapse of gas, and so clearly any useful model must represent this process in some form. The new ‘gas-model’ (Seiden & Gerola 1982) was based on the same grid as that used by the earlier models, but now each cell contained two gas components as well as (possibly) new star clusters. The gas components for the purpose of the simulation were labelled ‘active’ and ‘inactive’, with the probability of star formation, given the presence of a nearby supernova, being $P = P_{\text{st}} \rho_{\text{active}}^n$, where ρ_{active} is the density of ‘active’ gas. Note that this is assuming a Schmidt law (Schmidt 1959, 1963) type dependency for the star formation rate, i.e. the star formation rate is assumed to have a simple power-law dependence on the local gas density. If star formation did occur in a cell then all the gas became ‘inactive’ but was converted to ‘active’ again as the simulation progressed with a characteristic timescale τ . The total gas was distributed as an exponential disc with scale length chosen such that the star formation rate naturally tended to zero at the circumference of the grid, to reduce edge-effects arising from the finite, discrete nature of the simulation. A subsequent paper (Seiden 1983) re-interpreted the SSPSF mechanism as a two-step star formation process. The first is the creation of molecular clouds, and the second the formation of stars from the subsequent collapse of the cloud. This latter step occurs rapidly and (in the model) is guaranteed to occur. Therefore it is the formation of clouds that constitutes the rate-determining step and hence the ‘active’ gas can be identified as H I, i.e. the gas from which the clouds form and the ‘inactive’ as H II since once the gas is in this form there is nothing that can be done to enhance star formation in the cloud.

A more detailed review of the SSPSF gas-model can be found in Seiden & Schulman (1990).

This form of the model was used to investigate a wide range of galactic structures ranging from large spirals to dwarf galaxies. The applicability of this model to dwarf galaxies must however be limited by edge effects – it was in an attempt to avoid such problems that Seiden & Gerola used a larger grid than Mueller & Arnett. Nonetheless, grids with as few as seven cells were used (Gerola *et al.* 1980) – the star formation rate in such systems was found to be oscillatory. I used my own codification of the model (Sleath 1992) to investigate the generation of starbursts, i.e. episodes

Figure 2.1. Typical output from my codification of the SSPSF gas-model. The symbol size indicates the age of the cluster (largest being youngest and therefore brightest) and the circle delineates the edge of the grid.



of extremely rapid, unsustainable star formation which observations (Wynn-Williams 1986) had suggested often occur in systems of two or more interacting galaxies. Specifically, I introduced a radial infall of gas following a suggestion by Mihos *et al.* (1991) that such a flow is a consequence of the interaction of two galaxies. Star bursts could indeed be produced in this manner. Other N-body simulations (Olson & Kwan 1986) suggested that the gravitational interactions between galaxies led to starbursts through an enhancement in the collisional rate for molecular clouds. This was approximated in the simulations by enhancing the spontaneous star formation rate, but it was not found that starbursts could be induced in this manner.

The most recent studies using an SSPSF code are due to Jungwiert & Palouš (1994) who incorporated an anisotropic spatial probability distribution in an attempt to represent the differential shearing of the material swept up by supernova shocks. Rather than the triggering shock wave expanding spherically from the supernova centre, the shock front expands as an ellipse with eccentricity defined as an input to the model. The authors postulate that the Hubble sequence Sa-Sb-Sc-Sd-Sm-Irr follows from the variation of the eccentricity of the probability ellipse, and suggest that they can reproduce galaxy types which are modelled poorly by standard SSPSF. Once again however, it is flocculent and not grand-design spirals which are produced.

2.1.3 Percolation theory – a digression

Percolation theory, which was first introduced into the mathematical literature by Broadbent & Hammersley (1957), provides a simple theoretical framework for the study of a wide range of disordered, stochastic processes. Table 2.1 (reproduced here from Zallen 1983) lists some physical applications to which percolation theory has been successfully applied. Note that the range



Table 2.1. Applications of percolation theory. Table reproduced from Zallen (1983).

Phenomenon or system	Transition
Flow of liquid in a porous medium	Local/extended wetting
Spread of disease in a population	Containment/epidemic
Communication or electrical networks	Disconnected/connected
Conductor-insulator composite materials	Insulator/metal
Composite superconductor-metal materials	Normal/superconducting
Discontinuous metal films	Insulator/metal
Stochastic star formation in spiral galaxies	Nonpropagation/propagation
Quarks in nuclear matter	Confinement/nonconfinement
Thin helium films on surfaces	Normal/superfluid
Metal-atom dispersions in insulators	Insulator/metal
Dilute magnets	Para/ferromagnetic
Polymer gelation, vulcanisation	Liquid/gel
The glass transition	liquid/glass
Mobility edge in amorphous semiconductors	Localised/extended states

of scale-lengths involved spans some ~ 35 orders of magnitude, all the way from quark confinement in the nucleus (characteristic size 10^{-15} m) to star formation in galaxies (characteristic size 10^{20} m). Also note that the majority of applications come from solid-state physics and are related to phase transitions between states; it is the presence of a natural phase transition within percolation theory that makes it useful for investigating such systems.

For a detailed mathematical treatment there are a number of textbooks available (e.g. Grimmett 1989) – however, a useful feel for the ideas involved can be gained from considering a forest fire, a simple example which lends itself well to percolation studies. The rate at which such a fire spreads through the forest depends on many environmental conditions, for example the wind strength, local topography (fires travel faster uphill), age and type of trees (thick bark is more fire resistant) and recent rainfall. However, we can group all these factors together into a single constant P , the probability of the fire spreading from one tree to any of its nearest neighbours. A forest is modelled as a two-dimensional lattice (usually either square or triangular) with each vertex a tree. Trees can be in one of four states; (i) unburnt, (ii) burning, (iii) ‘warm’ (i.e. unburnt but adjacent to burning trees) and (iv) burnt, and hence not re-ignitable. The simulation is begun with one tree burning at the centre of the grid.

Clearly if $P = 1$ then the whole forest will be consumed whereas if $P = 0$ then the fire will not spread at all. For a percolating system there is a critical probability P_c for which the number of burning trees at any given time is approximately constant. For $P < P_c$ the number of burning trees tends to zero as time $t \rightarrow \infty$, whereas for $P > P_c$ then the number rises linearly with time (MacKay

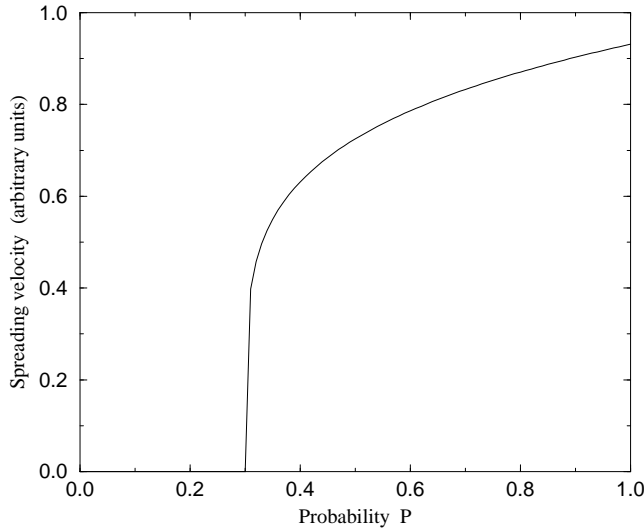


Figure 2.2

Example shape of the forest fire spreading speed as a function of the percolation probability P . The curve is plotted for $P_c = 0.3$ and critical exponent $\beta = 0.2$. For $P < P_c$ the fire dies out completely.

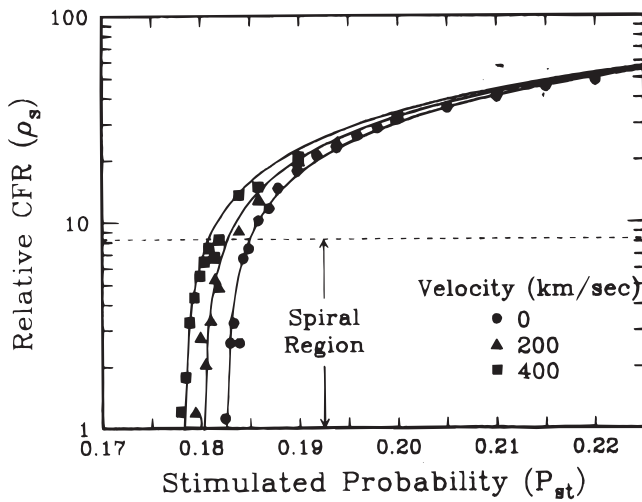


Figure 2.3

The phase transition in the star formation rate exhibited by the stellar SSPSF model as a function of the circular rotation velocity. Figure reproduced from Seiden & Gerola (1982) – the region of phase space deemed by them to exhibit good spirals is marked with a dashed line.

& Jan 1984). Equivalently the fire will reach the boundary of the grid in half of all realisations if $P = P_c$ (von Niessen & Blumen 1986). If we consider the asymptotic value of the spreading speed of the fire, v , then at $P = P_c$ the system undergoes what is known as a ‘percolation phase transition’ when the asymptotic spreading speed suddenly takes on non-zero values (Fig. 2.2). In common with other critical phenomena, for $P > P_c$ the spreading velocity is characterised by a critical exponent such that $v \propto (P - P_c)^\beta$, where β is a function of the exact nature of the system under consideration (i.e. the form of the grid and its dimensionality) (Ohtsuki & Keyes 1986).

The SSPSF stellar model is a much modified percolation process from the simple example above. For example, the grid on which the percolation is occurring is rotating differentially, and any given site can undergo star formation many times, with the only proviso being that a refractory time must elapse between subsequent events. However, it nonetheless demonstrates many of the characteristic features of the simple percolation. Figure 2.3 shows the variation of the star



formation rate with P_{st} – it shows a clear phase transition at a critical value for P_{st} which is a function of the refractory time used. The added complexity of the SSPSF gas model tends to blur the phase transition somewhat – there still exists a critical value of P_{st} , but the rise in SFR is much less rapid. My experiments with this model also suggested that the finite size of the grid also softened the phase transition, an effect known from more ‘traditional’ percolation studies. A detailed study of the percolation aspects of the SSPSF models is to be found in Schulman & Seiden (1983).

Although the new model (to be described in Chapter 3) is based on similar principles to the SSPSF models of Seiden, Gerola and Schulman, it incorporates a considerably more detailed representation of the propagating star formation mechanism, and perhaps more significantly, an attempt has been made to simulate the complicated dynamics of the ISM. Hence it is sufficiently far removed from a simple percolation model that the techniques developed for analysing percolation processes are unfortunately no longer useful.

2.2 Other galaxy models

The vast majority of galactic models have focussed on the dynamics of the stellar, and more recently, gaseous components, with in general little emphasis placed on star formation and its implications for galactic structure. The simulations divide naturally into two categories: N-body codes in which a collection of self-gravitating particles evolve under the Newtonian equations of motion, and hydrodynamic codes in which a continuous fluid is represented as discrete elements and allowed to evolve according to the appropriate equations for a compressible fluid. I will discuss N-body simulations first.

2.2.1 N-body codes

Many astrophysical systems have been investigated with N-body codes ranging in scale from small clusters of stars through globular clusters and galaxies to cosmological structures. Such models consider the systems of interest to be a collection of self-gravitating points with the simulation proceeding by calculating, at each discrete time-step, the force on each particle due to every other thus allowing the particle’s position and velocity to be updated. The most elementary method for doing this is the so called Particle–Particle (PP) approach where the total force is considered as the vector sum of all the two-body interactions. In its simplest form we have

$$\begin{aligned}\mathbf{F}_i &= \sum_{j, j \neq i} \mathbf{F}_{ij}, \\ \mathbf{v}_i^{\text{new}} &= \mathbf{v}_i^{\text{old}} + \frac{\mathbf{F}_i}{m_i} \Delta t, \\ \mathbf{x}_i^{\text{new}} &= \mathbf{x}_i^{\text{old}} + \mathbf{v}_i \Delta t,\end{aligned}$$

(Hockney & Eastwood 1981). There are however problems with this technique. The first is relaxation of the system due to close encounters. A real galaxy is essentially a collisionless system

at least as far as the stellar dynamics are concerned. However by representing a galaxy with, say, 10^5 particles rather than the 10^{11} required for one per star we increase the mass of each particle relative to the total by many orders of magnitude. This leads to a corresponding rise in the minimum impact parameter and frequency of strong deflections and the resulting scattering causes an unphysical dynamical relaxation of the system. To reduce this a ‘softened’ potential of the form

$$\phi = -\frac{GM}{(r^2 + \varepsilon^2)^{1/2}} \quad (2.1)$$

is generally used, essentially replacing the point masses by finite sized particles (Sellwood 1987). However a more fundamental restriction on the use of the direct N-body simulations is their scaling with increasing particle number N , the computational effort required increasing $\propto N(N-1)$. Many refinements of the naïve implementation are possible: the use of force polynomials to allow higher order integration using information from several previous epochs increases the accuracy available for given Δt , or alternatively, a larger Δt (and thus faster simulation) for the same level of accuracy. Regularisation (Stiefel & Scheifele 1971) permits a more rigorous treatment of close encounters by transforming the non-linear equation of motion ($\ddot{x} \propto x^{-2}$) to a linear form ($u'' \propto u$) via the relations $x = u^2$ and $d\tau = dx/x$, although this is more important for small N collisional systems. Finally choosing an individual time-step for each particle according to its circumstances (large Δt if the potential is smooth, small if it’s varying rapidly) can again lead to substantial improvements in the speed of the code. For a recent summary of such techniques see Aarseth (1994). However for $N \geq 10^4$ the time penalty associated with a direct integration method is too severe, and other approaches must be adopted.

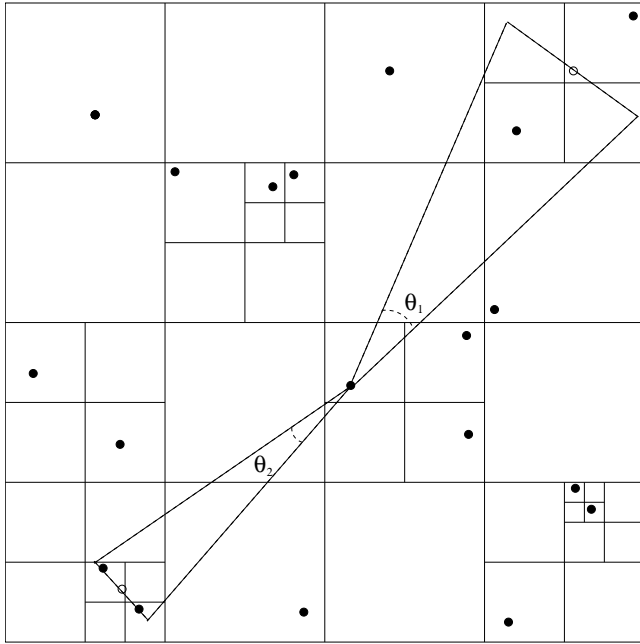
The Particle–Mesh (PM) approach differs from PP in the method used to calculate the inter-particle forces: rather than a direct sum, the particles are gridded into M cells (typically with $M \approx N$) and each cell assigned the corresponding total mass. Poisson’s equation is solved at the centre of each cell using a Fast Fourier Transform (FFT):

$$\rho(x) \xrightarrow{\text{FFT}} \tilde{\rho}(k) \xrightarrow{k^2} \phi(k) \xrightarrow{\text{FFT}} \phi(x) \xrightarrow{\nabla} g(x)$$

where ρ is the mass density of the cell and g is the resulting gravitational field. The force for each particle is then interpolated from the grid. The main advantage of this method is that the time required now scales as $O(M \log_2 M)$ (Press *et al.* 1992), but with the penalty of reducing the spatial resolution to that of the mesh, or worse when allowance is made for numerical errors. Moreover, the grid can impose an artificial geometry on the simulation and problems will be encountered if material should escape from the grid as the simulation proceeds. Some attempts have been made to combine multiple grids in an effort to overcome the resolution problem (for example in modelling two interacting galaxies, James & Weeks 1986) but this cannot be used in general when the locations of regions of particularly high particle density are unknown *a priori*.

A hybrid approach, the Particle–Particle–Particle–Mesh (P³M) combines some of the advantages of both the PP and PM techniques by directly summing the force from nearest neighbours and using the PM method for larger distances. The resulting codes are faster than PP and have much



**Figure 2.4**

Schematic illustrating the partition of a distribution of particles (filled circles) in a tree-code simulation. The angles θ_1 and θ_2 show the angle subtended by two cells of different size with centre-of-masses indicated by open circles. Figure based on Aarseth (1993).

greater spatial dynamic range than PM. The restrictions due to the fixed grid still apply though, and the PP calculations for nearest neighbours result in code which is considerably slower than PM. The technique has been successfully applied to systems with particularly large contrasts in density such as cosmological simulations of the early universe (Baugh & Efstathiou 1994; Efstathiou *et al.* 1985).

The most efficient methods, however, for dealing with large N are based on so called tree-codes. The system is partitioned into cells starting from the ‘root’ which contains all the particles. Using the Barnes–Hut (1986) formulation, subdivisions by factors of two (in length) are performed until each cell contains only one particle, thus building an oct tree (8 descendants per node in three dimensions) with each node representing a physical volume of space and containing information giving the total mass and position of centre-of-mass for the volume. (Fig. 2.4). The total force on any given particle is calculated by descending the tree from the root considering the angle subtended by the cells at the current level, $\theta = s/r$ where s is the size of the cell and r is the distance to its centre-of-mass from the particle in question. For some specified critical opening angle, θ_c , if $\theta < \theta_c$ then the force on the particle due to that cell is expressed as a multipole expansion about the cell’s centre-of-mass using a softened potential of the same form as equation 2.1 above. Clearly this condition will not generally be satisfied for the largest cells, in which case the descendants are considered until either a) a single particle is found or b) the angle subtended becomes sufficiently small. The accuracy that can be obtained in this manner is a compromise between critical angle θ_c and the order of the multipole expansion used. The method again scales as $O(N \log N)$ and it is now the preferred method for large N . A more detailed description of the traditional tree-code method can be found in Hernquist (1987). More recently McMillan & Aarseth (1993) have introduced a collisional tree-code method incorporating the refinements discussed above for the

PP method, including a high-order integration scheme, variable time-steps and regularisation to deal with close approaches, enhancing the accuracy obtainable at the expense of speed – only for $N \gtrsim 10^4$ does the new code out perform a direct approach.

2.2.2 SPH and hybrid schemes

An alternative to the ‘traditional’ N-body approaches, Smoothed Particle Hydrodynamics (SPH), was introduced by Lucy (1977) and Gingold & Monaghan (1977) as a technique for modelling continuous fluids. The equations of motion are solved using a Lagrangian formulation in which the fluid is represented by a collection of particles with the particle mass density proportional at any given point in space to the fluid density ρ . Clearly the number of particles is finite and hence to estimate ρ (and quantities related through the equations of motion) at later times it is necessary to interpolate between them to represent the smooth, continuous fields. If each particle has a mass m_i then

$$\rho(\mathbf{r}) = \sum_{i=1}^N m_i W(\mathbf{r} - \mathbf{r}_i, h)$$

where $W(\mathbf{r}, h)$ is an appropriate smoothing kernel and h is the smoothing length. Many kernels have been used in SPH codes; the easiest to interpret physically is Gaussian (Gingold & Monaghan 1977),

$$W(x, h) = \frac{1}{h\sqrt{\pi}} e^{-(x^2/h^2)}$$

whilst the form currently most favoured is based on spline functions (Monaghan & Lattanzio 1985). For further information on the implementation of SPH codes, including a derivation of the hydrodynamical equations expressed in terms of particle motions see Monaghan (1992).

One of SPH’s inherent advantages is that it is naturally adaptive with what is effectively a variable geometry grid to cope with regions with high density contrast. Codes have also been written in which the smoothing length h is itself variable both in space (thus varying the spatial resolution) and time (permitting each particle to have its own timestep to reduce unnecessary computation for a given accuracy), although doubts have been raised over the reliability of codes incorporating variable smoothing length (Hernquist 1993).

Recent studies employing SPH codes have ranged over the full range of astrophysical scales including; the impact of comet Shoemaker–Levy into Jupiter (Takata *et al.* 1994), merging neutron stars (Davies *et al.* 1994), accretion disks (Chakrabarti & Molteni 1995), collisions between clouds in the ISM (Habe & Ohta 1992), chemical evolution of the Galactic bulge (Tsujimoto *et al.* 1993), galaxy clusters (Metzler & Evrard 1994) and the formation of large-scale structure in the early universe (Navarro & White 1993). Plus, of course, spiral structure in normal galaxies (Patsis *et al.* 1994).

Smoothed particle hydrodynamics has been combined successfully with gravity tree-codes by Hernquist & Katz (1989), allowing a galactic model incorporating both evolution of a stellar component (tree-code to calculate inter-particle forces) and an ISM (using SPH). This formulation has



been employed in models of disk galaxy mergers (e.g. Hernquist & Weil 1993; Mihos & Hernquist 1994a) and galaxy formation (Katz & Gunn 1991; Katz 1992). Moreover, it is one of the only models based on an N-body/SPH approach which has been used to explicitly model star formation on a galactic scale (Mihos & Hernquist 1994b). The details of the mechanism, however, are not considered at all – the star formation rate is simply related to the local gas density through a Schmidt Law (Schmidt 1959, 1963), and is not in any way a consequence of the simulation. As will be shown below (§4.3), the new model presented here *predicts* a Schmidt Law on the basis of a simple model of the star formation process (Chapter 3).

References

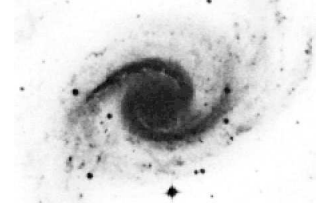
- Aarseth S. J., 1993, lecture notes from EADN Astrophysics School VI, Thessaloniki, unpublished
- Aarseth S. J., 1994, in *Galactic Dynamics and N-body Simulations*, eds Contopoulos G., Spyrou N. K., Vlahos L., Springer-Verlag, Berlin
- Avedisova V. S., 1988, in *Evolution of Galaxies, Proc. Eur. Reg. Meet. Astron. no. 10*, ed. Palouš J., p. 171, Publ. Inst. Czech Acad. Sci.
- Baade W., 1963, in *Evolution of Stars and Galaxies*, ed. Payne-Gaposchkin C., chap. 16, Harvard University Press
- Barnes J., Hut P., 1986, *Nature*, 324, 446
- Baugh C. M., Efstathiou G., 1994, *MNRAS*, 270, 183
- Blaauw A., 1984, *Irish Astron. J.*, 16, 141
- Broadbent S. R., Hammersley J. M., 1957, *Proc. Cambridge Phil. Soc.*, 53, 629
- Chakrabarti S. K., Molteni D., 1995, *MNRAS*, 272, 80
- Davies M. B., Benz W., Piran T., Thieleman F. K., 1994, *ApJ*, 431, 742
- Efstathiou G., Davis M., Frenk C. S., White S. D. M., 1985, *ApJS*, 57, 241
- Elmegreen B. G., 1985, in *Birth and Evolution of Massive Stars and Stellar Groups*, eds Boland W., van Woerden H., p. 227, D. Reidel Publishing Company
- Elmegreen B. G., 1991, in *Evolution of Interstellar Matter and Dynamics of Galaxies*, eds Palouš J., Burton W. B., Lindblad P. O., Cambridge University Press
- Elmegreen B. G., 1992, in *Star Formation in Stellar Systems*, eds Tenorio-Tagle G., Prieto M., Sánchez F., p. 381, Cambridge University Press
- Elmegreen B. G., Wang M., 1988, in *Molecular Clouds in the Milky Way and External Galaxies*, eds Dickman R. L., Snell R. L., Young J. S., Springer-Verlag, Berlin
- Gerola H., Seiden P. E., 1978, *ApJ*, 223, 129
- Gerola H., Seiden P. E., Schulman L. S., 1980, *ApJ*, 242, 517
- Gingold R. A., Monaghan J. J., 1977, *MNRAS*, 181, 375
- Grimmett G., 1989, *Percolation*, Springer-Verlag, NY
- Habe A., Ohta K., 1992, *Proc. Ast. Soc. Japan*, 44, 203
- Hernquist L., 1987, *ApJS*, 64, 715
- Hernquist L., 1993, *ApJ*, 404, 717
- Hernquist L., Katz N., 1989, *ApJS*, 70, 419
- Hernquist L., Weil M. L., 1993, *MNRAS*, 261, 804
- Heydari-Malayeri M., Testor G., 1983, *A&A*, 118, 116
- Heydari-Malayeri M., Niemala V. S., Testor G., 1987, *A&A*, 184, 300
- Heydari-Malayeri M., Magain P., Remy M., 1988, *A&A*, 201, L41
- Hobson M. P., Padman R., Scott P. F., Prestage R. M., Ward-Thomson D., 1993, *MNRAS*, 264, 1025
- Hockney R. W., Eastwood J. W., 1981, *Computer Simulation Using Particles*, McGraw-Hill

- James R. A., Weeks T., 1986, in *The Use of Supercomputers in Stellar Dynamics*, eds Hut P., McMillan S., Springer-Verlag, Berlin
- Jungwiert B., Palouš J., 1994, *A&A*, 287, 55
- Katz N., 1992, *ApJ*, 391, 502
- Katz N., Gunn J. E., 1991, *ApJ*, 377, 365
- Lucy L., 1977, *AJ*, 82, 1013
- MacKay G., Jan N., 1984, *J. Phys. A: Math. Gen.*, 17, L757
- McMillan S. L. W., Aarseth S. J., 1993, *ApJ*, 414, 200
- Meaburn J., Solomos N., Laspas V., Goudis C., 1989, *A&A*, 225, 497
- Metzler C. A., Evrard A. E., 1994, *ApJ*, 437, 564
- Mihos J. C., Hernquist L., 1994a, *ApJ*, 425, L13
- Mihos J. C., Hernquist L., 1994b, *ApJ*, 437, 611
- Mihos J. C., Richstone D. O., Bothun G. D., 1991, *ApJ*, 377, 72
- Monaghan J. J., 1992, *Ann. Rev. Astron. Astrophys.*, 30, 543
- Monaghan J. J., Lattanzio J. C., 1985, *A&A*, 149, 135
- Mueller M. W., Arnett W. D., 1976, *ApJ*, 210, 670
- Navarro J. V., White S. D. M., 1993, *MNRAS*, 265, 271
- Ohtsuki T., Keyes T., 1986, *J. Phys. A: Math. Gen.*, 19, L281
- Olson K. M., Kwan J., 1986, *ApJ*, 349, 480
- Öpik E. J., 1953, *Irish Astron. J.*, 2, 219
- Patsis P. A., Hiodelis N., Contopoulos G., Grosbøl P., 1994, *A&A*, 286, 46
- Press W. H., Teukolsky S. A., Vetterling W. T., Flannery B. P., 1992, *Numerical Recipes in FORTRAN*, Cambridge University Press, Cambridge, 2nd edn.
- Schmidt M., 1959, *ApJ*, 129, 736
- Schmidt M., 1963, *ApJ*, 137, 758
- Schulman L. S., Seiden P. E., 1983, *Ann. Israel Phys. Soc.*, 5, 251
- Seiden P. E., 1983, *ApJ*, 266, 555
- Seiden P. E., Gerola H., 1982, *Fundam. Cosmic Phys.*, 7, 241
- Seiden P. E., Schulman L. S., 1990, *Advances in Physics*, 39, 1
- Sellwood J. A., 1987, *Ann. Rev. Astron. Astrophys.*, 25, 151
- Sleath J. P., 1992, Dissertation submitted towards BA Natural Sciences (Physics and Theoretical Physics), University of Cambridge, not published
- Stiefel E. L., Scheifele G., 1971, *Linear and Regular Celestial Mechanics*, Springer-Verlag, New York
- Takata T., Okeefe J. D., Ahrens T. J., Orton G. S., 1994, *Icarus*, 109, 3
- Tsujimoto T., Nomoto K., Shigeyama T., Ishimaru Y., 1993, in *IAU Symposium 153*, p. 395, Kluwer, Dordrecht
- von Niessen W., Blumen A., 1986, *J. Phys. A: Math. Gen.*, 19, L289
- Wilding T., Alexander P., Crane P., Pooley G., 1993, in *Star Formation, Galaxies and the Interstellar Medium*, eds Franco J., Ferrini F., Tenorio-Tagle G., p. 301, Cambridge University Press
- Wynn-Williams C. G., 1986, in *IAU Symposium 115*
- Zallen R., 1983, *Ann. Israel Phys. Soc.*, 5, 3



Chapter 3

The model



In this chapter I discuss the physical basis underlying the model together with its implementation as a FORTRAN algorithm. The fundamental idea of the SSPSF approach is retained, and hence the detailed physics of the star formation process are largely subsumed into a single parameter M_{st} which plays a similar role to that of P_{st} in the simple SSPSF models (§2.1.2). The gas dynamics of the ISM are, however, modelled in considerably greater detail than has previously been done with a propagating star formation model. First, I consider the reasons why supernova/supershell shocks are considered suitable triggers for massive star formation, followed by a description of the manner in which the physics of the shock–cloud interactions plus the gas dynamics are implemented. Finally, some of the finer details of the computer code are discussed.

3.1 The physics of propagating star formation

One of the principal advantages of the propagating star formation approach is its simplicity – the detailed physics are lumped together into a single parameter. It must be remembered however that we are not modelling all modes of star formation since we are stating that a shock is required to initiate the process. This scenario ties in well with the scheme envisaged for massive star formation from giant molecular clouds (GMCs) (Turner 1988), but is not appropriate for the creation of low mass stars from small clouds. In this latter case proto-stellar clumps are created as a result of dissipation through intra-cloud turbulence, and a shock is not required.

If we now consider the interaction of a shock wave with an interstellar cloud we find that on the largest scales (i.e. the complete front) a shock increases the internal kinetic energy of the cloud, stabilising it against collapse, and possibly disrupting it. Thus star formation is inhibited. However, on scales of order the front thickness the shock enhances the density increasing the dissipation–collapse rate proportional to $n^{1/2}$, where n is the number density of the cloud. An increased particle density also leads to a higher rate of ambipolar diffusion, i.e. the rate at which the redistribution of magnetic flux occurs through the movement of charged species relative to the neutrals in the lightly ionised (by cosmic rays) cloud gas. The ions experience electromagnetic forces directly whilst the



neutrals can only interact indirectly with the field through collisions with the ions. Since the net force on the ions must be zero, by equating the Lorentz force with that arising from inter-particle collisions it can be shown that the rate of ambipolar diffusion scales as $\sim B^2 n^{-3/2} L^{-2}$ (Shu 1992), where the ionisation fraction has been taken as $\propto n^{-1/2}$, appropriate if all recombinations occur in the gas phase and the ionisation rate is proportional to the gas density. Shocks parallel to the cloud's magnetic field conserve B and nL and hence the ambipolar diffusion rate is $\propto n^{1/2}$, whilst perpendicular shocks conserve B/n and nL and therefore the diffusion rate for the field is $\propto n^{5/2}$.

The third consequence of a local density enhancement is the removal of angular momentum from the cloud. As the gas is translated to form regions of increased density it does so preferentially along field lines and hence its rate of rotation does not vary. Its angular momentum is reduced by the resulting tension in the B-lines acting as a torque. Hence, by three distinct mechanisms energy is removed from the cloud (in turbulent, magnetic and rotational forms) resulting in a more gravitationally bound cloud which is thus more prone to collapse – the first crucial step towards the formation of new stars.

Consequently, the scenario for massive star formation is the Jeans collapse of a giant molecular cloud triggered by a loss of supporting pressure due to an impinging shock. Initially the collapse is isothermal, but as the opacity rises it tends towards adiabatic. Under these conditions the temperature of the gas post-shock is important since it determines the minimum mass of the stars that can be formed through the relation

$$M_{\min} = 0.01 \left(\frac{M}{M_{\odot}} \right) \left(\frac{T}{10\text{K}} \right)^{2+\delta} M_{\odot},$$

where T is the temperature of the cloud before the onset of the collapse and δ is a function of the grain composition, taking values in the range 1–2 (Turner 1988).

In contrast low mass star formation can proceed without external stimulus. If a molecular cloud (of size L) is stabilised by turbulence, then it will have supersonic internal motions according to the empirical turbulence law $\Delta v = 1.2(L/\text{pc})^{0.3} \text{ km s}^{-1}$ where Δv is the internal velocity dispersion of the cloud. Hence internal shocks will exist and as a result distinct sub-units of enhanced density will be created which may be small enough such that their internal motions are entirely subsonic. The shock condensation of further, smaller units is then halted, and instead the clumps simply collapse gravitationally on a timescale comparable to the free-fall time, as their remaining internal energy is dissipated. We can identify a minimum mass for this process also – assuming that the clumps are supported only by thermal pressure then knowing typical cloud temperatures allows the internal velocity dispersion (Δv) to be estimated which through the turbulence law, allows the size of such clumps to be determined. Furthermore if the clumps are in virial equilibrium then $\Delta v = 0.48(M/M_{\odot})^{0.188} \text{ km s}^{-1}$ permitting a minimum mass to be estimated. For subsonic clump temperature of 10 K the minimum clump size is $\sim 0.1 \text{ pc}$ and minimum mass is $\sim 0.12 M_{\odot}$ with large uncertainties (Turner 1988). This latter estimate is consistent with the observational fact that the IMF in the local vicinity shows a downward trend below $\lesssim 0.1 M_{\odot}$.

3.2 The implementation

The simulation uses three components to model a galaxy. These are

- (i) a diffuse gaseous component,
- (ii) gas clouds,
- (iii) star clusters and associations, the distinction being unimportant for this work.

The clouds and stars are represented as test particles moving in an overall galactic potential which has both axisymmetric and spiral components. The number of cloud particles is fixed (typically at 32 000) whilst the number of star particles is allowed to vary – usually about 15 000 star particles are followed at any time. Whilst the central bulge and halo contribute to the potential, these regions are not populated with particles in this model since star formation has essentially ceased in these areas. As a result any pictorial representation of the results from the model shows a central hole (e.g. Fig. 5.4).

Although it would be easiest simply to label the gas clouds as being H_2 and the diffuse gas as $H\text{ I}$, the model actually represents the ISM more realistically than this. As will be discussed below (§3.2.1), the clouds accrete from the diffuse gas component so that a reasonable picture of them would be a molecular core surrounded by an atomic hydrogen halo. This seems to be in accord with observations – direct measurements of nearby clouds that are resolved show molecular cores surrounded by atomic envelopes (Wannier, Lichten & Morris 1983; Elmegreen 1985) and on a larger scale, Elmegreen & Elmegreen (1987) find that many CO complexes are associated with $H\text{ I}$ clouds. Observationally, the mass fraction of the molecular component decreases with galactocentric distance (Burton 1988), which we model by having the number of clouds at a given radius follow the H_2 distribution (Fig. 5.9).

This model represents an attempt to simulate a steady-state system in order that the effects of the propagation mechanism, galactic dynamics and cloud growth can be studied without the additional complications associated with the overall evolution of the galactic system. The Milky Way has had an approximately constant star formation rate over the last few Gyr (Noh & Scalo 1990) and it is galaxies in this state that we wish to study here. This aim is reflected in a number of simplifying assumptions concerning, for example, the orbital dynamics, the tenuous component of the ISM and the disc temperature, all of which are discussed in more detail below.

3.2.1 The star formation mechanism

The basic concept behind the star formation mechanism employed is stochastic, self-propagating star formation in which we take the propagating mechanism to be the triggering of cloud collapse by a supershell shock. Such a shock wave arises from a combination of stellar winds and supernovae explosions due to the most massive stars in the association (Tenorio-Tagle & Bodenheimer 1988). In the model, each cluster site is the source for one such super-bubble and we assume that it is a potential trigger for star formation up to the point at which its radius reaches 200 pc. If such a



shock wave impinges on a nearby molecular cloud then there is a chance, with well-defined probability, that star formation will be triggered within the cloud. Star formation is complete within 10^6 yr, and hence we are only following the formation of the most massive stars. Lower mass star formation is not modelled explicitly but would be expected to continue over a much longer period ($\sim 10^7$ yr) (Bodenheimer 1992). Recent observations (Zinneker 1996) suggest that the initial mass function (IMF) of stars born in OB associations shows no truncation at low masses, and hence all stars may be born as part of OB associations, a suggestion originally made by Miller & Scalo (1978).

In general the probability of star formation occurring will be a complicated function of the prevailing physical conditions, but without modelling the detailed interior dynamics of the clouds, we can expect the dominant term to be that due to the mass of the clouds. In general we expect the probability to be expressible as a power series in the cloud mass:

$$P_{\text{st}} = \sum_{k=1} a_k \left(\frac{M_i}{M_{\text{st}}} \right)^k,$$

where M_i is the cloud mass, M_{st} is a scaling mass controlling the stimulated star formation and the coefficients a_k will in general depend on the pressure, temperature and velocity structure of the cloud. For simplicity we take only the leading term of this series and assign the probability of stimulated star formation to be

$$P_{\text{st}} = \frac{M_i}{M_{\text{st}}},$$

putting $a_1 = 1$. Star formation can also occur spontaneously – if a cloud grows too large, then star formation will occur without external stimulus. Again we assume that this process can also be expressed as a power series in M_i of which we retain only the leading term:

$$P_{\text{sp}} = \frac{M_i}{M_{\text{sp}}},$$

where in this case M_{sp} determines the rate of spontaneous star formation. In every simulation discussed in this dissertation $M_{\text{st}} \ll M_{\text{sp}}$, typically by six orders of magnitude – therefore, propagating star formation is always the dominant mechanism.

When star formation occurs, the molecular cloud is disrupted and its mass is reduced so that $M_i \rightarrow \epsilon M_i$ with $(1 - \epsilon)M_i$ locked into newly formed stars or dispersed into the neutral ISM. Typically we take $\epsilon = 10^{-3}$ – note that this is *not* the same as the star formation efficiency, a typical value for which would be ~ 1 –5% (Lada *et al.* 1992), it is simply the factor by which the cloud is disrupted. That is not to say that we would expect a cloud to be almost totally destroyed by star formation – the creation of intermediate- to low-mass stars would continue. However, this is the simplest manner in which to model the effects which are thought to occur in a cloud which prevent subsequent episodes of *massive* star formation.

Clouds are not however destroyed permanently by a star formation episode. As each cloud orbits the galaxy it accretes matter from the interstellar H I, such that its mass is a function of the time elapsed since the most recent episode of star formation. Since the model is not concerned

with the evolution of the galaxy as a whole but rather with the development and rate of the star formation process, we consider the tenuous H I component to be fixed both spatially and in total mass. Processes such as stellar mass loss and the disruption of clouds are assumed to be capable of maintaining the constant H I distribution, although they are not modelled in detail.

We consider the accretion rate by the clouds of material from the ISM to be proportional to the cloud velocity, and hence

$$\dot{M}_i \propto \Sigma_i v \rho_{\text{HI}},$$

where Σ_i is the cloud cross-section. Since $\Sigma_i \propto M_i^{\frac{2}{3}}$ for a cloud of uniform density this gives

$$\dot{M}_i \propto M_i^{\frac{2}{3}} v \rho_{\text{HI}},$$

and hence

$$M_i(t) = (\gamma \rho_{\text{HI}} v t)^3 + \text{initial mass}. \quad (3.1)$$

The constant γ is chosen by comparison with Galactic values – we require a mean cloud growth time of $\sim 2 \times 10^8$ yr (Kwan & Valdes 1987) when typical values of ρ_{HI} (Burton 1988) and v (Stark & Brand 1989) are used. The interstellar H I is distributed in a manner appropriate for our Galaxy (Burton 1988), and remains unchanged as the simulation proceeds.

Ten million years after the formation of a star cluster, the O/B stars contained within it will explode as supernovae (SNe). We are interested in the formation of massive stars – in our model therefore, all star clusters act as progenitors for SNe. The expanding shell, which remains centred on the star cluster, is responsible for triggering subsequent star formation if it encounters a nearby cloud with sufficient mass. The shock is followed for a further 10^7 years (with radius increasing $\propto t^{2/5}$, i.e. adiabatic expansion) after which time it is considered to be too weak to trigger star formation. This corresponds to a maximum propagation radius of 200 pc, and is consistent with the size of supershells within our own Galaxy (Tenorio-Tagle & Bodenheimer 1988).

Note again that the star formation mechanism is purely self-propagating; there are no triggering effects from, for example, spiral shocks. In the next section we discuss the dynamics of the model – the clouds move in a gravitational potential which includes a component from a spiral density wave (SDW), the effect of which is to enhance the H_2 cloud density in the vicinity of the arm, and thus increase the chance that a supernova shock will cause stars to be formed.

3.2.2 The galactic potential and the SDW

Although the cloud particles are each assigned a mass, this is only used in the implementation of the propagating star formation mechanism. Both star and cloud particles orbit as test masses in an axisymmetric galactic potential due to Allen & Santillán (1991) upon which is superposed a spiral perturbation. The axisymmetric potential is considered to arise from three mass components:

- (i) a central bulge,

$$\phi_1(r, z) = \frac{-M_1}{(r^2 + z^2 + b_1^2)^{\frac{1}{2}}};$$



M_1	$1.41 \times 10^{10} M_\odot$
b_1	0.3873 kpc
M_2	$8.56 \times 10^{10} M_\odot$
a_2	5.3178 kpc
b_2	0.2500 kpc
M_3	$1.071 \times 10^{11} M_\odot$
a_3	12.0 kpc

Table 3.1

Constants defining the Galactic potential. Reproduced from Allen & Santillán (1991).

(ii) a disc component,

$$\phi_2(r, z) = \frac{-M_2}{\{r^2 + [a_2 + (z^2 + b_2^2)^{\frac{1}{2}}]^2\}^{\frac{1}{2}}};$$

(iii) and a spherical halo,

$$\phi_3(R) = -\frac{M_3 R^{1.02}}{a_3^{2.02}} \left[1 + \left(\frac{R}{a_3} \right)^{1.02} \right] - \frac{M_3}{1.02 a_3} \left\{ \frac{-1.02}{[1 + (\frac{R}{a_3})^{1.02}] + \ln \left[1 + \left(\frac{R}{a_3} \right)^{1.02} \right]} \right\}_R^{100 \text{ kpc}},$$

where,

$$R = \sqrt{r^2 + z^2}.$$

The constants a_2 , a_3 , b_1 , b_2 , M_1 , M_2 and M_3 (Table 3.1) are determined by considering the Galactic rotation curve and the orbits of stars with a large z -velocity, such that they sample the potential over a large volume. As such, the potential they produce is only strictly appropriate for an Sbc galaxy such as our own. The rotation curve is shown as Fig. 3.1 together with observational constraints from Allen & Martos (1986). Note also that the potential is well behaved everywhere (Fig. 3.2) and that the corresponding density is positive at all points, unlike certain other commonly used galactic potential models, for example that due to Ollongren (1962).

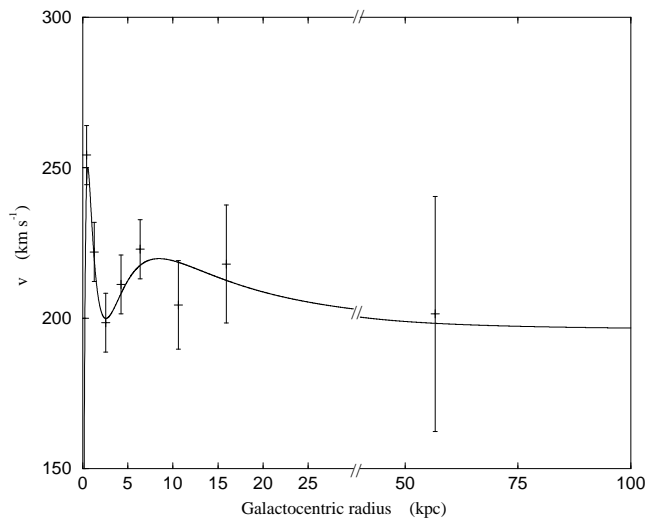
Superimposed on this potential is a logarithmic spiral component:

$$\phi_4 = -\frac{Ar^2}{(a_4^2 + r^2 + z^2)^2} \cos[n\theta - n\Omega_p t + \chi(r)],$$

where n is the number of arms, Ω_p is the pattern speed and $\chi(r)$ is the spiral shape function,

$$\chi(r) = \frac{\ln \left[1 + \left(\frac{r}{r_0} \right)^p \right]}{p \tan i_0}.$$

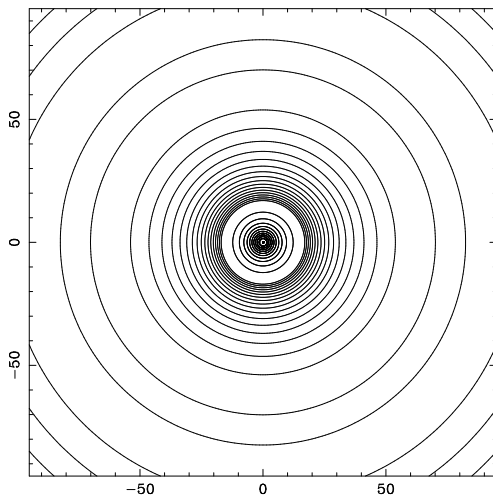
The spiral is barlike for $r < r_0$ and spiral outside, whilst p determines the sharpness of this transition. The pitch angle is defined as the angle, at the point of intersection between the spiral and a circle, of the respective tangents. Figure 3.3 shows the initial position of the crest of the potential perturbation.

**Figure 3.1**

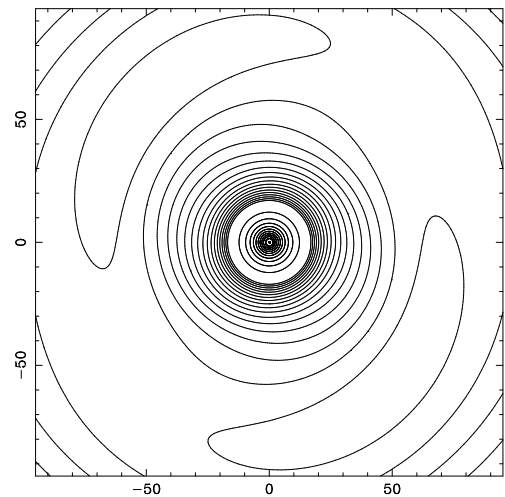
The Galactic rotation curve. The solid curve is derived from the potential model of Allen & Santillán (1991) and the points with error bars are observational constraints (Allen & Mar-tos 1986).

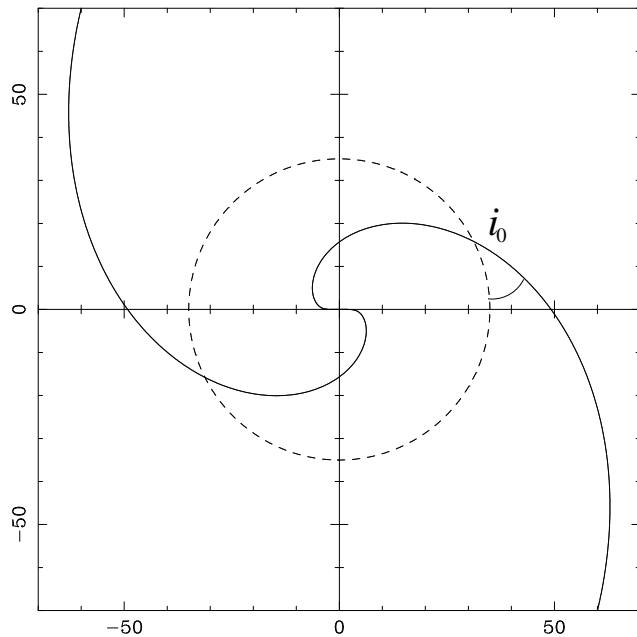
Figure 3.2. The gravitational potential. Shown are equipotential contours for two cases: (a) unperturbed, axisymmetric field and (b) with a spiral density wave of amplitude $0.08 \text{ pc}^4 \text{ yr}^{-2}$ superposed. Contours are plotted every $10^{10} \text{ m}^2 \text{ s}^{-2}$ from -1.8×10^{11} to $-7.0 \times 10^{10} \text{ m}^2 \text{ s}^{-2}$ and every $10^9 \text{ m}^2 \text{ s}^{-2}$ between -7.0×10^{10} and $-5.0 \times 10^{10} \text{ m}^2 \text{ s}^{-2}$. Axes are labelled in units of 200 pc.

(a)



(b)



**Figure 3.3**

The position of the crest of the SDW at time $t = 0$. The spiral is described by $n = 2$, $i_0 = 20^\circ$, $p = 5.0$ and $r_0 = 5.0 L$ (see Appendix A for a description of ‘model’ units).

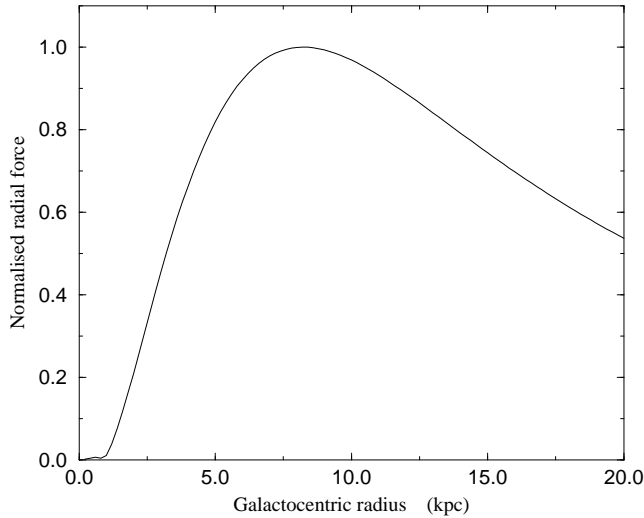
The constant a_4 is chosen such that the strength of the SDW peaks at a radius of 7 kpc (Roberts & Hausman 1984) whilst A is typically fixed such that the SDW contributes about 5% of the total radial force – for a given SDW amplitude the maximum relative strength of the perturbation is given by

$$\frac{\text{max SDW contribution to radial force}}{\text{total radial force}} = 0.56045 \left(\frac{A}{\text{pc}^4 \text{ yr}^{-2}} \right)$$

whilst the radial variation of the SDW contribution, normalised against the maximum value ($r = a_4$) is shown as Fig. 3.4.

Until the 1950s the majority consensus was that the arms of spiral galaxies were in some way a consequence of the galactic magnetic field. Lindblad however deduced that the spiral structure results from dynamical interactions between stellar orbits and the overall galactic potential. A formulation based on density waves was introduced by Lin & Shu (1964; 1966) – in particular they proposed that spiral arms were the visible effects of a quasi-stationary density wave. It is their hypothesis which underlies the treatment of spiral waves in most current studies of galactic structure and dynamics, including the current model.

A full N-body simulation would not require the spiral component of the potential to be implemented in this somewhat artificial manner, since an SDW arises as a natural instability of a thin, differentially rotating disc in such experiments (Thomasson *et al.* 1990), a fact also predicted by perturbation analysis (Binney & Tremaine 1987) and even laboratory experiments (Nezlin *et al.* 1986). Furthermore, although our potential is constant, we would expect the strength of the wave to vary as a function of time, for example, as a consequence of swing amplification. Nevertheless, current observations support the Lin–Shu hypothesis of a quasi-stationary wave, which is modelled satisfactorily by using a fixed potential as in our model. A detailed discussion of the physics

**Figure 3.4**

The radial force perturbation due to a spiral density wave as a function of galactocentric radius. The curve is normalised against its maximum value.

of spiral density waves can be found in Binney & Tremaine (1987) and Shu (1992). For a slightly less formal approach, Bowers & Deeming (1984) provide a good introduction.

A logarithmic spiral form for the potential was chosen for being, most importantly, a good fit to observational data. The most comprehensive survey of galactic spiral form is still that of Danver (1942) who tested six theoretical spirals against observations and concluded that the best fit was obtained with logarithmic spirals. As a consequence it is this form which is most commonly used in studies of galactic structure and dynamics.

3.2.3 The kinetic temperature of the cloud particles

If two clouds approach within a cross-sectional diameter of one another then a collision is said to have occurred. We take the collision to be inelastic and write

$$\begin{aligned} \mathbf{v}_1 &\rightarrow \eta \mathbf{v}_2, \\ \mathbf{v}_2 &\rightarrow \eta \mathbf{v}_1, \end{aligned} \quad (3.2)$$

as an approximation to the details of the collision. The energy and momentum dissipated is considered to be taken up by internal motions of the cloud and since the internal energy of the cloud is dissipated radiatively through collisional de-excitation of the gas atoms/molecules, cloud-cloud collisions reduce the total energy of the galactic system. We allow for the heating of the ISM by shocks etc. resulting from collisions between the clouds and the expanding supernova remnants (SNR) by giving any cloud which collides with a remnant an impulse along the line joining the cloud and SNR centres of size inversely proportional to their separation. The size of the velocity impulse is restricted to be less than some value v_{\max} . We also introduce a feedback mechanism to maintain an approximately constant cloud kinetic temperature since the ISM is observed to be in an approximately equilibrium state. As the galactic disc temperature rises, so the cloud cross-section is also increased to enhance the cloud-cloud collision frequency, and hence the cooling rate. This approach is consistent with our aim to model a steady-state system.



3.3 Computational considerations

Due to the natural symmetry of the simulation it is sensible to use cylindrical polar coordinates throughout. To ensure that all coordinates $(r, \theta, z, \dot{r}, \dot{\theta}, \dot{z})$ take values which can be represented accurately in single precision, all lengths, times and masses are scaled. Lengths are expressed in units of $L = 200$ pc, times in $T = 10^7$ yr and masses in $M = M_{\odot}$. In all cases discussed in the following chapters, the actual timestep used in the model has been 10^6 yr = $0.1T$, although it could in principle be varied since it is specified as an input to the model. All results quoted in this dissertation have been converted to physical units for the convenience of the reader.

The code has been written to be as fast and compact as possible allowing the simulations to be run on workstations rather than on the supercomputers required by many galaxy models. The CPU time needed on a Sun SPARC 10 is approximately 7 h for a simulated time of 10^9 yr. Typically a simulation reaches steady-state (i.e. a roughly constant SFR, see Fig. 3.9) after about this time, but results are not normally taken until the model has been running for at least ~ 18 h (an equivalent time of 2.5×10^9 yr), to provide a sufficient interval over which to average the SFR. To ensure that the code is as fast as possible care has been taken to ensure that the best choice of compiler optimisation has been made, that the number of computationally expensive operations (such as trigonometric functions and square roots) is minimised by the judicious use of dummy variables, and where necessary, techniques have been adopted to maximise speed at the expense of the memory required (§3.3.1).

A complete source code listing is provided as Appendix B.

3.3.1 Calculation of near neighbours

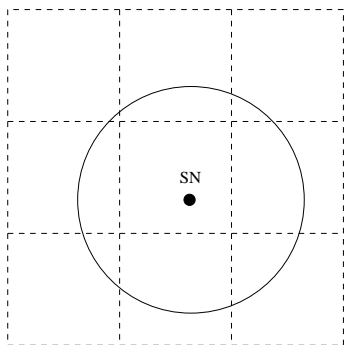
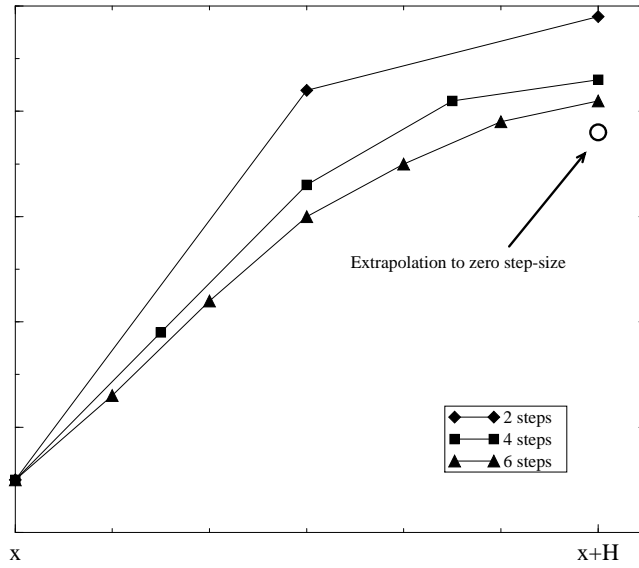


Figure 3.5.

To propagate the star formation it is necessary to determine which clouds are within the supernova shock at any instant. The direct approach of calculating the distance of each cloud from the relevant supernova centre, is prohibitively expensive however: at any timestep (10^6 yr) there are ~ 1000 supernova sites, so a simulation of 2.5×10^9 yr would require $\sim 10^{11}$ distance calculations. I adopt an alternative approach and grid the cloud particles after each rotation. The cell size is chosen to be the largest possible size of the supershell – the shocks are only deemed to be strong enough to trigger star formation for 10^7 yr in which time they attain a radius of 200 pc. In this manner only the 27 cells around the supershell centre need to be searched for clouds which are within the supershell (see Fig. 3.5). There are almost always less than 50 clouds per cell, thus less than ~ 1300 distance calculations per supershell per timestep have to be made. For ~ 1000 sites and a total run time of 2.5×10^9 yr, this results in a total of $\sim 10^9$ calculations, a reduction of about one hundred over the direct method. This leads to a much improved performance

**Figure 3.6**

Richardson extrapolation. The interval H is subdivided into a number of steps. As the number of steps increases, the calculated value of the integral converges to its true value which can thus be calculated by extrapolating the function describing the convergence to ∞ steps.

in terms of speed, at the expense of increased use of physical memory (approximately 80 MB). This in practice limits the number of cloud particles to 32 767 in our simulations, i.e. the largest number which can be represented as an `integer*2` variable. This is not a restriction however since this figure is close to the number ($\sim 30\,000$) of molecular clouds which are estimated to exist in our galaxy (Turner 1984).

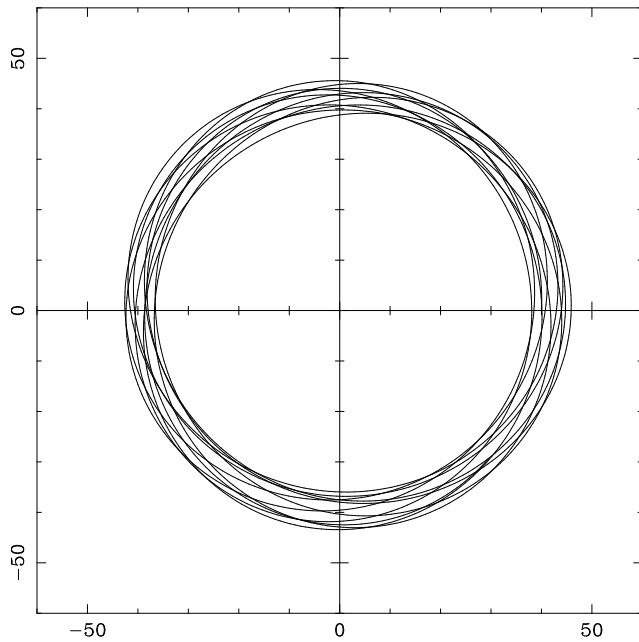
3.3.2 The rotation integration scheme

The three-dimensional particle orbits are derived from the derivative of the total potential using the Bulirsch-Stoer method (Stoer & Bulirsch 1980), a highly efficient algorithm for smooth integration problems such as we have here. Our implementation is derived from that given by Press *et al.* (1992). The key idea behind this integration scheme is that of “Richardson’s deferred approach to the limit”. For a given ‘large’ interval H , we can obtain better and better solutions to the integral by dividing H into more and more steps of size h . Moreover, by considering the behaviour of the approximations as h is reduced, it is possible to extrapolate the function to zero step-size to yield the final answer (see Fig. 3.6).

The actual integration is performed using the Modified Midpoint method. To integrate a function $y(x)$ from x to $x + H$ using n steps (such that $h = H/n$) we have,

$$\begin{aligned}
 y_0 &= y(x) \\
 y_1 &= y_0 + h \left. \frac{dy}{dx} \right|_x \\
 y_{m+1} &= y_m + 2h \left. \frac{dy}{dx} \right|_{x+mh} \quad \text{for } m = 1, 2, \dots, n-1 \\
 y(x+H) &\approx y_n \equiv \frac{1}{2} \left[y_n + y_{n-1} + h \left. \frac{dy}{dx} \right|_{x+H} \right]
 \end{aligned}$$



**Figure 3.7**

An example orbit for a single, isolated particle. The particle was started from position (35,0,0) with a total velocity dispersion of 18 km s^{-1} superimposed on the appropriate Keplerian velocity for its radius. A spiral potential component of strength 5% of the axisymmetric potential is present. Axes are labelled in units of 200 pc.

This is a second order method but in comparison with the second-order Runge-Kutta method, only one derivative calculation is required per step rather than two. Importantly for its use in the Bulirsch–Störmer method, the error can be expressed as a power series of even-powers of h (Gragg 1965), i.e.

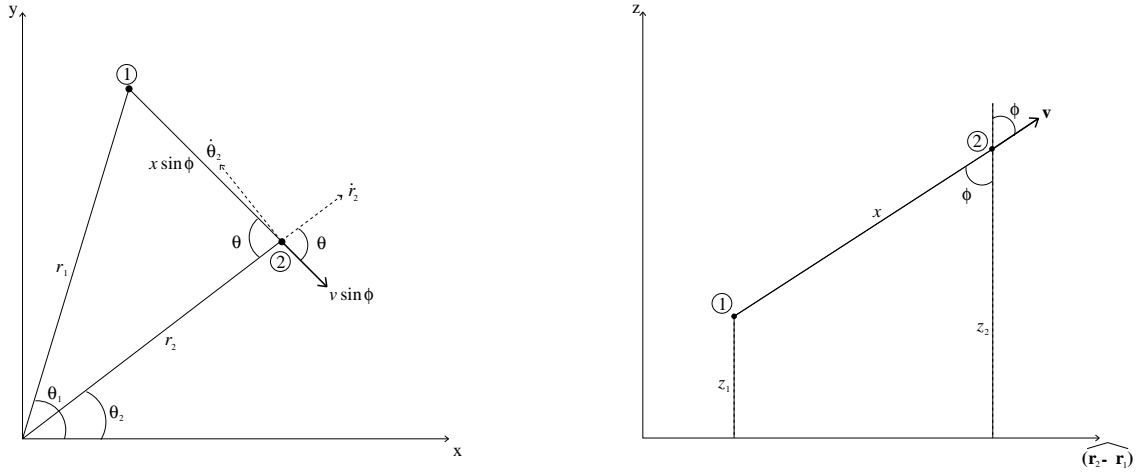
$$y_n - y(x + H) = \sum_{i=1}^{\infty} \alpha_i h^{2i}$$

hence the extrapolating polynomial can be expressed in terms of h^2 and not merely h , increasing the accuracy without compromising speed.

Since the clouds are regularly undergoing collisions which effectively randomise the cloud's velocity, it is not necessary to integrate to high accuracy. Hence single-precision arithmetic is used throughout, and the tolerance level for the convergence of the integral can be relaxed. Considering the final position of a single, isolated particle after 2500 timesteps (Fig. 3.7), it was found that the fractional error permitted on any individual timestep could be increased from 10^{-7} to 10^{-3} with no shift in its final coordinates to six significant figures. There was however a noticeable saving in CPU time (15–55%, depending on the exact values used for the dispersion velocities, radius of orbit etc.), and hence a tolerance value of 10^{-3} was used throughout the simulations.

In another attempt to minimise the computational effort required, much care was taken to ensure the greatest level of optimisation possible in the calculation of the derivatives. In particular, the number of square roots, powers and trigonometrical functions has been kept to the absolute minimum. Any values which are the same for each rotation calculation, but which are functions of the input parameters (for example $\tan i_0$) are calculated once only in an initialising subroutine. Despite this, the rotation of the star and cloud particles still constitutes a major fraction of the overall CPU time required.

Figure 3.8. Two views of the cloud–supershell remnant collision geometry. The supershell is labelled as ① and the cloud as ②.



3.3.3 Particle dynamics

In a similar manner we wish to minimise the computational effort required to calculate cloud–shock and cloud–cloud collisions. In the former case we already know which clouds are affected since they have been determined for the star formation propagation. The geometry of the situation is shown in Fig. 3.8. Simple trigonometry shows that the the change in cloud velocity components are given by

$$\begin{aligned}\Delta \dot{r} &= v \sin \phi \cos \theta \\ \Delta \dot{\theta} &= (v/r_2) \operatorname{sgn}(\theta_2 - \theta_1) \sin \phi \sin \theta \\ \Delta \dot{z} &= v \cos \phi\end{aligned}$$

where v is the magnitude of the velocity impulse to be given to the cloud ($\propto x^{-1}$ up to some maximum value v_{\max}) and all other symbols are illustrated in Fig. 3.8. Importantly, since both $\sin \phi$ and $\sin \theta$ are always positive these quantities can be calculated using the identity $\sin^2 \alpha + \cos^2 \alpha = 1$, knowing that $\cos \phi = (z_2 - z_1)/x$, eliminating the need for computationally expensive trigonometric operations. Thus cloud–shock collisions can be calculated (given that the grid has already been constructed for the propagation of the star formation) using only algebraic operations together with two square roots.

To determine if two clouds have collided we need to know first whether their centres are within a collisional cross-sectional diameter of each other, and second whether they are approaching or not. This second condition is necessary since the cross-sectional diameter of the clouds is variable (see below) and hence if the diameter increased between two timesteps it would be possible for two clouds to have collided at the earlier time (and hence be moving apart), but still be within a diameter of one another at the later. To test whether the clouds are sufficiently close together we need a grid with cell size at least greater than the cloud diameter so that for each cloud only the



surrounding 27 cells need to be checked. The grid is only recalculated if the one set up for the star formation propagation has too small a cell size, i.e. more than the twenty-seven nearest cells would need to be checked. If two clouds are considered to have collided then their velocities are reduced by some factor $\eta < 1$ and interchanged (equation 3.2), to approximate an inelastic collision. The inter-cloud separation s is given by

$$s^2 = r_1^2 + r_2^2 - 2r_1r_2\cos(\theta_1 - \theta_2) + (z_1 - z_2)^2,$$

and hence,

$$\dot{s} = s^{-1}[r_1\dot{r}_1 + r_2\dot{r}_2 - \dot{r}_1r_2\cos(\theta_1 - \theta_2) - r_1\dot{r}_2\cos(\theta_1 - \theta_2) + r_1r_2\dot{\theta}_1\sin(\theta_1 - \theta_2) - r_1r_2\dot{\theta}_2\sin(\theta_1 - \theta_2) + \dot{z}_1(z_1 - z_2) - \dot{z}_2(z_1 - z_2)].$$

Clearly only the term enclosed by brackets ([]) needs to be evaluated since we are only interested in determining whether the clouds are approaching and hence only the sign of \dot{s} . Again care has been taken to ensure that the minimum of operations are performed by the use of dummy variables for all quantities that are needed several times (e.g. $\theta_1 - \theta_2$).

If the galactic disc should become too hot, i.e. the star and cloud particles have too much kinetic energy, then the disc will expand radially. Since we modelling a system in steady-state, this is undesirable – observationally we do not see large spiral galaxies being disrupted in this manner. From a computational perspective this would also result in problems constructing the grid used to calculate near neighbours – the grid size is finite and fixed by array declarations. Hence to maintain an approximately constant particle temperature a feedback mechanism is employed which varies the cross-sectional diameter for cloud–cloud collisions, and hence the frequency of collisions and therefore the energy dissipation rate due to the inelasticity of the collisions. After each timestep the root mean square velocity dispersion, v_{rms} , of clouds within the galactocentric radius range $2 < r < 10$ kpc is calculated and compared with the ‘desired’ value, u_{rms} calculated during the initial dynamic equilibration of the model (§3.3.5). The cloud diameter is scaled according to

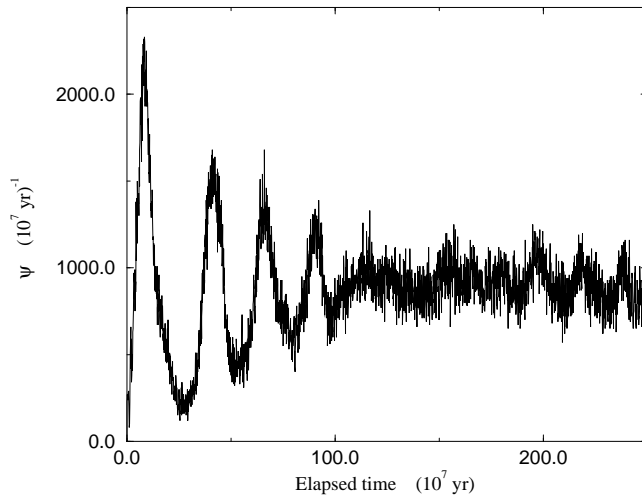
$$d_{\text{col}}^{\text{new}} = d_{\text{col}}^{\text{old}} \left(\frac{v_{\text{rms}}}{u_{\text{rms}}} \right)^{1.7}$$

where the power index was chosen by trial-and-error to give the best response – sufficiently high so that extreme values of v_{rms} could not be attained, but without inducing large oscillations.

3.3.4 Random number generation

The simulation requires a large number of random numbers: each time a decision is to be made on whether star formation has occurred in a given cloud, a uniform variate is compared with P_{st} . Hence for a typical simulation it is necessary to generate approximately 10^{6-7} random numbers. This is done using function G05CAF from the NAG library (NAG 1993), a uniform multiplicative congruential generator with the $(i + 1)$ 'th random number given by

$$b_{i+1} = 13^{13}b_i \pmod{2^{59}}.$$

**Figure 3.9**

The initial oscillations of the star formation rate. A constant value is reached after approximately 10^9 yr.

The initial value b_0 is seeded from the system clock (via subroutine G05CCF) to ensure that individual simulations are uncorrelated. The generator's period of 2^{57} is quite adequate and although it does show some signs of sequential correlations (Hobson 1994) this is not at a significant level in this context.

3.3.5 The initialisation of the model

It would be difficult, or even impossible to start off a simulation in a fully relaxed, but randomly chosen state. Instead the particles are laid down with the appropriate spatial and velocity distributions and then the model is allowed to dynamically relax without star formation. This is achieved by simply rotating the particles in the axisymmetric potential until the r.m.s. velocity distribution attains an approximately constant value. The SDW amplitude is set to zero during this process since it would otherwise act as a source of kinetic energy for the particles, preventing a steady state from being reached. Once equilibrium has been achieved, the final value of u_{rms} is used as a base level about which the disc temperature is maintained through the imposition of a feedback loop affecting the cloud collisional cross-section (§3.2.3 and §3.3.3). Now the simulation can begin properly – the SDW is switched on and star formation is allowed to propagate.

The clouds' positions are selected randomly such that they are initially arranged following the radial distribution of Galactic H_2 (Burton 1988), uniformly in azimuth and with a Gaussian profile perpendicular to the disc with scale-length of 200 pc. Velocities are set to the appropriate Keplerian value for the cloud's radius together with a randomly chosen dispersion velocity selected from a Gaussian distribution, the width of which is specified as an input to the model.

Clouds are also assigned masses (necessary for the propagation mechanism) which are chosen randomly from a distribution of the form $n(m) \propto m^{-1.58}$ (Sanders *et al.* 1985). Finally 0.3% of the clouds are associated with new star clusters which then act as seeds for the star formation process. This set-up is still somewhat out of equilibrium, and the SFR oscillates for a short period (see Fig. 3.9), before settling down to the desired, approximately constant level. It is this final value which



is used in the analysis described in subsequent chapters.

3.4 Running a simulation

The main simulation code is named GALAXY. Each simulation takes its input from a file named `input.suffix` where *suffix* is a machine identifier allowing the program to be run completely independently on several machines simultaneously, each with its own set of input parameters. All input is taken from the file such that GALAXY can be run in the background – essential considering the total run time required. An example input file with an explanation is provided in Appendix A. In addition, there are a number of UNIX scripts to facilitate the chaining together of several runs and automatic re-starting of GALAXY should the machines be re-booted. The produce a number of small files to facilitate the housekeeping.

Results are normally saved to disk every 200 time steps ($= 2 \times 10^8$ yr) although this can be changed in the input parameter list (see Appendix A). Each set of output includes full details of the simulation (e.g. cloud positions, velocities and ages) and derived quantities such as the SFR and r.m.s. velocity dispersion. This enables the simulation to be restarted at intermediate times if required. Moreover, it permits one run to be used as the starting point for a second simulation, perhaps with different parameters. Each simulation discussed in this dissertation was, however, started from scratch each time to ensure that the runs were completely independent. Due to the stochastic nature of the simulation it was necessary to average over many realisations for each set of input parameters before the model behaviour could be determined with any degree of certainty, and clearly this procedure would have been invalidated if the runs were in any way correlated.

References

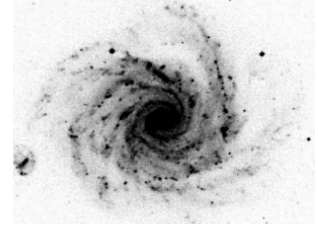
- Allen C., Martos M. A., 1986, *Rev. Mex. Astron. Astrofís.*, 13, 137
- Allen C., Santillán A., 1991, *Rev. Mex. Astron. Astrofís.*, 22, 255
- Binney J., Tremaine S., 1987, *Galactic Dynamics*, Princeton University Press, New Jersey
- Bodenheimer P., 1992, in *Star Formation in Stellar Systems*, eds Tenorio-Tagle G., Prieto M., Sánchez F., p. 16, Cambridge University Press
- Bowers R. L., Deeming T., 1984, *Astrophysics II: Interstellar matter and galaxies*, Jones and Bartlett Publishers Inc., Boston
- Burton W. B., 1988, in *Galactic and Extragalactic Radio Astronomy*, eds Verschuur G. L., Kellermann K. I., p. 332, Springer-Verlag, New York, 2nd edn.
- Danver C.-G., 1942, *Lund Obs. Ann.*, 10
- Elmegreen B. G., 1985, in *Birth and Infancy of Stars*, eds Lucas R., Omont A., Stora R., p. 215, Elsevier Science Publishers B.V., Amsterdam
- Elmegreen B. G., Elmegreen D. M., 1987, *ApJ*, 320, 182
- Gragg W., 1965, *J. SIAM Numer. Anal. Ser. B*, 2, 384
- Hobson M. P., 1994, private communication
- Kwan J., Valdes F., 1987, *ApJ*, 315, 92
- Lada E., Strom K., Myers P., 1992, in *Protostars and Planets III*, eds Levy E. H., Lunine J., Matthews M. S., University of Arizona Press

- Lin C. C., Shu F. H., 1964, *ApJ*, 140, 646
- Lin C. C., Shu F. H., 1966, *Proc. Nat. Acad. Sci.*, 229, 55
- Miller G. E., Scalzo J. M., 1978, *PASP*, 90, 506
- Nezlin M. V., Polyachenko V. L., Snezhkin E. N., Trubnikov A. S., Fridman A. M., 1986, *Pis'ma Astron. Zh.*, 12, 504
- Noh H.-R., Scalzo J., 1990, *ApJ*, 352, 605
- Numerical Algorithms Group Limited, 1993, *NAG Fortran Library Manual*, Mark 16
- Ollongren A., 1962, *Bulletin of the Astronomical Institutes of the Netherlands*, 16, 241
- Press W. H., Teukolsky S. A., Vetterling W. T., Flannery B. P., 1992, *Numerical Recipes in FORTRAN*, Cambridge University Press, Cambridge, 2nd edn.
- Roberts W. W., Hausman M. A., 1984, *ApJ*, 277, 744
- Sanders D. B., Scoville N. Z., Solomon P. M., 1985, *ApJ*, 289, 373
- Shu F. H., 1992, *The Physics of Astrophysics – volume II: Gas Dynamics*, University Science Books
- Stark A. A., Brand J., 1989, *ApJ*, 339, 763
- Stør J., Bulirsch R., 1980, *Introduction to Numerical Analysis*, Springer-Verlag, New York, §7.2.14
- Tenorio-Tagle G., Bodenheimer P., 1988, *Ann. Rev. Astron. Astrophys.*, 26, 145
- Thomasson M., Elmegreen B. G., Donner K. J., Sundelius B., 1990, *ApJ*, 356, L9
- Turner B. E., 1984, *Vistas Astron.*, 27, 303
- Turner B. E., 1988, in *Galactic and Extragalactic Radio Astronomy*, eds Verschuur G. L., Kellermann K. I., Springer-Verlag, New York, 2nd edn.
- Wannier P. G., Lichten S. M., Morris M., 1983, *ApJ*, 268, 727
- Zinneker H., 1996, in *The interplay between massive star formation, the ISM and galaxy evolution*, eds Kunth D., Guiderdoni B., Heydari-Malayeri M., Thuan T. X., Trân Thanh Vân J., Editions Frontières, Paris, in press



Chapter 4

The star formation rate



In this chapter I will describe the way in which the star formation rate derived from the model varies as a function of the input parameters. It will be shown that by choosing appropriate values for these inputs it is possible to predict the star formation rate of our Galaxy. We will also show that the star formation rate is related through a simple power-law to the total gas density, a result which has much empirical data in support of it, and is usually known as the Schmidt Law.

In the context of this model, what has been up to now called the star formation rate is strictly the cluster formation rate (CFR), i.e. the number of star clusters formed per unit time, given the symbol ψ . The term ‘star formation rate’ (SFR) is usually reserved for the *mass* of stars formed per unit time. This quantity is not directly accessible from the model since the exact fraction of a cloud that is converted into stars is not known. However, as will be seen below (§4.3) we can get a handle on the SFR by multiplying the CFR by a characteristic cloud mass and assuming that it is possible to define an efficiency for star formation that is constant for all galaxies. (The average efficiency of star formation observed in Galactic molecular clouds is $\sim 1\text{--}5\%$ (Lada *et al.* 1992)).

4.1 The effect of the input parameters on the CFR

With a total of 14 input parameters affecting the physics in some way (Appendix A), the possible parameter space of the model to be investigated is extremely large. To provide a fully comprehensive survey sampling all regions of this space would have required far more CPU time than was available and hence an alternative strategy was adopted. A ‘standard’ set of input parameters (Table 4.1) was chosen, based on values appropriate for our Galaxy, and then each parameter was varied individually about this value. Where parameters could not be set on the basis of observational constraints (for example M_{sp}), values consistent with the aims of the model were adopted – for example we required propagating star formation to be the dominant mechanism, and therefore M_{sp} had to be much larger than M_{st} , so that the probability of spontaneous star formation (P_{sp}) was much smaller than that for stimulated star formation (P_{st} – see §3.2.1). The graphs presented below



Quantity	Model value	'Real' value	Reason
Δt	0.1 T	10^6 yr	The orbital period of the innermost particle orbits is $\sim 10^7$ yr, and hence this Δt gives sufficient resolution to follow the dynamics.
N_c	32010		Similar to the number of clouds in our galaxy (Turner 1984), and also close to maximum possible value (§3.3.1).
a_0	0.3 LT^{-1}	5.9 km s^{-1}	Typical one-dimensional cloud velocity dispersion (Magnani <i>et al.</i> 1985; Belfort & Crovisier 1984; Liszt <i>et al.</i> 1984).
η	0.7		Many collisions will be glancing so average elasticity is moderately high.
v_{max}	0.51 LT^{-1}	10.0 km s^{-1}	Slightly larger than the Galactic cloud velocity dispersion.
M_{st}	$1.0 \times 10^5 M_{\odot}$		Typical GMC mass (Sanders <i>et al.</i> 1985).
M_{sp}	$1.0 \times 10^{11} M_{\odot}$		Much larger than M_{st} so that propagation is the dominant star formation mechanism.
ϵ	1.0×10^{-3}		Cloud is almost fully disrupted by star formation.
n	2		The dominant SDW mode – see §5.3.
Ω_p	0.14 T^{-1}	$13.7 \text{ km s}^{-1} \text{ kpc}^{-1}$	Galactic value (Bowers & Deeming 1984).
r_0	5.0 L	1.0 kpc	Small size for central bar (§5.1).
p	5.0		'Middle' value.
i_0	20.0°		Spiral pitch angle for the SDW in a Sbc galaxy. Results in a pattern pitch angle of 12° – see §7.2.1.
A	$5000 \text{ L}^4 \text{ T}^{-2}$	$0.08 \text{ pc}^4 \text{ yr}^{-2}$	Approximately 5% of total radial force (§3.2.2– a weak spiral perturbation).

Table 4.1. Standard input parameters adopted which define the areas of the model's parameter space investigated. For an explanation of 'model' units see Appendix A.

have all been calculated in this manner using the ‘standard’ set, and hence represent the variation of the CFR along the principal axes of the parameter space.

In order to smooth out the stochastic nature of the simulation, each point on the CFR curves presented below is the average value for an ensemble of a few runs (always at least three, rarely more than six), all with identical input parameters and with the error estimated from the sample standard deviation of the ensemble. The value for each individual run is an average over the last $(100-150) \times 10^7$ yr of the simulation to avoid any contamination from the initial oscillations of the CFR while the model equilibrates (Fig. 3.9). Even after this period the variation in CFR about the mean value for a single run is still $\sim 100 \times 10^{-7} \text{ yr}^{-1}$: however, the scatter in the means for an ensemble of runs is small (as can be seen from the error bars plotted in the graphs below), and hence, even a small number of runs can give a reliable estimate for the ‘true’ value of the CFR. In cases where it was found that the scatter was large, more simulations were performed until the average value converged.

The input parameters can be grouped into three main categories according to their affect on the simulation:

- (i) those which directly control the star formation – $M_{\text{st}}, M_{\text{sp}}$ and ϵ ;
- (ii) those which control the cloud dynamics – a_0, η and v_{max} ;
- (iii) those affecting the shape of the spiral potential – n, Ω_p, r_0, p, i_0 and A .

The results of changing the imposed spiral density wave will be discussed separately in Chapter 5, whilst the effects of parameters in groups (i) and (ii) will be considered below.

4.1.1 Star forming parameters

As would be expected, the scaling mass for the propagating star formation, M_{st} is found to be the most important parameter affecting the CFR, with $\psi \propto M_{\text{st}}^{-0.309 \pm 0.006}$ (Fig. 4.1a). As M_{st} is increased, the probability of any cloud having star formation triggered within it is reduced, and hence the overall CFR falls. In addition this has the consequence that on average a cloud is able to accrete for longer and hence the median cloud mass (M_{med}) and total cloud mass (M_{tot}) rise with M_{st} such that $M_{\text{med}} \propto M_{\text{st}}^{0.955 \pm 0.007}$ and $M_{\text{tot}} \propto M_{\text{st}}^{0.391 \pm 0.007}$ (Fig. 4.2). Note that although the CFR decreases with increasing M_{st} , the SFR rises proportional to $M_{\text{st}}^{0.6}$, since, as will be discussed below (§4.3.1), we can convert between the two by multiplying by the median cloud mass.

The dependence of the CFR on the other star formation parameters is much weaker, justifying the somewhat arbitrary choice of their ‘standard’ values, with $\psi \propto M_{\text{sp}}^{-0.005 \pm 0.001}$ and $\psi \propto \epsilon^{0.019 \pm 0.005}$. Again the form of these dependencies can be related to the mass of an average cloud and the time taken for it to regrow after a star formation event: as M_{sp} is increased the probability of spontaneous star formation drops, whilst if ϵ is increased, the time taken for a cloud to reach a mass $\sim M_{\text{st}}$ is reduced, and hence the star formation rate increases. However, as can be seen from Fig. 4.1(d), the cloud regeneration time is hardly affected by ϵ and hence we see an extremely weak relation between it and the cluster formation rate.



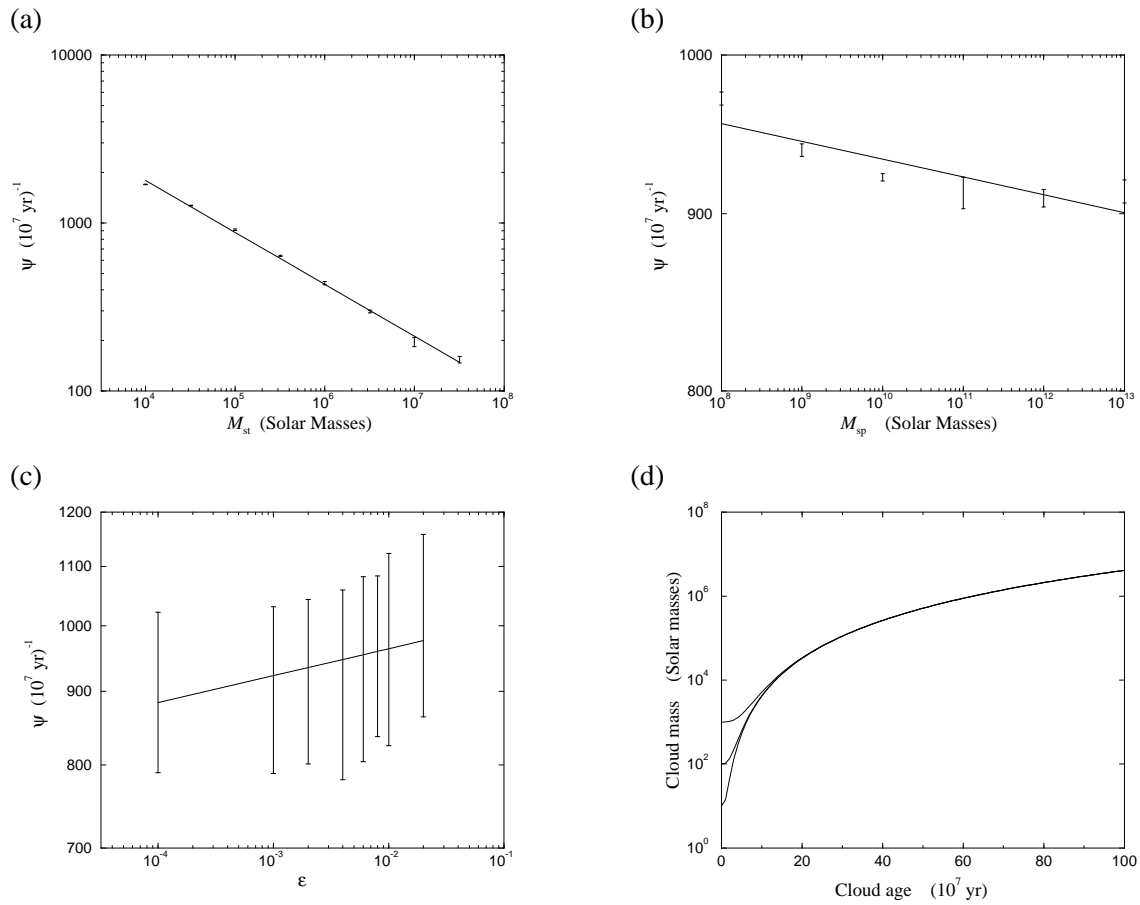


Figure 4.1. Graphs of cluster formation rate ψ versus (a) M_{st} , (b) M_{sp} and (c) ϵ . The fourth figure (d) shows cloud growth for three different initial masses. The initial mass is closely related to ϵ since when star formation occurs, the cloud mass is reduced by this factor.

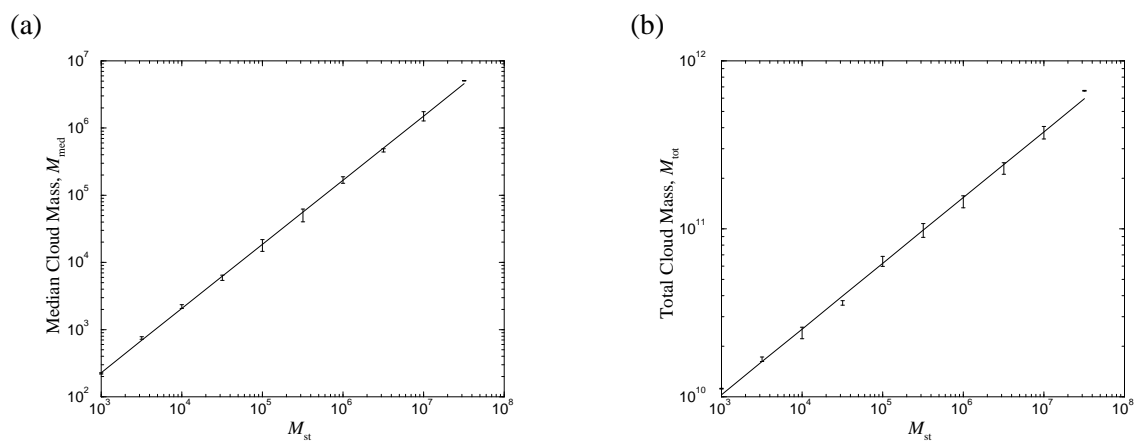
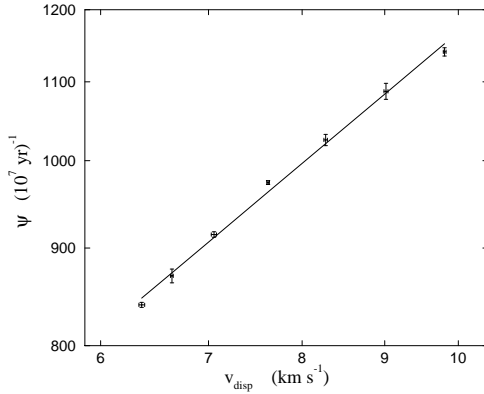


Figure 4.2. Correlation of (a) median and (b) total cloud mass with M_{st} . All axes are labelled in units of M_{\odot} .

**Figure 4.3**

Variation of the cluster formation rate, ψ with the one-dimensional cloud velocity dispersion.

4.1.2 Cloud dynamics parameters

The cloud dynamics are controlled through three distinct parameters affecting respectively the initial cloud velocity dispersion, cloud–cloud and cloud–SNR collisions. Inter-cloud collisions act to decrease the cloud kinetic temperature, and hence the mean velocity dispersion, whereas cloud–SNR interactions have the opposite effect. The relative importance of the two processes is controlled by a negative feedback loop working on the overall cloud velocity dispersion v_{disp} to maintain an approximately constant temperature determined by the initial value chosen for the velocity dispersion. The three input parameters thus interact in a non-trivial manner, and the dependence of the CFR on the cloud dynamics is best seen by considering ψ as a function of the mean cloud velocity dispersion v_{disp} . By systematically varying the input parameters a range of dispersion velocities can be investigated – it is found that $\psi \propto v_{\text{disp}}^{0.71 \pm 0.02}$ (Fig. 4.3). This can be interpreted by noting that as the velocity dispersion of the clouds rises, then the number of them that encounter any given supershell during the time that it is able to trigger star formation (and thus the star formation rate) also increases.

4.2 The Galactic cluster formation rate

We can use the relations above to determine the prediction of the model for the CFR of our Galaxy. To do this we require suitable values for the main input parameters to the model, such that they are consistent with observational constraints for the Galaxy. The majority of the ‘standard’ set of parameters were based on such data, and hence these could be used. The spiral potential is consistent with that deduced for an Sbc galaxy, with a maximum strength of 5% of the axisymmetric potential, and the cloud velocity dispersion was taken as $\sim 7 \text{ km s}^{-1}$ (Stark & Brand 1989). It is not possible to measure directly the values of those parameters relating to the propagating star formation mechanism. However, by fixing M_{sp} and ϵ at their standard values (which we are free to do since ψ has only a very weak dependence on these parameters), we can determine M_{st} from the observed molecular cloud mass distribution. It has already been shown that as M_{st} is increased, the time available for a cloud, on average, to accrete material from the ISM between star formation



episodes rises, and hence the average cloud mass also increases. Sanders *et al.* (1985) observe the median Galactic cloud mass to be $2.0 \times 10^5 M_{\odot}$, and hence, from Fig. 4.2, we can fix a suitable PSF scaling mass for the Galaxy to be $M_{\text{st}} = 1.2 \times 10^6 M_{\odot}$.

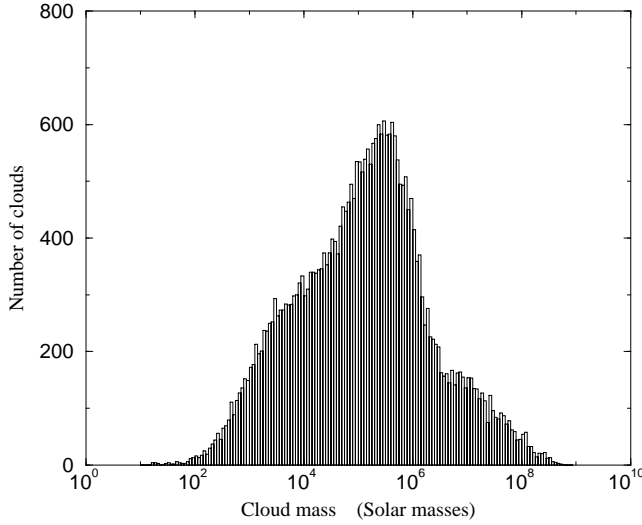
Now the predicted Galactic CFR, can be determined from Fig. 4.1 and is found to be $\psi = 4.0 \times 10^{-5} \text{ yr}^{-1}$. Moreover, star formation is restricted to within a radius of 10 kpc, and hence using this value the corresponding CFR per unit area is $1.3 \times 10^{-7} \text{ kpc}^{-2} \text{ yr}^{-1}$. The radius of star formation is constrained primarily by the distribution of H_2 – that used in the model is as reported by Burton (1988) for our Galaxy. The predicted value for the CFR compares excellently with that observed – $(2.5 \pm 1) \times 10^{-7} \text{ kpc}^{-2} \text{ yr}^{-1}$ (Elmegreen & Clemens 1985) – given the uncertainties in the observational inputs. Cloud masses in particular are prone to error since the H_2 mass is estimated from the CO luminosity using a standard conversion factor (Sanders *et al.* 1984) which is not well determined and moreover might be expected to vary from cloud to cloud depending on the previous star formation history. Taken together with other contamination and calibration errors, Gordon (1995) estimates that published molecular cloud masses may be in error by up to a factor of approximately 20, although this is likely to be a pessimistic calculation. Since the value of M_{st} is calculated from the median cloud mass, this will be the major source of uncertainty in the derivation of the Galactic CFR – assuming a factor of 20 error in M_{med} leads to an uncertainty by a factor of approximately six in the estimates for ψ . Of the parameters describing the SDW only the pitch angle is reasonably well constrained, although as has been seen, the CFR is only weakly dependent on these quantities.

One limitation of the model that has already been noted (§3.2.1) is that we only consider the formation of massive stars through the propagating mechanism. This, however, does not affect the validity of the argument presented above, since the model CFR measurements are based on the number of clusters similar in type to those used by Elmegreen & Clemens (1985) in their estimation of the Galactic CFR. The same authors also report a value for the formation rate of OB clusters of $\sim 2 \times 10^{-7} \text{ kpc}^{-2} \text{ yr}^{-1}$. Whilst the significance of this number being lower than the overall CFR is doubtful, it accords with the general idea of most, but not all, clusters containing at least one massive star. In the model, despite nominally all the model clusters being OB associations (since each has the potential to trigger star formation through a supershell shock), the stochastic nature of the simulation means that some clusters will not trigger star formation, and therefore effectively consist of lower mass stars.

4.3 The Schmidt law

The idea that the overall galactic star formation rate has a simple power-law dependence on the gas density was first proposed by Schmidt (1959; 1963), and his name has since been attached to any empirical star formation law of this form. The original formulation of the Schmidt Law was in terms of the HI gas volume density,

$$\dot{\rho}_* \propto \rho_{\text{HI}}^n, \quad (4.1)$$

**Figure 4.4**

Typical distribution of cloud masses. For this particular simulation $M_{\text{st}} = 1.0 \times 10^6 M_{\odot}$, although the general shape of the distribution is similar over the full range of M_{st} investigated.

where $\dot{\rho}_*$ is the rate of change of the mass density of stars, ρ_{HI} is the neutral hydrogen density and generally $n = 1-2$. Molecular hydrogen was not included since at the time its importance as a component of the ISM was unrecognised. Later, when the dominance of H_2 was understood, it was found that a better correlation could be obtained using either the H_2 (Rana & Wilkinson 1986) or the total gas density (Kennicutt 1989). Schmidt Laws of this form have been used in many models of galactic chemical evolution (e.g. Tosi & Díaz 1990; Firmani & Tutukov 1992), and are often invoked in N-body codes to estimate the star formation rate. An important feature of the model presented in this dissertation is that it *predicts* a Schmidt Law.

Observational determinations of the Schmidt Law index are usually based on surface densities, rather than volume densities, i.e.

$$\dot{\sigma}_* \propto \sigma_{\text{tot}}^N, \quad (4.2)$$

simply because it is the surface densities which can actually be measured, and a model for the z -distribution of the galactic material is required to extract the volume density. Equations 4.1 and 4.2 are only compatible if $n = N = 1$. Other difficulties exist with the experimental determination of the Schmidt Law – for example, the SFR is estimated from tracers of recent, but past star formation (e.g. O/B stars and H II regions), whereas the gas mass estimates necessarily reflect the gas that exists now. Hence we derive relationships based on the amount of gas that is left over after star formation, and not that which was available at the time of the star forming event. Radial gas flows further confuse the results and, finally, any variation in the conversion factor between CO and H_2 , which, as mentioned above, is usually taken to be a universal constant, will further increase the dispersion of the measured Schmidt Law.



4.3.1 The Schmidt Law for the new model

The new model predicts a standard Schmidt Law. To convert our measured cluster formation rates to a total SFR, i.e. the mass of stars formed per unit time, we need to multiply ψ by a characteristic mass, where in this case the median cloud mass M_{med} seems to be appropriate. A typical cloud mass distribution (Fig. 4.4) covers a large range of masses, and hence the mean cloud mass would be dominated by the most massive clouds. If this value were to be used in the CFR→SFR conversion then this would imply that the most massive clouds also dominate the rate of formation of new stars. But this is not the case – the probability of triggered star formation P_{st} is the same for all clouds with masses greater than M_{st} . The median cloud mass provides a more ‘typical’ value as it relates to the star formation process. Hence

$$\dot{\rho}_* V \propto (1 - \epsilon)\psi M_{\text{med}}, \quad (4.3)$$

where V is the volume of the galaxy and the $(1 - \epsilon)$ term reflects the amount of cloud material converted into stars. However, as has been seen (§4.1.1), ψ is only very weakly dependent on ϵ and hence we can absorb its value into the constant of proportionality. Thus, remembering that $\psi \propto M_{\text{st}}^{-0.309 \pm 0.006}$ and $M_{\text{med}} \propto M_{\text{st}}^{0.955 \pm 0.007}$, we have

$$\dot{\rho}_* V \propto M_{\text{st}}^{0.646 \pm 0.009} \quad (4.4)$$

$$\propto M_{\text{tot}}^{1.65 \pm 0.04}, \quad (4.5)$$

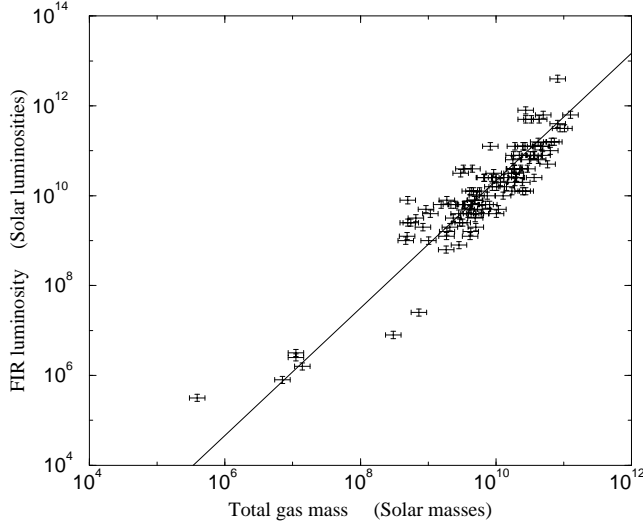
where, as before M_{tot} is the total cloud mass. Writing the total cloud mass divided by the galactic volume as ρ_{gas} , then,

$$\begin{aligned} \dot{\rho}_* &\propto \rho_{\text{gas}}^{1.65 \pm 0.04} V^{0.65 \pm 0.04} \\ &\propto \rho_{\text{gas}}^{1.65 \pm 0.04} D^{1.30 \pm 0.08}, \end{aligned} \quad (4.6)$$

if we assume $V \propto D^2$ as is appropriate for a thin disc.

All the dependencies used in the above derivations have been deduced from simulations using the ‘standard’ parameters for the model. In the spirit of normal Schmidt Law calculations, no attempt has been made to fold in variations of the SFR with, for example, the strength of the spiral density wave, primarily since such quantities are not readily available from observational measurements. However, as will be seen from Fig. 5.1, the exact form of the relation between ψ and A (in this case the slope of the linear region) varies with M_{st} – non-linearities in the model tie the parameters together making it impossible to extract a single, general relationship. If we assume that the ‘standard’ parameters are in some sense typical though, then the result can be considered to have a general application, averaging over galaxies.

We have tested this formulation of the Schmidt law against the observational data of Young *et al.* (1989). If the far infra-red (FIR) luminosity is assumed to be a good indicator of the star formation rate (see §4.3.2), then by comparing their observed FIR luminosity with gas mass meas-

**Figure 4.5**

The observational data of Young *et al.* (1989) together with the best-fitting line (slope=1.4). Error bars on each point are based on the estimates given in the paper and are $\pm 30\%$ in the total mass and $\pm 20\%$ in FIR luminosity.

measurements based on 21-cm and CO observations we can deduce a Schmidt Law from the data. Rewriting equation (4.5) we see that

$$L_{\text{FIR}} \propto \dot{\rho}_* V \propto M_{\text{tot}}^{1.65}. \quad (4.7)$$

Allowing for the appropriate errors in the flux measurements, (quoted as 20–30 per cent) on which the mass estimates are based, it is found that the observational data is well fit by a power law of index 1.4 ± 0.4 , in good agreement with our prediction.

4.3.2 Observational determinations of the SFR

Massive star formation leaves tracers which can be observed over a large range of the electromagnetic spectrum.

Massive star formation exhibits a number of characteristic features which can be readily observed over a large range of the electro-magnetic spectrum. Local measurements are available to calibrate the observations of external galaxies. The intense ultra-violet (UV) radiation produced by the OB stars ionises the immediate vicinity producing an H II region, most readily visible in the light from the H α transition. The number of ionising photons can be estimated from the H α flux which allows the number of young stars present in the galaxy to be calculated, assuming that the spectra for OB stars is known. This however, also requires knowledge of the initial mass function (IMF), i.e. the number of stars born with a given mass (given the symbol $\phi(m) dm$). This function is poorly known and constitutes one of the main sources of error in the calculation of the SFR. In symbols,

$$L_\nu = \dot{M}_* \frac{\int t_\nu(m) l(m) \phi(m) dm}{\int m \phi(m) dm} \quad (4.8)$$

where L_ν is the luminosity in the frequency band being considered, $l(m)$ is the luminosity of a star of mass m and $t_\nu(m)$ is the length of time for which the same star is emitting at that frequency



(Thronson & Telesco 1986). Assuming a Miller–Scalo (1979) IMF (one of the most widely adopted), Kennicutt (1983) finds that

$$\dot{M}_* = 5.6 \times 10^{-9} \left(\frac{L_{\text{H}\alpha}}{L_{\odot}} \right) M_{\odot} \text{ yr}^{-1}$$

for stellar masses $\gtrsim 10 M_{\odot}$, and

$$\dot{M}_* = 3.2 \times 10^{-8} \left(\frac{L_{\text{H}\alpha}}{L_{\odot}} \right) M_{\odot} \text{ yr}^{-1}$$

when considering all star formation. L_{\odot} is the bolometric luminosity of the Sun ($L_{\odot} = 3.90 \times 10^{26}$ W).

Before stars emerge from their surrounding proto-stellar cocoons, the dusty clouds emit copious amounts of far infra-red (FIR) radiation. This has an advantage over H α measurements since the extinction at such longer wavelengths is much lower. However, it is not entirely clear whether the cool dust heated by the general interstellar radiation field makes a significant contribution to the total FIR luminosity. Observed dust temperatures for spiral galaxies are 30–40 K, similar to those measured for Galactic star-forming regions (Scoville & Good 1989) and considerably higher than the 15–20 K expected for dust heated by the ambient inter-stellar radiation field (Cox *et al.* 1986). This has led some authors (e.g. Bothun, Lonsdale & Rice, 1989; Fitt & Alexander 1992) to postulate a variety of two-component models, with up to 70% of the FIR luminosity coming from the cool component (Lonsdale Persson & Helou 1987). However, others find that the *IRAS* fluxes between 60 μm and 1100 μm can be fit by a single temperature blackbody with $T = 30\text{--}50$ K (Eales *et al.* 1989) and furthermore, that by comparing *IRAS* and H α luminosities it is found that the energy contained in the FIR radiation is consistent with that expected from the number of OB stars required to provide the photons to ionise the hydrogen (Devereux & Young 1990).

A young star cluster will only be bright in the FIR whilst still surrounded by its initial dusty cloud. If the time taken to disrupt the surrounding material (τ_{FIR}) is constant independent of mass, then equation (4.8) can be simplified to

$$L_{\text{FIR}} = \frac{\dot{M}_{\text{FIR}} \tau_{\text{FIR}} \bar{L}}{\bar{M}}$$

(Thronson & Telesco 1986) where \bar{L}/\bar{M} is the luminosity to mass ratio of a young star cluster. Once again the uncertainties in the IMF are the major source of error, but Thronson & Telesco (1986) estimate

$$\dot{M}_* = 6.5 \times 10^{-10} \left(\frac{L_{\text{FIR}}}{L_{\odot}} \right) M_{\odot} \text{ yr}^{-1}.$$

The third method commonly used to estimate the SFR is to measure the non-thermal radio emission from the supernova remnants formed by the explosion of the massive stars. If we assume that all stars of mass $> M_{\text{SN}}$ explode as supernova to leave radio-emitting remnants then from the non-thermal (i.e. synchrotron) emission of a galaxy and using the known relationship between L_{sync} , ν and the supernova rate for our Galaxy (Condon & Yin 1990) we can calculate the death-

and hence, birth-rate of such massive stars. Once again assuming a certain form for the IMF it is then possible to calculate a more general SFR including lower mass stars which don't contribute to the non-thermal radio flux. Condon (1992), using a Miller–Scalo IMF finds

$$\dot{M}_* = 1.9 \times 10^{-22} \left(\frac{\nu}{\text{GHz}} \right)^\alpha \left(\frac{L_{\text{sync}}}{\text{W Hz}^{-1}} \right) M_\odot \text{ yr}^{-1}$$

for stellar masses $\gtrsim 5 M_\odot$, where $\alpha \sim 0.8$ is the non-thermal spectral index.

It is found that the FIR and radio continuum luminosity are extremely well correlated (many references in the last few years, see for example, Bica *et al.* 1995; Xu *et al.* 1994a) which, of course, we would expect if they can both be used as tracers of the star formation rate. The massive OB stars which heat the dust are also the progenitors of the supernovae which we detect by their synchrotron emission. The lifetime of the massive stars is sufficiently short ($\lesssim 10^7$ yr) that the two radiation types can be considered to be coming from the same population of objects. Note that although many authors use the entire radio continuum emission, if this is decomposed into thermal and non-thermal components then the correlation between the latter and the FIR luminosity is much improved over using the total radio flux (Xu *et al.* 1994b).

4.3.3 The observed Schmidt Law

Many attempts have been made to determine the appropriate form for the Schmidt Law in recent years. However, most of these have been based on some model which incorporates a Schmidt Law with some variable index n , and then fitting the results of the model to observational data. For example, Caimmi (1995) uses a chemical evolution code to deduce that the Schmidt exponent is approximately equal to one, whilst Arimoto *et al.* (1992) employ a model of the photometric evolution of galaxies and find that their results are essentially independent of the value of n ($=1,2$) used.

Clearly, these results will be heavily dependent on the model used to derive them – we need to compare such model-based answers with values for n calculated simply from an observed correlation of the SFR with the gas density whether it be of HI (σ_{HI}), H₂ (σ_{H_2}) or total gas (σ_{gas}). Below I summarise some recent results which have taken this approach.

- Dopita & Ryder (1994) collected optical surface photometry (bands I and V) data and H α images of a sample of 34 nearby galaxies, representing the full range of Hubble types. They postulated a ‘compound’ Schmidt Law of the form

$$\dot{\sigma}_* \propto \sigma_{\text{total matter}}^n \sigma_{\text{gas}}^m$$

(Dopita 1985; Dopita 1990) and found that $1.5 < (n + m) < 2.5$ fitted the data best. Furthermore, their observations ruled out correlations of the form $\dot{\sigma}_* \propto \sigma_{\text{gas}}$ and $\dot{\sigma}_* \propto \Omega \sigma_{\text{gas}}$. The latter formulation was proposed by Wyse & Silk (1989) on the basis of an analytic treatment of the stability of the molecular gas in a galactic disc rotating with angular velocity Ω .



- Li, Seaquist, Wrobel, Wang & Sage (1993) found that, for the Sa/pec galaxy NGC 7625, the H α and 20-cm radio continuum (both tracers of massive star formation, see §4.3.2) correlate well with the ^{12}CO distribution, yielding a Schmidt Law of the form

$$\dot{\sigma}_* \propto \sigma_{\text{H}_2}^{1.0 \pm 0.2}.$$

NGC 7625 is extremely gas-rich for an Sa spiral, but there is no sign of an active galactic nucleus contaminating the non-thermal radio emission, so the authors suggest that the peculiar nature of the galaxy is not significant in this context.

- Using the spatial distribution of H II regions in M 31 together with high resolution H I and CO images, Tenjes & Haud (1991) find that the surface density of the young star forming regions is related by a simple power law to the total gas density such that

$$\dot{\sigma}_* \propto \sigma_{\text{gas}}^{1.30 \pm 0.22},$$

or equivalently

$$\dot{\rho}_* \propto \rho_{\text{gas}}^{1.17 \pm 0.25},$$

where $\rho(z) \propto \text{sech}^2(z/z_0)$ has been assumed.

- Kennicutt (1989) used H α , H I and CO data for a sample of 15 mostly late-type spiral galaxies. Although the correlation between the H α emission and the surface densities of the individual gas phases was found to be poor, that between the H α emission and the total gas content was excellent, giving

$$\dot{\sigma}_* \propto \sigma_{\text{gas}}^{1.3 \pm 0.3}.$$

It was found that this Schmidt Law broke down at low gas densities which Kennicutt attributed to the onset of large scale instabilities in the gaseous disc.

- Buat *et al.* (1989) also used data from a sample of galaxies, this time UV, CO and H I data for 28 galaxies ranging from Sab \rightarrow Im, using the UV emission to trace the regions of recent, massive star formation. Once again, a good correlation was found between the SFR and the total gas density,

$$\dot{\sigma}_* \propto \sigma_{\text{gas}}^{1.65 \pm 0.32},$$

but that between the individual gas phases was poor, with H $_2$ proving the worst tracer of star formation.

- Rana & Wilkinson (1986) in contrast, found that the best correlation is between the H $_2$ density and the SFR, with

$$\dot{\sigma}_* \propto \sigma_{\text{H}_2}^{1.2 \pm 0.2}$$

based on data for our Galaxy.

The lack of correlation found by Kennicutt (1989) and Buat *et al.* (1989) between the SFR and the molecular gas content of a galaxy is curious – from any model of star formation, we would expect the molecular gas content to play the dominant role in determining the overall SFR. However, these two papers use a sample of galaxies and any variation in the actual CO/H₂ ratio within the group would act to wash out the correlation. Kennicutt also suggests that this could reflect a dependence on strictly the volume density and not the surface density.

Clearly, the prediction for the Schmidt law index (equation 4.6) agrees well with those determined from observations, although the exact conversion factor between $\dot{\rho}_*$ and $\dot{\sigma}_*$ is not clear. We also have a dependency on the diameter of the galaxy in our Schmidt Law. For a given average gas density then a larger total size will result in more regions undergoing star formation at any time, and therefore it is reasonable to expect that the SFR should be higher.

4.4 A magnetic origin for M_{st} ?

The interstellar magnetic field is not incorporated directly into the model, although since it provides an internal cloud pressure, it might be expected to have an effect on the star formation process. We can see from the virial theorem for a static cloud (Elmegreen 1992),

$$\frac{4\pi R^3}{3} \left(P + \frac{B^2}{2\mu_0} \right) = \frac{3MkT}{\mu} - \frac{3GM^2}{5R},$$

(where P is the boundary pressure, B is the magnetic field strength and μ is the mean molecular weight for a cloud of mass M , radius R and temperature T) that unless the cloud can lose its magnetic field through ambipolar diffusion then the field will prevent collapse – if the magnetic flux is completely frozen into the material then $B \propto R^{-2}$ and hence both the magnetic and gravitational energies scale as R^{-1} . For collapse to have a chance of occurring then the magnetic-field strength must not be too strong and the boundary pressure must be sufficiently large – Mouschovias & Spitzer (1976) calculate

$$\frac{B^3}{G^{3/2}\rho^2 M} < 9 \times 10^{-9},$$

or equivalently

$$M > M_{\text{mag}} = 1.1 \times 10^8 \frac{B^3}{G^{3/2}\rho^2}, \quad (4.9)$$

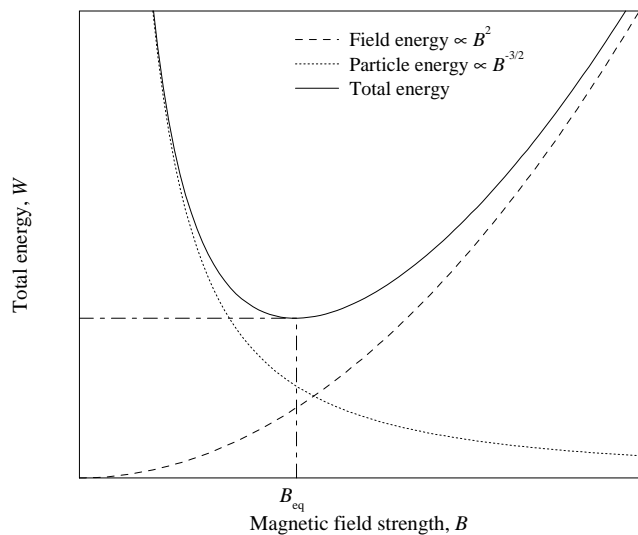
and

$$P > \frac{2.54v_s^8}{G^3 M^2 [1 - (M_{\text{mag}}/M)^{2/3}]^3},$$

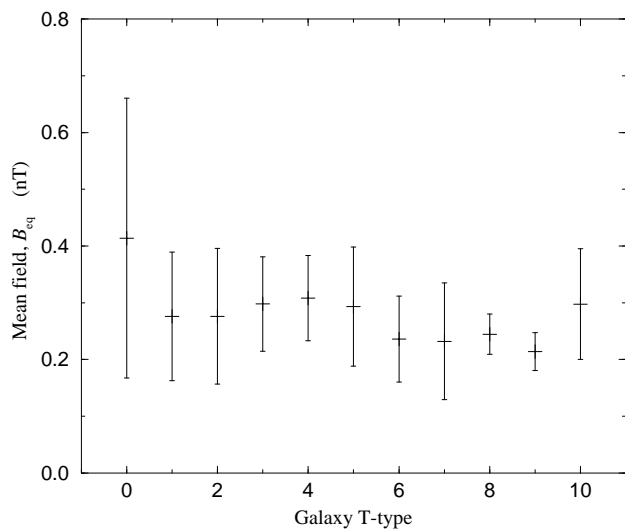
where all quantities are measured in SI units and $v_s = (\gamma kT/\mu)^{1/2}$ is the sound speed in the cloud. I have taken $\gamma = 5/3$ as is appropriate for molecular H₂ at temperatures $\lesssim 50$ K.

Is it possible to identify M_{st} with M_{mag} ? If this were the case then we would expect the observed SFR (derived from, for example, the FIR luminosity) for a galaxy to vary with its magnetic

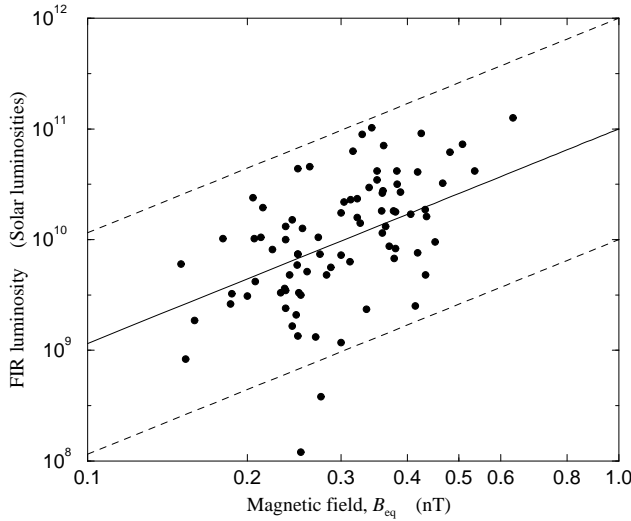


**Figure 4.6**

The minimum energy condition for magnetic fields. The energy stored in a galactic B-field rises as B^2 whereas the energy of the relativistic particles falls as $B^{-3/2}$, giving rise to a minimum in the total energy. It is assumed that a galaxy naturally adopts this minimum energy, and thus the B-field can be estimated from the radio surface brightness.

**Figure 4.7**

Average magnetic field B_{eq} as a function of galactic T-type. The data are taken from Fitt & Alexander (1993) and shows that the mean field strength is independent of galactic type and occupies a narrow range between 0.2–0.5 nT.

**Figure 4.8**

Variation of FIR luminosity with galactic magnetic field. No error bars are shown, but errors of 20–30% in FIR luminosity would be not unreasonable. The estimates of B_{eq} are more uncertain – see Longair (1994) for a discussion of the minimum energy method for estimating magnetic fields. Data are shown for 84 galaxies.

field. Unfortunately, magnetic fields are difficult to measure astronomically – for our own Galaxy, Zeeman splitting suggests values of 0.2–1.0 nT (Heiles 1990) and pulsar rotation measures give 0.2–0.7 nT (Lyne 1990). Neither of these direct techniques can be used for external galaxies; instead we have to fall back on the indirect approach of assuming that the total energy contained in relativistic particles and the magnetic field is minimised, despite there being no physical justification for this (see §19.5 of Longair (1994) and Fig. 4.6). However, with this assumption it can be shown that the estimated field B_{eq} depends only on the radio surface brightness, making it easy to measure, and the values calculated are similar to those estimated for our Galaxy (Fig. 4.7). Fitt & Alexander (1993) have used this approach to estimate the magnetic field strength for 146 spiral galaxies and by combining this data with FIR luminosity measurements from Young *et al.* (1989) and Cox *et al.* (1988) we get Fig. 4.8. Two sources for the FIR luminosities have had to be used since none of the three samples coincide directly, resulting in 84 galaxies for which both FIR luminosity and B_{eq} are known. Where the Young *et al.* and Cox *et al.* samples overlapped, the discrepancy was usually < 0.05 in $\log L_{\odot}$.

The solid line of Fig. 4.8 shows what would be expected if the star formation scaling mass were directly proportional to M_{mag} . The slope of this line was calculated from equations (4.4), (4.7) and (4.9) which give,

$$L_{FIR} \propto M_{st}^{0.646} \propto M_{mag}^{0.646} \propto B_{eq}^{1.938}, \quad (4.10)$$

The offset is undetermined and hence lines of this slope in the log–log plane have also been plotted slightly offset from the middle of the data. Clearly the result is inconclusive, although it is possible that some extension of the data can be seen along the slope of the line expected if $M_{st} \propto M_{mag}$. However, when the expected size of the error bars is taken into account, and more importantly, the systematic errors in the estimation of B_{eq} , it is not actually all that surprising that any correlation, if it does exist, has been washed out.

It is perhaps also worth noting that if the magnetic field did play a significant role in the determ-



ination of the galactic star formation rate, then given the lack of variation in B-field (on average) with galactic morphology (Fig. 4.7), we might expect the SFR to also be more or less independent of the form of the galaxy. This is indeed found to be the case – Devereux & Young (1991) consider *IRAS* fluxes for a sample of 983 galaxies, and find that star formation rates are comparable over the full range of galactic classes from Sa through to Scd.

References

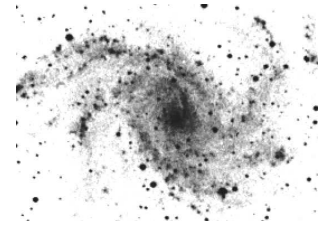
- Arimoto N., Yoshii Y., Takahara F., 1992, *A&A*, 253, 21
- Belfort P., Crovisier J., 1984, *A&A*, 136, 368
- Bica M. D., Kojoian G., Seal J., Dickinson D. F., Malkan M. A., 1995, *ApJS*, 98, 369
- Bothun G. D., Lonsdale C. J., Rice W., 1989, *ApJ*, 341, 129
- Bowers R. L., Deeming T., 1984, *Astrophysics II: Interstellar matter and galaxies*, Jones and Bartlett Publishers Inc., Boston
- Buat V., Deharveng J. M., Donas J., 1989, *A&A*, 223, 42
- Burton W. B., 1988, in *Galactic and Extragalactic Radio Astronomy*, eds Verschuur G. L., Kellermann K. I., p. 332, Springer-Verlag, New York, 2nd edn.
- Caimmi R., 1995, *A&A*, 295, 335
- Condon J. J., 1992, *Ann. Rev. Ast. Astrophys.*, 30, 575
- Condon J. J., Yin Q. F., 1990, *ApJ*, 357, 97
- Cox M. J., Eales S. A. E., Alexander P., Fitt A. J., 1988, *MNRAS*, 235, 1227
- Cox P., Krugel E., Mezger P. G., 1986, *A&A*, 155, 380
- Devereux N. A., Young J. S., 1990, *ApJ*, 350, L25
- Devereux N. A., Young J. S., 1991, *ApJ*, 371, 515
- Dopita M. A., 1985, *ApJ*, 295, L5
- Dopita M. A., 1990, in *The Interstellar Medium in Extnal Galaxies*, eds Thronson H. A., Shull J. M., p. 437, Dordrecht, Kluwer
- Dopita M. A., Ryder S. D., 1994, *ApJ*, 430, 163
- Eales S. A., Wyn-Williams C. G., Duncan W. D., 1989, *ApJ*, 339, 859
- Elmegreen B. G., 1992, in *Star Formation in Stellar Systems*, eds Tenorio-Tagle G., Prieto M., Sánchez F., p. 381, Cambridge University Press
- Elmegreen B. G., Clemens C., 1985, *ApJ*, 294, 523
- Firmani C., Tutukov A., 1992, *A&A*, 264, 37
- Fitt A. J., Alexander P., 1992, *MNRAS*, 258, 241
- Fitt A. J., Alexander P., 1993, *MNRAS*, 261, 445
- Gordon M. A., 1995, *A&A*, in press
- Heiles C., 1990, in *IAU Symposium 140, Galactic and Intergalactic Magnetic Fields*, eds Beck R., Kronberg P. P., Wielebinski R., p. 35, Reidel, Dordrecht
- Kennicutt R. C., 1983, *ApJ*, 272, 54
- Kennicutt R. C., 1989, *ApJ*, 344, 685
- Lada E., Strom K., Myers P., 1992, in *Protostars and Planets III*, eds Levy E. H., Lunine J., Matthews M. S., University of Arizona Press
- Li J. G., Seaquist E. R., Wrobel J. M., Wang Z., Sage L. J., 1993, *ApJ*, 413, 150
- Liszt H. S., Burton W. B., Xiang D., 1984, *A&A*, 140, 303
- Longair M. S., 1994, *High Energy Astrophysics*, vol. 2, Cambridge University Press, 2nd edn.
- Lonsdale Persson C. J., Helou G., 1987, *ApJ*, 314, 513

- Lyne A., 1990, in *IAU Symposium 140, Galactic and Intergalactic Magnetic Fields*, eds Beck R., Kronberg P. P., Wielebinski R., p. 41, Reidel, Dordrecht
- Magnani L., Blitz L., Mundy L., 1985, *ApJ*, 295, 402
- Miller G. E., Scalo J. M., 1979, *ApJS*, 41, 513
- Mouschovias T. C., Spitzer L., 1976, *ApJ*, 210, 326
- Rana N. C., Wilkinson D. A., 1986, *MNRAS*, 218, 497
- Sanders D. B., Solomon P. M., Scoville N. Z., 1984, *ApJ*, 276, 182
- Sanders D. B., Scoville N. Z., Solomon P. M., 1985, *ApJ*, 289, 373
- Schmidt M., 1959, *ApJ*, 129, 736
- Schmidt M., 1963, *ApJ*, 137, 758
- Scoville N. Z., Good J. C., 1989, *ApJ*, 339, 149
- Stark A. A., Brand J., 1989, *ApJ*, 339, 763
- Tenjes P., Haud U., 1991, *A&A*, 251, 11
- Thronson H. A., Telesco C. M., 1986, *ApJ*, 311, 98
- Tosi M., Díaz A. I., 1990, *MNRAS*, 246, 616
- Turner B. E., 1984, *Vistas Astron.*, 27, 303
- Wyse R. F. G., Silk J., 1989, *ApJ*, 339, 700
- Xu C., Lisenfeld U., Völk H. J., Wunderlich E., 1994a, *A&A*, 282, 19
- Xu C., Lisenfeld U., Völk H. J., 1994b, *A&A*, 285, 19
- Young J. S., Xie S., Kenney J. D. P., Rice W. L., 1989, *ApJS*, 70, 699



Chapter 5

Spiral density waves and galactic structure



One of the major advantages of the new model as compared with previous simulations using propagating star formation is the ease with which a spiral density wave (SDW) can be introduced in a natural way. This is found to have a major effect on the galactic structures that can be produced (in particular it is now possible to obtain long-lived, non-transient, grand-design spirals), but a fairly small effect on the overall star formation rate. This is contrary to many galactic models where star formation is considered to be triggered by shock waves arising directly from the SDW, but importantly is consistent with the observation that the strength of the spiral density wave in real galaxies does not correlate well with star formation rate (Elmegreen & Elmegreen 1986). This will be discussed in greater detail below as we consider the interplay between the SDW and the star formation rate.

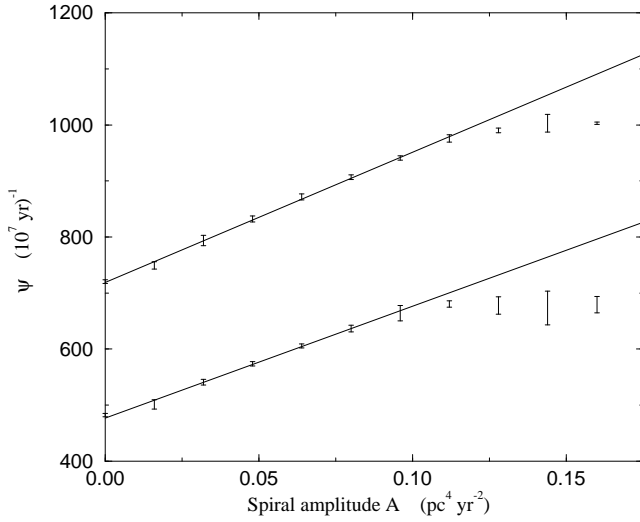
The galactic structures produced by the model clearly depend on the input parameters, both those controlling the star formation processes and also (perhaps more obviously) those affecting the form of the spiral potential. In this chapter I also present a brief survey of the range of galactic structures produced as a function of the input parameters. Ideally we would like some way of comparing the images quantitatively, both with other simulation results and also observational data. This important problem will be considered in Chapter 7.

5.1 The effect of the SDW on the cluster formation rate

The dependence of the CFR on the input parameters controlling the nature of the spiral perturbation to the gravitational field of the galaxy has been investigated in a manner similar to that described in Section 4.1. All other parameters have been kept fixed at their ‘standard’ values (Table 4.1) except when considering the CFR dependence on the amplitude of the SDW where two different values for M_{st} were used (Fig. 5.1). Once again each data point is the average of an ensemble of between three and six runs to take into account the stochasticity of the simulation.

The effects of varying the radius of the inner bar (r_0) and the sharpness of the transition from



**Figure 5.1**

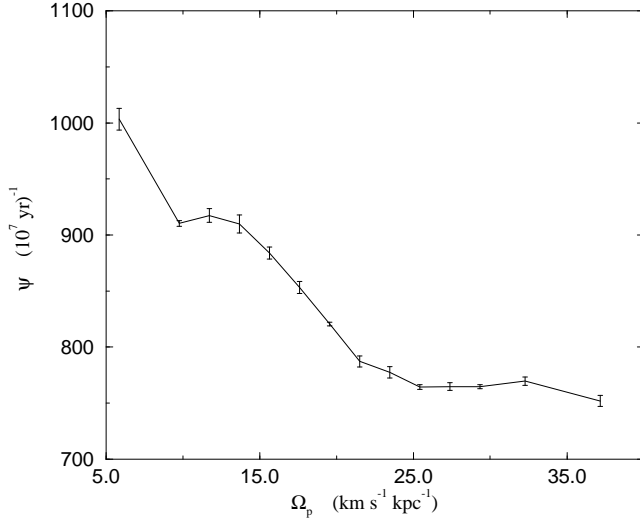
The effect of the amplitude of the spiral density wave on the cluster formation rate. The upper curve has been calculated with $M_{\text{st}} = 1.0 \times 10^5 M_{\odot}$ and the lower with $M_{\text{st}} = 3.2 \times 10^5 M_{\odot}$.

bar to normal spiral (p) were found to be very small with $\psi \propto r_0^{-0.055 \pm 0.008}$ and $\psi \propto p^{0.012 \pm 0.003}$. For normal, i.e. unbarred spirals, which are the focus of this study, r_0 must be small, and therefore changing r_0 or p can only affect the innermost regions of the galactic disc. This weak dependence is therefore not surprising since these regions are not considered explicitly in this model as both atomic and molecular gas densities drop to zero in the central regions (Fig. 5.9), thus preventing star formation.

The CFR does exhibit dependencies on the other SDW parameters however, which although weak, shed some interesting light on the feedback mechanisms acting within the model. These will be discussed individually below.

5.1.1 Amplitude of the SDW

As the amplitude of the SDW (A) is raised, the orbit crowding resulting from the spiral perturbation also increases. Furthermore, the particles move more slowly through the arm region as the depth of the spiral potential grows and the two effects taken together result in any given super-bubble shock being able to trigger many more star formation events – there are both more clouds which can be shocked, and the SN remnant spends an increasing time in the enhanced region. Hence we would expect the CFR to rise as A is increased: the dependence of the cluster formation rate on the amplitude of the spiral perturbation is shown in Fig. 5.1. Clearly ψ is linearly dependent on the strength of the SDW up to some limiting value which is a function of M_{st} , and furthermore the plateau cluster formation rate attained after the turnover has occurred is also a function of M_{st} . Both effects can be understood by considering the interplay of A , M_{st} and the average cloud regrowth time. First let us consider the plateau region. Here the cluster formation rate has saturated, and the rate at which new stars can be formed is limited by the time required for the mass of a molecular cloud to increase via accretion to a value such that there is a reasonable chance of star formation being triggered in the cloud. Writing the average cloud regrowth time as τ then from equation (3.1)

**Figure 5.2**

Star formation rate ψ as a function of the spiral pattern speed Ω_p .

we see that

$$M_{\text{st}} = (\gamma\rho_{\text{HI}}v\tau)^3 + \varepsilon M_{\text{st}}$$

and hence

$$\tau = \frac{\sqrt[3]{M_{\text{st}}(1 - \varepsilon)}}{\gamma\rho_{\text{HI}}v}. \quad (5.1)$$

Substituting some appropriate values we find that for $M_{\text{st}} = 1.0 \times 10^5 M_{\odot}$, $\tau \sim 3.0 \times 10^8$ yr. Now, the CFR above the turnover ψ_{plat} will be simply the reciprocal of τ multiplied by the number of clouds and therefore we would expect $\psi_{\text{plat}} \approx 1000 \times 10^{-7} \text{ yr}^{-1}$ for $M_{\text{st}} = 1.0 \times 10^5 M_{\odot}$. Furthermore we predict that $\psi_{\text{plat}} \propto M_{\text{st}}^{-1/3}$, both of which, as can be seen from Fig. 5.1, are indeed found to be the case.

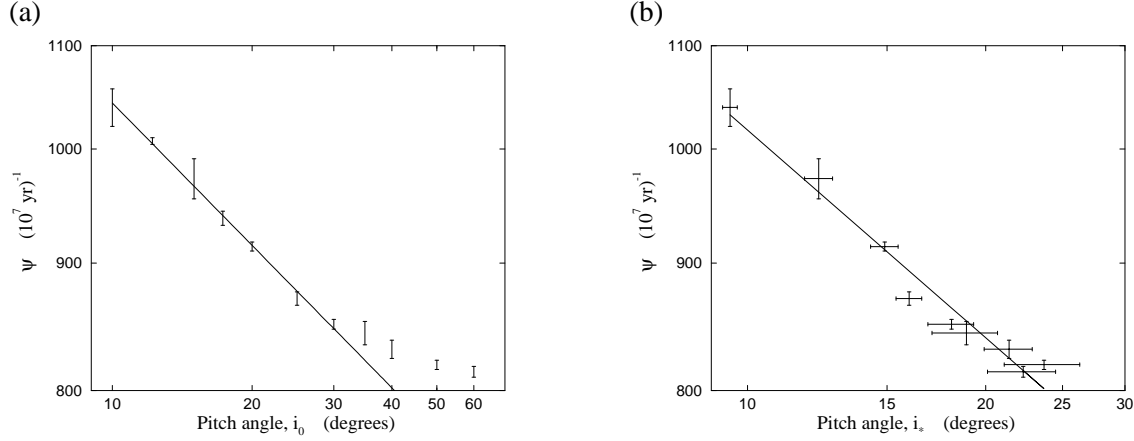
The shift of the turnover can be explained by the fact that τ rises with M_{st} and remembering that increasing A reduces the average time between successive supernova shock waves impinging on any given cloud. Hence the turnover, which occurs when this latter time scale becomes comparable with τ occurs at lower values of A for higher values of M_{st} , as is evident in Fig. 5.1.

5.1.2 Spiral pattern speed

The variation of the SFR with Ω_p (Fig. 5.2) shows a similar saturation at low values of the pattern speed. By varying the pattern speed we are investigating the same scaling regime of the star formation rate that is probed by varying the amplitude of the SDW. Hence the variation seen can also be understood by considering the respective timescales which govern the star formation process. At low pattern speeds, clouds and supernova remnants spend longer in the compressed, high density region of the spiral potential compared to when the pattern speed is high. A cloud is thus more likely to be triggered to form stars at low pattern speed, and hence in this limit the SFR is high. Note that if the triggering of cloud collapse was a result of shocks arising from the spiral



Figure 5.3. Star formation rate ψ as a function of (a) the pitch angle of the imposed spiral density wave i_0 and (b) the pitch angle of the pattern traced by young stellar clusters i_* .



potential then we would expect to see the opposite behaviour, since in this scenario, the increased frequency at which any given cloud was shocked would result in a rise in the star formation rate.

5.1.3 SDW pitch angle

We see from Fig. 5.3(a) that the variation of the pitch angle of the imposed spiral potential perturbation has only a small effect on the total star formation rate, and is well represented by a power law $\psi \propto i_0^{-0.188 \pm 0.008}$ for $i_0 < 30^\circ$. In this case we are investigating a different scaling regime than in the two previous cases. Instead of the star formation rate being controlled solely by time constants, here the dominant effect is geometrical. As the pitch angle is increased, the fraction of the galactic disc which is covered by the spiral density wave decreases, and since the potential minimum marks areas of enhanced star formation then we would expect the CFR to decrease with increasing i_0 as observed.

Fourier analysis techniques (Chapter 7) allow us to calculate the pitch angle of the actual distribution of OB associations tracing the spiral arm, i_* , which is a more important factor in controlling the CFR than i_0 since it is the distribution of young stars that directly affects the propagation. We will see (§7.2.1) that i_* varies non-linearly with i_0 and moreover is always less than it (Fig. 7.6), and hence it is interesting to consider the cluster formation rate as a function of i_* . From Fig. 5.3(b) we see that $\psi \propto i_*^{-0.28 \pm 0.02}$, which is a somewhat flatter slope than would be expected from a simple argument based on the premise that the CFR was directly proportional to the area covered by the arms. The total length of a logarithmic spiral out to some radius R is $L = R \text{ cosec}(i_*) \propto i_*^{-1}$ for the range of i_* under consideration, and so assuming that the width of the arm is constant both as a function of radius and i_0 we might also expect $\psi \propto i_*^{-1}$. However, as can be seen from Fig. 5.7, neither of these approximations are realistic and furthermore, we expect other factors to contribute. Any variation in the rate of star formation due to geometrical effects will alter the natural

timescales of the propagation process since the the average time between star formation events for any given cloud will also change. Unfortunately, we have to conclude that disentangling the situation is not possible in this case with a simplistic analysis such as we were able to use when considering the effect of the SDW amplitude (§5.1.1).

5.1.4 Number of spiral arms

In addition to the $n = 2$ cases considered above as part of the ‘standard’ set, I have also looked at the possibility of $n = 3$ spirals. From dynamical studies it can be easily shown that these are less favoured modes, with a lower range of radii for which they are stable (§5.3). However, three armed spirals have been detected observationally (Elmegreen *et al.* 1992) although always in the presence of a stronger two-armed component.

From the discussion above we can predict how the CFR will change if we impose an $n = 3$ spiral (without having an $n = 2$) – clouds will encounter a region of higher than average density more frequently, since there are more of them. Moreover, the fraction of the disc covered by the spiral density wave also rises compared with the two-armed case, and hence we see that the total effect is a combination of the factors identified above, and expect the star formation rate to rise. This is indeed found to be the case, with $\psi \sim 1020 \times 10^{-7} \text{ yr}^{-1}$, a small increase of approximately 10% over the equivalent $n = 2$ case.

Note that this is not a particularly realistic scenario, since the two-armed mode is always dominant. As will be seen (§7.2.1), Fourier analysis shows that a weak three-armed component is in fact often present in the structures produced by the model (see in particular Fig. 7.4(d)), and hence it is not really necessary, or appropriate, to force its occurrence.

5.1.5 Comparison with observations

The variation of the star formation rate with the parameters controlling the form of the spiral density wave can be readily understood by simple arguments. However, the relative importance of such changes in determining the total SFR is small – the input parameters to the model have been varied through all realistic values which could describe galaxies spanning the Hubble sequence and yet the variation of the CFR is only of order ± 10 per cent. Observationally, such a small effect would be considered to be constant within the measurement errors. Moreover, changing the value of M_{st} produces a far larger effect on the total rate at which stars are created (§4.1.1), and hence observationally, we would expect the SFR to be largely independent of the form or indeed existence of a spiral density wave. Elmegreen & Elmegreen (1986) present data for a sample of 745 galaxies which confirms this expectation – they find that spiral density waves are not responsible for directly triggering star formation (except possibly in some peculiar cases) but instead order the star formation and organise it into spiral structures. A similar result is reported by Elmegreen (1993) using more recent data, and also by Devereux & Young (1991) who, considering the star formation rate of massive stars, find that the SFR per unit molecular gas mass is comparable between early- (Sa–Sab), intermediate- (Sb–Sbc) and late- (Sc–Scd) type spirals.



5.2 Structure as a function of the input parameters

As we have seen, the parameters controlling the nature of the spiral perturbation have an interesting, but small effect on the overall rate of star formation. As would be expected however, the galactic structure is quite strongly dependent on the SDW, as indeed it is on the other input parameters as well. I present below a selection of galactic images for various values of the four input parameters which we would expect to have the largest effect on the galactic structure. The total age range of the clusters shown in each image is the same, and hence the observed structure will be strongly dependent on the star formation rate, and therefore M_{st} (Fig. 5.4). When a star cluster is created, it acquires the velocity of the progenitor cloud, and hence as v_{disp} rises, we would expect the structures to become increasingly amorphous, with the spiral arms becoming less well defined. In fact the effect is not as strong as might be expected (Fig. 5.5), primarily because the star formation rate rises with v_{disp} which acts to reinforce the importance of the arms. More predictably, the spiral arms become better defined with increasing A , and less tightly wound with increasing i_0 (Figs 5.6, 5.7). The transient, strong, spirals seen in the early SSPSF models (§2.1.2) are not generally present in the current simulation, even at low values of the SDW amplitude, since they are washed out by the velocity dispersion of the clouds. At much lower values of v_{disp} , then spiral structures due solely to the differential rotation of the galaxy do begin to appear. The velocity dispersion required for this ($< 0.02 \text{ km s}^{-1}$) is however, much lower than anything observed, and the conclusion must therefore be that spiral density waves have to be present in grand-design spirals. Flocculent spirals are also readily produced by the model, as is evident from a cursory inspection of Figs 5.4, 5.5, 5.6 and 5.7.

The images presented in Figs 5.4 to 5.7 are colour coded such that the youngest stars are shown as blue and the eldest (130 Myr) as red. This reflects the changing colour of an observed cluster as its most massive, blue OB stars die as supernovae, leaving only the cooler, red stars. The colours are however only meant to be illustrative, and should not be interpreted as representing the true cluster colour.

In a similar manner to the cluster formation rate studies, only one parameter has been changed at a time, with the others held fixed at their ‘standard’ values (Table 4.1). The galaxies represented in the following pages are ‘typical’ in the sense that they are selected at random from an ensemble of three to six runs. As a consequence of the stochastic nature of the simulation it is difficult to draw general conclusions from the images alone – a more quantitative description of the structure is required, and this will be the subject of Chapter 7.

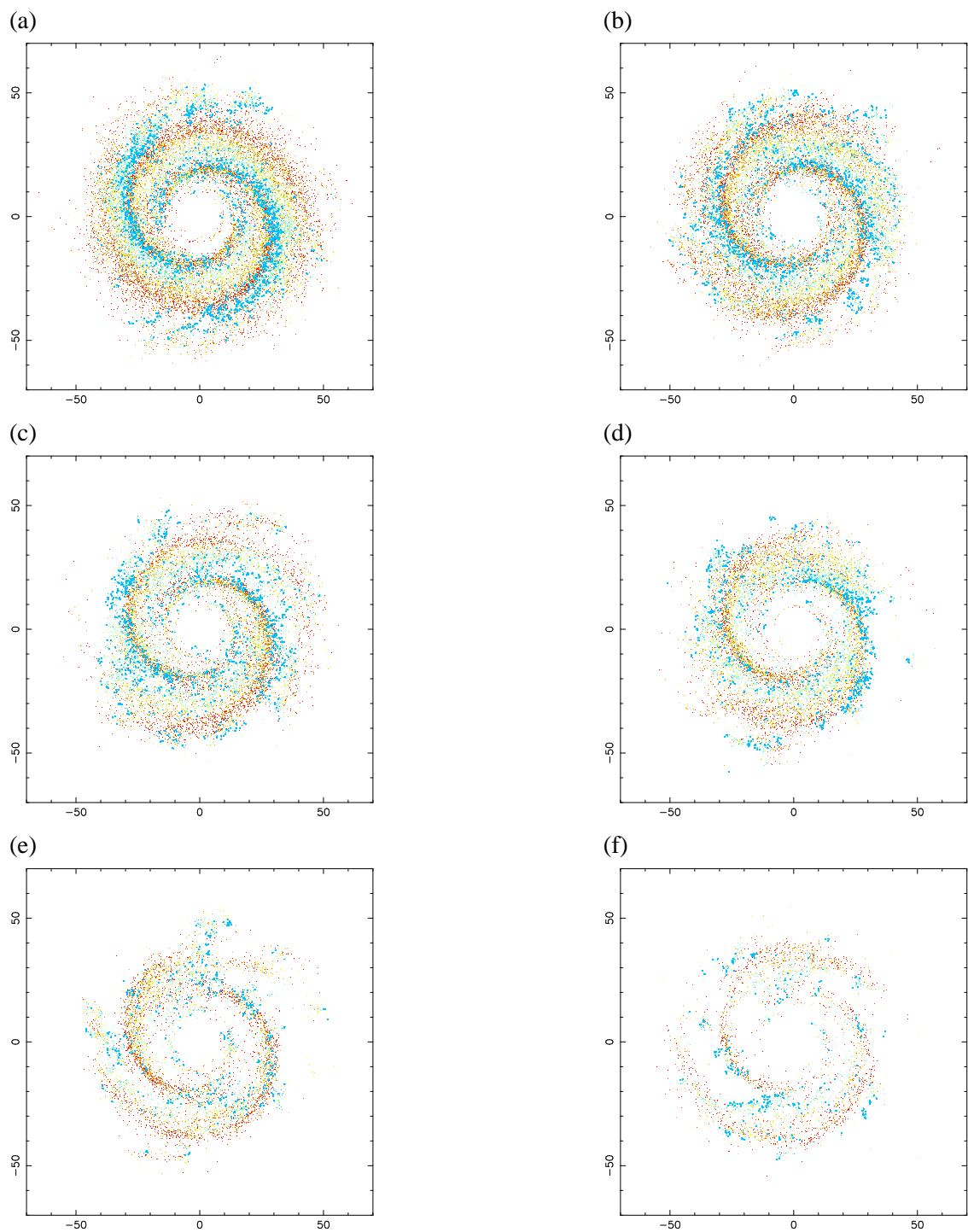


Figure 5.4. Galactic structure as a function of propagation scaling mass, M_{st} : (a) $1.0 \times 10^4 M_{\odot}$, (b) $3.2 \times 10^4 M_{\odot}$, (c) $1.0 \times 10^5 M_{\odot}$, (d) $3.2 \times 10^5 M_{\odot}$, (e) $1.0 \times 10^6 M_{\odot}$, (f) $3.2 \times 10^6 M_{\odot}$.



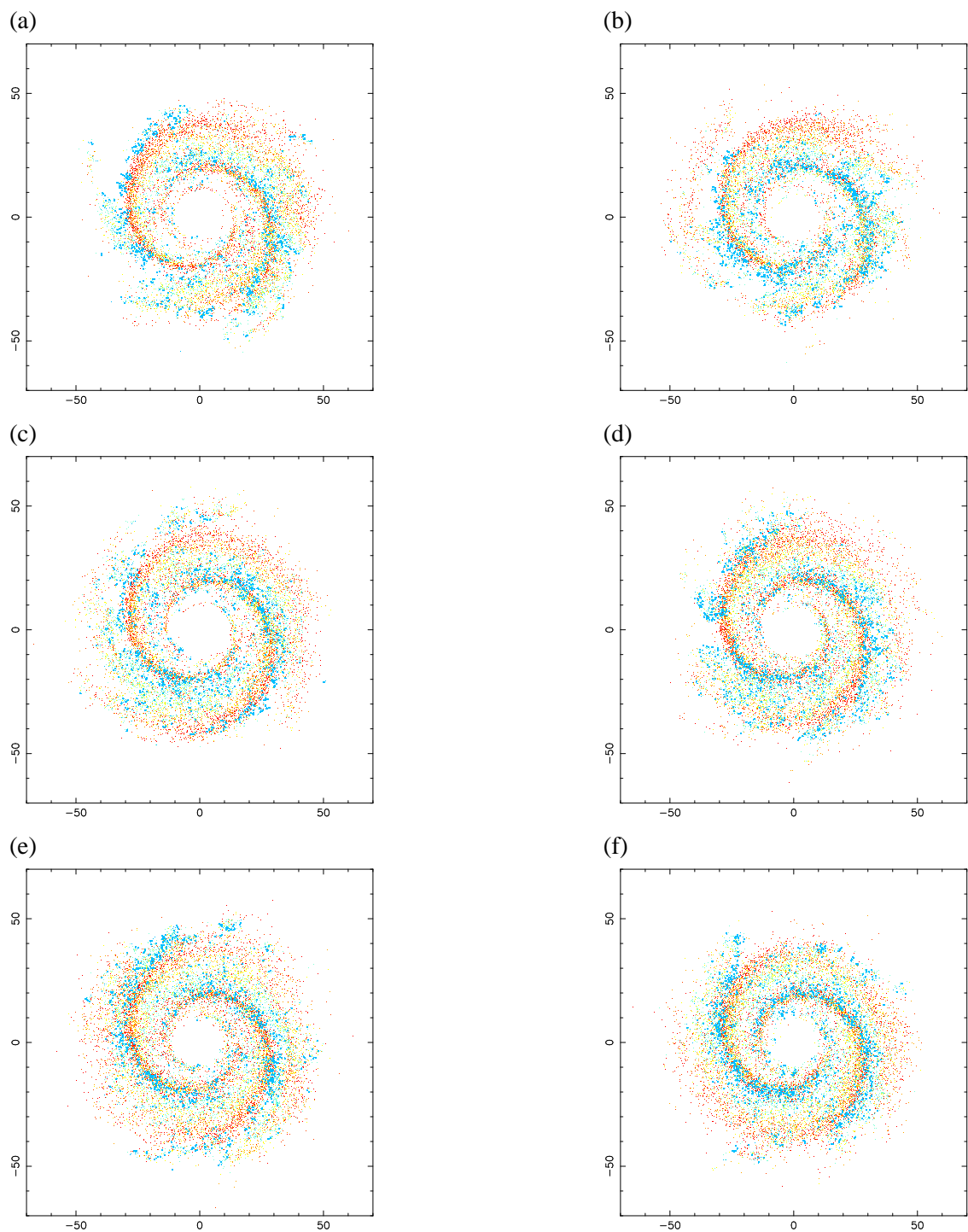


Figure 5.5. Galactic structure as a function of cloud velocity dispersion, v_{disp} : (a) 6.4 km s^{-1} , (b) 6.6 km s^{-1} , (c) 7.1 km s^{-1} , (d) 7.6 km s^{-1} , (e) 8.3 km s^{-1} , (f) 9.0 km s^{-1} .



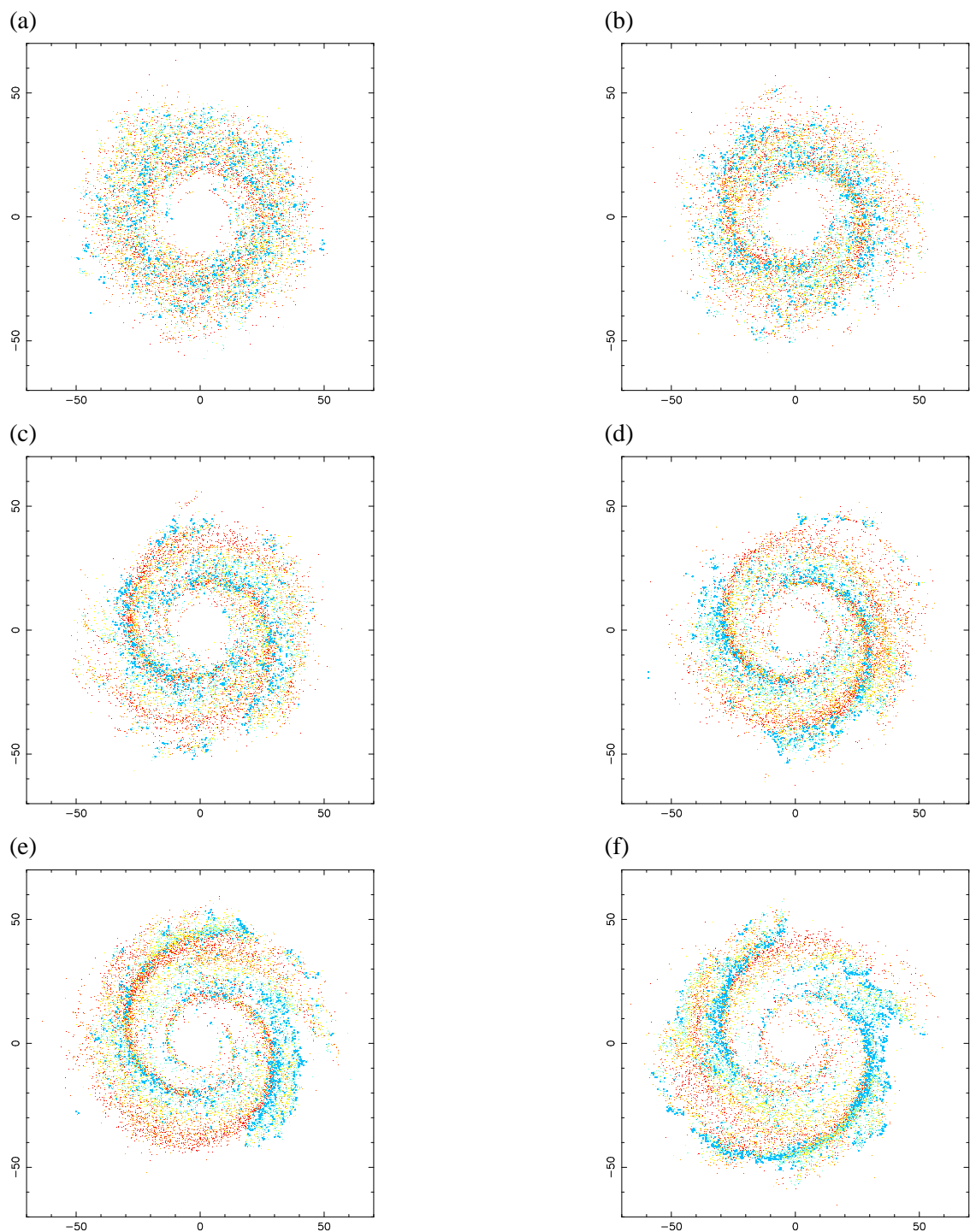


Figure 5.6. Galactic structure as a function of SDW amplitude, A : (a) $0.0 \text{ pc}^4 \text{ yr}^{-2}$, (b) $0.032 \text{ pc}^4 \text{ yr}^{-2}$, (c) $0.064 \text{ pc}^4 \text{ yr}^{-2}$, (d) $0.096 \text{ pc}^4 \text{ yr}^{-2}$, (e) $0.128 \text{ pc}^4 \text{ yr}^{-2}$, (f) $0.16 \text{ pc}^4 \text{ yr}^{-2}$.



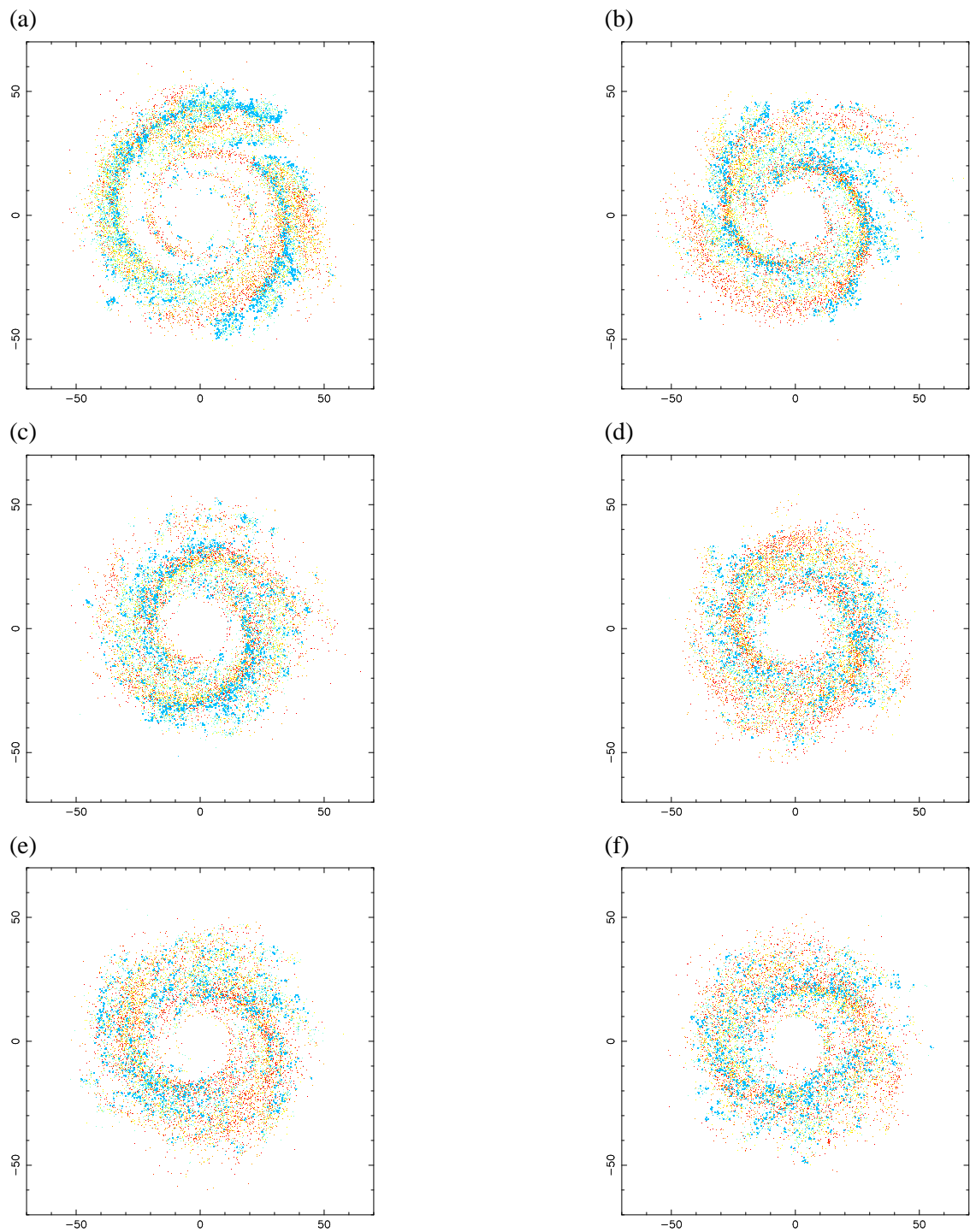
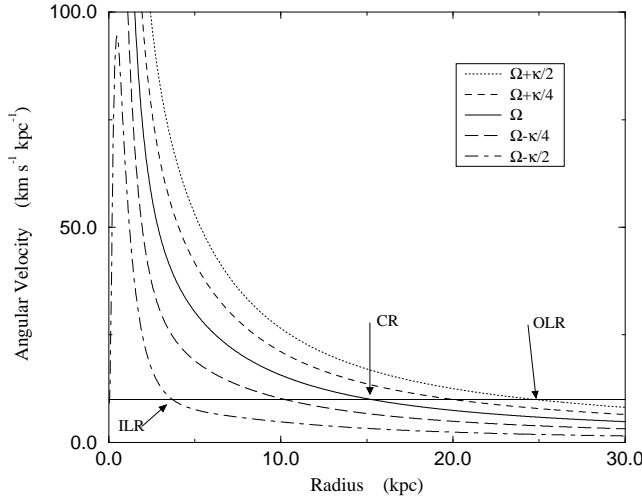


Figure 5.7. Galactic structure as a function of SDW pitch angle, i_0 : (a) 10° , (b) 20° , (c) 30° , (d) 40° , (e) 50° , (f) 60° .



**Figure 5.8**

Resonance curves arising from the model potential. The positions of the inner Lindblad resonance (ILR), co-rotation resonance (CR) and outer Lindblad resonance (OLR) are indicated for spiral pattern speed $\Omega_p = 10 \text{ km s}^{-1} \text{ kpc}^{-1}$.

5.3 Resonances and the radial distribution of star formation

Spiral density waves, as a perturbation to the otherwise axisymmetric galactic potential, provide a periodic force to stellar orbits in the galaxy. Hence there exists a resonant condition whenever the perturbing force has a frequency which matches that of the orbit, and at resonance the orbits will be unstable due to the large disturbance amplitude that results. As observed in a frame rotating with the appropriate Keplerian velocity (Ω) of the particle, an n -armed density wave has an angular frequency of $n(\Omega - \Omega_p)$, whereas, in the same frame of reference, the particle has a radial frequency equal to its epicyclic frequency κ given by

$$\kappa^2 = 4\Omega^2 \left(1 + \frac{r}{2\Omega} \frac{d\Omega}{dr} \right),$$

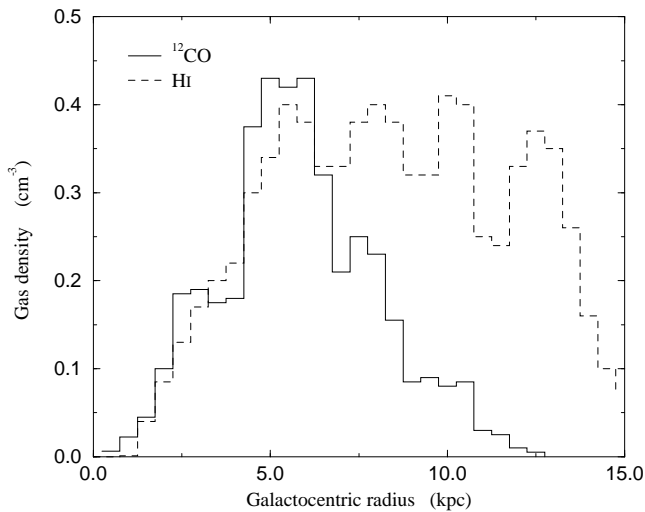
provided the eccentricity of the orbit is small (as we have here). Resonance will occur when the condition $n(\Omega - \Omega_p) = \pm\kappa$ is satisfied, with the positive sign indicating that the star is overtaking the crest of the potential and the negative sign that the faster moving perturbation is sweeping past the particle.

Furthermore, by substituting a spiral perturbation into the first order, linearised equations of motion, it is possible to calculate a dispersion relation for spiral density waves, and from this it can be shown that for quasi-stationary spiral modes, the condition

$$\Omega - \frac{\kappa}{n} \leq \Omega_p \leq \Omega + \frac{\kappa}{n}$$

must hold, i.e. an n -armed SDW can exist as a stable perturbation only in the region where this inequality is satisfied. The special cases of $n = 2$ are known as the inner and outer Lindblad resonances (ILR and OLR respectively) and when $n = 1$ the spiral pattern co-rotates (CR) with the galaxy. Curves showing the radial positions of the resonances for the potential used in the model (§3.2.2) are shown as Fig. 5.8 – clearly the stable region has the greatest extent for $n = 2$, and it is for this reason that grand-design spirals have two prominent arms. We will see later (§7.2.1),



**Figure 5.9**

Galactic gas distribution as used in the model. The data are reproduced from Burton (1988). The clouds are initially spread across the disc such that the distribution matches that of the ^{12}CO , and they accrete throughout the simulation from the HI which remains unchanged.

that the star formation disrupts the simple pattern, resulting in observed spiral components (using sites of recent star formation to trace the arms) with $n > 2$, although the underlying SDW is still bisymmetric.

A useful introduction to stellar orbital dynamics and the mathematics underlying the Lin–Shu quasi-stationary spiral density wave hypothesis (Lin & Shu 1964; Lin & Shu 1966) can be found in Bowers & Deeming (1984), whilst for a more comprehensive treatment the reader is referred to either Binney & Tremaine (1987) or Shu (1992).

At radii corresponding to the different resonances we might expect the perturbation to have a noticeable effect on the orbital dynamics of stars and gas clouds, and hence to appear in images of the galaxies. This indeed is the only way in which SDW pattern speeds can be measured for external galaxies. However, no consensus exists as to which resonance limits the maximum radius of the spiral density wave, and hence pattern speeds are only poorly known. For example, Elmegreen, Elmegreen & Montenegro (1992) propose that the OLR marks the greatest extent of the spiral pattern on the basis of an identification of three-armed components in selection of galaxies. In contrast Roberts, Roberts & Shu (1975) place co-rotation at the end of the spiral since it is at CR that the shock resulting from the relative velocity of gas with respect to the wave will vanish. A third theory due to Contopoulos & Grosbøl (1986) places the inner 4/1 resonance at the edge of the spiral pattern – they find that non-linear effects make it difficult to construct self-consistent stellar models of strong spirals outside this radius. Finally Elmegreen & Elmegreen (1995) propose, based on a sample of 173 galaxies, that the spiral pattern should be divided into inner and outer regions, the boundary being marked by co-rotation, and observationally by the point at which the two inner, symmetric arms broaden or bifurcate. This results in the OLR being at approximately the edge of the galaxy, and hence does not contradict their earlier work, although now the defining condition is different.

Our particles move ballistically as test masses in an imposed potential, and hence the model is unable to reproduce the sort of phenomena discussed above, since they arise from the collective

forces between all the particles. In particular, the radius out to which spiral arms can be traced is limited by the maximum radius at which star formation still has a reasonable probability of occurring, i.e. the extent of the spiral arms is constrained by the distribution of the gaseous components (H_2 and $H\ I$). This is not a variable quantity in the current model, but instead is fixed by the Galactic gas distributions (Fig. 5.9). Since the clouds are dynamic entities, the molecular gas distribution can change with time as the simulation proceeds (although it is found that the changes are small), whereas the $H\ I$ gas is fixed both spatially and temporally.

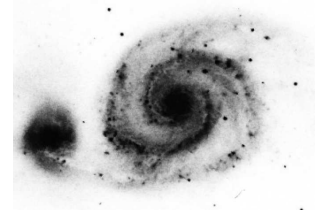
References

- Binney J., Tremaine S., 1987, *Galactic Dynamics*, Princeton University Press, New Jersey
- Bowers R. L., Deeming T., 1984, *Astrophysics II: Interstellar matter and galaxies*, Jones and Bartlett Publishers Inc., Boston
- Burton W. B., 1988, in *Galactic and Extragalactic Radio Astronomy*, eds Verschuur G. L., Kellermann K. I., p. 332, Springer-Verlag, New York, 2nd edn.
- Contopoulos G., Grosbøl P., 1986, *A&A*, 155, 11
- Devereux N. A., Young J. S., 1991, *ApJ*, 371, 515
- Elmegreen B. G., Elmegreen D. M., Montenegro L., 1992, *ApJS*, 79, 37
- Elmegreen D. M., 1993, in *Star Formation, Galaxies and the Interstellar Medium*, eds Franco J., Ferrini F., Tenorio-Tagle G., p. 108, Cambridge University Press
- Elmegreen D. M., Elmegreen B. G., 1986, *ApJ*, 311, 554
- Elmegreen D. M., Elmegreen B. G., 1995, *ApJ*, 445, 591
- Lin C. C., Shu F. H., 1964, *ApJ*, 140, 646
- Lin C. C., Shu F. H., 1966, *Proc. Nat. Acad. Sci.*, 229, 55
- Roberts Jr. W. W., Roberts M. S., Shu F. H., 1975, *ApJ*, 196, 381
- Shu F. H., 1992, *The Physics of Astrophysics – volume II: Gas Dynamics*, University Science Books



Chapter 6

The observational sample



We have seen how the model predictions of the star formation rate and related quantities can be compared with observational data from our own Galaxy. However, when considering the structures produced then clearly it is necessary to have a sample of external galaxies with which to compare the model results, a selection of which were shown in Chapter 5. I present below the galaxy sample used in this work, before going on in the following chapter to consider quantitative tools with which to characterise the nature of the galaxies' structure.

6.1 Tracers of star formation

Regions of recent star formation are traced most easily by the $H\alpha$ emission from the ionised hydrogen which results from the interaction between the massive OB stars and the embedding cloud, and it is on the basis of the availability of a catalogue of H II regions for any given galaxy that the sample was chosen. The data is summarised in Table 6.1, and the optical images and H II distributions of each galaxy are presented as Fig. 6.3. It should be noted that such catalogues are of necessity somewhat subjective since from the original $H\alpha$ image it is often difficult to distinguish between one large H II region and a complex comprised of many smaller ones. It is then up to the compiler of the catalogue to make his/her decision – see Hodge & Kennicutt (1983) for a discussion of the problems encountered in producing such a list.

It is noticeable that the vast majority of the galaxies for which data are available are of type later than Sbc (Fig. 6.1). This is an unfortunate consequence of the fact that the H II regions are much easier to pick out in these galaxies – indeed it could be considered a defining feature of late-type spirals. The model is however, optimised to simulate Sb galaxies similar to our own - many of the defining characteristics of the model have been constrained by Galactic values, for example the gas distributions (both H I and H_2) and the relative importance of the bulge compared to the disc (which determines the orbital dynamics). Any future studies would benefit greatly from extending the sample to remove this bias.



Table 6.1. Observations of H II regions

Galaxy	No. H II regions ^a	Inclination ^b	P.A. ^b	Inclination ^c	P.A. ^c	T-type ^c
IC 342	665	22°	32°	12°	—	6
NGC 628	727 ^d	8°	23°	24°	25°	5
NGC 925	132	54°	102°	56°	102°	7
NGC 1232	529	33°	86°	29°	108°	5
NGC 2403	604	55°	121°	56°	127°	6
NGC 2805	117	39°	116°	41°	125°	7
NGC 2835	125	42°	168°	49°	8°	5
NGC 3031	801	58°	150°	58°	157°	2
NGC 3184	144	13°	90°	21°	135°	6
NGC 3344	151	28°	164°	24°	—	4
NGC 3486	153	42°	80°	42°	80°	5
NGC 3521	149	64°	166°	62°	163°	4
NGC 3556	192	—	—	75°	80°	6
NGC 3938	160	10°	24°	24°	—	5
NGC 4254	214	30°	6°	29°	—	5
NGC 4303	289	29°	135°	27°	—	4
NGC 4321	286	28°	146°	32°	30°	4
NGC 4535	221	44°	1°	45°	0°	5
NGC 4654	107	56°	120°	55°	128°	6
NGC 5055	138	58°	103°	55°	105°	4
NGC 5194	160 ^e	20°	170°	52°	163°	4
NGC 5457	471	24°	38°	21°	—	6
NGC 5962	112	43°	117°	45°	110°	5
NGC 6384	142	48°	41°	49°	30°	4
NGC 6814	734 ^f	20° ^f	167° ^f	21°	—	4
NGC 6946	540	34°	64°	32°	—	6
NGC 7331	124	74°	167°	69°	171°	3

^aHodge & Kennicutt (1983) unless otherwise stated

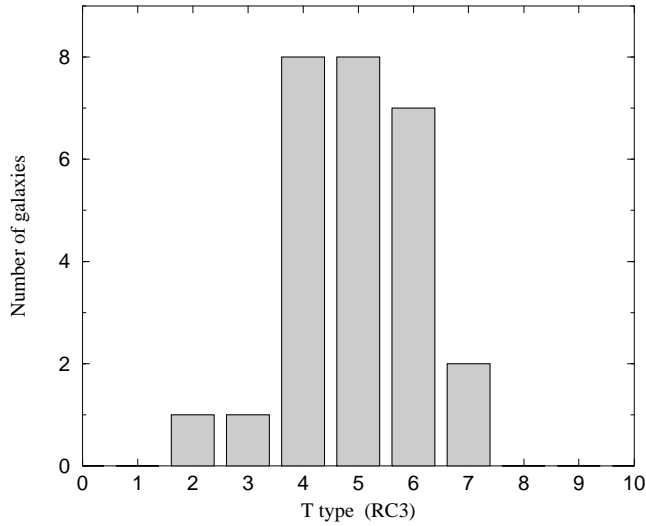
^bGarcía-Gómez & Athanassoula (1991) unless otherwise stated

^cde Vaucouleurs *et al.* (1991)

^dHodge (1976)

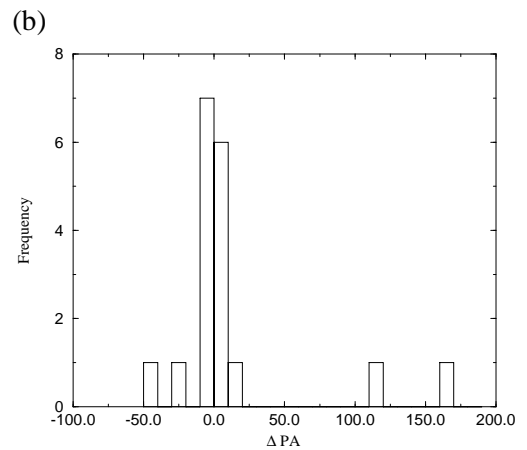
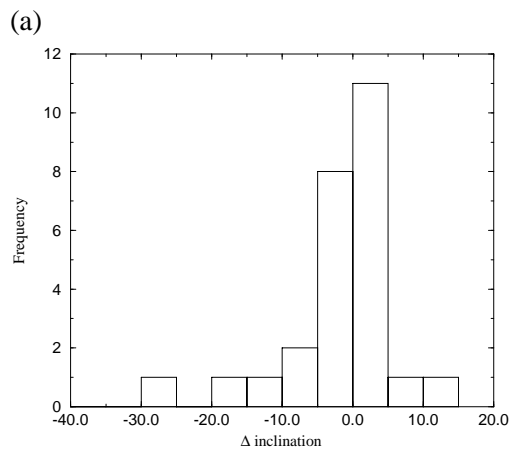
^eCarranza, Crillon & Monnet (1969)

^fKnapen *et al.* (1993)

**Figure 6.1**

Distribution of morphological types in the observational sample. Classifications are from de Vaucouleurs *et al.* (1991).

Figure 6.2. Discrepancies between PA and inclination values for the observational sample. The inclination data (a) have been binned at 5° and the (b) PA data have been binned at 10° .



6.2 Galaxy orientation

Real galaxies are, of course, randomly orientated with respect to an Earth-bound observer. To allow for comparisons between data-sets it is necessary to de-project the galaxy such that it appears as if it were face-on to us. This requires knowledge of both the position angle (PA) of the major axis (normally measured from North through East) and its inclination (i) to the line of sight. The corrected positions of the individual H II regions are then given by

$$\begin{pmatrix} x' \\ y' \end{pmatrix} = \begin{pmatrix} \sec(i) \cos(\text{PA}) & \sec(i) \sin(\text{PA}) \\ -\sin(\text{PA}) & \cos(\text{PA}) \end{pmatrix} \begin{pmatrix} x \\ y \end{pmatrix},$$

where the standard astronomical convention of having East to the left has been used. Note however, that many of the H II catalogues effectively flip this round by assigning points to the East with positive x -coordinate.

In all subsequent analysis, I have used the PA and inclination values of García-Gómez & Athanassoula (1991) since they provide the more complete set of consistent values, the obvious exception being NGC 3556. García-Gómez & Athanassoula calculated their values averaging over a number of techniques, giving most weight to H I velocity field measurements. This should be the most reliable technique available, assuming that the disc can be represented as being planar, since it samples information from the whole disc. Galaxy inclination angles are not listed directly in de Vaucouleurs *et al.* (1991), but instead values of R_{25} are quoted, i.e. the ratio of the major to minor axes of the surface brightness $\mu_B = 25.0 \text{ mag arcsec}^{-2}$ isophote. Recently it has been shown that spiral galaxies are optically thick out to this radius (Valentijn 1990; de Vaucouleurs *et al.* 1991) and can therefore be treated as an opaque circular disc, which implies that the inclination angle is given by $i = \arccos(R_{25}^{-1})$. This is contrary to what had been believed previously (de Vaucouleurs *et al.* 1976), and is not true for galaxies of $T \leq 0$. In this case an inclination dependent correction factor has to be applied since we observe a greater column density along the minor than the major axis.

The two sets of PA and inclination data agree reasonably well (Fig. 6.2) in most cases, although there are the odd examples where there is a large discrepancy (e.g. NGC 2835).

The deprojected H II distributions of the observational sample (using the data of García-Gómez & Athanassoula) are shown as Fig. 6.3, together with the Digitized Sky Survey (DSS) image of the galaxy. Whereas spiral structures are often clear in the optical continuum images, they are generally disappointingly difficult to pick out in the H II maps.

References

- Carranza G., Crillon R., Monnet G., 1969, *A&A*, 1, 479
 de Vaucouleurs G., de Vaucouleurs A., Corwin Jr. H. G., 1976, *Second Reference Catalogue of Bright Galaxies*, University of Texas Press, Austin
 de Vaucouleurs G., de Vaucouleurs A., Corwin Jr. H. G., Buta R. J., Paturel G., Fouqué P., 1991, *Third Reference Catalogue of Bright Galaxies*, Springer-Verlag, New York

REFERENCES

77

- García Gómez C., Athanassoula E., 1991, *A&AS*, 89, 159
Hodge P. W., 1976, *ApJ*, 205, 728
Hodge P. W., Kennicutt Jr. R. C., 1983, *AJ*, 88, 296
Knapen J. H., Arnth-Jensen N., Cepa J., Beckman J. E., 1993, *AJ*, 106, 56
Valentijn E. A., 1990, *Nature*, 346, 153



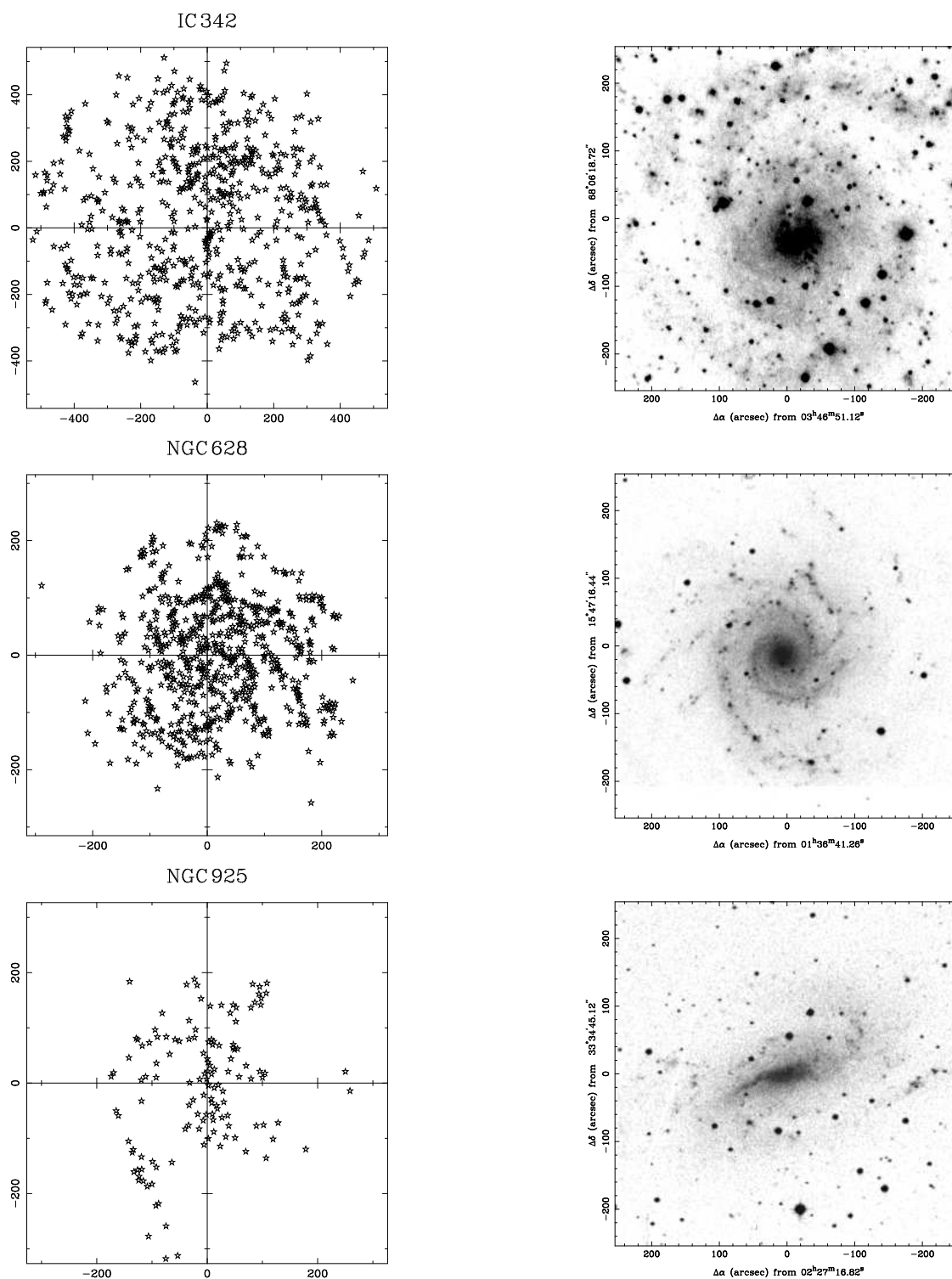


Figure 6.3. The observational sample. The left-hand frame show the deprojected H II region distributions, and the right-hand the DSS image of the galaxy in question. The H II images are of arbitrary size and orientation as a consequence of the deprojection process. The DSS images are labelled using J2000 coordinates.

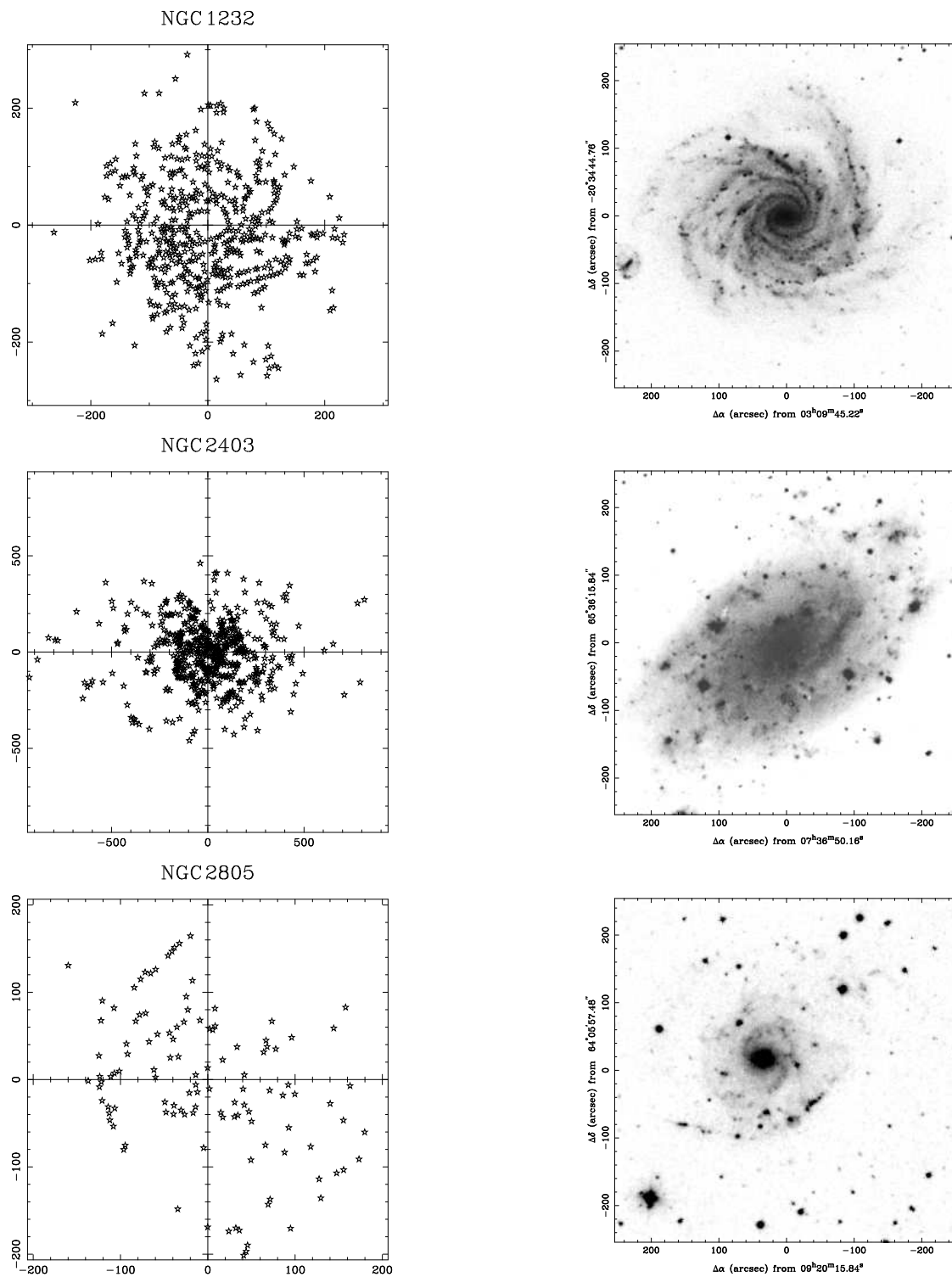


Figure 6.3. (cont.)



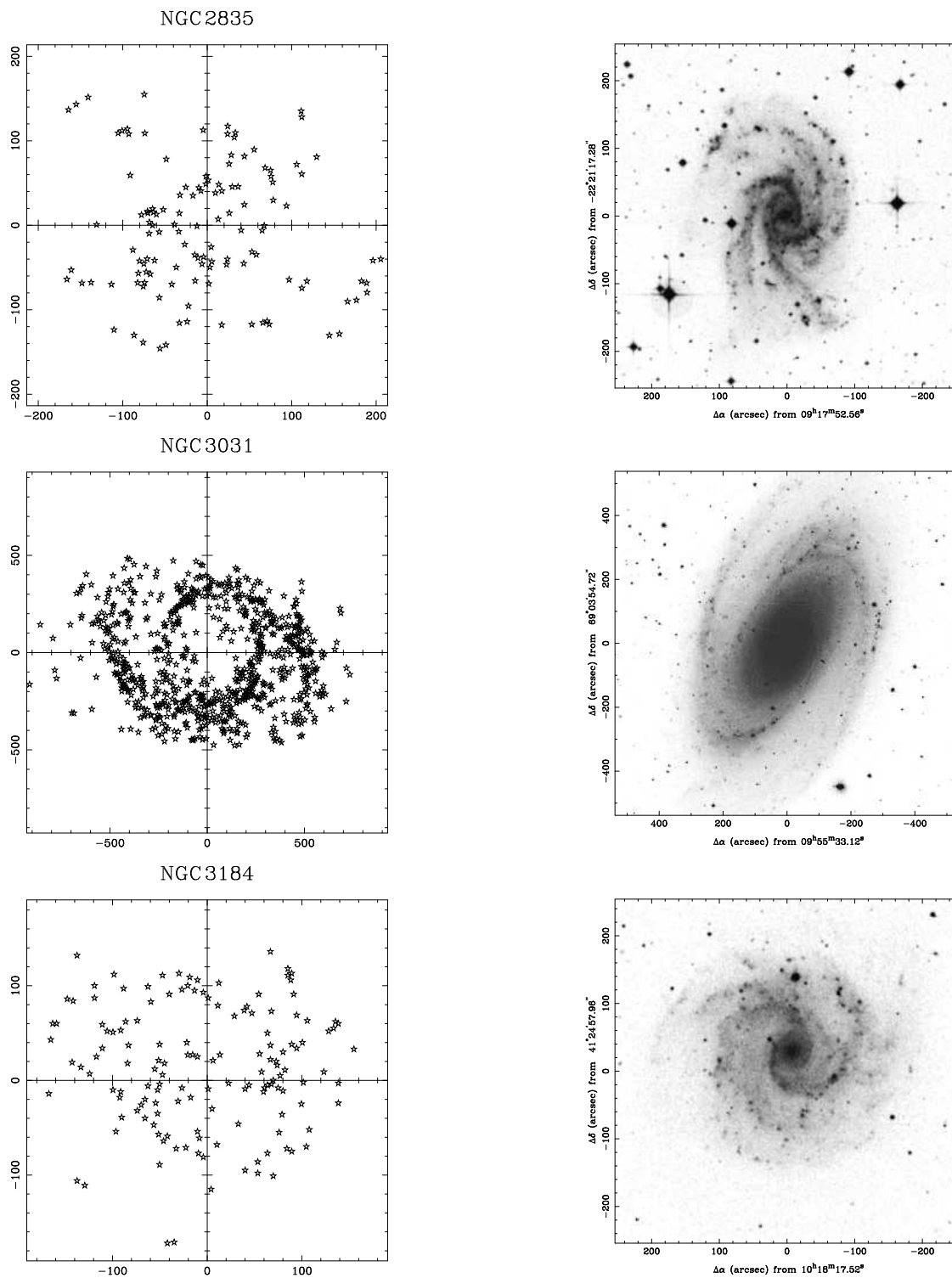


Figure 6.3. (cont.)

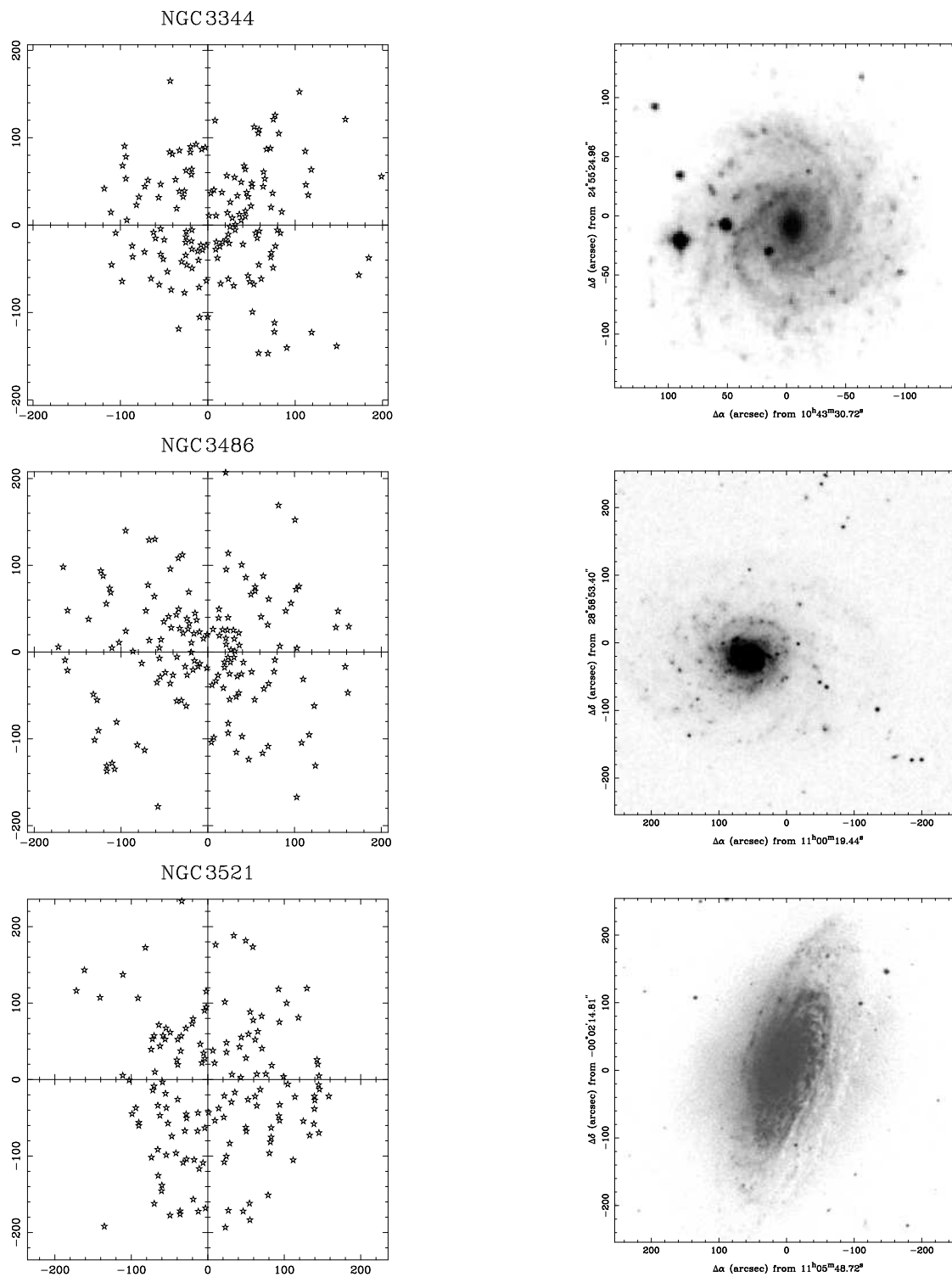


Figure 6.3. (cont.)



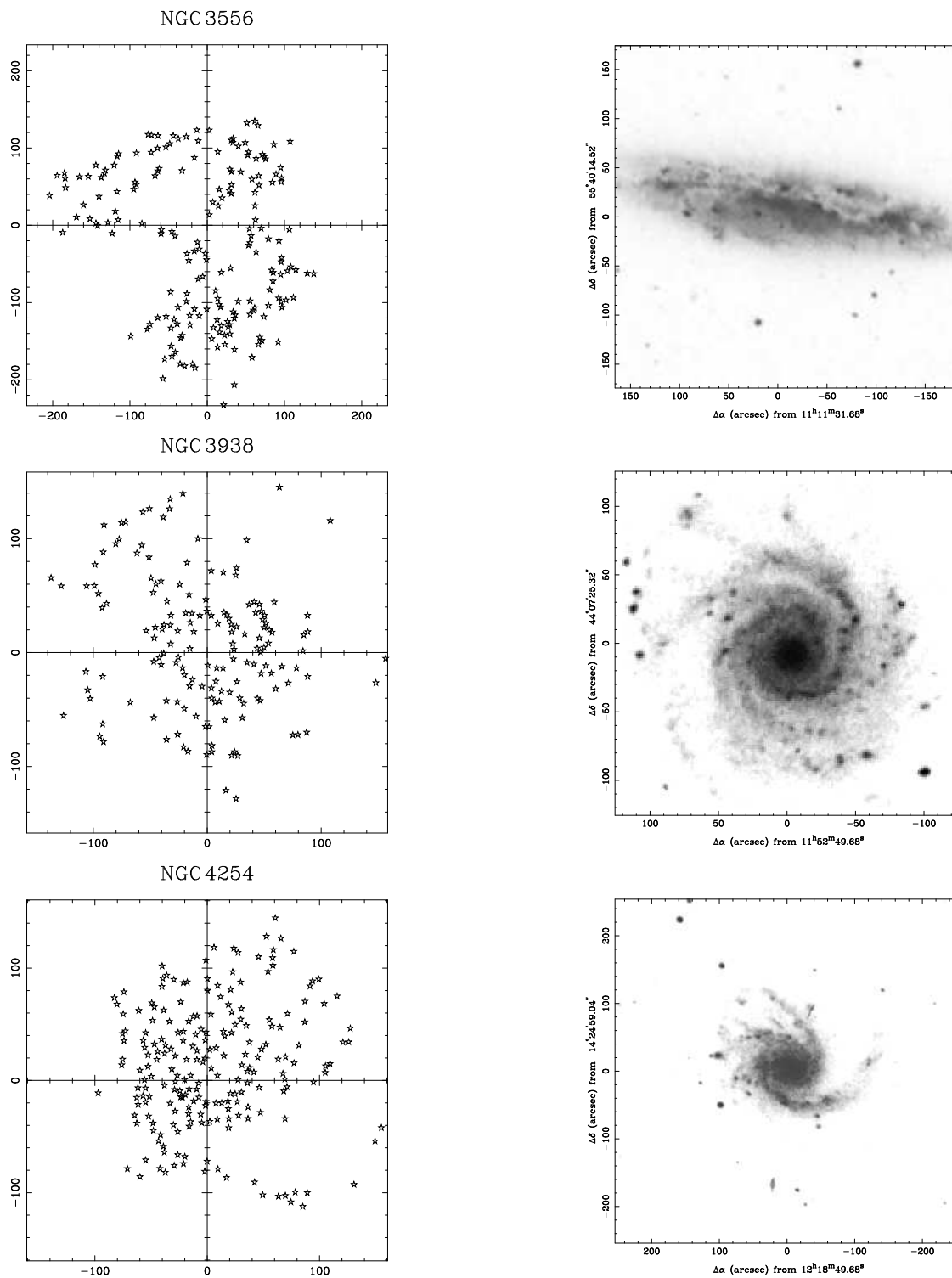


Figure 6.3. (cont.)

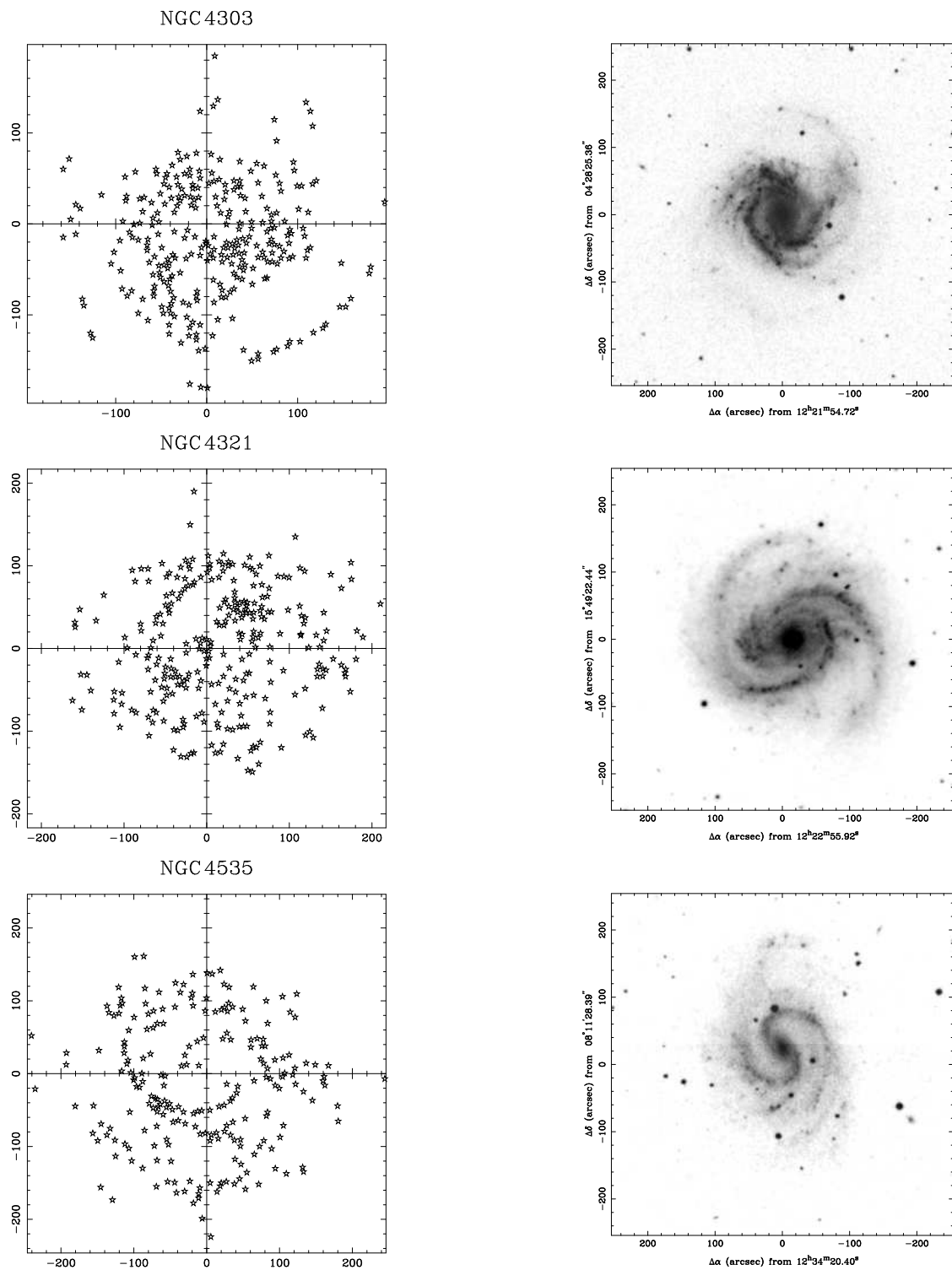


Figure 6.3. (cont.)



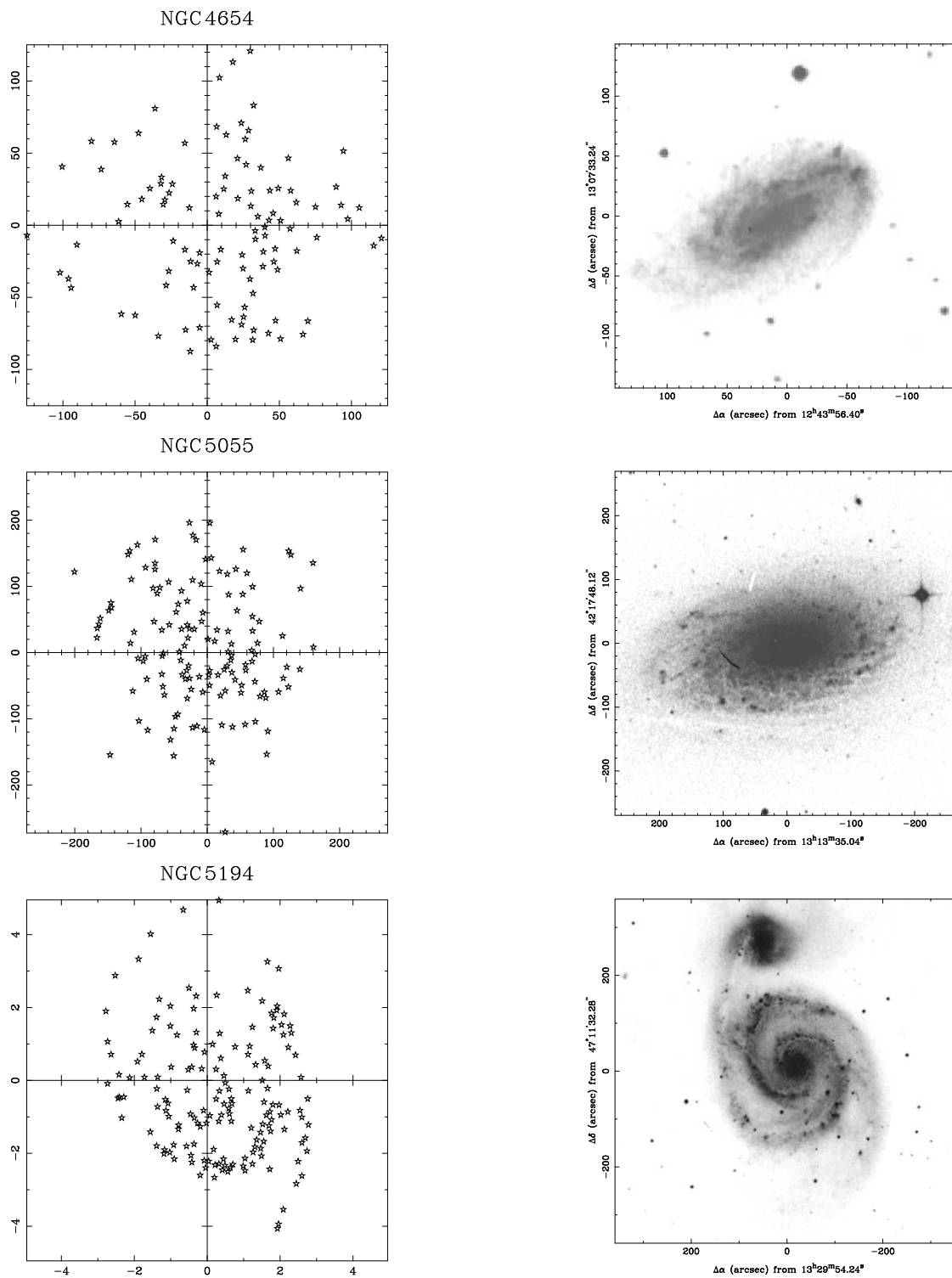


Figure 6.3. (cont.)

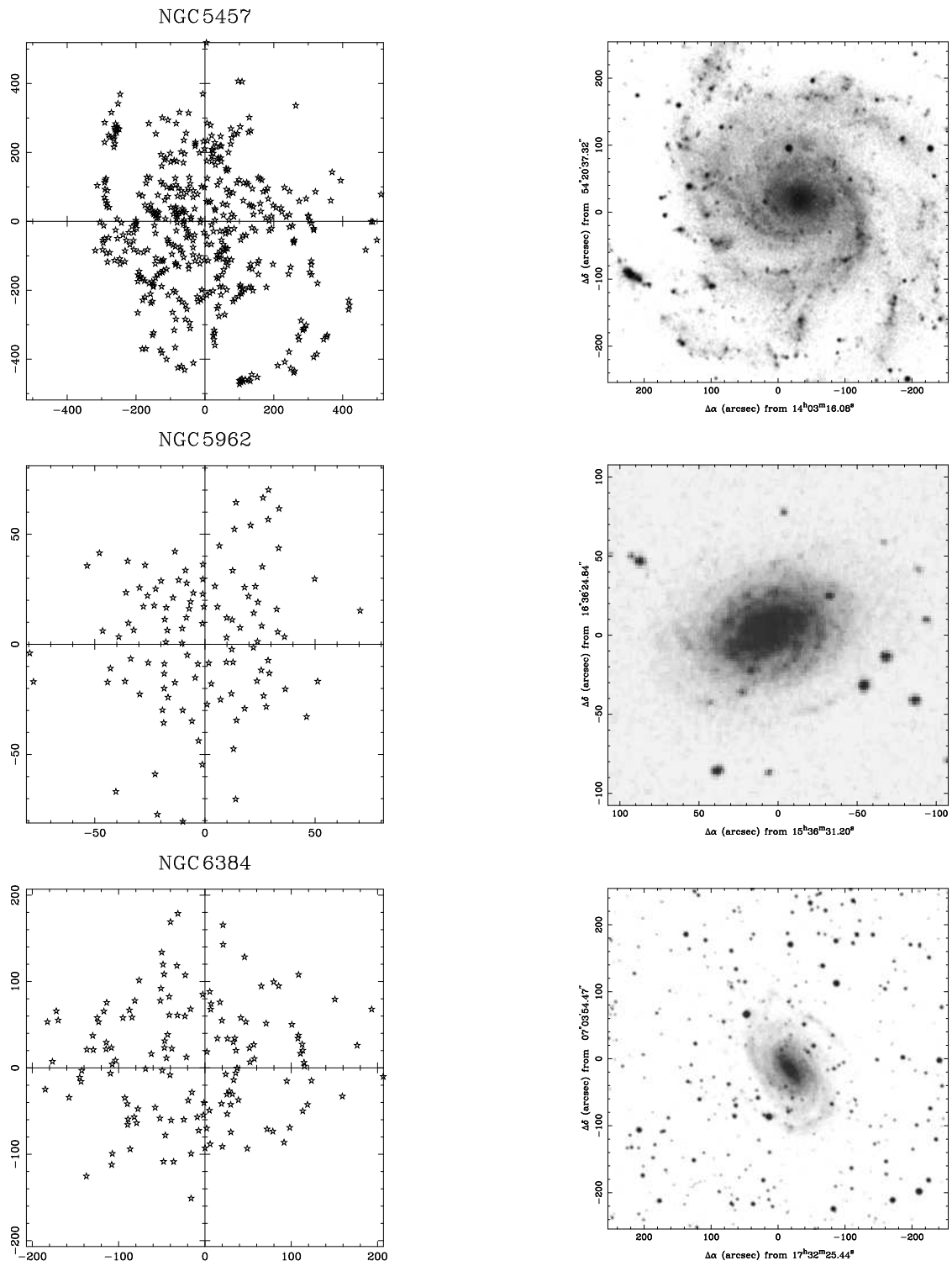


Figure 6.3. (cont.)



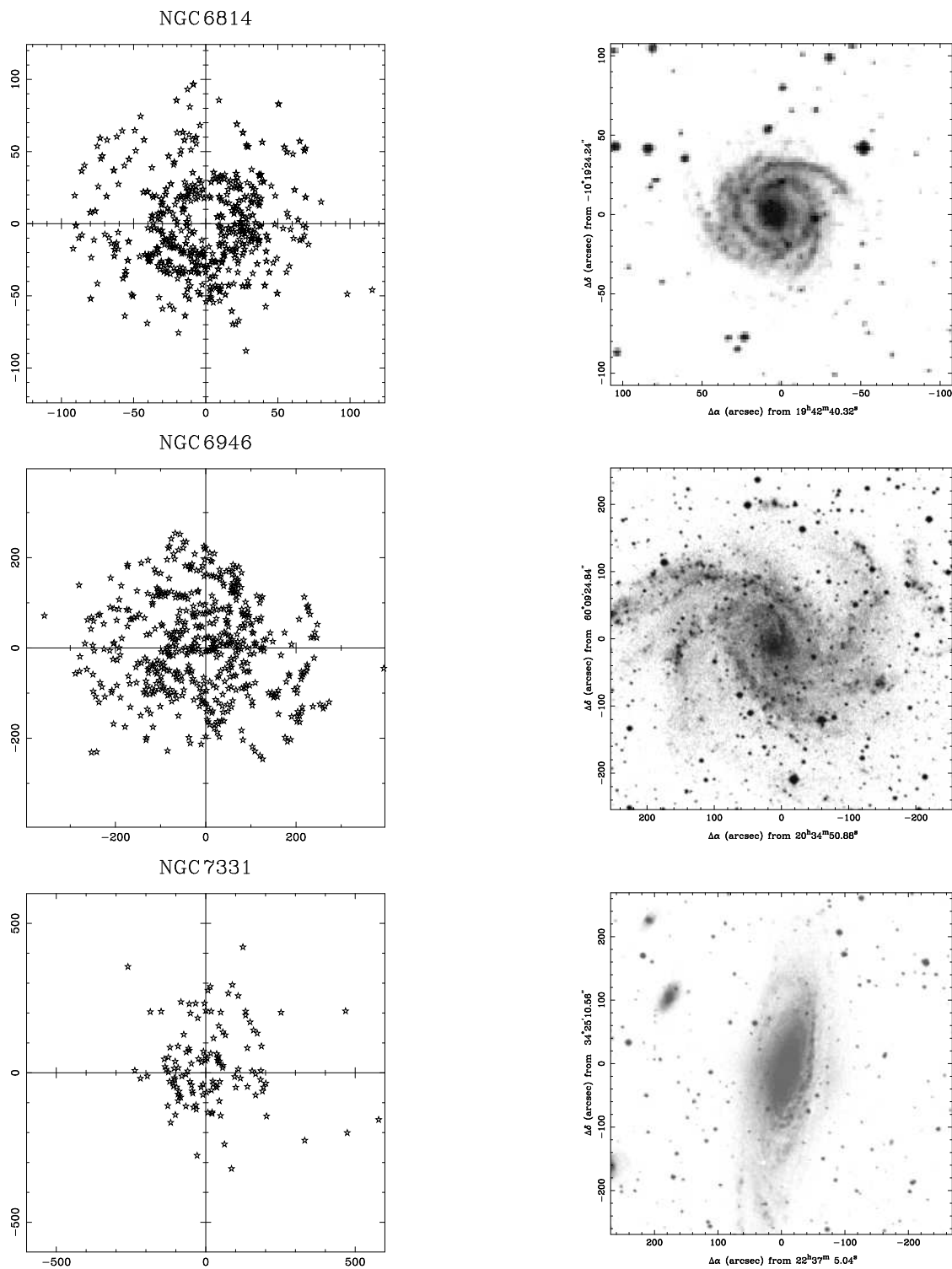
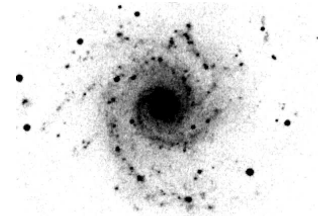


Figure 6.3. (cont.)

Chapter 7

Quantitative measures of galactic structure



A comparison of the predicted and observed star formation rates gives a quantitative feel for the worth of the model. However, the defining feature of spiral galaxies is their morphology and not the rate at which stars are being created; indeed observationally the SFR shows remarkably little variation with the structure of the galaxy (Devereux & Young 1991). Since the human eye is extremely adept at seeing patterns where there are none (Frisby 1979), and can be overwhelmed by a mass of data and thus ignore fine structure, an automated, quantitative method for characterising galactic morphology is required, and this will form the subject of this chapter.

7.1 Description of the techniques

Many schemes already exist for classifying galaxies by their optical morphology, depending on a variety of a wide range of parameters such as the bulge to disc luminosity ratio, the presence of a bar, etc. – a brief summary of the most commonly used schemes for normal galaxies is given in Appendix C. All such schemes are, however, somewhat subjective, since they usually rely on visual inspections of optical images. Changing the exposure time of the observation, or tweaking the contrast etc. with a suitable image-processing package can greatly affect the appearance of a galaxy and hence its classification. It would therefore be preferable if some completely uniform, repeatable procedure could be adopted. I have considered three such approaches; Fourier analysis, minimal-spanning-tree spectra and multifractal dimensions. The Fourier analysis is tailored in such a way as to make it especially suitable for the study of spiral galaxies and it has been used before for a large selection of spiral galaxies (Considère & Athanassoula 1982; Puerari & Dottori 1992; García Gómez & Athanassoula 1993), whereas the other techniques have not previously been utilised to investigate galactic structure. They have however, found astronomical application in the categorisation of large-scale structure (Barrow *et al.* 1985; Martínez *et al.* 1990; Borgani *et al.* 1993).



7.1.1 Fourier analysis

The most obvious feature of the galaxies under consideration in this dissertation is their spiral structure. What we require is some way to enhance this structure without being distracted by the underlying, axisymmetric component. Fourier techniques are widely used in such filtering applications for both time series and spatial distributions. For any Fourier based approach, it is always sensible to choose the basis functions carefully, in order to minimise the information content of the high order components. Whilst for many applications harmonic functions are best, we have in this case a system where we know the form of the dominant feature in which we are interested. Danver (1942) compared photographic images of a sample of galaxies and fitted the arms to six different analytic forms for spirals; Archimedean, Cotes, hyperbolic, gravitational, parabolic and logarithmic. He found that logarithmic spirals provided the best fit to the observational data, a result that was confirmed later by Kennicutt (1981). It is therefore sensible to use logarithmic spirals as the basis functions for our Fourier expansion. Of course, doing this does not in any way bias the results towards logarithmic spirals, as opposed to any other type. It simply means that we hope to be able to represent the structure of the galaxy with as few as possible Fourier components by using a ‘natural’ basis set.

An n -armed logarithmic spiral has the form

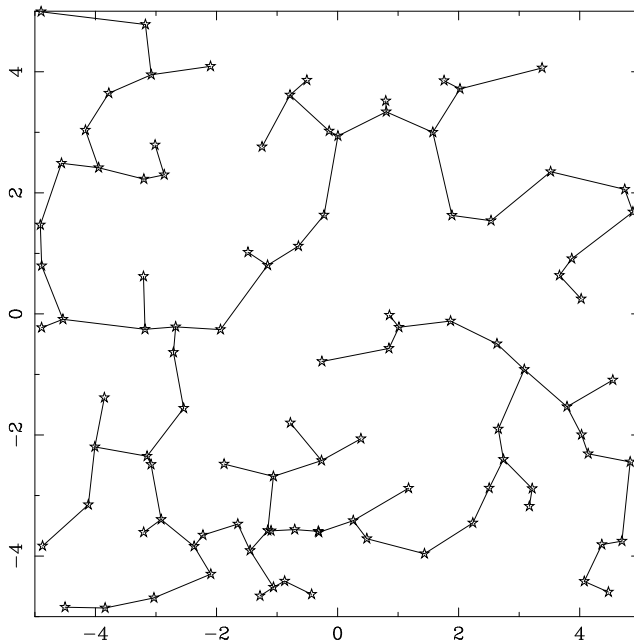
$$r = r_0 e^{-n\theta/q}$$

where q is related to the pitch angle and number of arms of the spiral by $\tan i_0 = -n/q$. At a fixed radius, the function is sinusoidal in θ with the wavelength inversely dependent on the number of arms, giving us a first set of conjugate variables (θ, n) . Similarly at fixed azimuthal angle, the function is sinusoidal in $\ln r$ with the wavelength this time a function of the both the pitch angle of each arm and also the number of arms comprising the pattern, resulting in the second set of conjugate variables $(u = \ln r, q)$. Furthermore, we can represent a distribution of points as the sum of δ -functions distributed in the (u, θ) plane, and hence can write the Fourier transform of the 2-D distribution as,

$$\begin{aligned} A(q, n) &= \int_{-\infty}^{\infty} \int_{-\pi}^{\pi} \frac{1}{N} \sum_{i=1}^N \delta(u - u_i) \delta(\theta - \theta_i) e^{-i(qu+n\theta)} du d\theta, \\ &= \frac{1}{N} \sum_{i=1}^N e^{-i(qu_i+n\theta_i)}, \end{aligned}$$

(Considère & Athanassoula 1982), where each point has been given equal weight. When using simulation data, it would in principle be possible to weight each point according to its age in order to enhance the contribution due to, for example, the youngest clusters. Such information is however, not available for the observational sample, and hence uniform weighting was used in all cases.

Whilst this is undoubtedly a powerful technique, care must be taken in the interpretation of the Fourier spectra produced. The presence of a strong signal for any given n does not necessarily

**Figure 7.1**

Example of a minimal spanning tree (MST) for a set of randomly distributed points.

imply the existence of an n -armed spiral, although the converse is true. This is most noticeable for $n = 1$ where any asymmetry in the distribution of points about a mirror-plane is reflected as a strong $n = 1$ signal in the Fourier spectrum.

7.1.2 Minimal spanning tree spectra

Given a point distribution it is possible to calculate a unique network joining each point without loops such that the total edge length is minimised – a construct known as the minimal spanning tree (MST). An example of a minimal spanning tree, calculated for a set of randomly positioned points using the algorithm of Whitney (1972), is shown as Fig. 7.1. The number distribution of edge-lengths (l_i) comprising the tree can then be used to characterise a given structure, with different spectra being compared using either the Kolmogorov–Smirnov (KS) test (Press *et al.* 1992) or Kuiper test (Kuiper 1962), resulting in a single number, *viz.* the probability of the two spectra being identical, with which to intercompare both model and observational data.

Both the Kolmogorov–Smirnov and Kuiper tests are based on comparisons of the cumulative distribution functions (C_1 and C_2) of two data sets with N_1 and N_2 points respectively. (Alternatively, one of these could be replaced by a known distribution function to enable data to be compared to a theoretical model). The KS statistic is then defined as

$$K = \max_{-\infty < x < \infty} |C_1(x) - C_2(x)|,$$

whereas the Kuiper statistic is defined as

$$D = K_+ + K_- = \max_{-\infty < x < \infty} \{C_1(x) - C_2(x)\} + \max_{-\infty < x < \infty} \{C_2(x) - C_1(x)\}$$



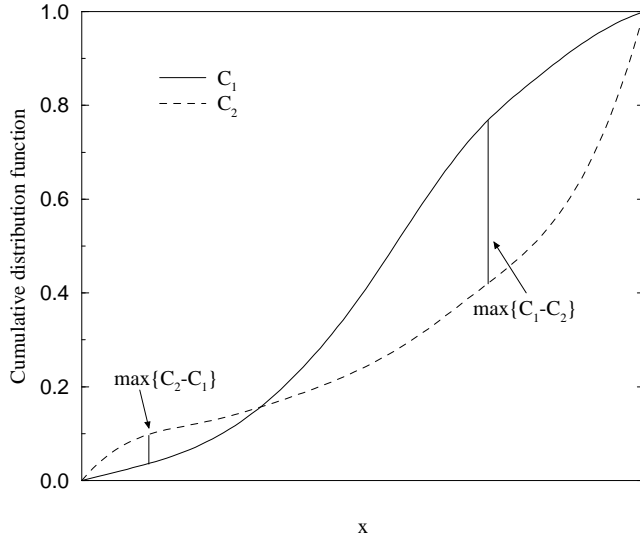
**Figure 7.2**

Illustration of the Kolmogorov–Smirnov and Kuiper tests. For the two cumulative distribution functions C_1 and C_2 , the KS statistic K is given by the length of the longer of the two lines marking points of maximum difference between the curves, whereas the Kuiper statistic D is defined as the sum of the lengths of the two marked lines.

(see Fig. 7.2), i.e. whereas the KS test measures the maximum absolute deviation between the distributions, the Kuiper test is the sum of the maximum differences above and below between C_1 and C_2 . The significance of the (easily) measured value of these statistics is then calculated as,

$$\text{Probability}(\text{data identical}) = Q_K \left(K \left[\sqrt{N_0} + 0.12 + 0.11/\sqrt{N_0} \right] \right)$$

for the KS test, where

$$Q_K(\lambda) = 2 \sum_{j=1}^{\infty} (-1)^{j-1} e^{-2j^2\lambda^2} \quad \text{and} \quad N_0 = \frac{N_1 N_2}{N_1 + N_2},$$

and for the Kuiper test,

$$\text{Probability}(\text{data identical}) = Q_D \left(D \left[\sqrt{N_0} + 0.155 + 0.24/\sqrt{N_0} \right] \right)$$

where

$$Q_D(\lambda) = 2 \sum_{j=1}^{\infty} (4j^2\lambda^2 - 1) e^{-2j^2\lambda^2}.$$

The KS test is the most widely used technique for comparing two unbinned data sets (with χ^2 being the preferred method for binned data), but has the disadvantage of being more sensitive to values of x around the median (such that $C(x) = 0.5$) than to the extremes of the data. This results in the test being good at picking out shifts in the median value of the distribution, but rather less useful for finding spreads. In contrast, the Kuiper test is equally sensitive over all values of x , with the inevitable drawback that it is then more prone to giving misleading answers due to outliers. The tests do however complement each other in their respective sensitivity ranges. A number of additional techniques based on the same theme are also sometimes used, but have not been implemented for this work – see Press *et al.* (1992) for further information.

Whilst experimenting with this technique it quickly became clear that the cumulative distribution functions were dominated by fluctuations in the large number of short edges which contributed little to the larger scale structures which are of interest here. Moreover, as a consequence of observational constraints, the sample of real galaxies has no short edges at all (see Chapter 6) and hence it would not have been feasible to compare real with simulated structures if the shortest edges had not been removed. Unfortunately this introduces an additional parameter into the technique, namely the short-edge cutoff expressed as a fraction of the mean edge-length, \bar{l} .

The spectra were also truncated at long edge-lengths to reduce the effect of the small number of outlying points. It was however found that that the value of the cutoff made only a minor difference to the statistical tests (as would be expected since they are based on the cumulative distribution functions) – in general a constraint of $l/\bar{l} < 4$ was imposed.

7.1.3 Multi-fractals

Many texts exist which expound on the theory of fractals and multifractals in great mathematical detail. My aim here, however, is to introduce the topic from a slightly more physical point of view, which although lacking somewhat in mathematical rigour, does have the advantage of being more intuitive. I will follow a path similar to that taken by Schroeder (1991) – for a more rigorous approach see, for example, Mandelbrot (1982), Feder (1988) or Falconer (1990).

First consider a large cubic volume of edge length L which is sub-divided into cells of size λ . Then the number of small cells into which the large volume can be split is given by

$$N(\varepsilon) = \varepsilon^{-3} \quad (7.1)$$

where $\varepsilon = \lambda/L$. Now suppose that a number of point-like particles are spread throughout the large cube, and that λ is chosen such that there is no more than one particle in each cell. Then, if the point distribution is uniform, the number of cells required to form a covering of the set of particles will also be given by equation (7.1), whereas for a non-uniform set, the number of cells required to form a covering is more generally given by

$$N(\varepsilon) = \varepsilon^{-D_H} \quad (7.2)$$

where D_H is known as the fractal (Hausdorff) dimension of the distribution, and can vary between zero and the embedding dimension of the space. Equation (7.2) is more normally re-written in the form,

$$D_H = \lim_{\varepsilon \rightarrow 0} \frac{\ln N(\varepsilon)}{\ln(1/\varepsilon)}. \quad (7.3)$$

Note that this picture accords with the definition of a fractal given by Mandelbrot (1982), *viz.* that the fractal dimension exceeds the topological dimension, which for a point set is of course zero.

A perfect, self-similar fractal, only requires a single dimension to characterise it, since on whatever scale we look the distribution of points will appear the same. Physical systems however,



rarely exhibit this monofractal nature – instead they are multifractals where the scale length under consideration is of importance. Hence the Hausdorff dimensions need to be generalised in some way to make allowance for this.

The easiest way to start is to first consider a slightly different fractal dimension. Rényi, in an attempt to generalise the entropy function for a point distribution introduced a formula based on the moments of the probabilities $p_i(\epsilon) = n_i(\epsilon)/N$, i.e. the probability of finding n_i points in the i th cell. The generalised entropy can be written

$$S_q = \frac{-1}{q-1} \ln \sum_{i=1}^N p_i^q,$$

which reduces in the limit $q \rightarrow 1$ to the more familiar form,

$$S_1 = - \sum_{i=1}^N p_i \ln p_i.$$

In a similar manner, the Rényi multifractal dimensions (Rényi 1970) are defined as

$$D_q = \lim_{\epsilon \rightarrow 0} \frac{1}{q-1} \frac{\ln \sum_{i=1}^N p_i^q}{\ln \epsilon}; \quad D_1 = \lim_{q \rightarrow 1} D_q. \quad (7.4)$$

For a self-similar fractal, with equal $p_i = 1/N$ then equation (7.4) becomes

$$\begin{aligned} D_q &= \lim_{\epsilon \rightarrow 0} \frac{1}{q-1} \frac{\ln N(1/N)^q}{\ln \epsilon} \\ &= \lim_{\epsilon \rightarrow 0} \frac{\ln N}{\ln(1/\epsilon)} \end{aligned}$$

which has the same form as equation (7.3) independent of q . Furthermore, we see that for $q = 0$, equation (7.4) reduces once again to equation (7.3), and hence $D_0 \equiv D_H$. The most commonly used notation introduces another variable $\tau(q)$, where,

$$\tau(q) = \lim_{\epsilon \rightarrow 0} \frac{\ln \sum_{i=1}^N p_i^q}{\ln \epsilon},$$

and hence, from equation (7.4),

$$\tau(q) = (q-1)D_q. \quad (7.5)$$

From a more physical point of view, the exponents q control the weight given to regions of differing densities in the sum. High density regions, with large p_i will contribute most when q is large and positive, whilst the low density regions will dominate when q is large and negative. In the limits,

$$D_\infty = \lim_{\epsilon \rightarrow 0} \frac{\ln p_{\max}}{\ln(1/\epsilon)} \quad D_{-\infty} = \lim_{\epsilon \rightarrow 0} \frac{\ln p_{\min}}{\ln(1/\epsilon)}$$

where p_{\max} and p_{\min} are the maximum and minimum values respectively of p_i over the whole distribution. Hence $D_{-\infty} \geq D_\infty$. Furthermore, in general,

$$D_q \geq D_{q'} \quad \text{for} \quad q < q', \quad (7.6)$$

and thus D_q is a monotonically decreasing function of q .

The Rényi dimensions have been shown to approximate to the simple Hausdorff dimension in the limit $q \rightarrow 0$. It is also possible to extend the normal definition of the Hausdorff dimension, although unfortunately this takes us away from the path where physical intuition is of any use. Without the formal definition however, the techniques used to estimate the fractal dimensions for a real distribution of points would seem to be plucked from nowhere. Formally, the Hausdorff multifractal dimensions are defined as follows (Martínez *et al.* 1990): for a set of points embedded in a Euclidian space we can construct sets of coverings (Υ^ϵ) of the distribution using (hyper)-spheres of size $\epsilon_i \leq \epsilon$. Also for any general measure of the set (we have been using p up to now), we can define the counterpart for each member of a set of coverings,

$$\mu_i = \int_{i\text{-set}} d\mu.$$

Finally, we can define the partition sum

$$\Gamma(q, \tau) = \lim_{\epsilon \rightarrow 0} \inf_{\Upsilon^\epsilon} \sum_i \frac{\mu_i^q}{\epsilon_i^\tau} \quad (7.7)$$

and use this to define the function $\tau(q)$ by the requirement,

$$\Gamma(q, \tau) = \text{constant}.$$

This is the same function $\tau(q)$ as was used above, and the fractal dimensions can be hence be calculated via equation (7.5). To distinguish between the Rényi dimensions and the Hausdorff dimensions I shall use $D(q)$ for the latter and D_q for the former, following the usage of van de Weygaert (1992).

We are now in a position to consider some of the techniques used to estimate the function $\tau(q)$ for real, finite point sets, for which the limit $\epsilon \rightarrow 0$ cannot be taken. A number of such methods exist (Borgani *et al.* (1993) suggest four), but we shall focus on just two, the Minimal Spanning Tree method and the Correlation–Sum method.

The Minimal Spanning Tree method, originally proposed by Martínez *et al.* (1990) (see also van de Weygaert *et al.* 1992; Martínez *et al.* 1993) makes use of the MST to approximate the minimal covering of the point set by placing spheres with the tree edges as their diameters. Randomly chosen subsamples of the total point distribution are used to produce sets of edge-lengths $\{l_i\}_{i=1}^m$ with $m = N_R - 1$ and N_R being the number of points in the subsample. We can then define a partition function

$$Z(\tau, m) = \frac{1}{m} \sum_{i=1}^m l_i(m)^{-\tau} \propto m^{q-1}$$

which approximates equation (7.7) with $\epsilon_i \sim l_i$ and $\mu_i \sim 1/m$. By fitting this relationship for a range of m , we obtain $q(\tau)$ and hence, by inverting to give $\tau(q)$, $D(q)$ by equation (7.5).

From an algorithmic point of view, it is found that the results can be unstable due to the finite number of points been selected in the random subsamples. In an attempt to overcome this, it



usual to calculate $Z(\tau, m)$ for several realisations of a subset of m points, and then to average over the ensemble. Additional problems are caused by both the extreme edges in the MST edge-length distribution where the Poisson sampling noise associated with the small numbers can result in the value of S being distorted, particularly at larger $|q|$. This problem can be circumvented by discarding the shortest and longest edges – van de Weygaert *et al.* (1992) recommend to use only edges in the range $0.01 < l/\bar{l} < 10$. One further point to note, is that by choosing random subsamples, this method mixes the scale lengths over which the calculation is performed, and hence in some senses averages over the scale-dependent behaviour, which is what we are interested in for this work.

Whereas the Minimal Spanning Tree method is an estimator for the Hausdorff generalised dimensions, the Correlation–Sum method (Grassberger & Procaccia 1983) approximates to the Rényi dimensions. We now consider spheres of radius r centred on each of the N points in our set. Let the number of points contained within the sphere centred on the i th point be n_i , and define $p_i = n_i/N$. Then the partition sum

$$Z(q, r) = \frac{1}{N} \sum_{i=1}^N p_i^{q-1} \propto r^\tau \quad (7.8)$$

allows us, by varying r for a given value of q , to derive the function $\tau(q)$ from which, as before, we can derive D_q . (NB no inversion of $q(\tau)$ is required this time). Again, discreteness effects can disrupt the calculation particularly for $q < 1$ where any cells with $n_i = 0$ will cause equation (7.8) to diverge. However, this technique does not suffer from problems associated with mixing scale lengths; instead the range of scales is fixed by the range over which r is varied to calculate the fit.

7.2 Application of the techniques

7.2.1 Fourier spectra of galaxies

The Fourier spectra for a selection of the simulated galaxies are shown in Figs 7.3 and 7.4 (the corresponding structures being shown in Figs 5.6 and 5.4). The spectra have been calculated using the positions of the youngest stellar clusters only ($t < 10^7$ yr) since these will be equivalent to the H II regions used to trace the spiral arms in the observational sample. Moreover, the typical number of points used to calculate the model spectra is then of the same order as the number of points available for a real galaxy.

As we have seen (§5.2), the spiral structure becomes increasingly well defined as the amplitude of the spiral density wave is increased, a fact which is reflected in the increasing amplitude of the $n = 2$ Fourier component, $A(q, 2)$ – see Fig. 7.3. At the extreme high values of SDW amplitude, the average value of $A(q, 2)$ levels off (Fig. 7.5) in a manner reminiscent of the trend in the cluster formation rate (Fig. 5.1). However, in this case it is not the number of stars which is changing, but instead it shows that the spiral pattern deviates increasingly from a simple two-armed logarithmic

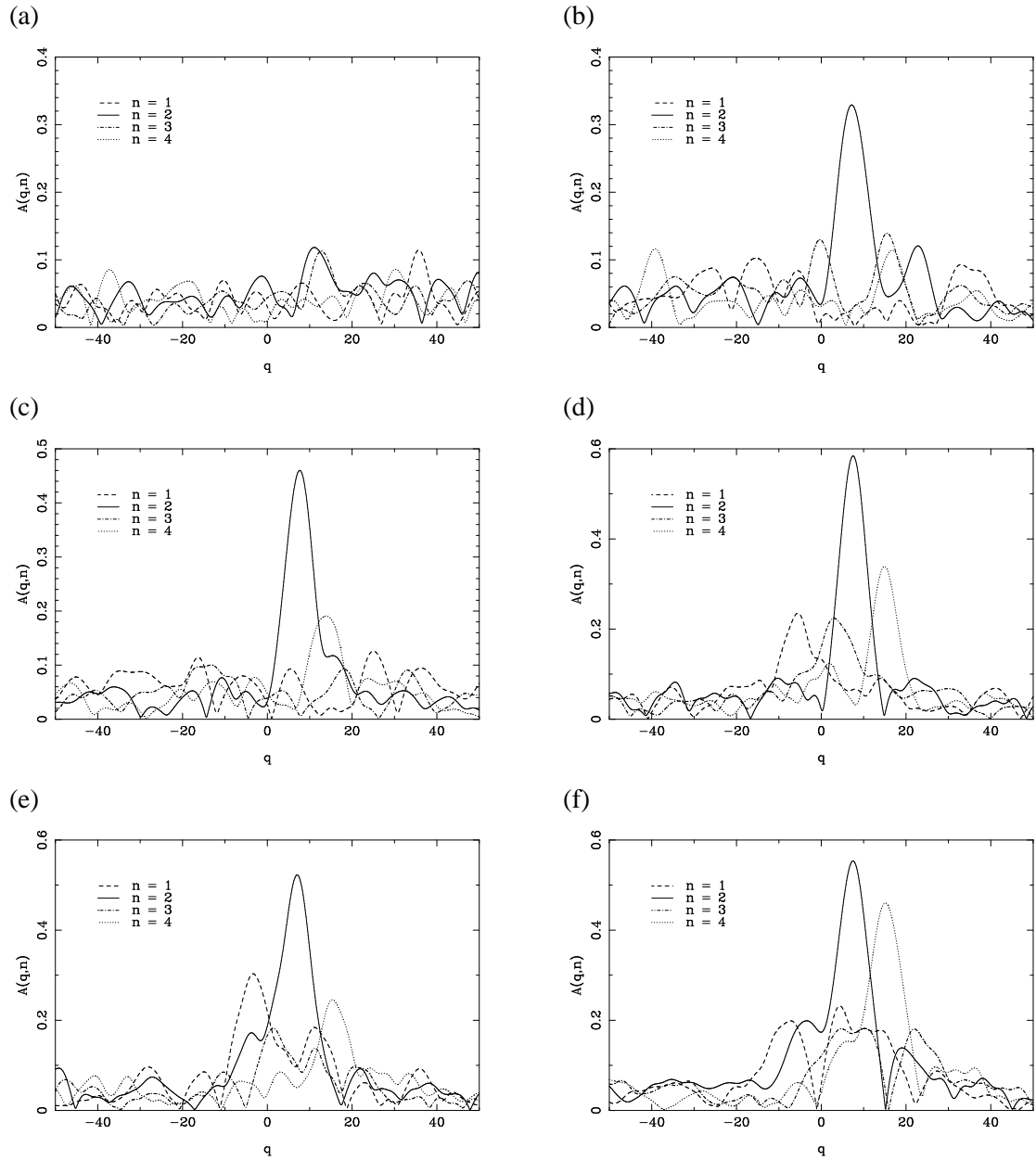


Figure 7.3. Effect of varying SDW amplitude A on Fourier spectra of model galaxies.
 (a) $A = 0.0 \text{ pc}^4 \text{ yr}^{-2}$, (b) $A = 0.032 \text{ pc}^4 \text{ yr}^{-2}$, (c) $A = 0.064 \text{ pc}^4 \text{ yr}^{-2}$, (d) $A = 0.096 \text{ pc}^4 \text{ yr}^{-2}$,
 (e) $A = 0.128 \text{ pc}^4 \text{ yr}^{-2}$, (f) $A = 0.16 \text{ pc}^4 \text{ yr}^{-2}$.



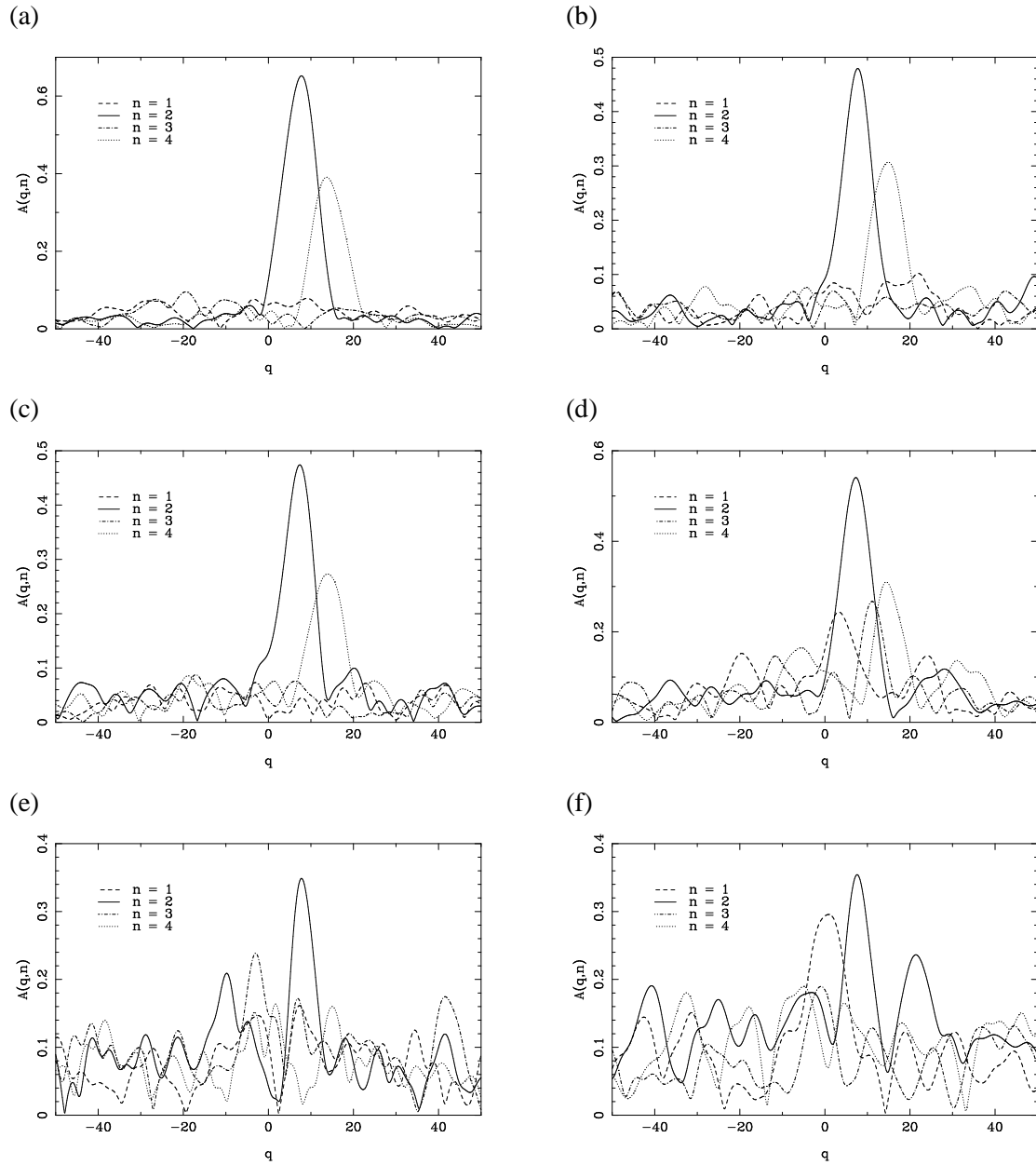
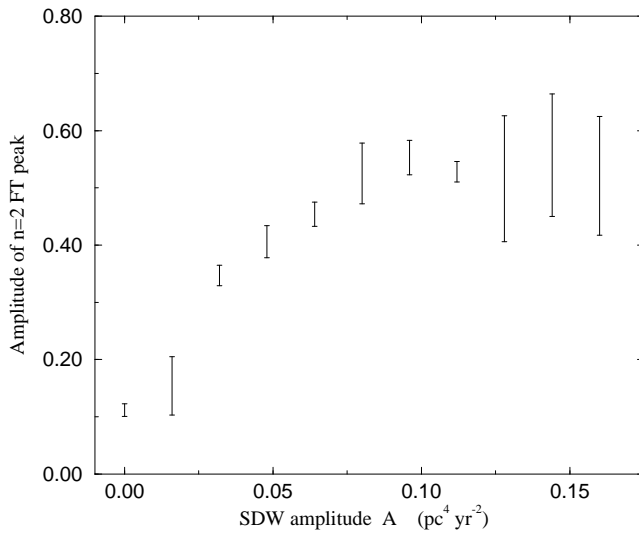
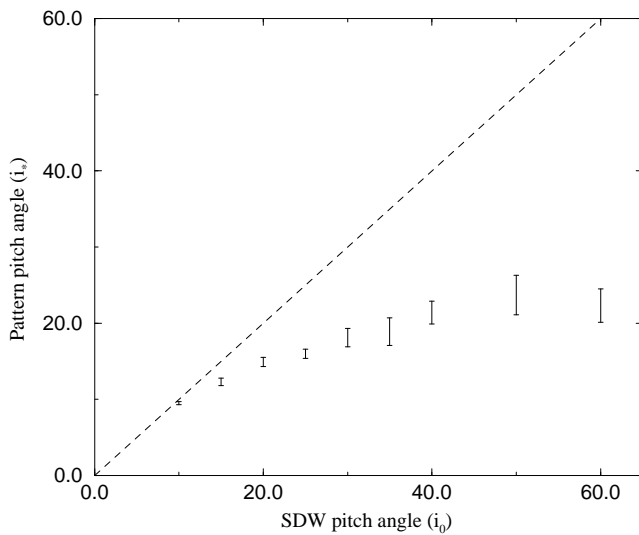


Figure 7.4. Effect of varying M_{st} on Fourier spectra of model galaxies.

(a) $M_{st} = 1.0 \times 10^4 M_{\odot}$, (b) $M_{st} = 3.2 \times 10^4 M_{\odot}$, (c) $M_{st} = 1.0 \times 10^5 M_{\odot}$, (d) $M_{st} = 3.2 \times 10^5 M_{\odot}$,
 (e) $M_{st} = 1.0 \times 10^6 M_{\odot}$, (f) $M_{st} = 3.2 \times 10^6 M_{\odot}$.

**Figure 7.5**

Variation of the ensemble average of the amplitude of the $n = 2$ Fourier component as a function of the strength of the imposed spiral density wave. Each point is the average of between three and five simulations.

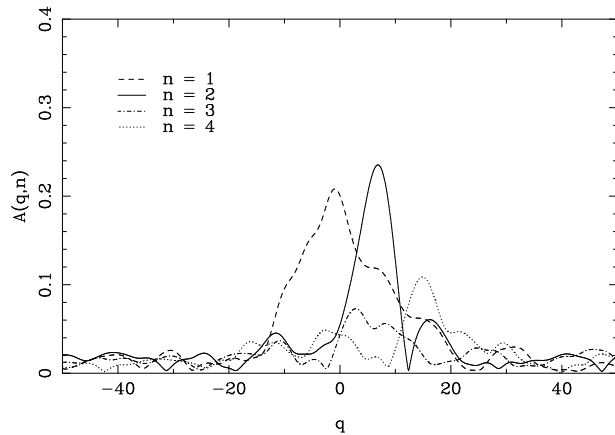
**Figure 7.6**

Observed pitch angle of the spiral arms (i_*) as a function of the pitch angle of the applied SDW (i_0). The dashed line indicates $i_* = i_0$.

spiral as the strength of the perturbation increases. Note the presence of a strong $n = 4$ component in those simulations with higher SDW amplitude (Fig. 7.3) indicating that the distribution of the young stellar content is not following exactly the underlying perturbation in the gravitational potential. A similar, but more obvious effect is seen when considering the structures produced by varying the pitch angle of the imposed SDW (i_0), as shown in Fig. 5.7. For the extremely high values of i_0 , the spirals do not appear to be noticeably more tightly wound than for the intermediate values of the SDW pitch angle.

This can be quantified by reading from the Fourier spectra the actual pitch angle of the various components – as is shown in Fig. 7.6, it is found that the pitch angle of the arms as traced by regions of recent star formation (i_*) is always less than the pitch angle of the SDW (i_0). The arms delineated in this way are material arms, and hence are wound up by the differential rotation of the galaxy, with arms which are intrinsically less tightly wound experiencing a larger effect. Moreover, i_* has



**Figure 7.7**

Fourier transform of the same simulation as was used in Fig. 7.3(d), but now including older clusters in the calculation. Note how the $n = 2$ component has been washed out to such an extent that it now has the same significance as the overall asymmetry of the image ($n = 1$).

a limiting value of $\sim 25^\circ - 30^\circ$, entirely consistent with the maximum spiral pitch angle observed for real galaxies (Kennicutt 1981). For our own Galaxy, the measured pitch angle is $\sim 12^\circ$ (Vallée 1995; Davies 1994; Taylor & Cordes 1993) and hence the underlying SDW should have a pitch angle of 20° , which was the value used in Chapter 4 when predictions were made for the cluster formation rate of the Milky Way. The maximum value for i_* will be a function of the rotation speed of the galaxy in question – if the rotation curve is approximately flat then a higher circular speed will result in a greater angular velocity gradient, and more tightly wound arms.

Being material arms, it might be expected that the spiral arms seen in the model would wind up more completely over time. This is not the case due to the underlying SDW which organises the star formation such that it is concentrated along the potential arms. Thus the visible pattern remains approximately constant in time although the individual star clusters that trace the visible arms at any given time are continually changing. As the clusters age and move away from the minimum of the spiral potential the pattern becomes smeared out due to (i) the velocity dispersion of the stars and (ii) the continued winding up of the material arm. This can be seen clearly in the Fourier spectrum of the same $A = 0.096 \text{ pc}^4 \text{ yr}^{-2}$ simulation as shown in Fig. 7.3, but now including older stars of age up to 10^8 yr (Fig. 7.7).

The Fourier analysis of the observational sample (Fig. 7.8) is a little disappointing – despite all the galaxies having reasonably clearly defined spiral arms in photographic images, the arms are more difficult to trace in the H II region distributions (Fig. 6.3) as is clear from even a simple, visual inspection. This is reflected in the Fourier spectra as well, with very few of the galaxies showing any components significantly stronger than the noise level (which in most cases is comparable to that for the modelled galaxies). The obvious exceptions are NGC 3031 (M 81), NGC 5194 (M 51) and, to a lesser extent, NGC 6946. NGC 3031 in particular could be considered to be the archetypal grand-design spiral and it is encouraging that this galaxy can be modelled with some degree of accuracy (compare its Fourier spectrum with that of Fig. 7.3(b)). This perhaps also reflects the closeness in Hubble type of NGC 3031 to that of our own Galaxy, on which the ‘standard’ parameters of the model were chosen.

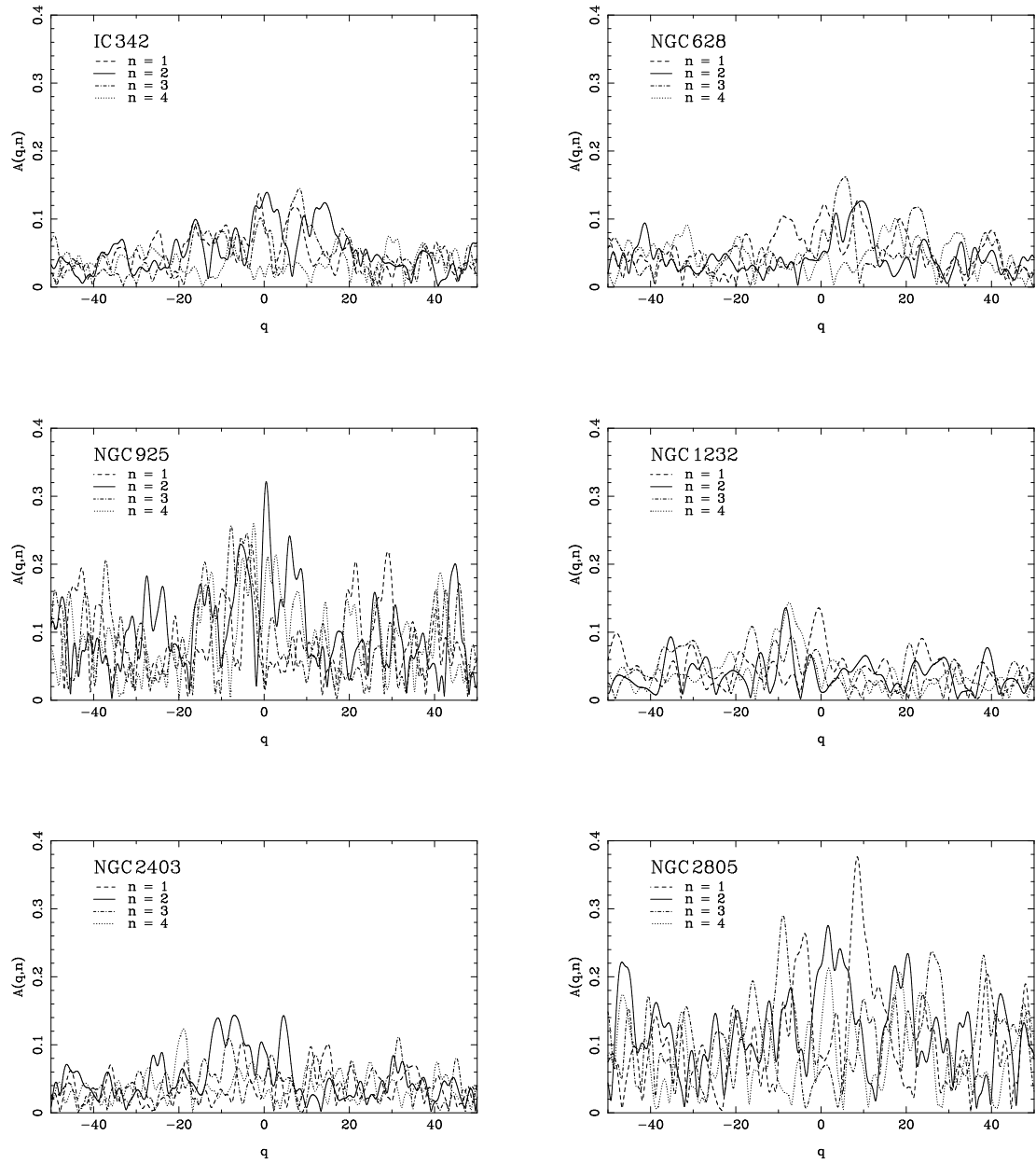
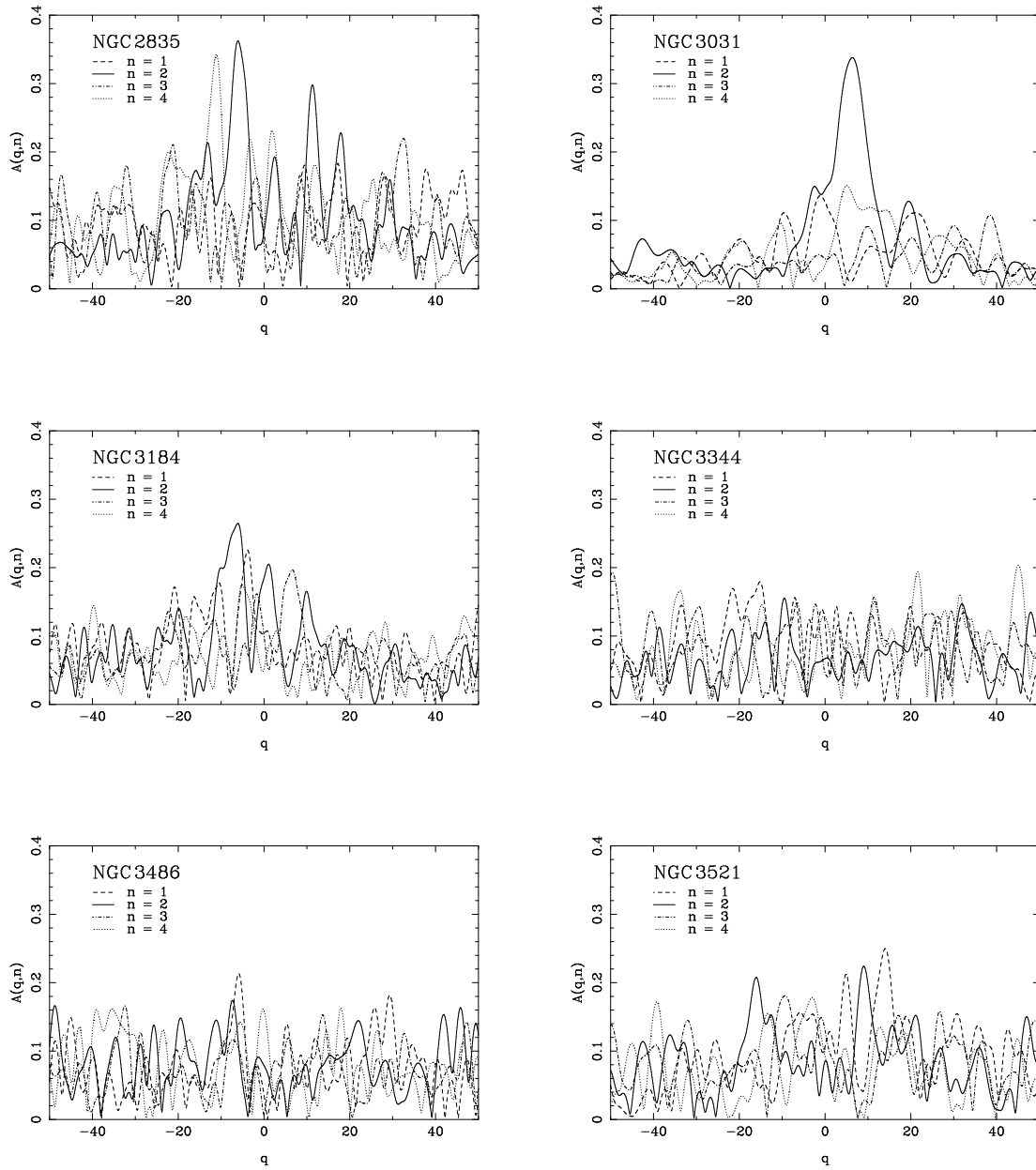
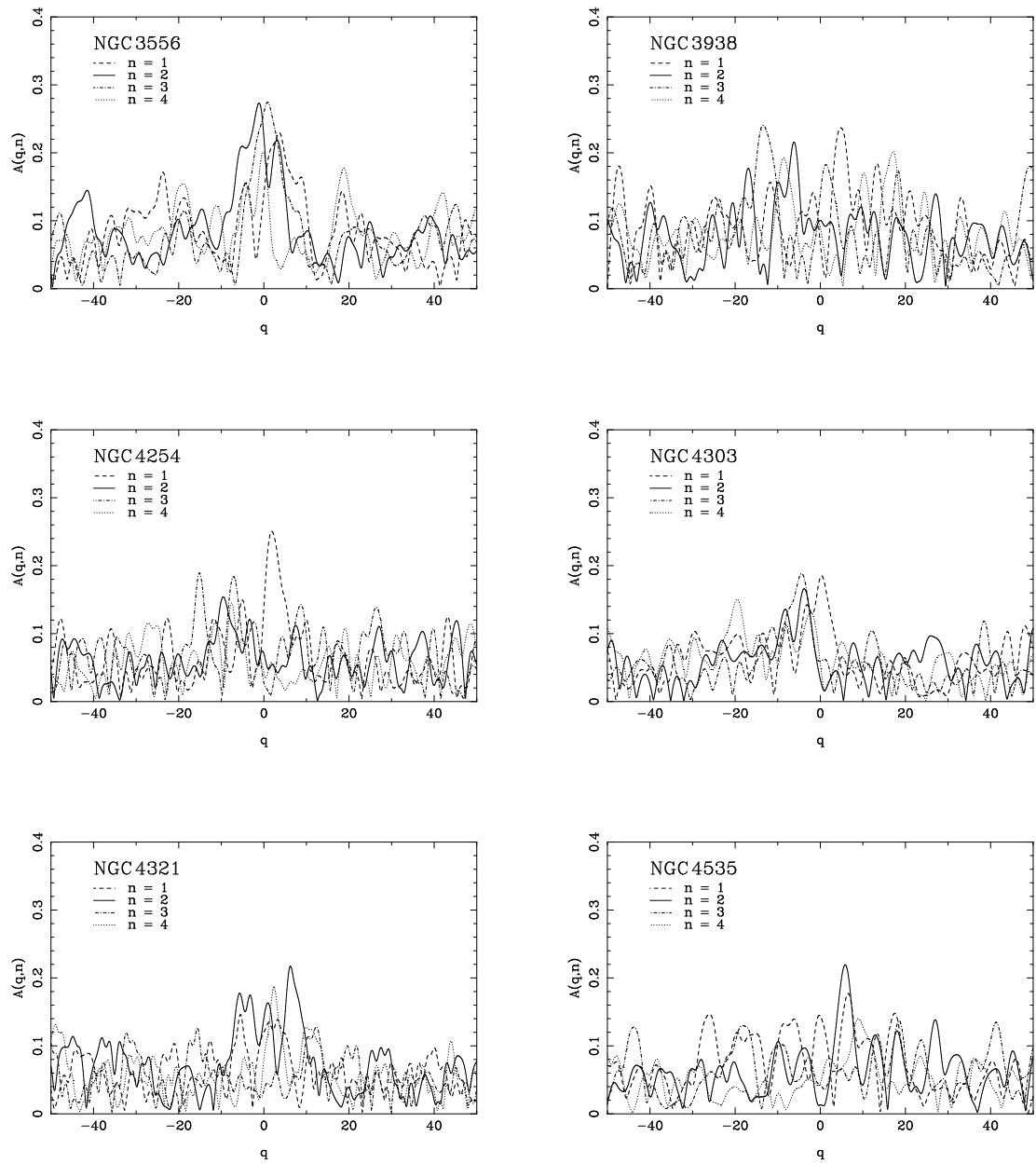
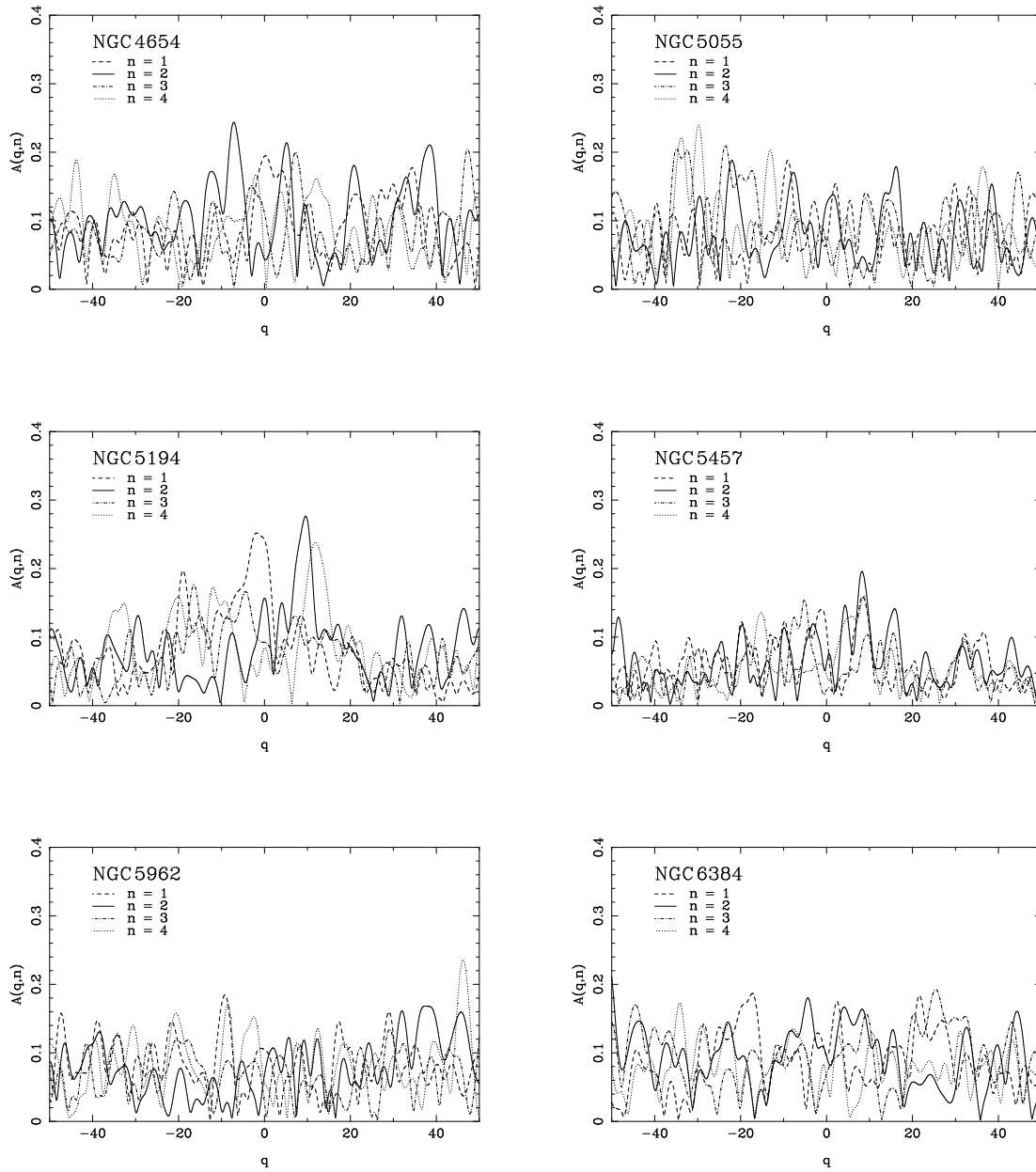


Figure 7.8. Fourier spectra of the observational sample. Only the first four components are shown for clarity, although it is clear that for many of the galaxies there is still significant power in the $n = 4$ component, and we would therefore also expect the $n > 4$ components to be important.



**Figure 7.8.** (cont.)

**Figure 7.8.** (*cont.*)

**Figure 7.8.** (cont.)

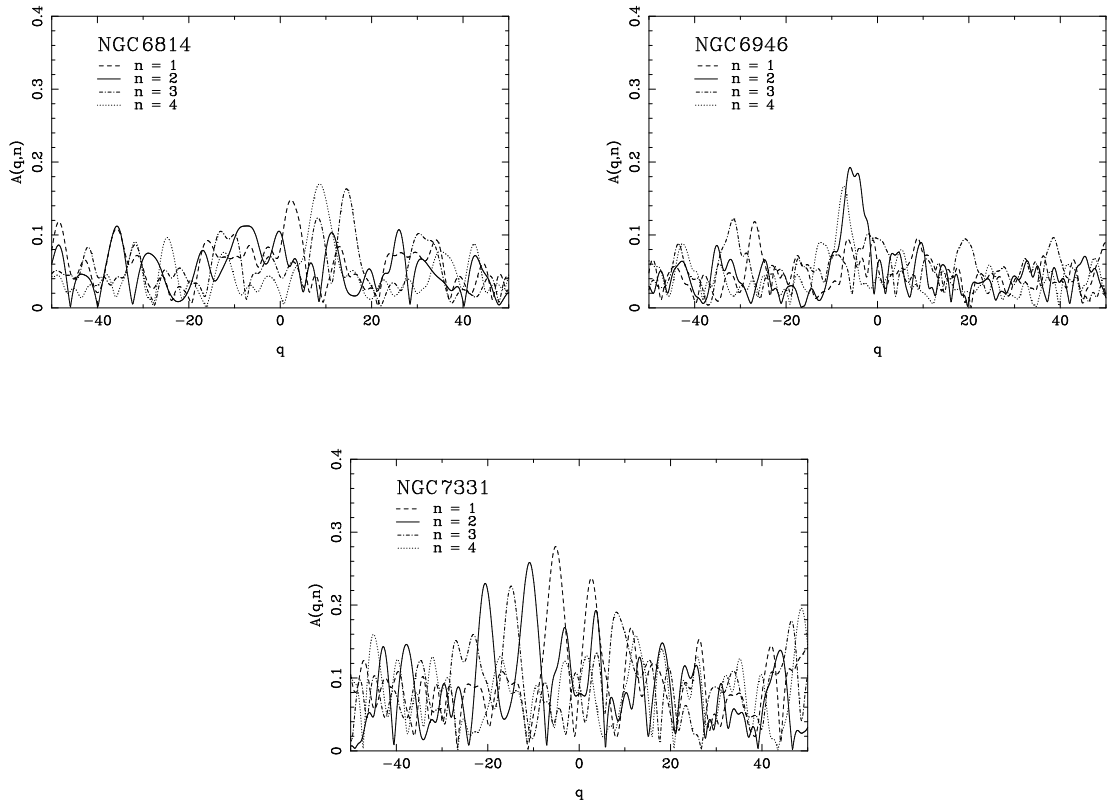
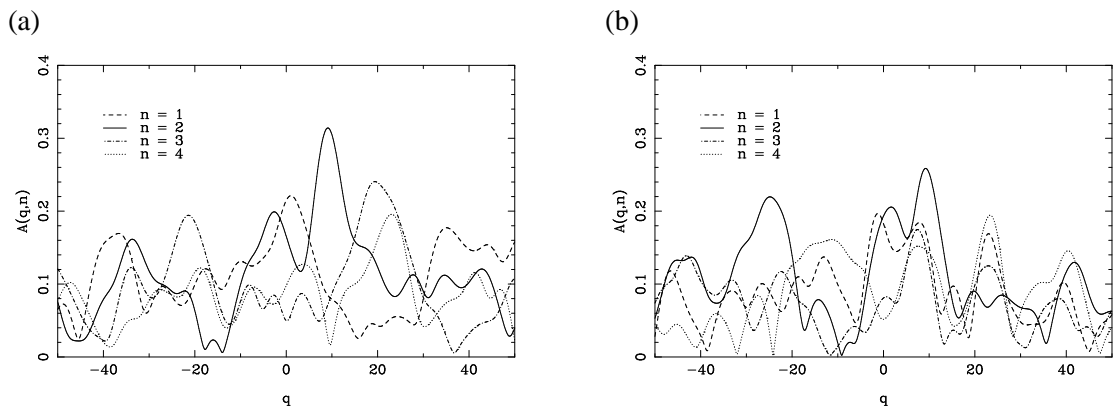


Figure 7.8. (*cont.*)

Figure 7.9. Fourier transforms of non-standard simulations, produced in an attempt to match those calculated for the observational sample. The spectra are derived from simulations calculated with (a) $M_{\text{st}} = 3.2 \times 10^6 M_{\odot}$, $A = 0.032 \text{ pc}^4 \text{ yr}^{-2}$ and (b) $M_{\text{st}} = 3.2 \times 10^6 M_{\odot}$, $A = 0.016 \text{ pc}^4 \text{ yr}^{-2}$. Standard values were used for the other parameters.



The other galaxies seem, from the Fourier analysis, to have considerably weaker spiral density waves than has been taken as the standard for this work. Such structures can be reproduced by the model by choosing a high value for M_{st} and a low one for A . Figure 7.9 shows two transforms with slightly differing parameters, which are a closer match to those calculated for the real galaxies.

It would be interesting in the future to constrain all the model parameters (including those specifying the axisymmetric potential and hence the rotation curve) using observational data based on one of the galaxies shown here as opposed to the Milky Way. To infer M_{st} however, requires a measurement of the median H_2 cloud mass which is not yet possible for galaxies external to our own (although the largest GMCs can be resolved in the nearest galaxies). Alternatively, M_{st} could be fixed from the observed CFR if only the structural properties are of interest.

All the galaxies for which Fourier spectra are presented above, are those with a two-armed perturbation to the overall gravitational potential. The Fourier analysis reveals however that weak three-armed components are often to be found in the stellar distribution, as indeed they are in the observational data also (cf. NGC 3556, NGC 4303). Puerari & Dottori (1992) find similar results using the same Fourier technique for a number of other galaxies, and Elmegreen *et al.* (1992) use an image enhancement process to find weak $n = 3$ modes in 17 out of a sample of 18 galaxies. (Interestingly, they also show that in 15 cases the limits of the three-armed spirals occur at the inner and outer 3:1 resonances – see §5.3). If a three-armed SDW is imposed instead, then as expected, the Fourier spectrum shows a strong $n = 3$ peak, contrary to observations. The results presented here suggest that it is not necessary to postulate the existence of an $n > 2$ perturbation to explain the presence of $n = 3$ components in the Fourier spectrum.

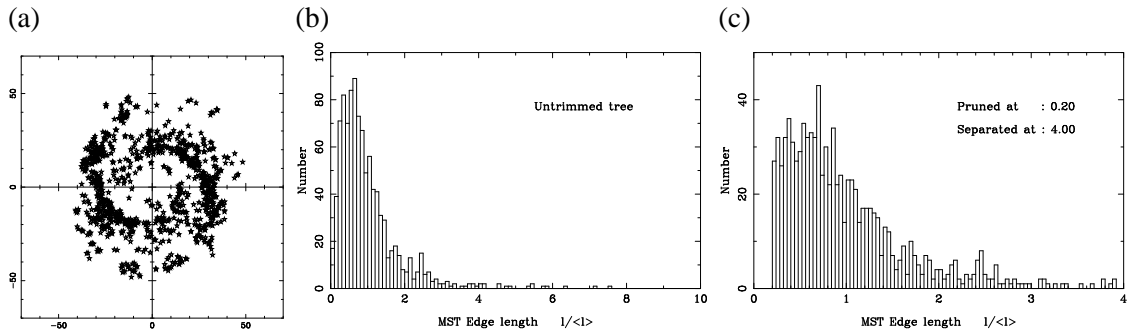
7.2.2 Experiments with MST edge-length spectra

Unlike the Fourier analysis described above, the comparison of MST edge-length spectra is a technique which has not previously been applied to galactic structure, although it has found application in astronomy through studies of the distribution of galaxies on cosmological scales (Barrow *et al.* 1985). Hence it is first essential to establish the validity of the technique for this application before going on to apply it to the data sample as a whole.

A typical edge-length spectrum, together with the H II region distribution (i.e. clusters $< 10^7$ yr old) are shown as Fig. 7.10 for a simulation calculated with the standard parameters. Frame (c) shows the spectrum after edges shorter than $0.2 l/\bar{l}$ and longer than $4 l/\bar{l}$ have been discarded. Removing the shortest edges prevents the tight, propagating knots of clusters having inappropriate weight in the spectrum since such a tight group has a small effect on the overall structure, whilst removing the longest edges ensures that outliers have no effect on the results.

Now consider an ensemble of runs (i)→(v) all calculated using the standard parameters. Although fluctuations arising due to the stochastic nature of the simulation will make each structure slightly different, we would perhaps hope that all runs with the same parameter set had more or less consistent MST edge-length spectra. Table 7.1 shows the probabilities of pairs of spectra being the same calculated with both the KS and Kuiper test using clusters younger than 10^7 yr. In

Figure 7.10. Example MST edge-length spectrum for a standard simulation. Frame (a) shows the H II distribution, (b) the untrimmed spectrum and (c) the trimmed spectrum.



each case the MST spectra have been trimmed such that only edges with $0.2 < l/\bar{l} < 4.0$ are considered. From this set it would appear that the Kuiper test is better at recognising simulations with the same initial parameters. However, if we now consider the results of the same procedure but using clusters of age less than 2×10^7 yr (Table 7.2) the situation is not so clear. Now the Kuiper test too informs us that the chances of (iv) and (v) being the same is less than 20% and runs (i) and (ii) which using only the youngest clusters seemed to be quite similar are now (at least according to the Kuiper test) quite different.

It must be noted that these discrepancies are in fact a result of the technique being too sensitive. A visual inspection of the distribution the young stellar population (Figs 7.11 and 7.12) reveals that there are indeed obvious differences between the individual members of the ensemble. The technique would be more useful however if it was able in some senses to average out the fluctuations arising from the stochasticity of the model and to reveal the gross, overall form.

Similar conclusions are reached when considering the similarity of MST edge-length spectra calculated from (randomly selected) simulations with different values of M_{st} (Table 7.3). The general trends are what might be expected, i.e. as one descends a column to the leading diagonal and

Table 7.1. Results of comparing MST edge-length spectra for simulations with identical input parameters, using only clusters of age less than 10^7 yr. The tables show the probability of the spectra calculated for the individual runs (i)→(v) being identical, determined by the (a) Kolmogorov–Smirnov test and (b) Kuiper test.

(a)	(i)	(ii)	(iii)	(iv)	(v)	(b)	(i)	(ii)	(iii)	(iv)	(v)
(i)	1.0	0.969	0.688	0.594	0.824	(i)	1.0	0.879	0.577	0.966	0.821
(ii)	—	1.0	0.928	0.353	0.879	(ii)	—	1.0	0.879	0.655	0.719
(iii)	—	—	1.0	0.242	0.358	(iii)	—	—	1.0	0.551	0.645
(iv)	—	—	—	1.0	0.246	(iv)	—	—	—	1.0	0.556
(v)	—	—	—	—	1.0	(v)	—	—	—	—	1.0



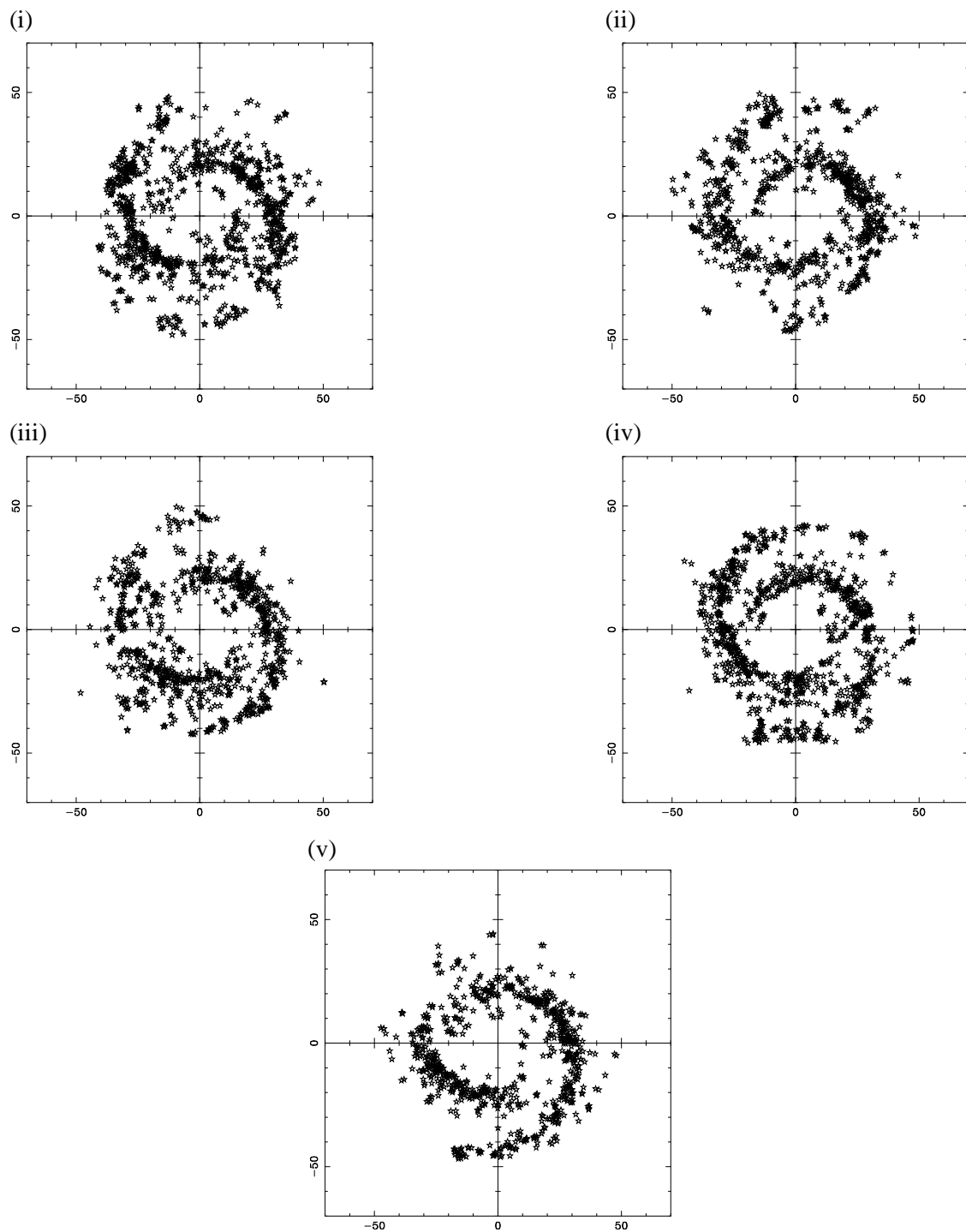


Figure 7.11. Distribution of clusters younger than 10^7 yr for ensemble of standard simulations.



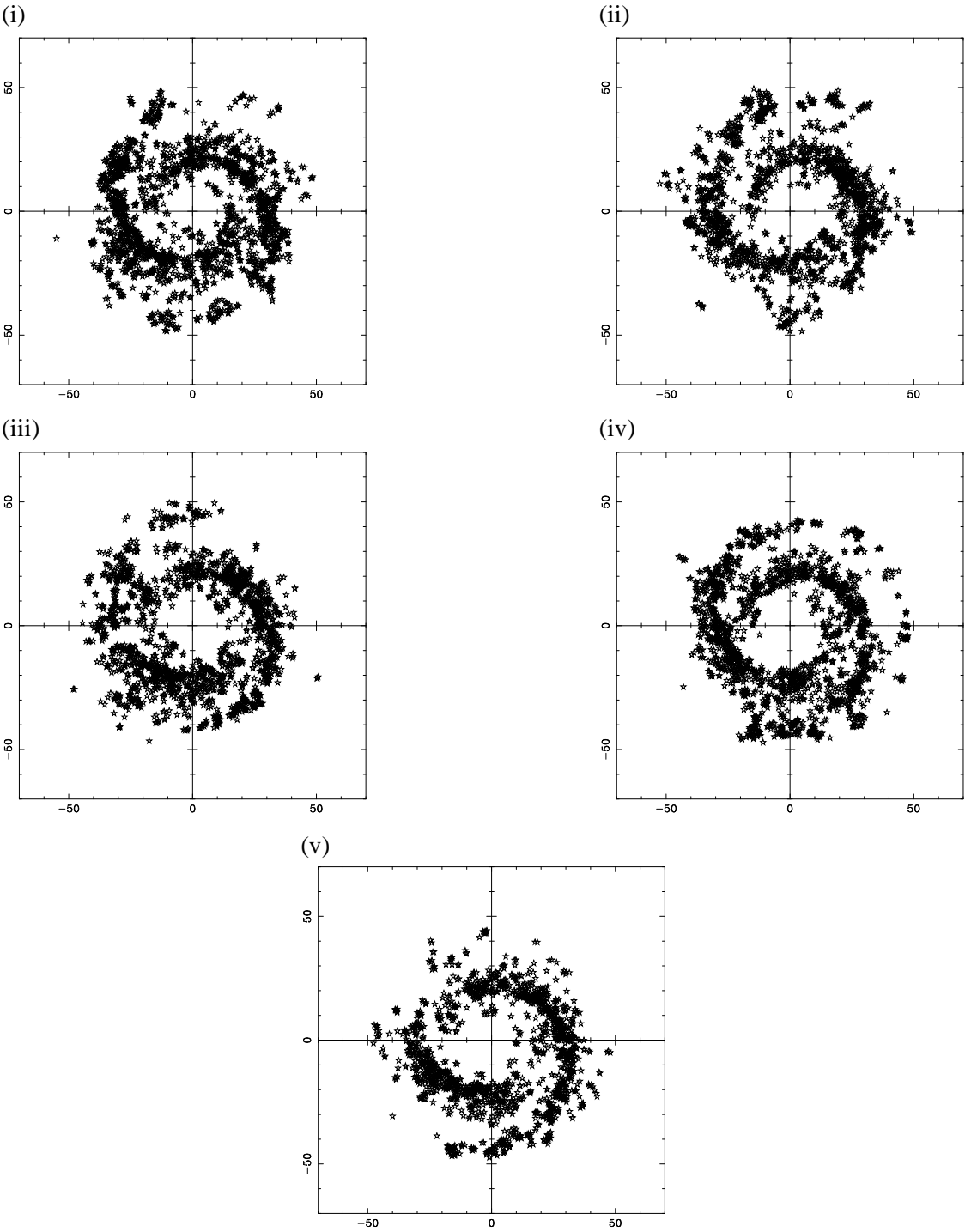


Figure 7.12. Distribution of clusters younger than 10^8 yr for ensemble of standard simulations.

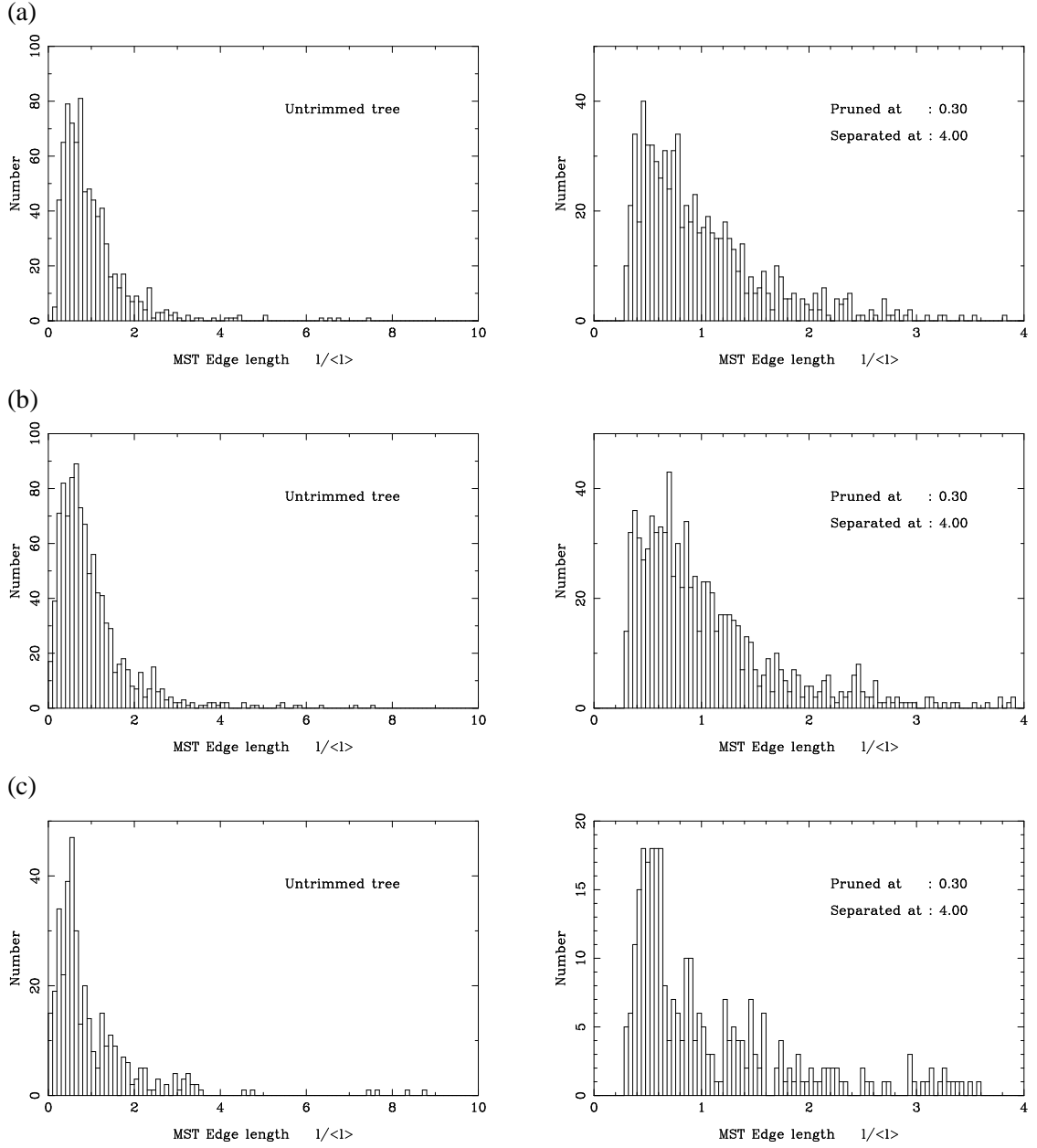


Figure 7.13. MST edge length spectra used to calculate Table 7.4. Both the untrimmed and the most alike trimmed (short edge cutoff at $0.3 l/\bar{l}$) spectra are shown for (a) NGC 3031, (b) simulation with $M_{\text{st}} = 10^5 M_{\odot}$ and (c) simulation with $M_{\text{st}} = 10^6 M_{\odot}$.



Cutoff l/\bar{l}	M_{st}/M_{\odot}	
	10^5	10^6
0.0	0.003	0.0
0.1	0.023	0.0
0.2	0.406	0.002
0.3	0.781	0.024
0.4	0.591	0.007
0.5	0.704	0.023
0.6	0.632	0.004

Table 7.4

Comparison of MST edge-length spectra as a function of lower cutoff. The two simulation runs have been individually compared with the data for NGC 3031. In each case the upper cutoff was kept constant at a value of $4 l/\bar{l}$ and only clusters younger than 10^7 yr were included in the calculation.

then follows the appropriate row across, the probability of the two spectra being the same rises to a maximum on the diagonal and then falls. However, the scatter is large and given two simulations, one of known M_{st} , it would not be possible to deduce the other value of M_{st} from the table. Moreover, the short edge cutoff can be seen to have a considerable and variable effect, making some structures more similar, and some less.

This sensitivity to the value chosen for the short edge cutoff is probably the weakest feature of this method. Comparing the edge-length spectrum of NGC 3031 with those of simulations with $M_{\text{st}} = 10^5 M_{\odot}$ and $M_{\text{st}} = 10^6 M_{\odot}$ (Fig. 7.13) we see (Table 7.4) that depending on the cutoff used, that the spectra could be considered to be anywhere between almost identical and really quite different! The Fourier analysis of NGC 3031 demonstrates that is the galaxy for which the simulations are best able to reproduce the observed structure, and hence similar MST edge-length tests have not been performed using data from the other members of the observational sample.

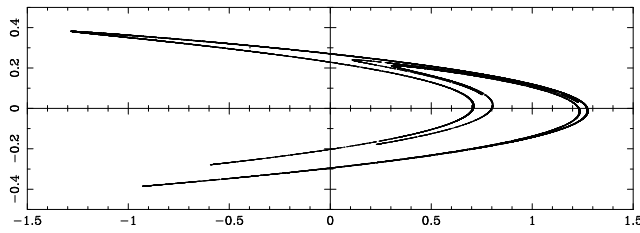
7.2.3 Multi-fractal techniques

The initial investigations using fractal techniques were performed using the MST method only, primarily on the recommendations of Martínez *et al.* (1993) who indicated that the technique was particularly well suited to problems involving small data sets. Clearly, with the galaxy data we do not have sample of many thousands of points, and so this was an important consideration.

Before attempting to calculate the fractal dimension of some galaxy data, either real or simulated, it was essential to verify that the algorithm, as coded, worked as intended. In order to do this, we tested the method on the Hénon attractor (Hénon 1976) for which the spectrum of multifractal dimensions is well known (Arneodo *et al.* 1987; van de Weygaert *et al.* 1992; Martínez *et al.* 1993). The attractor is defined by the recursion relation

$$\begin{aligned} x_{n+1} &= 1 - ax_n^2 + y_n, & a &= 1.4 \\ y_{n+1} &= bx_n, & b &= 0.3 \end{aligned}$$

and Fig. 7.14 shows the first 20 000 points, when initial values of $x_0 = y_0 = 0$ are used. Unfortunately, despite using an identical procedure to that described by van de Weygaert (1992), we

**Figure 7.14**

The first 2×10^4 points of the Hénon attractor, starting with $x_0 = y_0 = 0$.

were unable to reproduce the exact values for $D(0)$ and $D(1)$ using the MST method, although the qualitative form of the $D(q)$ curve was correct. We were unable to track down the discrepancy (subsequent studies with a different coding of the algorithm produced similar results), but since the form of the curve was approximately correct, it seemed that the technique could still be of some use in comparing simulation and observational data. Although we might not be calculating precisely the generalised Hausdorff dimensions, we still potentially had a viable method of distinguishing data sets.

As with the investigations of the Fourier and MST edge-length spectra techniques, we first considered simulations which had been calculated with a range of values of M_{st} . Some results are shown as Fig. 7.15, including both the $q(\tau)$ and $D(q)$ curves. In each case, only clusters younger than 1.5×10^7 yr have been included in the calculation. Clearly there is a significant difference between the $D(q)$ for each simulation, and therefore by, for example, comparing the fractal dimension at a fixed q value we have a single number to associate with each run.

However, when the fractal dimension was calculated for some of the observational sample, it became clear that there were severe problems with this technique (Fig. 7.16). In particular, many of the fractal spectra show ‘U’ shaped profiles (for example IC 342, NGC 3031) which violates the fundamental constraint on multifractals, given by equation (7.6), that the $D(q)$ curve must be a monotonically decreasing function of q . The other galaxies (for example NGC 1232) give rise to $D(q)$ curves which also show rising portions for $q \gtrsim 1$, and in addition are extremely noisy for $q \lesssim 1$ with points showing large excursions from a smooth curve and also large errors (derived from the fit of $\ln Z$ with m). I suspect that this is due to a weakness in the approach adopted to invert the $q(\tau)$ curve, which involved using a high-order Chebyshev polynomial (~ 15 – 20 , although lower if a good fit could still be made) as an interpolating function. However, the fact that the $D(q)$ curve was rising for *all* the observational sample in the region $q \gtrsim 1$ is the more pressing concern. Many of the model sets also exhibited similarly rising $D(q)$ curves in this region, but no ‘U’ shaped profiles were seen.

Clearly further tests were required to ensure the efficacy of the algorithm. One simple check that could be made was to ensure that the fractal dimensions calculated were independent of the scaling of the galaxy – if not then perhaps this could explain the problems with the observational sample which are all scaled differently. However, when the coordinates of the H II regions of NGC 6814 were scaled up by a constant factor, the $D(q)$ curve remained unchanged, as indeed it should. Also, if the noisiness of the multifractal dimensions was in some way a consequence of a numerical instability due to the precise values of the data themselves, then shifting each point by



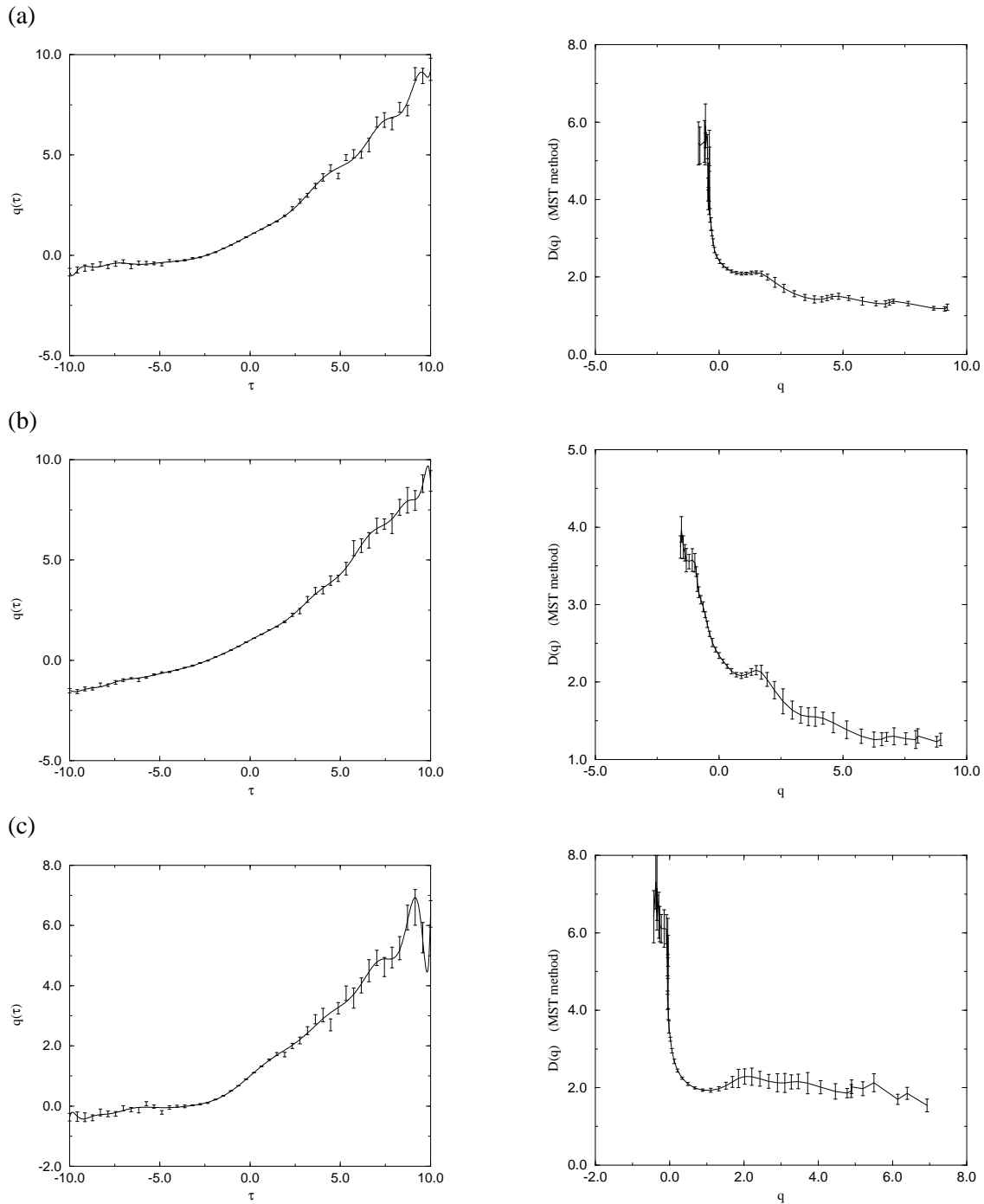


Figure 7.15. Multifractal dimensions and $q(\tau)$ plots for (a) $M_{st} = 10^4 M_{\odot}$, (b) $M_{st} = 10^5 M_{\odot}$ and (c) $M_{st} = 10^6 M_{\odot}$. Also shown are the Chebyshev polynomials used to interpolate $q(\tau)$ in order to invert the function. The order of the polynomial fits are 18, 20 and 19 for (a), (b) and (c) respectively.

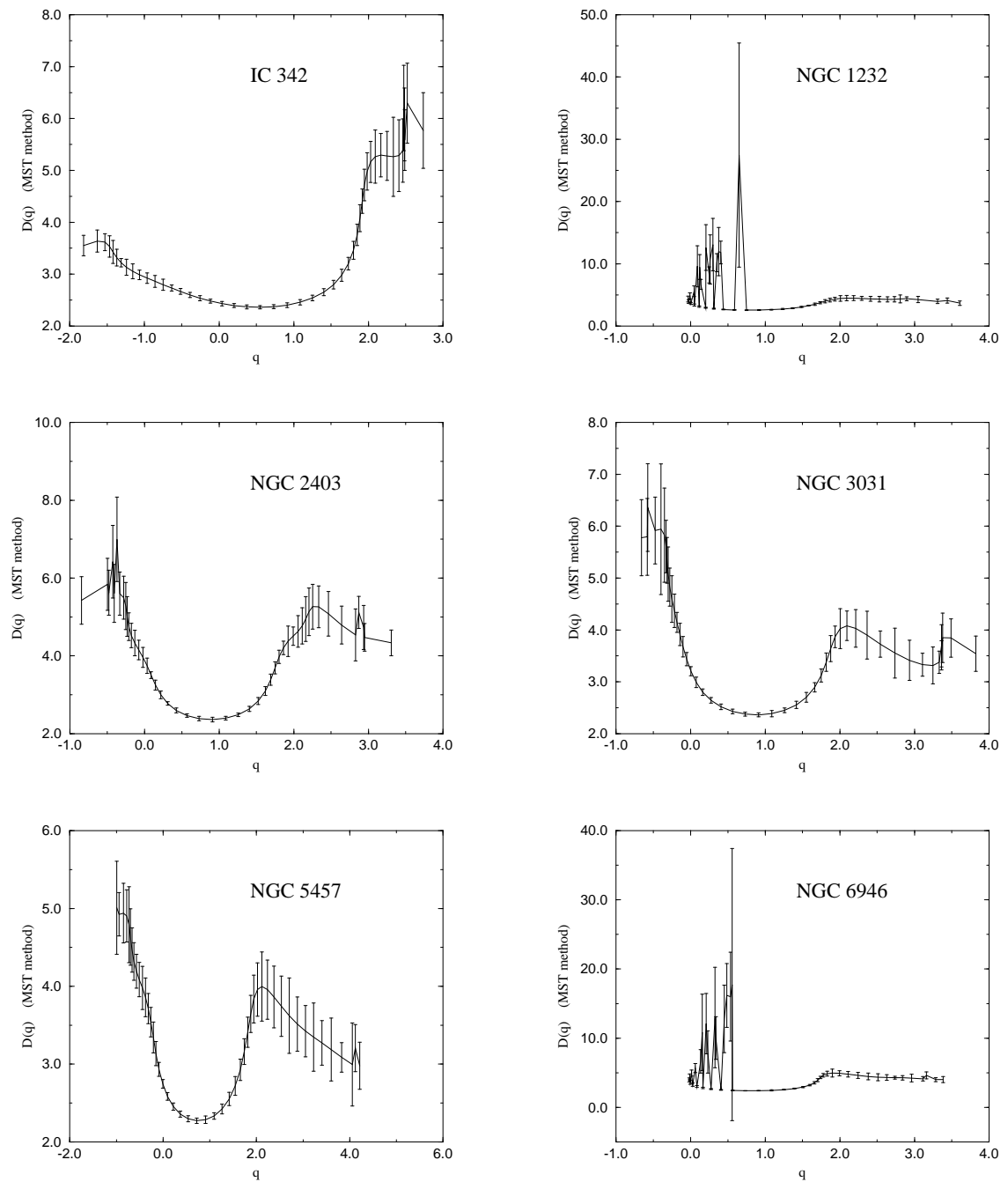
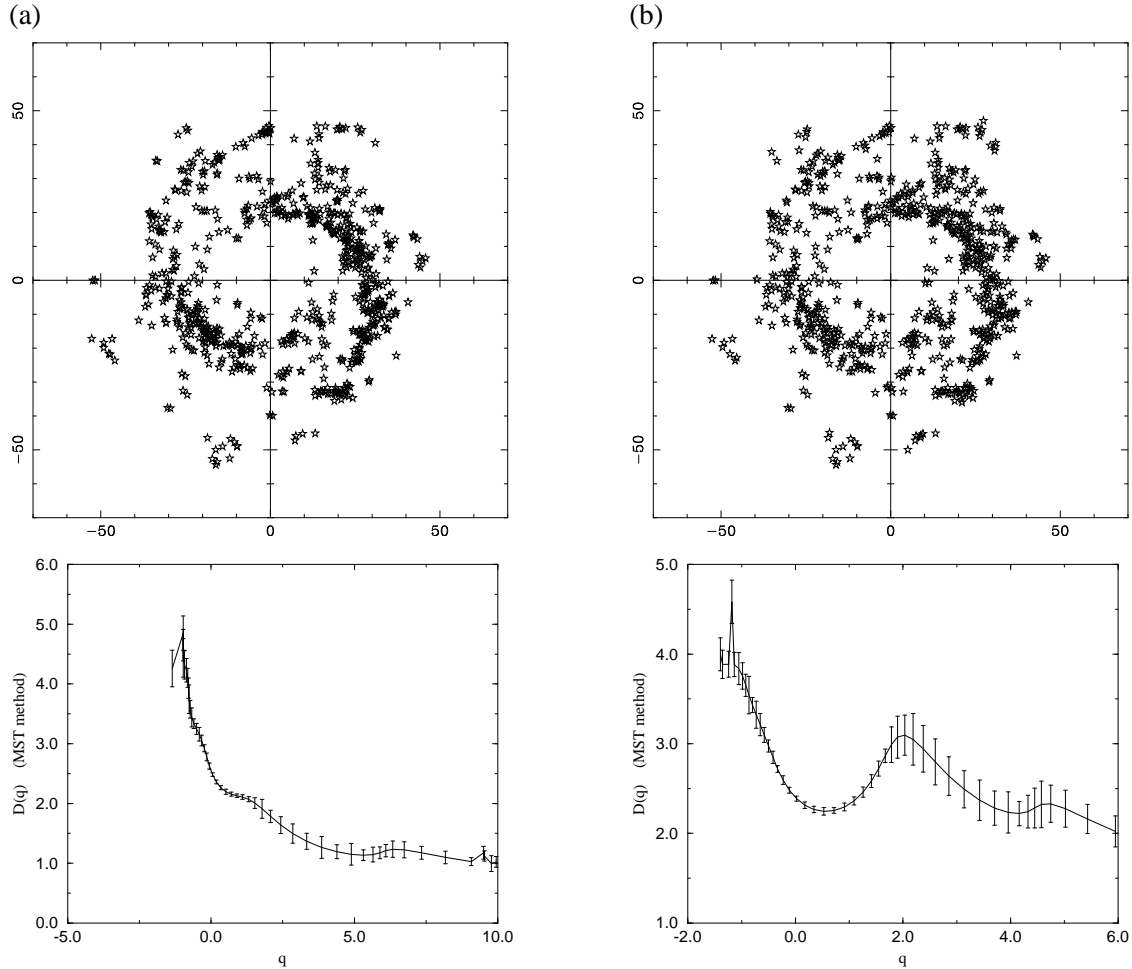


Figure 7.16. Multifractal dimensions for selection of observed galaxies, calculated using the MST method.



Figure 7.17. The effect of pixellation on a ‘standard’ model data set. Shown are the H II positions and $D(q)$ curves for (a) normal data and (b) data which has been pixellated using the technique described in the text.



a small amount would be expected to have a large effect on $D(q)$. Again this was tried, with each point being displaced in a random direction by a random amount which was less than the undisturbed minimum point spacing. Since the MST method cannot investigate scaling regimes of size smaller than its shortest branch, this would ensure that the fractal dimensions calculated would be largely unchanged if the routine was working correctly. Once again, the algorithm behaved as expected.

There is an important difference between the model and observational data sets, and this is the dynamic range of the scale lengths in the H II point distribution. If we consider the ratio of the minimum distance between any two points and the maximum, then for a ‘standard’ simulation the value is $\sim 10^{-4}$ whereas for an observed galaxy it is $\sim 10^{-3}$ (NGC 3031). At larger values of q , where the fractal spectra for the real galaxies shows an upturn, we are investigating the more

dense regions, and hence it would seem that it is the lack of short inter-point spacings for the observational data which is causing the problem. As mentioned in Chapter 6, this arises from the difficulty of distinguishing individual H II regions in compact, complex clumps of H α emission. In an attempt to simulate this effect, caused by the limited resolution of the optical images, model data was placed onto a 70×70 grid, and all stellar particles within a given cell were replaced by a single particle at the centre of mass of the cell (all clusters given equal weight). To take into account the loss of particles, the age range of clusters included in the fractal calculation was increased a little – in Fig. 7.17, the unchanged data set includes clusters younger than 8 Myr (resulting in 730 particles), whereas the pixellated set uses clusters younger than 10 Myr (to give 731 particles). To the eye, the structures look similar, although the dynamic range of the pixellated image is reduced to $\sim 10^{-3}$. Moreover, the $D(q)$ curve now shows the ‘U’ shape which we have seen is characteristic of the multifractal dimensions of the observed galaxies, and we conclude that for this reason, the MST method is not able to produce sensible results for the data sets in which we are interested.

Further studies, performed in collaboration with K. K. S. Wu and P. Alexander (Wu *et al.* 1995), have also investigated the MST method, but using a modified coding of the algorithm. It was used to examine both the Hénon attractor and also the multifractal known as the multiplicative random β -model (described in Borgani *et al.* 1993) for which D_q can be calculated analytically. In both cases it was found that changing the acceptance range of edge-lengths could have a major effect on the curves calculated, but it was possible to reproduce exactly neither the theoretical values for the multiplicative random model, nor the dimensions calculated by other authors for the Hénon attractor.

Wu also coded the Correlation–Sum method and tested it on the same theoretical multifractals. We found that it worked well for both cases in the region $q \geq 1$ and that by choosing the minimum sphere radius to be larger than the maximum distance between neighbouring points (so that all cells contain at least one other point and hence the sum in equation (7.8) remains bounded), reasonable answers could be obtained for $q < 1$ also. With these findings, I decided that it would be worth repeating some of the earlier studies done using the MST method, but this time with the Correlation–Sum technique.

A direct comparison of the two estimators can be made from Fig. 7.18, which shows the multifractal dimensions for three simulations, calculated with different M_{st} . The simulations for which data are shown here are the same as were used for Fig. 7.15, and hence the $D(q)$ curves are the same as previously shown. Clearly there are significant differences between the multifractal spectra returned by the two techniques, although they seem to converge at high q . We would also expect them to converge at $q = 0$ since at this point the definitions of the Rényi and Hausdorff generalised dimensions are identical, but this is not seen. Moreover, if both the estimators were working correctly, then the difference between D_q and $D(q)$ would be small (many authors treat them as the same), and certainly less than the estimated error bars.

Figure 7.19 shows the same D_q curves as Fig. 7.18 together with the equivalent curves calculated with a different scaling range for the radii of the covering circles. The curves which extend



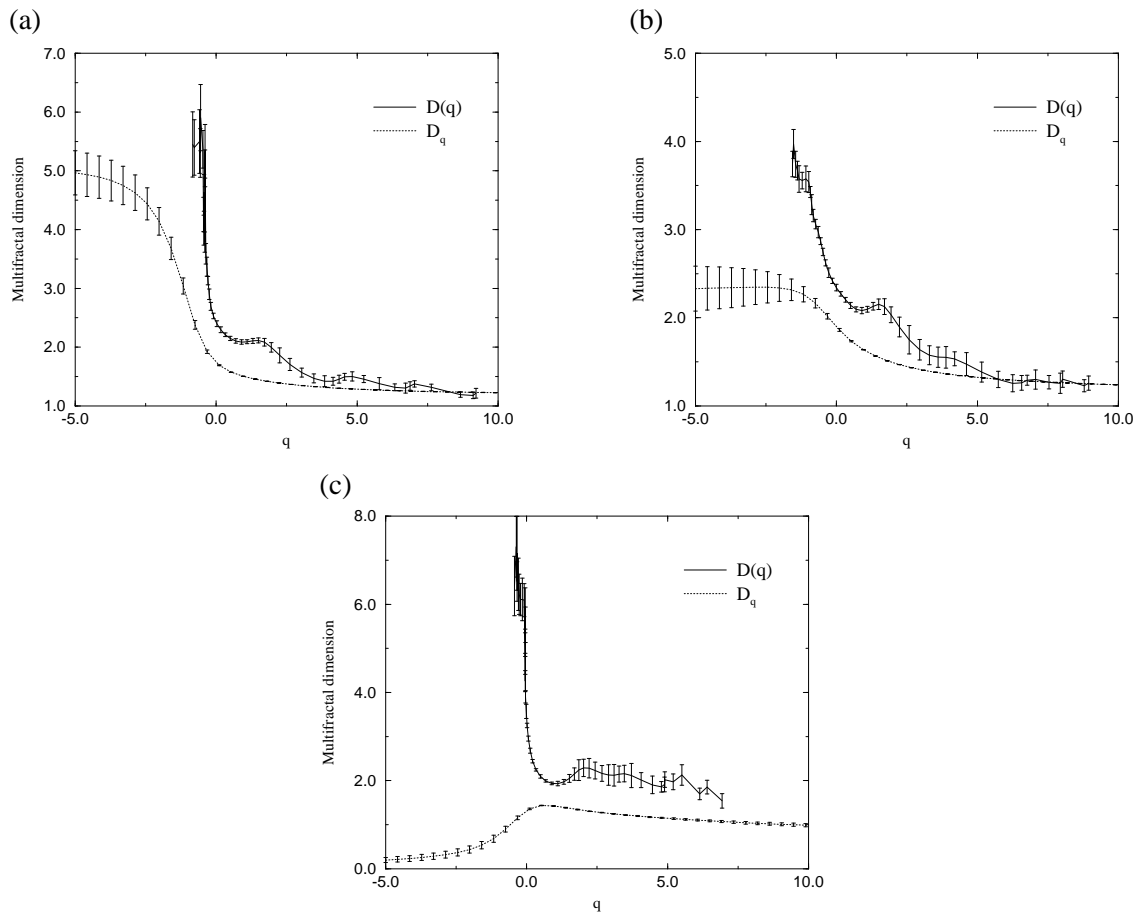


Figure 7.18. Comparison of multifractal dimensions calculated using the two different methods, for three values of M_{st} ; (a) $10^4 M_\odot$, (b) $10^5 M_\odot$ and (c) $10^6 M_\odot$.

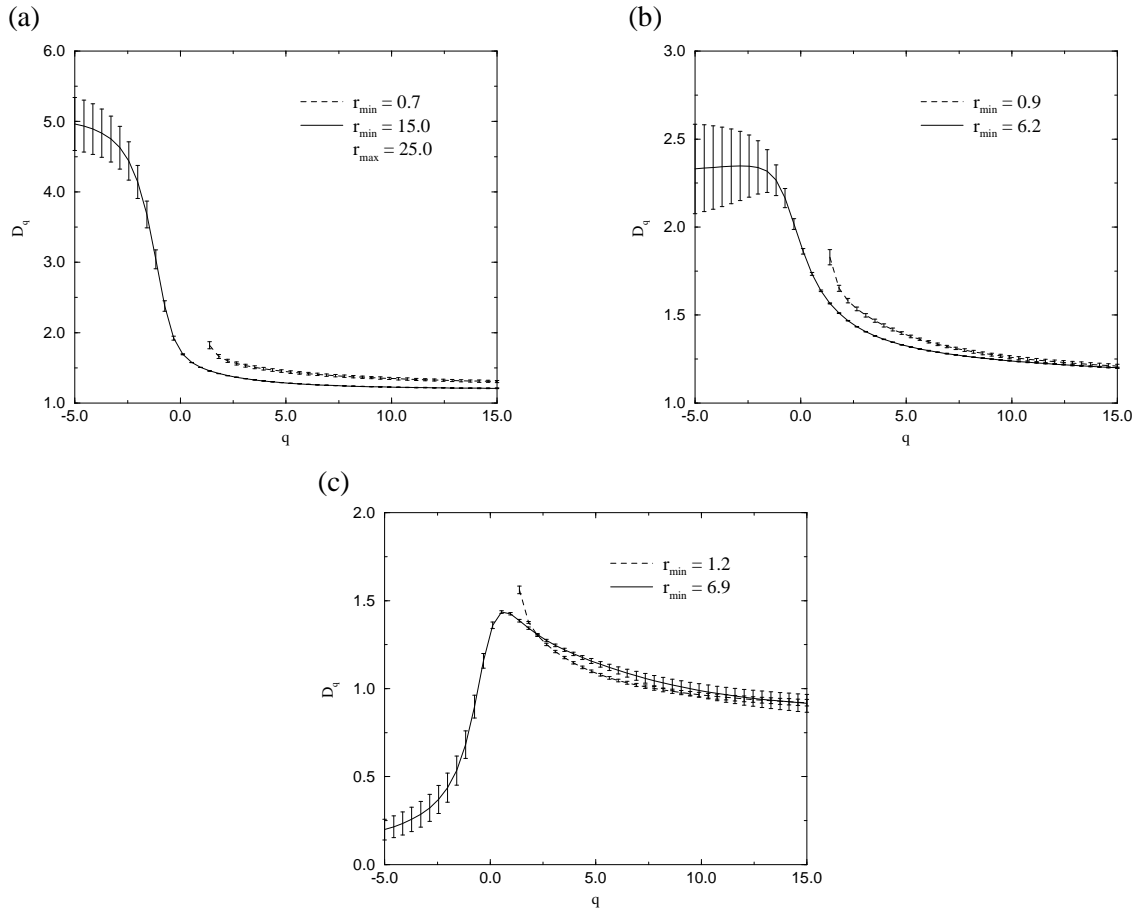


Figure 7.19. Multifractal dimension for the same galaxies as used in Fig. 7.15, but now calculated with the Correlation-Sum method; (a) $M_{\text{st}} = 10^4 M_{\odot}$, (b) $M_{\text{st}} = 10^5 M_{\odot}$ and (c) $M_{\text{st}} = 10^6 M_{\odot}$. In each case D_q has been calculated for $r_{\min} = \text{mean neighbour distance}$ and $r_{\max} = \text{max. neighbour distance}$. In all cases $r_{\max} = 15$ except for the the ‘max. neighbour distance’ curve of (a), for which $r_{\max} = 25$ because $r_{\min} = 15$. As usual, only clusters younger than 10^7 yr have been included in the calculation.



to $q < 1$ were produced using a lower value for the range of radii (r_{\min}) equal to the maximum separation between any two neighbouring points, such that there was always at least one other point within all the circles, whereas the other curve was calculated setting r_{\min} equal to the mean neighbour separation. In this case the sum of equation (7.8) is divergent for $q < 1$. As is evident from the $M_{\text{st}} = 10^6 M_{\odot}$ case, even when r_{\min} is equal to the maximum neighbour separation, the values of D_q are not reliable for $q < 1$, since in this case we have a rising function, violating equation (7.6). In addition we can see that the choice of scaling range can have quite a significant effect on any given value of D_q – although not shown here, changing the choice for the maximum scaling radius (r_{\max}) out to which equation (7.8) is fitted also has an important effect (the curves of Fig. 7.19 have all been calculated with $r_{\max} = 15 L$ – see Appendix A for explanation of internal model units).

Nonetheless, it does seem possible to adopt a standard procedure and thereby extract useful results from the Correlation–Sum approach. Calculated using constant values of $r_{\min} = 5 L$ and $r_{\max} = 15 L$ and including only clusters younger than 10^7 yr irrespective of the simulation parameters, Fig. 7.20 shows $D_{1.4}$, D_6 and D_{15} as a function of M_{st} and SDW amplitude. The trends are clear, and the scatter seems to reflect the actual differences between the runs (cf. Figs 5.4 and 5.6). It was hoped that the graphs for D_{15} would show less scatter than the equivalent D_6 since, from Fig. 7.19 it would appear that the effect of the precise value of r_{\min} lessens at higher q values, although this does not appear to be the case.

It is also interesting to compare the curves here with the Fourier spectra of the same simulations presented earlier. Considering the variation of D_q with SDW amplitude, we see that at high A the multifractal dimensions tend towards a constant value. This form of curve has been seen before in relation to the SDW strength, when we investigated the amplitude of the $n = 2$ Fourier component (Fig. 7.5). Indeed when we plot $D_{1.4}$ and D_{15} against the peak value of the $n = 2$ Fourier component (Fig. 7.21) we see that the two quantities are well correlated, and hence conclude that the two analyses are predominantly picking out the same structural features. At higher q values, the sum of equation (7.8) is dominated by the most dense regions, i.e. the youngest, percolating clusters of which there are relatively few. Hence Fig. 7.21(b) shows a larger scatter due to the small number of points which are important in the calculation. In contrast $q = 1$ samples all density regimes with equal weighting, and therefore all the clusters (of age younger than 10 Myr) are included, tightening the correlation. Therefore, although the Fourier transform contains more information (with the complete set of complex $A(q, n)$ it is possible to reproduce the structure precisely), the multifractal dimension has shown itself to be a more useful tool, in that it is able to distinguish reliably between different structures and characterise each with a single number. The scatter is still larger than would be ideal, and although for model galaxies this can be countered by increasing the number of points within the summation, we have preferred not to do this, such that we have a standard technique which can be applied to observational data as well.

Having said that, applying the technique to the observational sample of galaxies does, however, require a little more care since the relative scaling of each one is different, in contrast with the

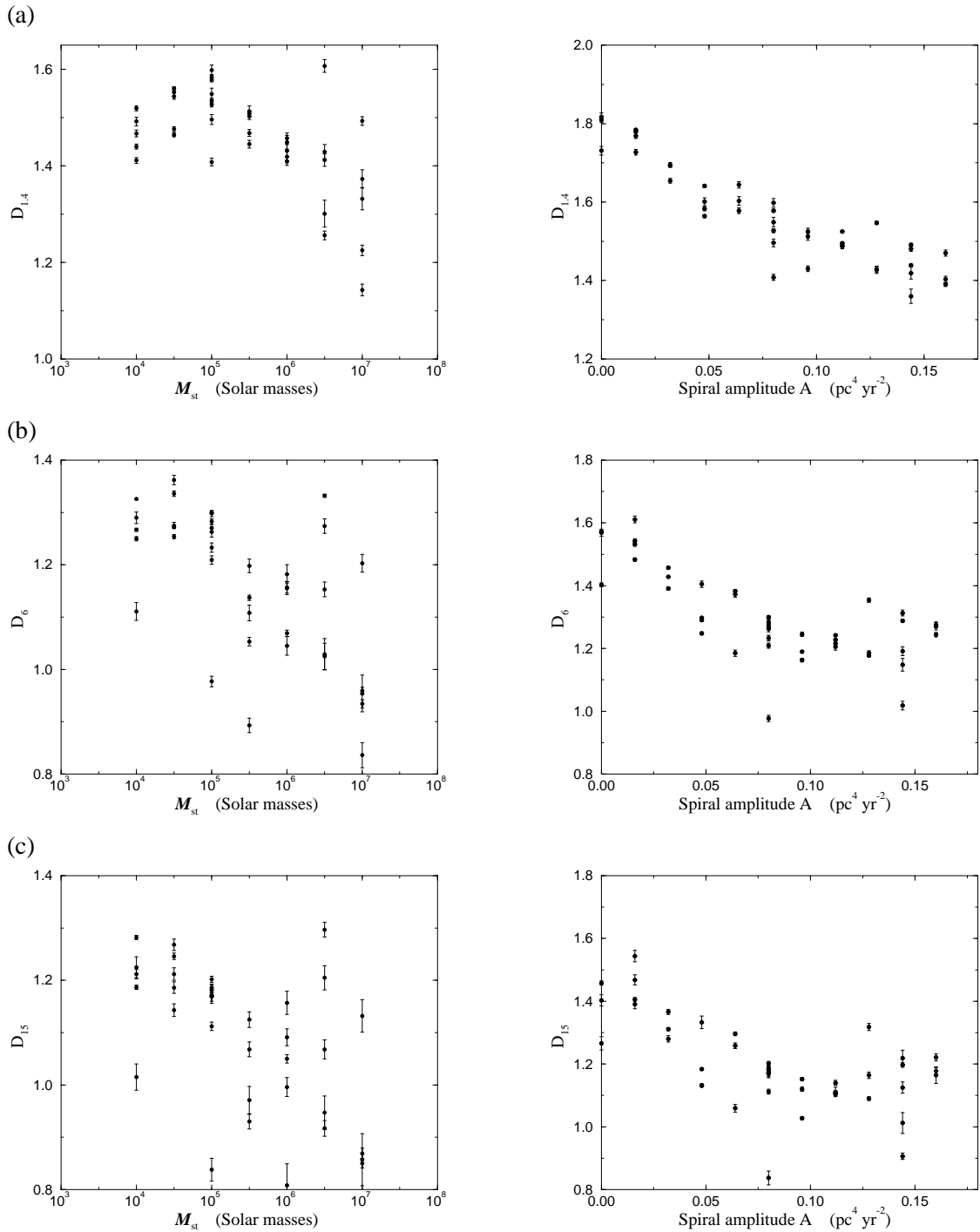


Figure 7.20. Multifractal dimensions (a) $D_{1.4}$, (b) D_6 and (c) D_{15} as a function of model input parameters M_{st} and A . All results were derived using constant values of $r_{\min} = 5.0 \text{ L}$ and $r_{\max} = 15.0 \text{ L}$, and including only stellar particles younger than 10^7 yr .



Figure 7.21. Correlation of Fourier transform peak amplitude with multifractal dimension for two values of q : (a) $q = 1.4$ and (b) $q = 15$. Also shown is the unweighted least-squares fit to the data.

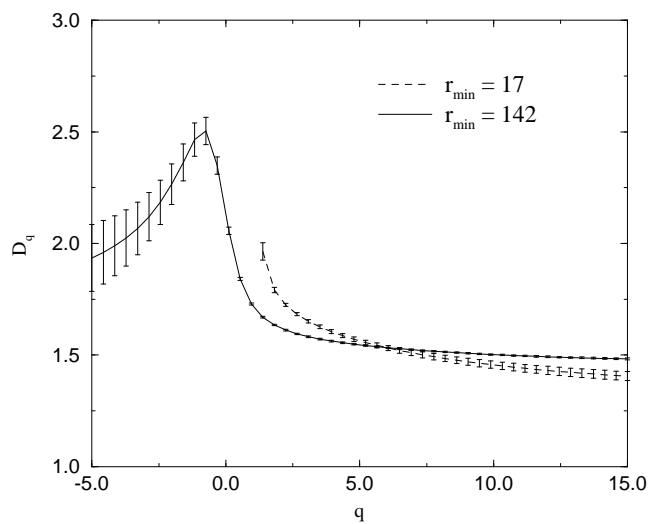
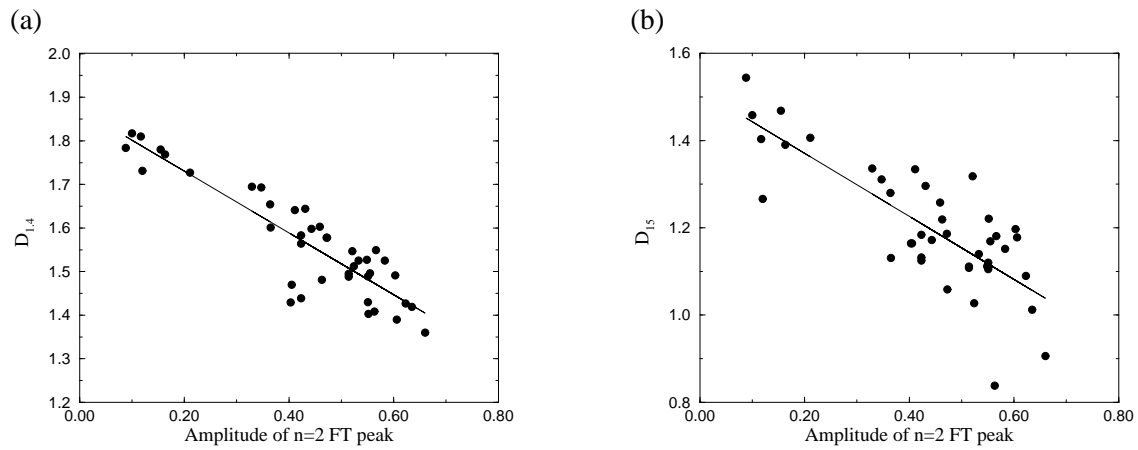
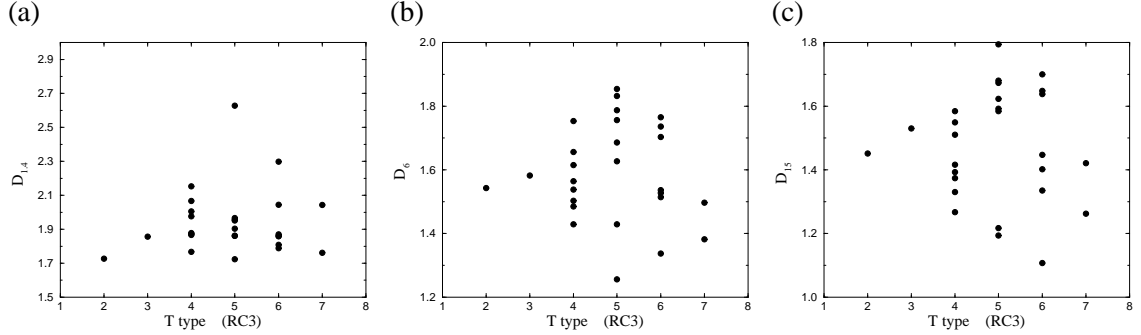


Figure 7.22
Multifractal dimensions of NGC 3031 calculated using the Correlation–Sum method.

Figure 7.23. Multifractal dimensions (a) $D_{1.4}$, (b) D_6 and (c) D_{15} as a function of Hubble morphological class

model data for which all galaxies have approximately the same size $R_{\text{model}} = 55 \text{ L}$ (to within 2% for $M_{\text{st}} = 10^4 \rightarrow 10^6 M_{\odot}$). However, by scaling r_{min} and r_{max} for each galaxy individually, according to the radius (R_{obs}) within which all the H II regions are to be found, such that

$$r_{\text{min}}^{\text{obs}} = \left(\frac{r_{\text{min}}^{\text{model}}}{R_{\text{model}}} \right) R_{\text{obs}} = \left(\frac{15}{55} \right) R_{\text{obs}}$$

$$r_{\text{max}}^{\text{obs}} = \left(\frac{r_{\text{min}}^{\text{model}}}{R_{\text{model}}} \right) R_{\text{obs}} = \left(\frac{5}{55} \right) R_{\text{obs}}$$

we would expect the results to be directly comparable to those above.

The Fourier analysis demonstrated that NGC 3031 was the member of the observational sample best reproduced by the model. Its multifractal spectrum is shown in Fig. 7.22, and we see that the D_q curve best matches that of Fig. 7.19(c), confirming our expectation based on the Fourier analysis – there again NGC 3031 shows a similar spectrum to a simulation with $M_{\text{st}} = 10^6 M_{\odot}$ (Figs 7.4 and 7.8). The D_q values have been calculated, as for Fig. 7.19, using two values of r_{min} equal to the mean- and maximum-neighbour separation respectively, with r_{max} fixed at a value of 253 (arbitrary units), which is equivalent to the 15 L used for the model data.

Unfortunately, it would seem that multifractal analysis fails at the final hurdle. Figure 7.23 shows the multifractal dimension as a function of the Hubble T-type (de Vaucouleurs *et al.* 1991) for three different values of q . Clearly, there is no correlation present in any of these data sets which we would require for the Correlation–Sum multifractal to be a widely applicable technique for both observational and model galaxies. In the light of the close empirical link between the Fourier transforms and the multifractal dimensions, and given the Fourier results presented in Fig. 7.8, it is not, however, surprising that this is the case. Whilst the galaxies produced by the model *look* correct, they fundamentally do not have the same structural form (at least when considering the traditional tracers of star forming regions, *viz.* H II regions) as those that are observed in the Universe. (This is obvious even from a visual inspection of the H II region distributions – compare Figs 6.3, 7.11 and 7.12). Whether this is a real effect, and therefore reflects a deficiency of the model, or an observational, instrumental limitation remains to be seen.



References

- Arneodo A., Grasseau G., Kostelich E. J., 1987, *Phys. Lett. A*, 124, 426
- Barrow J. D., Bhavsar S. P., Sonoda D. H., 1985, *MNRAS*, 216, 17
- Borgani S., Plionis M., Valdarnini R., 1993, *ApJ*, 404, 21
- Considère S., Athanassoula E., 1982, *A&A*, 111, 28
- Danver C.-G., 1942, *Lund Obs. Ann.*, 10
- Davies R. D., 1994, in *Cosmical Magnetism*, ed. Lynden-Bell D., vol. 422 of *NATO ASI Series C*, p. 131, Kluwer, Dordrecht
- de Vaucouleurs G., de Vaucouleurs A., Corwin Jr. H. G., Buta R. J., Paturel G., Fouqué P., 1991, *Third Reference Catalogue of Bright Galaxies*, Springer-Verlag, New York
- Devereux N. A., Young J. S., 1991, *ApJ*, 371, 515
- Elmegreen B. G., Elmegreen D. M., Montenegro L., 1992, *ApJS*, 79, 37
- Falconer K. J., 1990, *Fractal Geometry: mathematical foundations and applications*, John Wiley & Sons Ltd., Chichester
- Feder J., 1988, *Fractals*, Plenum Press, New York
- Frisby J. P., 1979, *Seeing: illusion, brain and mind*, Oxford University Press
- García Gómez C., Athanassoula E., 1993, *A&AS*, 100, 431
- Grassberger P., Procaccia I., 1983, *Phys. Rev. Lett.*, 50, 346
- Hénon M., 1976, *Commun. Math. Phys.*, 50, 69
- Kennicutt R. C., 1981, *AJ*, 86, 1847
- Kuiper N. H., 1962, *Proc. Koninklijke Nederlandse Akademie van Wetenschappen, ser. A*, 63, 38
- Mandelbrot B. B., 1982, *The Fractal Geometry of Nature*, W. H. Freeman & Co., San Francisco
- Martínez V. J., Jones B. J. T., Domínguez-Tenreiro R., van de Weygaert R., 1990, *ApJ*, 357, 50
- Martínez V. J., Domínguez-Tenreiro R., Roy L. J., 1993, *Phys. Rev. E*, 47, 735
- Press W. H., Teukolsky S. A., Vetterling W. T., Flannery B. P., 1992, *Numerical Recipes in FORTRAN*, Cambridge University Press, Cambridge, 2nd edn.
- Puerari I., Dottori H. A., 1992, *A&AS*, 93, 469
- Rényi A., 1970, *Probability Theory*, North-Holland, Amsterdam
- Schröder M., 1991, *Fractals, Chaos, Power Laws. Minutes from an infinite paradise*, W. H. Freeman & Co., New York, Chpt. 9
- Taylor J. H., Cordes J. M., 1993, *ApJ*, 411, 674
- Vallée J. P., 1995, *ApJ*, in press
- van de Weygaert R., Jones B. J. T., Martínez V. J., 1992, *Phys. Lett. A*, 169, 145
- Whitney V. K. M., 1972, *Commun. ACM*, 15, 273
- Wu K. K. S., Sleath J. P., Alexander P., 1995, *MNRAS*, in prep.

Chapter 8

Concluding remarks



The computer model discussed within this dissertation is based on an idea originally postulated several decades ago, namely propagating star formation. It was not until the early 1980s however, that computing power became sufficient to implement the hypothesis, and then only in a limited manner. This new work advances the simulation of propagating star formation a considerable distance by removing the limitations of a fixed grid and, more importantly, by widening the scope of the physical processes considered. Before discussing possible future studies with the model (or a derivative thereof), I will summarise the work that has been described in greater detail elsewhere in this dissertation.

8.1 Summary of work to date

The hypothesis of propagating star formation states that the collapse of molecular clouds to form new stars is triggered by a shock wave generated by the death of one or many members of the previous generation of stars in a nearby OB association. The expanding supershell resulting from the supernovae is able to enhance the dissipation of the magnetic field and turbulent and rotational energies from the cloud, and as a result gravity comes to dominate, inevitably resulting in collapse and subsequent star formation. Since the precise details of the physical processes occurring are only poorly known, we treat the star formation as a stochastic process, i.e. we assign a probability to a cloud collapsing, given that it is shocked, which is proportional to the cloud's mass, and scaled by an input parameter to the model.

Clouds and stellar clusters/associations orbit the galaxy as test masses, moving under the influence of a realistic gravitational potential. This also has the major advantage of allowing us to impose, in a natural way, a spiral density wave as a small perturbation to the otherwise axisymmetric potential (§3.2.2). Hydrodynamic N-body simulations have confirmed that spiral density waves are a fundamental instability of thin, self-gravitating discs, and so it is reasonable for us to impose one in such a manner. It has the effect of organising the star formation, but, unlike some other models, we do not have shocks from the density wave triggering star formation directly. The particulate nature of the simulation also provides for the inclusion of cloud–cloud and cloud–shock



interactions (§3.2.3), the former resulting in a net dissipation of energy, and the latter acting as a source of cloud kinetic energy. The temperature of the galactic disc is maintained through a feedback loop between these two processes, since we aim to model a steady-state system.

One of the major successes of the model is its prediction of the cluster formation rate for the Milky Way (§4.2). The number of input parameters to the model is quite large, specifying the form of the spiral density wave, the dynamics of the clouds and most importantly the scaling mass for the star formation. However, *all* of these can be fixed by observations of our Galaxy, resulting in a definite prediction for the rate of formation of star clusters which is within a factor of two of the observed value. When account is taken of the observational uncertainties inherent in the input parameters to the simulation, this indeed represents a triumph for the model.

We are also able to predict a form for the Schmidt Law (§4.3). This empirical relation associates the galactic star formation rate to the average gas density through a power law. By considering the various scalings of the star formation rate, median cloud mass etc. on the input parameters to the model, we suggest that the power law index should have a value of 1.65, which is in excellent agreement with observational indications.

The most obvious feature of the galaxies considered in this work is their spiral structure. By varying the input parameters to the model, we can generate a wide range of morphologies. It is important to compare the structures produced by the model with observed galaxies – indeed, a computer simulation whose results cannot be compared with the real world could be considered a waste of time. Hence we have collected H II region data for a sample of galaxies (Chapter 6), and have contrasted this with model data, not only in a qualitative way (i.e. by simple visual inspection of the images), but also using a number of mathematical techniques (Chapter 7), with varying degrees of success. Fourier analysis has been used by other authors to investigate galactic structure, and is the best method of extracting information such as the spiral pitch angle. It does not however, provide a single number with which to characterise the galaxy, which was the ultimate aim of this part of the study. Another technique considered, namely the comparison of the distribution of the edge-lengths of minimal spanning trees constructed using the H II regions as nodes, suffers from a similar limitation in that it can only be used to compare two galaxies, and has no absolute level. Moreover, it seems excessively sensitive to small differences in structure. In contrast a multifractal analysis provides a simple spectrum of dimensions, and is sensitive to similar sorts of structure as the Fourier transform. By choosing a specific scaling regime (i.e. value for q) it is possible to determine a single number with which to characterise the galactic morphology. Unfortunately, it, like all the methods discussed, works better with model data, and hence the ability to compare model and observation is restricted.

Nonetheless, the undoubted successes of the model demand that further work be done, to both extend our understanding of the current model, and to develop it further, with the aim of enhancing its physical realism. As computing power continues to grow, increasingly ambitious models become possible, and I discuss below (§8.3) some possible approaches which could be adopted. But first, what remains to be done with the model as it has been described here?

8.2 Future studies with the current model

The parameter space of the model has almost exclusively been investigated along its axes. This has enabled the scaling relationships between the parameters and the star formation rate to be determined, something which would have been difficult to do had more than one parameter been varied in any given simulation. Significant non-linear behaviour will however, result in cross-correlations between the effects of the parameters, and this regime remains to be studied. As an example we have seen how the spiral pattern traced by the star forming regions does not follow the underlying the SDW (in particular having a different pitch angle) and this is likely to be related to the rotation curve of the galaxy and the pattern speed of the density wave. By varying the pitch angle of the imposed spiral perturbation and its rotation speed to build up a two dimensional mesh of simulations, it may be possible to disentangle the effect.

An analytic approximation would form an important aid to understanding the behaviour of the model in response to varying conditions. A zero'th order approximation has already been made, when in equation (5.1) we derived a characteristic timescale for cloud regrowth after a star formation event has occurred. If we assume that the cluster formation rate is inversely proportional to this timescale, then we have $\psi \propto M_{\text{st}}^{-1/3}v$, and we saw in Chapter 4 that in fact $\psi \propto M_{\text{st}}^{-0.3}$ and $\psi \propto v^{0.7}$. A considerably more sophisticated treatment for the older SSPSF models (Seiden & Gerola 1982) has been done by Neukirch & Feitzinger (1988), but was of considerable complexity, and it has not as yet been possible to formulate an analytic approximation for the current model.

Further techniques for classifying the structural properties of galaxies also need to be investigated. A number of other estimators for the multifractal dimensions are described in the literature, and it may prove to be the case that one of these is more robust for the small, noisy data sets with which we have to work. Furthermore, considering the difficulties experienced with the observational data sets available (all of which are now quite old), and in particular their lack of spatial dynamic range it would be useful to re-map a number of large, nearby galaxies with high resolution so that the tight knots of ionised hydrogen can be disentangled. A greater range of morphological classes must also be studied since the current data is biased heavily in favour of late-type spirals, increasing the difficulty of establishing a correlation between the traditional morphological classifications (Appendix C) and any new technique.

8.3 Developing the model

Even over the duration of the current project, the computing power available has increased many-fold. When the current model was originally devised, great care had to be taken to ensure that it was sufficiently simple such that it would be feasible to calculate the large number of runs required in a sensible amount of time. As a consequence, it was decided not to model the structure of the diffuse HI component in any detail, nor to consider the mass interchange between the stars, stellar remnants and the various phases of the ISM. It is important to note, that we would expect these effects to play a relatively minor role in the propagating star formation process itself, which is a



function of the cloud mass and is not dependent on what happens to that material once star formation has occurred, beyond the fact that the cloud is disrupted and is therefore unable to undergo subsequent star formation events until it has had time to regrow. Hence, the fundamental results presented above would be largely unchanged.

However, if the spiral density wave also perturbed the H I distribution, then this would make the spiral arms still more important in their regulation of the star formation rate. Clouds spend a longer time in the potential minima and are more closely packed there. Both effects already work to concentrate the star formation along (or just behind) the spiral arms, and if the H I density were also to be higher in these regions, then this would increase the mass growth rate of the clouds, and hence further enhance the rate of star formation. If it were also possible to treat the mass lost from the clouds, either locked up into stars or dispersed into the diffuse ISM, then this would result in local fluctuations in the H I density.

Furthermore, it is possible that a value for M_{st} might emerge as a natural consequence of a fully self-consistent model of the cloud population. It was noted earlier (§2.1.3) that the model described here does not exhibit a percolation threshold. We might hope that one would however, return to a model in which the interchange of material between the various phases of the ISM was simulated, with the onset of percolation defining the best value to be used for M_{st} .

The H I could be modelled in one of (at least) two ways. The first borrows an idea from Smooth Particle Hydrodynamic codes (§2.2.2) and would require a particulate representation, with each particle having one unit of H I gas mass; hence the volume density of particles would specify the gas density. A full hydrodynamic treatment is not required here – instead the particles would move in the total galactic gravitational potential (in the same way as the cloud and star particles) and would therefore respond naturally to the spiral density wave. The H I density at any point would be given by interpolating from the particle density using a suitable kernel function and hence accretion of H I by the molecular clouds would be modelled by the cloud removing H I particles as it orbited; not through inter-particle collisions, but by a smoothed reduction of the local number density in the wake of the cloud. Similarly, when a cloud was disrupted by star formation, or a star cluster produced an expanding supershell through multiple supernovae explosions, then the local number of H I particles would rise, reflecting the increasing quantity of gas in the neutral phase.

The second treatment would distribute the neutral gas across a differentially rotating grid, such as was used in the earliest propagating star formation models. The total gas mass in each cell would vary to reflect the local processes occurring as described above. This approach would not however allow the spiral density wave to be included in a realistic manner, and goes against the philosophy adopted for the current model. As a consequence, the first approach is preferred.

The material transferred between supershells and the diffuse ISM will be chemically enriched as a result of having been processed through stars. It is possible to use a simple parameterisation of this process (Edmunds 1990), and thus the chemical evolution of the galaxy could be modelled. This also allows the possibility of making the probability of star formation a function of the local metallicity, potentially opening up a whole range of interesting, new behaviour.

Finally, the requirement of having to impose a spiral perturbation onto the gravitational potential is often regarded as a weakness of the current formulation. As was mentioned previously (§3.2.2), a spiral density wave is a natural instability of a galactic-disc system, and would arise without being imposed if we were to model the collective, gravitational force between the particles. A first step would be to use a restricted N-body code to calculate a self-consistent overall potential due to the stellar component (which contributes $\sim 90\%$ of the total mass) and then to move the gas within the derived field, either as is done in the current model, or using one of the enhanced techniques for modelling the gas described above.

The new model described in this dissertation is, I believe, a valuable addition to the field of galactic simulations. I have adopted a simple, but not simplistic approach, yet have been able to make a number of concrete predictions regarding the star formation rate which correspond extremely well with observational values. The multifractal analysis is encouraging, if as yet not fully developed, and with ever-increasing computer power, many exciting enhancements of the model are now possible. Paul Alexander, my supervisor throughout this project, has a number of students continuing this line of research over the next few years – I hope that they will find the initial studies described within these pages to be of some use.

References

- Edmunds M. G., 1990, *MNRAS*, 246, 678
Neukirch T., Feitzinger J. V., 1988, *MNRAS*, 235, 1343
Seiden P. E., Gerola H., 1982, *Fundam. Cosmic Phys.*, 7, 241



Appendix A

Running a simulation

A.1 Input parameter file

There are a total of 17 input parameters to the model (Table A.1) of which three control the running of the simulation (`source`, `itmax` and `dump`) whilst the others determine the physics, and are discussed in greater detail in Chapter 3. The initial parameters are read from a namelist file (example below), with all quantities specified in ‘model units’ (Table A.2).

```
$indata
  source='none'
  itmax=2500
  timestep=0.1
  ncloud=32000
  dump=200
$end
$gasdyn
  a0=0.3
  elas=0.7
  vmax=0.51
$end
$sspsf
  mst=1.0e5
  msp=1.0e11
  eff=1.0e-3
$end
$spdata
  narm=2
  omegap=0.14
  r0=5.0
  p=5.0
  ang=20.0
  amp=8000.0
$end
```



Name	Explanation	Symbol in text
source	Name of existing run to be used as start point	—
itmax	Number of timesteps in units of $\tau_{\text{step}} \times 10^7$ yr	—
tstep	Size of timestep in units of 10^7 yr	Δt
ncloud	Number of cloud particles	N_c
dump	Time between output files written in units of τ_{step}	—
a0	rms velocity dispersion	v_{disp}
elas	fraction of cloud energy remaining after collisions	η
vmax	maximum velocity imparted to clouds by SNR interactions	v_{max}
mst	Stimulated SF scaling mass	M_{st}
mSP	Spontaneous SF scaling mass	M_{sp}
eff	Fraction of cloud remaining after star formation	ϵ
narm	Number of arms in spiral density wave	n
omegap	Spiral pattern speed	Ω_p
r0	size of bar	r_0
p	rate of transition from bar to outer regions	p
ang	Spiral density wave pitch angle	i_0
amp	Spiral density wave amplitude	A

Table A.1.

Quantity	Model unit	'standard' unit
Length	L	200 pc = 6.172×10^{18} m
Time	T	10^7 yr
Mass	M	$M_{\odot} = 1.989 \times 10^{30}$ kg
Linear velocity	LT^{-1}	19.56 km s $^{-1}$
Angular velocity	T^{-1}	97.78 km s $^{-1}$ kpc $^{-1}$
Gravitational potential	$L^2 T^{-2}$	3.825×10^8 m 2 s $^{-2}$
SDW amplitude	$L^4 T^{-2}$	1.60×10^{-5} pc 4 yr $^{-2}$

Table A.2.

A.2 Useful UNIX scripts

The following UNIX script chains together a number of simulations, using a new input file for each. Once all the numbered input files have been processed the simulations halt. On completion of each run, the data files produced are compressed, with the name of the directory to be compressed being read from a file written by GALAXY.

```
#!/bin/csh -f

# 11/01/94   jps18 and tj105   ver 2.1
# 30/09/94   jps18           ver 3.0  SOLARIS
#
#   CHAIN
#
#   Shell script to chain a series of GALAXY runs together.  The
#   resulting files are automatically compressed at the end of each
#   run.  CHAIN can be run on 'mraosa', 'mraosb', 'mraose' and
#   'mraosf' simultaneously without cross-interference.
#   The input files must be in a directory ./infile.
#
#   Chain can be called with an argument (eg. "chain 5 &").  In this
#   case execution commences with file 'input?5'.
#
# INITIALISE
set workdir = /home/jps18/model/ver7
cd $workdir
set hidpath = /home/jps18/model/cron

# SET INITIAL FILE NUMBER
if ( $1 >= 1 ) then
    set i = $1
else
    set i = 1
endif

# SET suffix TO 'a', 'e' OR 'f' AS APPROPRIATE
set suffix=`/usr/ucb/hostname | awk '{print substr($1,length,1)}'`
if (-e $hidpath/num$suffix) rm $hidpath/num$suffix
echo $i > $hidpath/num$suffix

# LOOP WHILE INPUT FILES EXIST
while ( -e ./infile/input$suffix$i )

# COPY INPUT FILE TO WORKING DIRECTORY
    cp ./infile/input$suffix$i input$suffix
```



```

# RUN SIMULATION RE-DIRECTING STANDARD OUTPUT TO FILE
if ( -e gal$suffix.log ) then
  galaxy >>& gal$suffix.log
else
  galaxy >& gal$suffix.log
endif

# INCREMENT FILE COUNTER
@ i = ($i + 1)

# OUTPUT NEXT FILE NUMBER TO FILE. THIS INFORMATION IS USED BY
# 'bootcheck' TO RESTART 'chain' FROM THE CORRECT PLACE SHOULD THE
# SYSTEM BE REBOOTED.
if ( -e $hidpath/num$suffix) rm $hidpath/num$suffix
echo $i > $hidpath/num$suffix

# COMPRESS FILES. USES HIDDEN FILE '.gale' OR '.galf' WHICH CONTAINS
# THE PATH OF THE OUTPUT FILES FROM THE LATEST RUN. THIS FILE IS
# WRITTEN BY 'galaxy'.
cd `cat .gal$suffix`
/usr/local/bin/gzip *.dp?? *.im??
cd $workdir
rm .gal$suffix

# FINISH LOOP
end

# WRITE '-1' TO THE FILE USED BY 'bootcheck'. THIS INDICATES THAT THE
# CHAIN HAS TERMINATED AND PREVENTS 'bootcheck' FROM RESTARTING CHAIN
# FROM THE BEGINNING.
if ( -e $hidpath/num$suffix) rm $hidpath/num$suffix
echo '-1' > $hidpath/num$suffix

```

The script below checks to see whether the program GALAXY is still running, and if not whether it finished normally. If this is not found to be the case (e.g. if the machine has been rebooted), the GALAXY is automatically restarted.

```

#!/bin/csh -f

# 11/01/94   jps18 and tj105   ver 1.0
#
# BOOTCHECK
#
# Checks to see whether the machine on which this program is being
# run has been rebooted, and if so restarts the appropriate chain
# starting with the simulation that was interrupted. This script

```

```
# uses the files $hidpath/num? to determine the point from which
# to restart chain.
# This program should be copied to 'cronexec' after a chain has been
# started on either machine. Once chain has successfully completed
# the file 'cronstop' should be copied to 'cronexec', although this
# is not crucial.
# 'cron' is machine specific, i.e. a 'crontab' file needs to exist on
# both machines. This file must be the same on both machines and
# have the form
# "0 0,4,8,12,16,20 * * * /home/jps18/model/cron/cronexec".
# This would cause 'cronexec' to be executed every four hours on
# every day of the week.
#

# SET PATHNAMES FOR START NO. FILES, LOG FILES AND CHAIN RESPECTIVELY
set hidpath = /home/jps18/model/cron
set logpath = /home/jps18/model/ver7
set chpath = /home/jps18/model/ver7

# SET suffix TO 'e' OR 'f' AS APPROPRIATE
set suffix = `/usr/ucb/hostname | awk '{print substr($1,length,1)}'`

# CHECK TO SEE IF 'chain' IS STILL RUNNING
set test = `ps -ef | grep -c chain`

# IF NOT THEN RESTART
if ( $test == 1 ) then

# DETERMINE STARTING POINT FOR 'chain'
if ( -e $hidpath/num$suffix ) then
    set start = `cat $hidpath/num$suffix`
else
    set start = 1
endif

# UNLESS 'chain' HAS FINISHED NORMALLY (IN WHICH CASE start=-1)
# RESTART chain WRITING AN APPROPRIATE MESSAGE TO THE LOG FILE
if ( $start != '-1' ) then
    echo >> $logpath/gal$suffix.log
    echo >> $logpath/gal$suffix.log
    echo RESTARTING `hostname` >> $logpath/gal$suffix.log
    date >> $logpath/gal$suffix.log
    echo >> $logpath/gal$suffix.log
    nice +19 $chpath/chain $start &
endif

endif
```



Appendix B

Simulation source code

For convenience, the code is split up into a number of individual files, grouping the subroutines by their function. The listing below indicates in which file each subroutine can be found. The main data arrays are all held in `common` blocks to reduce the memory requirement, and these are specified in `include` files to ensure consistency between subroutines, which are listed after the subroutines. For completeness I have also provided the code for two routines (`FPHANDLER` and `DCOSRULE`) which formed part of my personal library suite. If these libraries are not available, then it will be necessary to alter the `Makefile`.

Routines not listed below include `G05CAF` (Numerical Algorithms Group Limited 1993) and `BSSTEP` (Press *et al.* 1992) since these are widely available. Use has been made of a suite of local libraries for the file-handling and system specific operations which are also not listed below – routines performing similar tasks can be expected to exist on all systems.

Subroutines contained in `model.f`.

```
c    31/08/94    jps18    ver 7.5
c
c *****
c
c    program galaxy
c
c    Galaxy simulation program.
c
c    SUBROUTINES AND FUNCTIONS USED:
c    init          ver 8.4 INITIALISES DATA ARRAYS
c    data_read     ver 6.1 READS IN DATA FROM PREVIOUS RUNS
c    sfr_read      ver 1.0 READS IN SFR ETC FROM PREVIOUS RUN
c    exists        ver 1.0 CHECKS TO SEE IF FILE EXISTS, AND
c                  UN-ZIPS IF NEEDED
c    rotate        ver 7.1 ROTATES THE WHOLE GALAXY
c    derivs        ver 2.0 CALCULATES THE DERIVATIVES OF POS/VEL
```



```

c
c          COORDINATES
c    dphi      ver 2.3 CALCULATES THE PARTIAL DERIVATIVES OF
c              THE GALACTIC POTENTIAL
c    potential ver 2.1 CALCULATES GALACTIC POTENTIAL
c    pot_init  ver 1.0 SETS UP PARAMETERS DESCRIBING POTENTIAL
c    propagate ver 8.2 IMPLEMENTS SSPSF TO PROPAGATE STAR
c              FORMATION
c    cloud_mass ver 2.1 INCREMENTS CLOUD MASS BY ACCRETION
c    hldensity ver 1.0 DISTRIBUTION OF HI
c    nearneigh ver 5.1 CALCULATES NEIGHBOURING POINTS
c    neighgrid ver 1.2 SETS UP GRID REQUIRED BY nearneigh
c    cloud_cloud ver 1.3 INTER-CLOUD COLLISIONS
c    cloud_snr  ver 2.2 CLOUD/SNR INTERACTIONS
c    energy_bal ver 1.1 ADJUSTS CLOUD MEAN FREE PATH TO
c              MAINTAIN DISC TEMPERATURE
c    equilibrate ver 1.2 ALLOWS SYSTEM TO DYNAMICALLY RELAX
c    vcirc      ver 1.0 CALCULATES CIRCULAR SPEED FOR EACH CLOUD
c    output     ver 2.5 FILE HANDLING AND DATA OUTPUT
c    geom_entropy ver 3.1 CALCULATES GEOMETRIC ENTROPY OF
c              MOLECULAR CLOUD DISTRIBUTION
c    fphandler  ver 1.1 FLOATING POINT EXCEPTION HANDLER
c    dcosrule   ver 1.0 COSINE RULE
c
c    ROUTINES USED FROM 'NUMERICAL RECIPES'
c    bsstep, mmid, pzextr, spline, splint
c
c    ROUTINES USED FROM NAG LIBRARY
c    g05ccf, g05caf, g05ddf
c
c    ROUTINE USED FROM IOLIB
c    io_system
c
c    INCLUDE FILES REQUIRED
c    /home/jps18/model/ver7/common.inc
c    /home/jps18/model/ver7/header.inc
c    /home/jps18/model/ver7/neighblk.inc
c    /home/jps18/model/ver7/potential.inc
c
c    *****
c
c    MAIN DATA ARRAY DECLARATIONS
c
c    include 'common.inc'
c
c    NAMELIST DECLARATIONS
c
c    include 'header.inc'
c    namelist /indata/ source,itmax,tstep,dump,ncloud
c    namelist /gasdyn/ a0,elas,vmax
c    namelist /sspsf/ mst,msp,eff
c    namelist /spdata/ narm,omegap,r0,p,ang,amp

```

```

c      LOCAL DECLARATIONS

      integer  dunit,          ! DUMP FILE UNIT
+          iunit,            ! IMAGE FILE UNIT
+          sunit,            ! SFR FILE UNIT
+          vernum,           ! CURRENT VERSION NUMBER
+          verold,           ! SOURCE FILE VERSION NUMBER
+          nptsav,           ! NO. OF POINTS IN SOURCE FILE
+          icount,           ! COUNTER
+          imnum,            ! IMAGE FILE NUMBER
+          len,chr_lenb,      ! LENGTH OF HOSTNAME
+          iflag,            ! SUBROUTINE RETURN CODE
+          i                  ! COUNTER
      parameter (vernum=701)
      real     atime,          ! TOTAL SIMULATION TIME
+          otime,            ! OUTPUT/PROPAGATION TIME
+          stime,            ! EQUILIBRATION TIME
+          source_time,      ! ELAPSED SOURCE TIME
+          elap,             ! TOTAL ELAPSED RUN TIME
+          runtime(2),       ! USER AND SYSTEM RUN TIMES
+          sfr,              ! STAR FORMATION RATE
+          vrms,             ! INITIAL RMS VEL. DISPERSION
+          vact,             ! ACTUAL RMS VEL DISPERSION
+          xrad,             ! EFFECTIVE CLOUD RADIUS
c                               FOR COLLISIONS
+          entropy,          ! GEOMETRICAL ENTROPY
+          dum1(3000),dum2(3000), ! } DUMMY ARRAYS FOR READING
+          dum3(3000),dum4(3000), ! } OLD SFR DATA
+          dum5(3000)        ! }
      character path*48,      ! SOURCE PATH
+          host*6,           ! HOST MACHINE
+          sourcesav*12      ! SAVED NAME OF SOURCE FILE

c      FUNCTION DECLARATIONS

      integer  hostnm         ! RETURNS NAME OF HOST MACHINE
c      integer  ieee_handler, fphandler
c      external fphandler
      real     etime           ! ELAPSED RUN TIME
      logical  exists         ! CHECKS TO SEE IF FILE EXISTS

      data iunit,dunit,sunit /10,11,12/
      data iflag /0/

c
c -----
c
c      INITIALISE FLOATING POINT EXCEPTION HANDLER (DEBUGGING)
c
c      iflag = ieee_handler ('set','common',fphandler)
c      if (iflag.ne.0) then
c          print*,'Couldn't establish fp signal handler'

```



```
c      stop
c      endif

c      INITIALISE RANDOM NUMBER GENERATOR

      call g05ccf

c      READ INPUT DATA

      iflag = hostnm(host)
      len = chr_lenb(host)
      open (sunit,file='input'//host(len:len),status='old',
+        form='formatted')
      read (sunit,indata)
      read (sunit,gasdyn)
      read (sunit,sspsf)
      read (sunit,spdata)
      close (sunit)

c      CHECK FOR ERRONEOUS INPUT

      if (ncloud.gt.nclmax) then
        print*,'Insufficient array size (cloud)'
        stop 'ERROR TERMINATION'
      endif

c      INITIALISE PARAMETERS FOR POTENTIAL

      call pot_init

c      SET UP INITIAL CONDITIONS IF STARTING FROM SCRATCH

      if (source(1:4).eq.'none') then
        call init
        call equilibrate (vrms,stime,iflag)
        call geom_entropy (ncloud,entropy)
        if (iflag.ne.0) stop 'ERROR TERMINATION'
        xrad = 0.07
        sfr = 0.0
        source_time = 0.0

c      OR INITIALISE USING PREVIOUS RUN

      else
        sourcesav = source

        call sfr_read (source,sunit,dum1,dum2,dum3,dum4,dum5,iflag)
        source = sourcesav

        path = '/home/jps18/model/data/'//source//'/source'
        if (.not.exists(path))
```

```

+      stop '**ERROR* Source file does not exist'
      open (iunit,file=path,status='old',form='unformatted')
      call data_read (iunit,verold,iflag)
      close (iunit)
      if (iflag.ne.0) stop '**ERROR** in data_read'
      source = sourcesav

      sfr = dum2(itmax+1)
      vrms = 0.0
      do 10 i=1,itmax
        vrms = vrms + dum3(itmax)
10     continue
      vrms = vrms/float(itmax)
      xrad = dum4(itmax+1)
      entropy = dum5(itmax+1)
      source_time = float(itmax)*tstep

c      RE-READ CURRENT PARAMETERS

      nptsav = ncloud
      open (sunit,file='input'//host(len:len),status='old',
+        form='formatted')
      read (sunit,indata)
      read (sunit,gasdyn)
      read (sunit,sspsf)
      read (sunit,spdata)
      close (sunit)
      ncloud = nptsav
endif

c      SUBROUTINE propagate COUNTS DOWNWARDS THROUGH ARRAY stage.
c      IF THE AGE OF THE STAR IS LESS THAN 2.0 THEN THE LOOP IS
c      EXECUTED. TO JUMP OUT OF THE LOOP WHEN THE ZERO'TH ELEMENT
c      IS REACHED, SET THE ZERO'TH AGE LARGE.

      stage(0) = 9999

c      INITIALISE OUTPUT

      call output (dunit,iunit,sunit,0.0,0,vernum,iflag)
      if (iflag.ne.0) stop '**ERROR TERMINATION**'
      icount = 0
      imnum = 1
      write (sunit,510) source_time,sfr,vrms,xrad,entropy

c      MAIN LOOP

      do 100 i=1,itmax
        otime = tstep*float(i) + source_time
        atime = stime + otime
        call rotate (ncloud,atime,0,tstep,iflag)

```



```

call rotate (nstar,atime,1,tstep,iflag)
call vcirc (ncloud,atime)
call propagate (ncloud,nstar,tstep,mst,msp,eff,sfr,iflag)
call cloud_cloud (xrad,iflag)
call energy_bal (ncloud,vrms,vact,xrad)
call geom_entropy (ncloud,entropy)

if (iflag.ne.0) then
  print*,'ERROR TERMINATION - output dumped to file'
  print*,'Terminated after ',i,' time steps'
  goto 1000
endif

write (sunit,510) otime,sfr,vact,xrad,entropy
510 format (5(1pe12.5,3x))

icount = icount + 1
if (icount.eq.dump) then
  call output (dunit,iunit,sunit,otime,imnum,vernum,iflag)
  imnum = imnum + 1
  icount = 0
endif
100 continue

c WRITE FINAL DATA TO FILES

1000 continue
if (icount.ne.0) call output (dunit,iunit,sunit,
+ tstep*float(itmax),imnum,vernum,iflag)
close (dunit)
close (iunit)
close (sunit)

c DETERMINE TIME USED FOR THIS RUN

elap = etime(runtime)
write (*,600) elap/3600.0,runtime(1)/3600.0,runtime(2)
600 format (' Total elapsed time = ',f5.2,'hr'/
+ ' User time = ',f5.2,'hr'/
+ ' System time = ',f5.1,'s'/)

end

```

Subroutines contained in collisions.f.

```

c 21/12/93 jps18 ver 1.3
c
c *****
c
c subroutine cloud_cloud (xrad,iflag)

```

```

c
c   If two clouds are within XRAD of one another then a collision
c   is deemed to have occurred.  The collisions are dealt with
c   in the manner described in my notebook (30/08/93).
c
c   INPUT VARIABLES:
c       xrad   - effective cloud radius
c
c   OUTPUT VARIABLE:
c       iflag  - return status code
c
c *****
c
c   include 'common.inc'
c   include 'neighblk.inc'
c   include 'header.inc'
c
c       integer nneigh,          ! NO. OF PARTICLES WITHIN xrad
c   +         iflag,             ! SEE ABOVE
c   +         i,j                 ! LOOP COUNTERS
c   real      xrad,              ! MEAN FREE PATH
c   +         sepdot,            ! TIME DERIVATIVE OF SEPARATION
c                                     OF PARTICLES
c   +         angvel,            ! ANGULAR SPEED OF CLOUD
c   +         r1,r2,             ! RADII
c   +         r1d,r2d,           ! TIME DERIVATIVES OF RADII
c   +         t1d,t2d,           ! TIME DERIVATIVES OF AZIMUTH
c   +         q1,q2,q3,q4,q5     ! TEMPORARY VALUES
c
c -----
c
c   SET UP NEAR-NEIGHBOUR GRIDS IF NECESSARY, ADJUSTING GRID SIZE
c
c   if (gsize.lt.xrad) then
c       gsize = xrad
c       call neighgrid (ncloud,iflag)
c       do while (iflag.ne.0)
c           if ((iflag.eq.1).or.(iflag.eq.2)) gsize = gsize*1.2
c           iflag = 0
c           call neighgrid (ncloud,iflag)
c           if (iflag.eq.3) then
c               print*,'*ERROR* gsize too large (CLOUD_CLOUD)'
c               return
c           endif
c       enddo
c   endif
c
c   CYCLE THROUGH ALL CLOUDS, TRANSFORMING TO LOCAL REST FRAME
c
c   do 10 i=1,ncloud
c       r1 = cloud(1,i)

```



```

call nearneigh(r1,cloud(2,i),cloud(3,i),0.0,xrad,nneigh,iflag)
if (iflag.ne.0) return
angvel = vrot(i)/r1           ! NEED vrot TO BE UP TO DATE
cloud(5,i) = cloud(5,i) - angvel

c   IF CLOUDS CLOSER THAN xrad THEN COLLISION MIGHT HAVE OCCURRED
c   - CHECK TO SEE IF APPROACHING IN LOCAL REST FRAME

do 20 j=1,nneigh
  r1d = cloud(4,i)
  t1d = cloud(5,i)
  r2 = cloud(1,neigh(j))
  q1 = cloud(2,neigh(j)) - cloud(2,i)
  q2 = cos(q1)
  q3 = r1*r2
  q4 = cloud(3,neigh(j)) - cloud(3,i)
  q5 = sin(q1)
  r2d = cloud(4,neigh(j))
  cloud(5,neigh(j)) = cloud(5,neigh(j)) - angvel
  t2d = cloud(5,neigh(j))
  sepdot = r1*r1d + r2*r2d - r1d*r2*q2 - r1*r2d*q2 + q3*t1d*q5
+      - q3*t2d*q5 + cloud(6,i)*q4 - cloud(6,neigh(j))*q4

c   IF CLOUDS ARE APPROACHING THEN SWAP VELOCITY VECTORS,
c   AND REDUCE MAGNITUDE BY FACTOR elas

  if (sepdot.lt.0.0) then
    q1 = cloud(4,i)
    q2 = cloud(5,i)
    q3 = cloud(6,i)
    cloud(4,i) = elas*cloud(4,neigh(j))
    cloud(5,i) = elas*cloud(5,neigh(j))
    cloud(6,i) = elas*cloud(6,neigh(j))
    cloud(4,neigh(j)) = elas*q1
    cloud(5,neigh(j)) = elas*q2
    cloud(6,neigh(j)) = elas*q3
  endif

c   RETURN TO INERTIAL FRAME

  cloud(5,neigh(j)) = cloud(5,neigh(j)) + angvel
20  continue
  cloud(5,i) = cloud(5,i) + angvel
10  continue

return
end

```

```

c      21/12/93   jps18   ver 2.2
c
c      *****
c
c      subroutine cloud_snr (istar,icloud,x)
c
c      Given that a cloud (specified by ICLLOUD) has encountered a
c      supernova remnant centred on ISTAR, this subroutine
c      calculates the velocity impulse the cloud receives from
c      the shock wave.
c
c      INPUT VARIABLES:
c      istar - star/SN number
c      icloud - cloud number
c      x      - distance between cloud and SN
c
c      *****
c
c      include 'common.inc'
c      include 'header.inc'
c
c      integer icloud,          ! SEE ABOVE
+      istar          ! SEE ABOVE
c      real x,                ! SEE ABOVE
+      drdot,         ! }
+      dthtdot,      ! } CHANGE IN VEL COMPONENTS
+      dzdot,        ! }
+      a1,a2         ! TEMPORARY VALUE
c      real*8 v,          ! SPEED GIVEN TO CLOUD
+      r1,r2,         ! RADIAL COORDINATE OF SNR/CLOUD
+      xd,           ! DISTANCE BETWEEN CLOUD AND SN
+      q1,q2,q3,q4,q5,q6 ! TEMPORARY VALUES
c
c      -----
c
c      PREVENT ERRORS DUE TO x=0
c
c      if (x.lt.1.e-6) x = 1.e-6
c
c      DETERMINE MAGNITUDE OF VELOCITY IMPULSE
c
c      v = dble(min(vmax,0.1/x))
c
c      r1 = dble(star(1,istar))
c      r2 = dble(cloud(1,icloud))
c      xd = dble(x)
c
c      USE ALGORITHM DESCRIBED IN NOTEBOOK TO CALC. INCREMENTS
c      IN VELOCITY COORDS
c
c      q1 = dble(cloud(3,icloud)-star(3,istar))/xd

```



```

q2 = 1.0d0 - q1*q1
q3 = dsqrt(q2)
q4 = (r2*r2 + xd*xd*q2 - r1*r1)/(2.d0*r2*xd*q3)
if (abs(q4).gt.1.0d0) q4 = 1.0d0      ! ROUNDING ERRORS
q5 = dsqrt(1.0d0 - q4*q4)
q6 = v*q3
a1 = cloud(2,icloud) - star(2,istar)
a2 = sign(1.0,a1)

drdot = sngl(q4*q6)
dthtdot = a2*sngl(q5*q6/r2)
dzdot = sngl(v*q1)

cloud(4,icloud) = cloud(4,icloud) + drdot
cloud(5,icloud) = cloud(5,icloud) + dthtdot
cloud(6,icloud) = cloud(6,icloud) + dzdot

return
end

c      14/10/93   jps18   ver 1.1
c
c *****
c
c      subroutine energy_bal (ncloud,vrms,v,xrad)
c
c      Computes mean dispersion velocity for clouds within an
c      annulus from RMIN to RMAX, and uses this to adjust XRAD
c      such that the system attains thermal equilibrium.
c
c      INPUT VARIABLES:
c      ncloud - number of cloud particles
c      xrad   - initial value for effective cloud radius
c      vrms   - desired value for the rms dispersion velocity
c
c      OUTPUT VARIABLES:
c      v      - achieved rms dispersion velocity
c      xrad   - adjusted value for effective cloud radius
c
c      CONTROL VARIABLES:
c      rmin   - } limiting radii of annulus
c      rmax   - }
c
c *****
c
c      include 'common.inc'

```

```

integer ncloud,           ! SEE ABOVE
+   icount,
+   i                     ! LOOP COUNTER
real   xrad,             ! SEE ABOVE
+   vrms,                ! SEE ABOVE
+   rmin,rmax,          ! LIMITING RADII OF ANNULUS
+   v                     ! RMS SPEED

data rmin,rmax / 10.0, 50.0 /
c
c -----
c
v = 0.0
icount = 0

c   CALCULATE RMS VEL. DISPERSION WITHIN ANNULUS

do 10 i=1,ncloud
  if ((cloud(1,i).ge.rmin).and.(cloud(1,i).le.rmax)) then
    v = v + cloud(4,i)**2 + cloud(6,i)**2 +
+      ((cloud(1,i)*cloud(5,i))-vrot(i))**2
    icount = icount + 1
  endif
10 continue
v = sqrt(v/float(icount))

c   SCALE EFFECTIVE CLOUD RADIUS TO MAINTAIN ENERGY STABILITY

xrad = xrad*(v/vrms)**1.7

return
end

```

Subroutines contained in data_read.f.

```

c   28/01/94   jps18   ver 7.0
c
c *****
c
c   subroutine data_read (dunit,version,iflag)
c
c   Reads data from opened main data file (on unit DUNIT)
c   according to the format specified by VERSION. This
c   subroutine can deal with data written in either '7'
c   or '701' format (see notebook 28/01/94).
c
c   INPUT VARIABLE:
c   dunit - file unit from which data is to be read
c
c   OUTPUT VARIABLES:

```



```

c      version - format version number
c      iflag   - return status code
c
c *****
c
c      include 'common.inc'
c      include 'header.inc'
c
c      integer dunit,           ! FILE UNIT
c      +      version,         ! FORMAT SPECIFIER
c      +      iflag,          ! STATUS RETURN CODE
c      +      i,j              ! COUNTERS
c
c -----
c
c      DETERMINE FILE FORMAT NUMBER
c
c      read (dunit,err=500) version
c      rewind (dunit)
c
c      LATEST FILE FORMAT
c
c      if (version.eq.701) then
c          read (dunit,err=500) version,source,ncloud,nstar,itmax,
c      +      tstep,a0,elas,vmax,mst,msp,eff,narm,
c      +      omegap,r0,p,ang,amp
c          do 10 i=1,ncloud
c              read (dunit,err=500) (cloud(j,i),j=1,7),clage(i)
c      10  continue
c          do 20 i=1,nstar
c              read (dunit,err=500) (star(j,i),j=1,6),stage(i)
c      20  continue
c          iflag = 0
c          return
c
c      OTHER SUFFICIENTLY SIMILAR FORMATS
c
c      else if (version.eq.7) then
c          read (dunit,err=500) version,source,ncloud,nstar,itmax,tstep,
c      +      a0,mst,msp,eff,narm,omegap,r0,p,ang,amp
c          do 30 i=1,ncloud
c              read (dunit,err=500) (cloud(j,i),j=1,7),clage(i)
c      30  continue
c          do 40 i=1,nstar
c              read (dunit,err=500) (star(j,i),j=1,6),stage(i)
c      40  continue
c          elas = 0.7      ! } USED CONSTANT VALUES FOR THESE PARAMETERS
c          vmax = 0.51    ! }
c          iflag = 0
c          return

```

```

c      DEFINITELY NON-COMPATIBLE FORMATS

      else
        print*, 'Incorrect version (DATA_READ)'
        iflag = 1
        return
      endif

c      ERROR RETURN

500 print*, 'Error on reading data (DATA_READ)'
    iflag = 2
    return

    end

c      23/03/94   jps18   ver 1.0
c
c      *****
c
c      subroutine sfr_read (file,sunit,t,sfr,vrms,xrad,ent,iflag)
c
c      Reads data from .sfr and .ent files where appropriate.
c      All file handling is done within the subroutine.  The
c      subroutine is able to cope with the old and new style files.
c
c      INPUT VARIABLES:
c      file - galaxy name
c      sunit - file unit to be used
c
c      OUTPUT VARIABLES:
c      t      - times
c      sfr    - star formation rates
c      vrms   - mean cloud speeds
c      xrad   - cloud cross-sections
c      ent    - entropies
c      iflag  - return status code
c
c      *****
c
c      include 'header.inc'

      integer  sunit,          ! SEE ABOVE
+           iflag,           ! SEE ABOVE
+           itype,           ! FILE TYPE
+           ntime,          ! NUMBER OF DATA POINTS IN FILE
+           idum,           ! DUMMY INTEGER

```



```

+         vernum,           ! VERSION NUMBER
+         i                 ! LOOP COUNTER
real      t(*),            ! TIME ARRAY
+         sfr(*),          ! SFR ARRAY
+         vrms(*),         ! vrms ARRAY
+         xrad(*),         ! xrad ARRAY
+         ent(*),          ! ENTROPY ARRAY
+         lnn              ! LOG OF NUMBER OF CLOUDS
character file*12,        ! SEE ABOVE
+         path*52,         ! FULL PATH
+         cdum*1           ! DUMMY CHARACTER
logical   exists          ! FUNCTION
c
c -----
c
      path = '/home/jps18/model/data/../../../../file//../../../../file//'.sfr'

c      CHECK THAT FILE EXISTS

      if (.not.exists(path)) then
        print*,'**ERROR** sfr file does not exist (SFR_READ)'
        iflag = 1
        return
      endif

c      OPEN FILE AND DETERMINE FORMAT

      open (sunit,file=path,form='formatted',status='read')
      read (sunit,'(a1)',err=999) cdum
      if (cdum.eq.'%') then
        itype = 0
      else
        itype = 1
      endif
      rewind (sunit)

c      OLD STYLE FILES

      if (itype.eq.0) then

c      READ IN SFR DATA

      read (sunit,500,err=999) ntime,idum
500  format (8x,i4/8x,i1)
      do 10 i=1,ntime
        read (sunit,510,err=999) t(i),sfr(i),vrms(i),xrad(i)
10   continue
510  format (4(1pe12.5,3x))
      read (sunit,520,err=999) source,ncloud,nstar,itmax,tstep,
+         a0,elas,vmax
520  format (a12/3(i5/),3(1pe11.4/),1pe11.4)

```

```

        if (elas.lt.1.0) then
            read (sunit,530,err=999) mst,msp,eff,narm,
+                               omegap,r0,p,ang,amp
530    format (3(1pe11.4/),i1/5(1pe11.4/))

        else          ! REALLY OLD FILES, WITHOUT elas AND vmax SET
            mst = elas
            msp = vmax
            elas = 0.7
            vmax = 0.51
            read (sunit,540,err=999) eff,narm,omegap,r0,p,ang,amp
540    format (1pe11.4/i1/5(1pe11.4/))
        endif

c      READ IN ENTROPY DATA AND CONVERT TO CORRECT FORM

        path = '/home/jps18/model/data/'//file//'/file//'.ent'
        if (exists(path)) then
            lnn = log(float(ncloud))
            open (sunit,file=path,form='formatted',status='read')
            read (sunit,'(i5)',err=999) idum
            do 20 i=2,ntime
                read (sunit,'(1pe12.5)',err=999) ent(i)
                ent(i) = lnn + ent(i)/float(ncloud)
20         continue
            ent(1) = ent(2)
            close (sunit)
        else
            do 30 i=1,ntime
                ent(i) = 0.0
30         continue
        endif

c      OR NEW STYLE FILES

        else

            read (sunit,'(i5)',err=999) vernum
            read (sunit,550) source,ncloud,nstar,itmax,tstep,a0,elas,
+                               vmax,mst,msp,eff,narm,omegap,r0,p,ang,amp
550    format (a12/3(i5/),7(1pe11.4/),i1/5(1pe11.4/))

            do 40 i=1,itmax+1
                read (sunit,560,err=999) t(i),sfr(i),vrms(i),xrad(i),ent(i)
40         continue
560    format (5(1pe12.5,3x))
            close (sunit)

        endif

```



```

return

c      ERROR ON READING

999 print*, '**ERROR** on reading data (SFR_READ)'
      iflag = 2
      return

end

c      19/04/94   jps18   ver 1.0
c
c      *****
c
c      function exists (path)
c
c      Checks to see if file exists, returning .true. if it does.
c      If the file is compressed then is is first unzipped.
c
c      INPUT VARIABLE:
c      path - full path name of file to be checked
c
c      OUTPUT VARIABLE:
c      exists - set .true. if file exists, .false. otherwise
c
c      *****
c
c      integer   iflag           ! RETURN STATUS CODE
c      character path*(*)       ! SEE ABOVE
c      logical   exists         ! SEE ABOVE
c
c      -----
c
c      CHECK TO SEE IF FILE EXISTS

      inquire (file=path,exist=exists)

c      IF NOT THEN SEE IF IT EXISTS IN ZIPPED FORM

      if (.not.exists) then
        inquire (file=path//'.gz',exist=exists)

c      UNCOMPRESS FILE IF NECESSARY

      if (exists) then
        write (*,*) 'Uncompressing data file ...'
        call io_system ('gunzip '//path//'.gz',iflag)

```

```

        if (iflag.ne.0) then
            write (*,*) 'Problem encountered'
            exists = .false.
        endif
    endif

endif

return
end

```

Subroutines contained in entropy.f.

```

c      23/03/94   jps18   ver 3.1
c
c      *****
c
c      subroutine geom_entropy (ncloud,entropy)
c
c      Calculates the geometric entropy of the galactic molecular
c      cloud by considering the integral of  $f(\ln f)$ , where  $f$  is
c      the phase space distribution function. The DF is not
c      available to us, so instead the coarse-grained DF is
c      determined using a planar 1kpc grid of 1024 cells.
c      If the clouds have already been gridded on scales of 1.0 or
c      5.0 then the existing grid is used. Otherwise, a new grid
c      is calculated. Subroutine NEIGHGRID is not called since
c      with a 5.0 grid the number of particles is likely to be
c      greater than NEIGHMAX - a problem if nearest neighbours are
c      being investigated, but not if only the number of points in
c      a cell is required.
c
c      INPUT VARIABLE:
c      ncloud - number of cloud particles
c
c      OUTPUT VARIABLE:
c      entropy - calculated value of geometric entropy
c
c      *****
c
c      include 'common.inc'
c      include 'neighbblk.inc'
c
c      integer    ncloud,                ! SEE ABOVE
+              ncell,                  ! SIZE OF ENTROPY GRID
+              nx,ny,                  ! GRID INDICES
+              ishift,                 ! OFFSET OF ENTROPY GRID
+              i,j,k,l,m               ! LOOP COUNTERS
parameter (ncell=32)
integer    egrid(ncell,ncell)        ! ENTROPY GRID

```



```

      real      entropy,          ! SEE ABOVE
+      half    ! HALF SIZE OF GRID

      intrinsic float,log
c
c -----
c
c      ZEROISE ARRAY

      do 5 i=1,ncell
        do 6 j=1,ncell
          egrid(j,i) = 0
6      continue
5      continue

c      USE PREVIOUSLY EXISTING GRID IF POSSIBLE

      if (gsize.eq.1.0) then
        do 10 j=1,ncell
          do 20 i=1,ncell
            do 30 k=1,5
              do 40 l=1,5
                do 50 m=1,ncellz
                  egrid(i,j)=egrid(i,j)+ngrid(5*(i-1)+l,5*(j-1)+k,m)
50              continue
40              continue
30              continue
20              continue
10              continue

        else if (gsize.eq.5.0) then
          ishift = (ncellx-ncell)/2
          do 60 j=1,ncell
            do 70 i=1,ncell
              do 80 m=1,ncellz
                egrid(i,j) = egrid(i,j)+ngrid(ishift+i,ishift+j,m)
80              continue
70              continue
60              continue

c      OTHERWISE SET UP NEW GRID

      else
        half = float(ncell/2)
        do 90 i=1,ncloud
          nx = int(cloud(1,i)*cos(cloud(2,i))/5.0 + half) + 1
          ny = int(cloud(1,i)*sin(cloud(2,i))/5.0 + half) + 1
          if (nx.ge.1.and.nx.le.ncell.and.ny.ge.1.and.ny.le.ncell)
+          egrid(nx,ny) = egrid(nx,ny) + 1
90        continue
      endif

```

```

c      CALCULATE ENTROPY

entropy = 0.0

do 100 i=1,ncell
  do 110 j=1,ncell
    if (egrid(j,i).gt.0) then
      entropy=entropy+float(egrid(j,i))*log(float(egrid(j,i)))
    endif
110  continue
100  continue

entropy = log(float(nccloud)) - entropy/float(nccloud)

return
end

```

Subroutines contained in init.f.

```

c      26/10/93   jps18   ver 8.4
c
c      *****
c
c      subroutine init
c
c      Initialises the main data arrays.  The clouds are placed
c      across the disc according to the radial molecular hydrogen
c      distribution, with uniform azimuthal distribution and a
c      Gaussian z-dependence.  Each cloud is given a random velocity
c      taken from a Gaussian distribution plus the appropriate
c      circular speed.  The mass of each cloud is taken from a power
c      law.  To seed the star formation a small fraction of clouds
c      are given associated star clusters, which will propagate
c      star formation on the first time step.
c
c      CONTROL VARIABLES:
c      zhgt - scale length for z-distribution of particles
c      drv  - radial spacing of escape speed table
c      ydist - radial distribution of molecular clouds
c
c      *****
c
c      include 'common.inc'
c      include 'header.inc'
c
c      integer  ipt,                ! POINT COUNTER
+             ndist,              ! POINT DIST. ARRAY SIZE
+             nvmax,              ! ESCAPE VEL. TABLE SIZE
+             isum,                ! DUMMY COUNTER

```



```

+       iage,                ! INITIAL AGE OF STARS
+       i,j                  ! LOOP COUNTERS
parameter (ndist=80,nvmax=150)
real    r,                  ! RADIUS
+       vesc(nvmax),        ! ESCAPE VELOCITY
+       rdist(ndist),      ! RADII FOR DISTRIBUTION TABLE
+       ydist(ndist),      ! RADIAL DISTRIBUTION TABLE
+       v,                  ! TOTAL VELOCITY OF PARTICLE
+       phi0,phi1,         ! POTENTIAL AT POINT
+       dr2,                ! HALF SPACING BETWEEN DIST RINGS
+       drv,                ! RADIAL SPACING FOR ESCAPE
c                               VELOCITY TABLE
+       rlow,               ! INNER RADIUS OF DIST RING
+       ampsav,             ! SAVED VALUE FOR SPIRAL AMP.
+       rnd,                ! RANDOM NUMBER
+       sum,                ! DUMMY COUNTER
+       pi2
parameter (pi2=6.2831853071796)
real*8  g05caf,g05ddf,dum,  ! RANDOM NUMBER GENERATORS
+       da0,                ! WIDTH OF VELOCITY DISTRIBUTION
+       zhgt,               ! Z-DISTRIBUTION SCALE LENGTH
+       voffset             ! OFFSET IN MEAN FOR
c                               Z-VELOCITY DISTRIBUTION

external g05caf,g05ccf,g05ddf,potential
intrinsic sngl,dbble,dsqrt,float,abs

data drv /0.5/
data zhgt /1.0d0/

data rdist /3.90625E-01,1.17188E+00,1.95312E+00,2.73438E+00,
+          3.51562E+00,4.29688E+00,5.07812E+00,5.85938E+00,
+          6.64062E+00,7.42188E+00,8.20312E+00,8.98438E+00,
+          9.76562E+00,1.05469E+01,1.13281E+01,1.21094E+01,
+          1.28906E+01,1.36719E+01,1.44531E+01,1.52344E+01,
+          1.60156E+01,1.67969E+01,1.75781E+01,1.83594E+01,
+          1.91406E+01,1.99219E+01,2.07031E+01,2.14844E+01,
+          2.22656E+01,2.30469E+01,2.38281E+01,2.46094E+01,
+          2.53906E+01,2.61719E+01,2.69531E+01,2.77344E+01,
+          2.85156E+01,2.92969E+01,3.00781E+01,3.08594E+01,
+          3.16406E+01,3.24219E+01,3.32031E+01,3.39844E+01,
+          3.47656E+01,3.55469E+01,3.63281E+01,3.71094E+01,
+          3.78906E+01,3.86719E+01,3.94531E+01,4.02344E+01,
+          4.10156E+01,4.17969E+01,4.25781E+01,4.33594E+01,
+          4.41406E+01,4.49219E+01,4.57031E+01,4.64844E+01,
+          4.72656E+01,4.80469E+01,4.88281E+01,4.96094E+01,
+          5.03906E+01,5.11719E+01,5.19531E+01,5.27344E+01,
+          5.35156E+01,5.42969E+01,5.50781E+01,5.58594E+01,
+          5.66406E+01,5.74219E+01,5.82031E+01,5.89844E+01,
+          5.97656E+01,6.05469E+01,6.13281E+01,6.21094E+01/
data ydist /0.00000E+00,0.00000E+00,0.00000E+00,0.00000E+00,

```

```

+          0.00000E+00,0.00000E+00,0.00000E+00,0.00000E+00,
+          1.73721E-04,7.71931E-04,1.65283E-03,2.70761E-03,
+          3.81031E-03,4.86009E-03,5.74095E-03,6.36298E-03,
+          6.77460E-03,7.08021E-03,7.38691E-03,7.65134E-03,
+          7.75802E-03,7.61172E-03,7.55639E-03,8.28175E-03,
+          1.05588E-02,1.43880E-02,1.88267E-02,2.27314E-02,
+          2.53732E-02,2.69629E-02,2.78643E-02,2.84570E-02,
+          2.90317E-02,2.98905E-02,3.12551E-02,3.27200E-02,
+          3.36040E-02,3.32163E-02,3.14940E-02,2.87994E-02,
+          2.55526E-02,2.23510E-02,1.99851E-02,1.93153E-02,
+          2.05766E-02,2.28049E-02,2.48201E-02,2.56864E-02,
+          2.54568E-02,2.43963E-02,2.27656E-02,2.06799E-02,
+          1.82071E-02,1.54465E-02,1.27670E-02,1.07215E-02,
+          9.87653E-03,1.01890E-02,1.09500E-02,1.13751E-02,
+          1.11209E-02,1.06762E-02,1.06477E-02,1.13459E-02,
+          1.20874E-02,1.19541E-02,1.02233E-02,7.51224E-03,
+          4.95050E-03,3.62271E-03,3.48488E-03,3.77504E-03,
+          3.70218E-03,3.03421E-03,2.13899E-03,1.42936E-03,
+          1.10643E-03,9.79321E-04,8.07080E-04,3.36053E-04/
c
c -----
c
c
c   CALCULATE ESCAPE VELOCITY TABLE

      ampsav = amp
      amp = 0.0
      do 10 i=1,nvmax
         r = drv*float(i)
         call potential (r,0.0,0.0,0.0,phil)
         vesc(i) = sqrt(-2.0*phil)
10    continue
      amp = ampsav

c
c   DISTRIBUTE POINTS ACROSS GALAXY

      isum = 0
      dr2 = 0.5*(rdist(2)-rdist(1))
      do 30 i=1,ndist
         rlow = rdist(i) - dr2
         ipt = int(ydist(i)*ncloud + 0.5)
         do 20 j=1,ipt
            cloud(1,isum+j) = rlow + 2.0*dr2*sngl(g05caf(dum))
            cloud(2,isum+j) = pi2*sngl(g05caf(dum))
            cloud(3,isum+j) = sngl(g05ddf(0.0d0,zhgt))
20    continue
         isum = isum + ipt
30    continue
      ncloud = isum

c
c   SET INITIAL VELOCITIES FROM GAUSSIAN DISTRIBUTION

```



```

da0 = dble(a0)
call vcirc (ncloud,0.0)    ! CALCULATE LOCAL CIRCULAR SPEEDS

do 40 i=1,ncloud
500  cloud(4,i) = sngl(g05ddf(0.0d0,da0))
      cloud(5,i) = (vrot(i)+sngl(g05ddf(0.0d0,da0)))/cloud(1,i)
      call potential (cloud(1,i),cloud(2,i),0.0,0.0,phi0)
      call potential (cloud(1,i),cloud(2,i),cloud(3,i),0.0,phi1)
      if (phi1-phi0.le.0.0) then    ! DUE TO ROUNDING ERRORS
          voffset = 0.0
      else
          voffset = dble(sqrt(phi1-phi0))
      endif
      if (cloud(3,i).ge.0.0) then
          cloud(6,i) = sngl(g05ddf(-voffset,da0))
      else
          cloud(6,i) = sngl(g05ddf(voffset,da0))
      endif
      v = cloud(4,i)**2+cloud(5,i)**2+cloud(6,i)**2
      if (v.gt.vesc(int(cloud(1,i)/drv))) goto 500

c    SET INITIAL MASSES AND AGES OF MOLECULAR CLOUDS

      rnd = sngl(g05caf(dum))
      do while (rnd.gt.0.772)
          rnd = sngl(g05caf(dum))
      enddo
      cloud(7,i) = 6.39e4*(rnd)**(-0.633)
      clage(i) = int(2.15*(cloud(7,i)**0.3333333) + 0.5)
40  continue

c    ASSOCIATE 0.3% OF CLOUDS WITH NEW STAR CLUSTERS

      iage = 0
      sum = 0.0
      do while (sum.lt.1.0)
          iage = iage + 1
          sum = sum + tstep
      enddo
      nstar = int(0.003*float(ncloud))
      do 50 i=1,nstar
          ipt = int(dble(ncloud)*g05caf(dum)) + 1
          do 60 j=1,6
              star (j,i) = cloud(j,ipt)
60      continue
          stage(i) = iage
50  continue

      return
      end

```

```

c      18/10/93   jps18   ver 1.2
c
c      *****
c
c      subroutine equilibrate (vrms,stime,iflag)
c
c      Allows the system to relax to dynamic equilibrium,
c      and then calculates the rms velocity dispersion.
c
c      OUTPUT VARIABLES:
c      vrms   - rms velocity dispersion
c      stime  - start time for rest of simulation
c      iflag  - return status code
c
c      *****
c
c      include 'common.inc'
c      include 'header.inc'
c
c      integer iflag,          ! SEE ABOVE
c      +      icount,         ! COUNTER
c      +      i               ! LOOP INDEX
c      real   vrms,           ! SEE ABOVE
c      +      stime,          ! SEE ABOVE
c      +      vrmsold,        ! PREVIOUS VALUE OF vrms
c      +      v,              ! RMS SPEED FOR SINGLE TIME STEP
c      +      vsum,           ! SUM OF RMS SPEEDS FOR SINGLE STEPS
c      +      diff,          ! ABSOLUTE FRACTIONAL DIFFERENCE
c      +                      ! BETWEEN SUBSEQUENT vrms
c      +      ampsav         ! STORED VALUE OF SPIRAL AMPLITUDE
c      logical cont           ! LOOP CONTROL
c
c      data icount /1/
c      data vsum,v /0.0,0.0/
c      data cont   /.true./
c
c      -----
c
c      SET SPIRAL AMPLITUDE TO ZERO TO PREVENT HEATING OF DISC
c      (CAUSED BY BAR) WHICH PREVENTS THE VELOCITY DISPERSION
c      FROM CONVERGING
c
c      ampsav = amp
c      amp = 0.0
c
c      ROTATE A FEW TIMES INITIALLY TO REDUCE TIME TAKEN
c      FOR vrms TO CONVERGE
c
c      stime = 0.0
c      do 10 i=1,int(4.0/tstep)
c          stime = stime + tstep

```

```

    call rotate (ncloud,stime,0,tstep,iflag)
    call rotate (nstar,stime,1,tstep,iflag)
    if (iflag.ne.0) return
10 continue
    call vcirc (ncloud,stime)
    vrms = 0.0

c    CALCULATE R.M.S. VELOCITY DISPERSION

    do while (cont.and.(icount.le.int(10.0/tstep)))
        do 20 i=1,ncloud
            v = v + cloud(4,i)**2 + cloud(6,i)**2 +
+            ((cloud(1,i)*cloud(5,i))-vrot(i))**2
20    continue
        v = sqrt(v/float(ncloud))          ! RMS VALUE FOR THIS TIME STEP
        vsum = vsum + v
        vrmsold = vrms                    ! AVERAGE FROM PREVIOUS TIME
        vrms = vsum/float(icount)         ! NEW AVERAGE
        diff = abs((vrmsold-vrms)/vrms)   ! FRACTIONAL DIFFERENCE

        if (diff.le.1.0e-3) then          ! EXIT ON NEXT ITERATION
            cont = .false.
        else                                ! KEEP GOING UNTIL CONVERGES
            stime = stime + tstep
            icount = icount + 1
            call rotate (ncloud,stime,0,tstep,iflag)
            call rotate (nstar,stime,1,tstep,iflag)
            if (iflag.ne.0) return
            call vcirc (ncloud,stime)
        endif

    enddo

    if (icount.gt.int(10.0/tstep)) then
        print*,'**ERROR** vel dispersion not converging (EQUILIBRATE)'
        iflag = 1
    endif

c    RESTORE SPIRAL AMPLITUDE

    amp = ampsav

    return
end

```

Subroutines contained in neighbour.f.

```

c      16/11/93   jps18   ver 5.2
c
c      *****
c
c      subroutine nearneigh (r,theta,z,ann1,ann2,nneigh,iflag)
c
c      Determines the array indices of all clouds within
c      the annulus defined by ANN1 and ANN2 centred on
c      the point (R,THETA,Z) and returns the values in
c      array NEIGH (passed via common). The distance
c      between the clouds and the central point is also
c      calculated and returned in array RNEIGH (also in common).
c      Subroutine neighgrid MUST be called before nearneigh if
c      a) the position of any of the particles has changed
c      b) the grid spacing has changed
c
c      INPUT VARIABLES:
c      r      - }
c      theta  - } coordinates of central point
c      z      - }
c      ann1   - } inner and outer radii of annulus of interest
c      ann2   - }
c
c      OUTPUT VARIABLES:
c      nneigh - number of neighbours within annulus
c      iflag  - return status code
c
c      *****
c
c      include 'common.inc'
c      include 'neighblk.inc'
c
c      integer nx,ny,nz,           ! GRID INDICES
c      +      nxinc(27),nyinc(27), ! } RELATIVE SHIFTS OF
c      +      nzinc(27),           ! } NEXT DOOR GRID CELL
c      +      nneigh,             ! SEE ABOVE
c      +      iflag,              ! SEE ABOVE
c      +      ipt,                ! POINTER
c      +      icount,             ! LOOP THIS NUMBER OF TIMES
c      +      i,j                 ! COUNTERS
c      real   r,theta,z,          ! SEE ABOVE
c      +     ann1,ann2,           ! SEE ABOVE
c      +     ann1sq,ann2sq,       ! SQUARES OF ABOVE
c      +     sep                  ! SEP. OF CLOUD AND CENTRAL POINT
c      real*8 r1,r2,             ! RADII OF CENTRAL POINT
c      +                                     AND NEARBY CLOUD
c      +     delta,               ! ANG COORD OF POINT - THETA
c      +     dcosrule             ! FUNCTION

```



```

intrinsic sin,cos,int,dble
external dcosrule

data nxinc / 0,-1, 1, 1, 0, 0,-1,-1, 0,
+           1,-1, 1, 1, 0, 0,-1,-1, 0,
+           0, 1, 1, 0, 0,-1,-1, 0, 1/
data nyinc / 0,-1, 0, 0, 1, 1, 0, 0,-1,
+           0,-1, 0, 0, 1, 1, 0, 0,-1,
+           -1, 0, 0, 1, 1, 0, 0,-1, 0/
data nzinc / 0,-1, 0, 0, 0, 0, 0, 0, 0,
+           0, 1, 0, 0, 0, 0, 0, 0, 0,
+           1, 0, 0, 0, 0, 0, 0, 0, 0/

c
c -----
c
  if (ann2.gt.gsize) then
    print*,'**ERROR** Invalid grid spacing (NEARNEIGH)'
    iflag = 1
    return
  endif

c  INITIALISE

  nneigh = 0
  ann1sq = ann1*ann1
  ann2sq = ann2*ann2

c  DETERMINE GRID CELL OF SPECIFIED POINT

  nx = int(r*cos(theta)/gsize + halfx) + 1
  ny = int(r*sin(theta)/gsize + halfx) + 1
  nz = int(z/gsize + halfz) + 1
  if (nx.gt.ncellx.or.nx.lt.1.or.ny.gt.ncellx.or.ny.lt.1) then
    print*,'**ERROR** x/y coordinate out of range (NEARNEIGH)'
    iflag = 1
    return
  else if (nz.gt.ncellz.or.nz.lt.1) then
    print*,'**ERROR** z coordinate out of range (NEARNEIGH)'
    iflag = 2
    return
  endif

c  CHECK CELLS FOR CLOUDS WITHIN RADIUS rcirc

  do 30 j=1,27
    nx = nx + nxinc(j)
    ny = ny + nyinc(j)
    nz = nz + nzinc(j)
    if (nx.eq.0.or.ny.eq.0.or.nz.eq.0.or.nx.eq.ncellx+1.or.
+     ny.eq.ncellx+1.or.nz.eq.ncellz+1) then
      icount = 0

```

```

else
  icount = ngrid(nx,ny,nz)
endif
do 40 i=1,icount
  ipt = igrd(i,nx,ny,nz)
  r1 = dble(r)
  r2 = dble(cloud(1,ipt))
  delta = dble(theta - cloud(2,ipt))
  sep = sngl(dcosrule(r1,r2,delta)) +
+      (z-cloud(3,ipt))**2
  if ((sep.gt.ann1sq).and.(sep.le.ann2sq)) then
    nneigh = nneigh + 1
    neigh(nneigh) = ipt
    rneigh(nneigh) = sqrt(sep)
  endif
40 continue
30 continue

return
end

```

```

c      15/10/93   jps18   ver 1.3
c
c *****
c
c      subroutine neighgrid (npt,iflag)
c
c      Initialises grid used by subroutine nearneigh to calculate
c      nearest neighbours. This routine must be called before
c      nearneigh if
c      a) the position of any of the particles has changed
c      b) the radius around each point in which one is
c      interested has changed
c
c      INPUT VARIABLES:
c      npt - number of particles in galaxy
c
c      OUTPUT VARIABLES:
c      iflag - return status code
c
c      The main output from this program (the arrays igrd and ngrid)
c      is passed via common 'nblk' to subroutine nearneigh, the
c      only other routine to use this data.
c *****
c
c      include 'common.inc'
c      include 'neighblk.inc'

```



```

integer    npt,                ! SEE ABOVE
+          nx,ny,nz,          ! GRID INDICES
+          iflag,             ! SEE ABOVE
+          i,j,k              ! COUNTERS

intrinsic sin,cos

c
c -----
c
c INITIALISE ARRAY

do 20 i=1,ncellz
  do 30 j=1,ncellx
    do 40 k=1,ncellz
      ngrid(k,j,i) = 0
40    continue
30    continue
20    continue
  halfx = float(ncellx/2)
  halfz = float(ncellz/2)

c CALCULATE GRID

do 10 i=1,npt
  nx = int(cloud(1,i)*cos(cloud(2,i))/gsize + halfx) + 1
  ny = int(cloud(1,i)*sin(cloud(2,i))/gsize + halfx) + 1
  nz = int(cloud(3,i)/gsize + halfz) + 1

c IF POINT OUTSIDE GRID

if (nx.gt.ncellx.or.ny.gt.ncellx.or.nx.lt.1.or.ny.lt.1) then
  iflag = 1
  return
else if (nz.gt.ncellz.or.nz.lt.1) then
  iflag = 2
  return
endif

ngrid(nx,ny,nz) = ngrid(nx,ny,nz) + 1
if (ngrid(nx,ny,nz).gt.neighmax) then ! TOO MANY POINTS
  iflag = 3
  return
endif
igrid(ngrid(nx,ny,nz),nx,ny,nz) = i
10 continue

return
end

```

Subroutines contained in output.f.

```

c      31/08/94   jps18   ver 2.5
c
c *****
c
c      subroutine output (dunit,iunit,sunit,elapsed,imnum,vernum,iflag)
c
c      Subroutine to perform the majority of output, including
c      file naming and handling.  The file for SFR, velocity
c      dispersion and geometric entropy output is only opened
c      and a head record written - the main bulk of the data
c      is written by MAIN.
c
c      INPUT VARIABLES:
c      dunit   - unit number for main dump file
c      iunit   - unit number for compressed image files
c      sunit   - unit number for SFR data
c      elapsed - elapsed time for labelling of image files
c      imnum   - image file number for naming.  If imnum.eq.0
c              then the file handling is initiated.
c      vernum  - galaxy version number
c
c      OUTPUT VARIABLE:
c      iflag   - return status code
c *****
c
c      include 'common.inc'
c      include 'header.inc'
c
c      integer  dunit,                ! SEE ABOVE
c      +       iunit,                ! SEE ABOVE
c      +       sunit,                ! SEE ABOVE
c      +       imnum,                ! SEE ABOVE
c      +       iflag,                ! SEE ABOVE
c      +       date(3),              ! TODAY'S DATE
c      +       num,                  ! FILE COUNTER
c      +       len,chr_lenb,         ! LENGTH OF HOSTNAME
c      +       vernum,              ! SEE ABOVE
c      +       i,j                    ! LOOP COUNTERS
c      integer*2 i2r,                ! SCALED RADIUS
c      +       i2tht,               ! SCALED AZIMUTH
c      +       i2z,                 ! SCALED Z
c      +       i2age                 ! AGE OF POINT
c      real     elapsed,            ! SEE ABOVE
c      +       rscale,              !}
c      +       thtscale,            !} COORDINATE SCALING FACTORS
c      +       zscale               !}
c      character path*48,          ! FULL FILE NAME
c      +       suffix*5,           ! FILE NAME SUFFIX

```



```

+          host*6,                ! MACHINE ON WHICH PROGRAM
c          IS BEING RUN
+          fdate*24              ! CURRENT DATE AND TIME
logical    ex                    ! .true. IF FILE EXISTS

integer hostnm                  ! FUNCTION

save path

data rscale, thtscale, zscale /320.0, 5000.0, 500.0/
c
c -----
c
c  INITIALISATION IF FIRST CALL TO 'OUTPUT'

if (imnum.eq.0) then
  call idate (date)
  ex = .true.
  num = 0

c  GET PATH NAME

  do while (ex)
    num = num + 1
    write (path,100) date(1),date(2),date(3)-1900,num,
+                   date(1),date(2),date(3)-1900,num
100    format ('/home/jps18/model/data/gal',3(i2.2),'_',i2.2,
+           '/gal',3(i2.2),'_',i2.2)
    inquire (file=path//'.sfr',exist=ex)
    if (num.eq.99) ex = .false.
  enddo

  write (*,120) fdate(),path(37:48)      ! WRITE TO LOG FILE
120  format (/a24,3x,a12)

c  WRITE PATH TO FILE TO BE USED LATER BY SCRIPT chain

  iflag = hostnm(host)
  len = chr_lenb(host)
  open (sunit,file='.gal'//host(len:len),form='formatted')
  write (sunit,*) path(1:35)
  close (sunit)

c  CREATE DIRECTORY

  call io_system ('mkdir '//path(1:35),iflag)

c  OPEN .sfr FILE AND WRITE HEADER

  open (sunit,file=path//'.sfr',form='formatted')
  write (sunit,'(i5)') vernum

```

```

        write (sunit,500) source,ncloud,nstar,itmax,tstep,a0,elas,
+           vmax,mst,msp,eff,narm,omegap,r0,p,ang,amp
500  format (a12/3(i5/),7(1pe11.4/),i1/5(1pe11.4/))
        open (20,file=path//'.rad',form='unformatted')

        return

c    START HERE IF NOT FIRST CALL TO output

        else if (imnum.gt.99) then
            print*,'Too many output files'
            iflag = 2
            return
        endif

c    MOVE OLD DUMP FILE

        if (imnum.gt.1) then
            write (suffix,105) imnum-1
105  format ('.dp',i2.2)
            call rename (path,path//suffix)
        endif

c    OUTPUT TO DUMP FILE

        open (dunit,file=path,form='unformatted')
        write (dunit) vnum,source,ncloud,nstar,itmax,tstep,a0,elas,
+           vmax,mst,msp,eff,narm,omegap,r0,p,ang,amp
        do 10 i=1,ncloud
            write (dunit) (cloud(j,i),j=1,7),clage(i)
10  continue
        do 20 i=1,nstar
            write (dunit) (star(j,i),j=1,6),stage(i)
20  continue
        close (dunit)

c    OUTPUT TO IMAGE FILE

        write (suffix,110) imnum
110  format ('.im',i2.2)
        open (iunit,file=path//suffix,form='unformatted')
        write (iunit) vnum,source,ncloud,nstar,itmax,tstep,a0,elas,
+           vmax,mst,msp,eff,narm,omegap,r0,p,ang,amp
        write (iunit) elapsed,rscale,thtscale,zscale
        do 30 i=1,nstar
            i2r = int(rscale*star(1,i))
            i2tht = int(thtscale*star(2,i))
            i2z = int(zscale*star(3,i))
            i2age = stage(i)
            write (iunit) i2r,i2tht,i2z,i2age
30  continue

```



```
close (iunit)
```

```
return
```

```
end
```

Subroutines contained in propagate.f.

```
c      21/12/93   jps18   ver 8.2
c
c *****
c
c      subroutine propagate (ncloud,nstar,tstep,mst,msp,eff,sfr,iflag)
c
c      Propagates star formation throughout galaxy.
c
c      INPUT VARIABLES:
c      ncloud - number of cloud particles
c      nstar  - number of star particles
c      tstep  - simulation time step
c      mst    - critical mass for stimulated star formation
c      msp    - critical mass for spontaneous star formation
c      eff    - cloud disruption factor
c
c      OUTPUT VARIABLES:
c      sfr    - star formation rate
c      iflag  - return status code
c *****
c
c      include 'common.inc'
c      include 'neighblk.inc'
c
c      integer ncloud,          ! SEE ABOVE
+      nstar,                  ! SEE ABOVE
+      nneigh,                 ! NO. NEIGHBOURS FOR ANY GIVEN POINT
+      kpre,                   ! NO. TIME STEPS BEFORE STAR EXPLODES
+      iage,                   ! AGE OF INDIVIDUAL STAR, UNITS tstep
+      ipt,                    ! INDEX COUNTER
+      nnew,                   ! NUMBER OF NEW CLUSTERS CREATED
c                               ON THIS STEP
+      agemax,                 ! MAX AGE OF STARS KEPT IN ARRAY
+      iflag,                  ! STATUS RETURN CODE
+      icount,                 ! COUNTER
+      i,k,                    ! LOOP COUNTERS
c      real tstep,             ! SEE ABOVE
+      mst,msp,                ! SEE ABOVE
+      eff,                    ! SEE ABOVE
+      rsn(0:50),              ! RADIUS OF SNR AS FUNCTION OF TIME
+      prob,                   ! PROBABILITY OF STAR FORMATION
+      sfr,                    ! SEE ABOVE
```

```

+      age,          ! AGE OF STAR, UNITS 10**7 YRS
+      sum,          ! SUM OF tstep
+      geom
real*8  g05caf,dum   ! RANDOM NUMBER GENERATOR
logical first

intrinsic exp,dbble,sngl,int
external  neighgrid,nearneigh,g05caf

save dum,first,kpre,agemax,rsn

data first  /.true./
data geom  /2.3873241463784300453e-01/
c
c -----
c
c
c   IF FIRST CALL TO propagate THEN SET UP rsn TABLE

if (first) then
  kpre = 0
  k = 0
  sum = 0.0
  do while (sum.lt.1.0)
    kpre = kpre + 1
    sum = sum + tstep
  enddo
  kpre = kpre - 1
  rsn(0) = 0.0
  do while (sum.le.2.0)
    k = k + 1
    rsn(k) = (float(k)*tstep)**0.4
    sum = sum + tstep
  enddo
  first = .false.
  agemax = int(13.0/tstep)
endif

c   INITIALISE FOR THIS TIME ROUND

nnew = 0
gsize = 1.0

c   SET UP NEIGHBOUR GRIDS, ADJUSTING GRID SIZE TO OPTIMISE

call neighgrid (ncloud,iflag)
i = 1
do while ((iflag.ne.0).and.(i.lt.6))
  if ((iflag.eq.1).or.(iflag.eq.2)) then
    gsize = gsize*2.0
  else if (iflag.eq.3) then
    gsize = gsize*0.5
  end if
  i = i + 1
enddo

```



```

        endif
        iflag = 0
        i = i + 1
        call neighgrid (ncloud,iflag)
    enddo
    if (i.eq.6) then
        print*,'*ERROR* unable to set up neighbour grids (PROPAGATE)'
        iflag = 1
        return
    endif

c    UPDATE MASSES OF CLOUDS

    call cloud_mass (ncloud,tstep)

c    CLOUD - SUPERNOVA INTERACTIONS

    icount = nstar
    iage = stage(icount)
    age = tstep*float(iage)

    do while (age.lt.2.0)
        if (age.ge.1.0) then
            call nearneigh (star(1,icount),star(2,icount),
+                star(3,icount),rsn(iage-kpre-1),
+                rsn(iage-kpre),nneigh,iflag)
            if (iflag.ne.0) return

            do 10 k=1,nneigh
                ipt = neigh(k)

c                PERCOLATION

                prob = geom*cloud(7,ipt)/mst
                if (g05caf(dum).lt.prob) then
                    cloud(7,ipt) = cloud(7,ipt)*eff
                    clage(ipt) = 0
                    nnew = nnew + 1
                    nstar = nstar + 1
                    stage(nstar) = 0
                    do 20 i=1,6
                        star(i,nstar) = cloud(i,ipt)
20                continue

                    write (20) star(1,nstar)

                endif

c                HEAT INPUT TO ISM - CLOUD/SNR COLLISIONS

                call cloud_snr (icount,ipt,rneigh(k))

```

```

10     continue
      endif

c     NEXT SNR

      icount = icount - 1
      iage = stage(icount)
      age = timestep*float(iage)
    enddo

c     SPONTANEOUS STAR FORMATION

    do 30 i=1,ncloud
      if (clage(i).ne.0) then
        prob = timestep*cloud(7,i)/msp
        if (g05caf(dum).lt.prob) then
          cloud(7,i) = cloud(7,i)*eff
          clage(i) = 0
          nnew = nnew + 1
          nstar = nstar + 1
          stage(nstar) = 0
          do 40 k=1,6
            star(k,nstar) = cloud(k,i)
40          continue

          write (20) star(1,nstar)

          endif
        endif
      endif
    30 continue

c     GET RID OF OLD STARS FROM ARRAY

      icount = 1
      do while ((stage(icount).eq.agemax).and.(icount.le.nstar))
        icount = icount + 1
      enddo
      icount = icount - 1
      do 70 i=icount+1,nstar
        stage(i-icount) = stage(i)
        do 80 k=1,6
          star(k,i-icount) = star(k,i)
80        continue
70      continue
      nstar = nstar - icount

c     INCREMENT AGES

    do 50 i=1,ncloud
      clage(i) = clage(i) + 1

```



```

50 continue
  do 60 i=1,nstar
    stage(i) = stage(i) + 1
60 continue

sfr = float(nnew)/float(ncloud)

return
end

c      02/11/93   jps18   ver 2.1
c
c *****
c
c      subroutine cloud_mass (ncloud,tstep)
c
c      Increments cloud masses due to accretion from HI, as
c      described in notebook (16/09/93).
c
c      INPUT VARIABLES:
c      ncloud - number of cloud particles
c      tstep - simulation time step
c
c *****
c
c      include 'common.inc'
c
c      integer ncloud,          ! SEE ABOVE
+      i              ! LOOP COUNTER
c      real    tstep,          ! SEE ABOVE
+      gamma,         ! COEFFICIENT
+      dm,           ! MASS INCREMENT
+      v,            ! SPEED OF CLOUD
+      q1,           ! TEMPORARY VALUE
+      hldensity     ! HI DENSITY AT GIVEN RADIUS
c
c      data gamma /7.0e-5/
c
c -----
c
c      do 10 i=1,ncloud
c      v = sqrt(cloud(4,i)**2 + (cloud(1,i)*cloud(5,i)-vrot(i))**2
+      + cloud(6,i)**2)
c      q1 = (tstep*gamma*hldensity(cloud(1,i))*v)**3

```

```

        dm = q1*0.111111111*(float(clage(i))**2)
        cloud(7,i) = cloud(7,i) + dm
10 continue

return
end

c      29/06/93   jps18   ver 1.0
c
c *****
c
c      real function hldensity (r)
c
c      Interpolates from HI cloud given by Burton in 'Galactic
c      and Extragalactic Radio Astronomy' to return HI density
c      at any given radius.
c
c      INPUT VARIABLE:
c      r - radius
c *****
c
c      integer nbin,          ! NO. OF HI DATA POINTS
c      +      i              ! LOOP COUNTER
c      parameter (nbin=30)
c      real    r,            ! SEE ABOVE
c      +      rh1(nbin),     ! RADIUS VALUES FOR DISTRIBUTION
c      +      h1(nbin),      ! HI DISTRIBUTION
c      +      dh12(nbin),    ! 2nd DERIV OF DISTRIBUTION
c      +      d1,d2,         ! 1st DERIV AT BOUNDARY POINTS
c      +      dum,           ! TEMPORARY VALUE
c      +      conv           ! CONVERSION FROM cm-3 TO L-3
c      parameter (conv=1.96e5)
c      logical first
c
c      save first,rh1,h1,dh12
c      data first /.true./
c
c      data rh1/0.00, 0.75, 1.25, 1.75, 2.25, 2.75, 3.25, 3.75,
c      +      4.25, 4.75, 5.25, 5.75, 6.25, 6.75, 7.25, 7.75,
c      +      8.25, 8.75, 9.25, 9.75, 10.25, 10.75, 11.25, 11.75,
c      +      12.25, 12.75, 13.25, 13.75, 14.25, 14.75 /
c      data h1 /0.00, 0.001, 0.04, 0.085, 0.13, 0.17, 0.20, 0.22,
c      +      0.30, 0.34, 0.40, 0.38, 0.33, 0.33, 0.38, 0.40,
c      +      0.38, 0.32, 0.32, 0.41, 0.40, 0.25, 0.24, 0.33,
c      +      0.37, 0.35, 0.26, 0.16, 0.10, 0.07 /
c
c -----
c
c

```

```

c      SET UP SPLINE INTERPOLATION IF FIRST CALL TO FUNCTION

      if (first) then
        do 10 i=1,nbin
          rh1(i) = rh1(i)*5.0
          h1(i) = conv*h1(i)
10      continue
        d1 = (h1(2)-h1(1))/(rh1(2)-rh1(1))
        d2 = (h1(nbin)-h1(nbin-1))/(rh1(nbin)-rh1(nbin-1))
        call spline (rh1,h1,nbin,d1,d2,dh12)
        first = .false.
      endif

c      USE CUBIC SPLINE INTERPOLATION TO CALCULATE HI DENSITY
c      AT GIVEN RADIUS

      call splint (rh1,h1,dh12,nbin,r,dum)
      if (dum.lt.0.0) dum = 0.0
      hldensity = dum

      return
      end

```

Subroutines contained in rotate.f.

```

c      26/10/93   jps18   ver 7.1
c
c      *****
c
      subroutine rotate (npt,stime,type,tstep,iflag)
c
c      Uses subroutine bsstep to compute the new position of
c      each of the particles. For information on the use of
c      bsstep refer to 'Numerical Recipes', Press et al.,
c      2nd edition, chpt 16
c
c      INPUT VARIABLES:
c      npt   - number of particles
c      stime - initial time
c      type  - type of particles to be rotated (0=cloud, 1=star)
c      tstep - total time through which particle is to be integrated
c
c      OUTPUT VARIABLES:
c      iflag - return status code
c
c      CONTROL VARIABLE:
c      eps   - integration tolerance
c
c      *****
c

```

```

include 'common.inc'

integer npt,          ! SEE ABOVE
+   type,            ! SEE ABOVE
+   iflag,           ! SEE ABOVE
+   i,k              ! COUNTERS
real   timestep,     ! SEE ABOVE
+   eps,             ! SEE ABOVE
+   time,            ! TIME FOR PARTICLE AFTER EACH INT STEP
+   stime,          ! SEE ABOVE
+   y(6),            ! INTEGRATION VECTOR
+   dydt(6),        ! DIFFERENTIAL OF INTEGRATION VECTOR
+   yscal(6),       ! ERROR SCALING VECTOR
+   dt,              ! TIME STEP FOR NEXT INTEGRATION
+   dtdid,          ! TIME STEP ACHIEVED
+   dtnext,         ! MAX TIME STEP NEXT INTEGRATION
+   pi2
parameter (pi2=6.2831853071796)

intrinsic float
external bsstep,derivs

data eps /1.e-3/
c
c -----
c
do 10 i=1,npt

c   SET INITIAL CONDITIONS FOR THIS POINT

    if (type.eq.0) then
        do 5 k=1,6
            y(k) = cloud(k,i)
5       continue
    else
        do 6 k=1,6
            y(k) = star(k,i)
6       continue
    endif
    time = stime
    dt = timestep

c   CALCULATE NEW POSITION WITH TOTAL TIME STEP OF timestep

    do while (dt.gt.3.0e-5)
        call derivs (time,y,dydt)
        do 30 k=1,6
            yscal(k) = abs(y(k))+abs(dt*dydt(k))+1.e-30
30       continue
        call bsstep (y,dydt,6,time,dt,eps,yscal,dtdid,dtnext,
+                   derivs,iflag)

```



```

        dt = dtnext
        if (iflag.ne.0) then          ! GIVE UP ON THIS INTEGRATION
            dt = -9.9e10
            iflag = 0
        endif
        if (time+dt-stime.ge.tstep) dt = tstep - (time-stime)
    enddo

c    REASSIGN DATA ARRAY

        do while (y(2).ge.pi2)
            y(2) = y(2) - pi2
        enddo
        do while (y(2).lt.0.0)
            y(2) = y(2) + pi2
        enddo

        if (type.eq.0) then
            do 40 k=1,6
                cloud(k,i) = y(k)
40         continue
            else
                do 50 k=1,6
                    star(k,i) = y(k)
50         continue
            endif

10 continue

        return
        end

c    23/08/93   jps18   ver 2.0
c
c    *****
c
c    subroutine derivs (t,y,dydt)
c
c    Subroutine required by bsstep to calculate the derivative
c    of the coordinate vector.
c
c    INPUT VARIABLES:
c        t      - time
c        y      - coordinate vector
c
c    OUTPUT VARIABLE:
c        dydt  - derivative of y with respect to t
c
c    *****

```

```

c      real t,                ! SEE ABOVE
+      y(*),                ! SEE ABOVE
+      dydt(*),            ! SEE ABOVE
+      dpdr,dpdtht,dpdz    ! DERIVATIVES OF POTENTIAL
c                               W.R.T. r, theta & z
      external dphi        ! CALCULATES PARTIAL DERIVATIVES
c
c -----
c
      dydt(1) = y(4)
      dydt(2) = y(5)
      dydt(3) = y(6)

      call dphi (y(1),y(2),y(3),t,dpdr,dpdtht,dpdz)
      dydt(4) = (y(1)*y(5)*y(5)) - dpdr
      dydt(5) = -(2.*y(4)*y(5)+(dpdtht/y(1)))/y(1)
      dydt(6) = -dpdz

      return
      end

c      17/11/93   jps18   ver 2.3
c
c *****
c
      subroutine dphi (r,theta,z,t,dpdr,dpdtht,dpdz)
c
c      Returns the values for the partial derivatives of the
c      overall potential at any given point in space and time.
c      N.B. Subroutine POT_INIT must be called before this
c      subroutine is used.
c
c      INPUT VARIABLES:
c      r      - radial position
c      theta  - angular position
c      z      - coordinate perpendicular to plane
c      t      - time required
c
c      OUTPUT VARIABLES:
c      dpdr   - partial derivative w.r.t. r
c      dpdtht - partial derivative w.r.t. theta
c      dpdz   - partial derivative w.r.t. z
c
c *****
c
      include 'header.inc'

```



```

include 'potential.inc'

real r,theta,z,          ! SEE ABOVE
+   t,                  ! SEE ABOVE
+   dpdr,               ! SEE ABOVE
+   dpdtht,            ! SEE ABOVE
+   dpdz,               ! SEE ABOVE
+   phi,                ! POTENTIAL
+   dr1,dr2,dr3,dr4,   ! COMPONENTS OF dpdr
+   dz1,dz2,dz3,       ! COMPONENTS OF dpdz
+   ph1,ph2,ph3,ph4,   ! COMPONENTS OF POTENTIAL
+   q1,q2,q3,q4,q5,q6,q7, !} TEMPORARY VALUES
+   q8,q9,q10,q11,q12,q13, !}
+   fn,                 ! NUMBER OF ARMS
+   pi

parameter (pi=3.1415926535897)

intrinsic sin,cos,log
c
c -----
c
c ENSURE r IS POSITIVE

if (r.lt.0.0) then
  r = abs(r)
  theta = theta + pi
endif

c CENTRAL BULGE COMPONENT

q1 = r*r
q2 = z*z
q4 = 1.0/(sqrt(q1+q2+b1sq))**3
dr1 = gm1*r*q4
dz1 = gm1*z*q4

c DISC COMPONENT

q4 = sqrt(q2+b2sq)
q5 = a2+q4
q6 = q5*q5
q7 = 1.0/(sqrt(q1+q6))**3
dr2 = r*gm2*q7
dz2 = z*gm2*q5*q7/q4

c HALO COMPONENT

q3 = q1 + q2
q4 = q3**0.01
q5 = sqrt(q3)
q6 = q4*q5

```

```

q7 = q4/q5
q8 = gm3*q7*a3_202/(1.0+q6*a3_102)
dr3 = r*q8
dz3 = z*q8

c   SPIRAL COMPONENT

fn = float(narm)
q4 = amp*r
q5 = (r/r0)**p
q6 = 1.0 + q5
q8 = fn*(theta-t*omegap+log(q6)*rtang/p)
q9 = cos(q8)
q10 = q1 + a4sq
q11 = q10*q10
q12 = 1.0/q11
q13 = sin(q8)

dr4 = -2.*q4*q9*q12+q4*q13*fn*q5/q6*rtang*q12+
+      4.*amp*q1*r*q9/q11/q10
dpdtht = amp*q1*q13*fn*q12

c   SUM ALL CONTRIBUTIONS

dpdr = dr1 + dr2 + dr3 + dr4
dpdz = dz1 + dz2 + dz3

return

c
c   06/11/93   jps18   ver 2.1
c
c   *****
c
c   entry potential (r,theta,z,t,phi)
c
c   Returns value of potential at point (r,theta,z) and at time t.
c
c   INPUT VARIABLES:
c       r      }
c       theta  } - coordinates
c       z      }
c       t      } - time
c
c   OUTPUT VARIABLES:
c       phi    } - potential
c
c   *****
c

```



```

c      CENTRAL BULGE COMPONENT

      q1 = r*r
      q2 = z*z
      ph1 = -gm1/sqrt(q1+q2+b1sq)

c      DISC COMPONENT

      ph2 = -gm2/sqrt(q1+(a2+sqrt(q2+b2sq))**2)

c      HALO COMPONENT

      q3 = sqrt(q1+q2)
      q4 = (q3/a3)**1.02
      q5 = 1.0 + q4
      q6 = -gm3*q4/a3/q5
      q7 = 1.02*a3
      q8 = -gm3*(log(q5)-1.02/q5)/q7
      q9 = 1.0 + 500.0/a3
      q10 = gm3*(log(q9)-1.02/q9)/q7
      ph3 = q6 + q8 + q9

c      SPIRAL COMPONENT

      q5 = (r/r0)**p
      q6 = 1.0 + q5
      q8 = float(narm)*(theta-t*omegap+log(q6)*rtang/p)
      q9 = cos(q8)
      q10 = (q1 + a4sq)**2
      ph4 = -amp*q1*q9/q10

c      SUM COMPONENTS

      phi = ph1 + ph2 + ph3 + ph4

      return
      end

c      06/11/93   jps18   ver 1.0
c
c      *****
c
c      subroutine pot_init
c
c      Initialises common block for potential calculations by
c      defining constants.
c
c      *****
c
c

```

```

include 'header.inc'
include 'potential.inc'

data a2,a3,a4,b1,b2 / 26.59, 60.0, 35.0, 1.937, 1.25 /
data gm1,gm2,gm3    / 7.93e2, 4.81e3, 6.02e3 /
c
c -----
c
c
a4sq = a4*a4
b1sq = b1*b1
b2sq = b2*b2

a3_202 = a3**(-2.02)
a3_102 = a3**(-1.02)

rtang = 1.0/tand(ang)

return
end

c
c 24/09/93   jps18   ver 1.0
c
c *****
c
c   subroutine vcirc (ncloud,t)
c
c   Calculates circular speed for each cloud particle, and
c   stores results in array VROT passed via common 'vrotblk'.
c
c   INPUT VARIABLES:
c   ncloud - number of cloud particles
c   t      - simulation time
c
c *****
c
c   include 'common.inc'

integer ncloud,          ! SEE ABOVE
+      i                ! LOOP COUNTER
real    t,              ! TIME
+      dpdr,dpdtht,dpdz ! POTENTIAL DERIVATIVES
c
c -----
c
c

```



```

do 10 i=1,ncloud
  call dphi (cloud(1,i),cloud(2,i),cloud(3,i),t,
+          dpdr,dpdtht,dpdz)
  vrot(i) = sqrt(dpdr*cloud(1,i))
10 continue

return
end

```

Library routines

```

c      25/11/92   jps18   ver 1.0
c
c *****
c
c      function dcosrule (r1,r2,theta)
c
c      Evaluates a**2 where
c      a**2 = r1**2 + r2**2 -2*r1*r2*cos(theta)
c      Routine uses double precision.
c
c *****
c
c      real*8 r1,r2,theta,dcosrule
c      intrinsic dcos
c
c      dcosrule = (r1*r1)+(r2*r2)-(2.d0*r1*r2*dcos(theta))
c      return
c      end

c      05/05/93   jps18   ver 1.1
c
c *****
c
c      integer function fphandler (sig,code,sigcontext,addr)
c
c      Floating point exception handler. The type and address of any
c      exception is printed to standard output. The hex address can
c      be interpreted by running the program within the debugger and
c      setting a breakpoint using stopi at 0x[hex address].
c
c *****
c
c      integer sig,code,sigcontext(5)
c      integer addr

```

```
character*9 excep(49:53)
data excep /'INEXACT  ', 'DIV ZERO ', 'UNDERFLOW',
+          'INVALID ', 'OVERFLOW '/
c
c -----
c
write (*,11) excep(loc(code)/4),loc(addr)
11 format ('ieee exception ',a9,' occurred at address ',z8)

return
end
```



Include files.

```

c   30/08/93  jps18  ver 7.0
c
c   COMMON.INC
c
c   Declarations for main data common blocks

integer  nclmax,          ! MAX NUMBER OF CLOUD PARTICLES
+        nstmax          ! MAX NUMBER OF STAR PARTICLES
parameter (nclmax=32750,nstmax=32750)
integer  clage(nclmax),  ! AGES OF CLOUD PARTICLES
+        stage(0:nstmax) ! AGES OF STAR PARTICLES
real     cloud(7,nclmax), ! COORDINATES AND MASSES OF CLOUDS
+        star(6,nstmax)  ! COORDINATES OF STARS

common /clblk/ cloud,clage
common /stblk/ star,stage

c   Declarations for circular rotation speed table

real     vrot(nclmax)

common /vrotblk/ vrot

c   21/12/93  jps18  ver 6.2
c
c   HEADER.INC
c
c   Declarations for common block containing header information

integer  ncloud,        ! NUMBER OF CLOUDS
+        nstar,         ! NUMBER OF STARS
+        itmax,        ! NUMBER OF TIME STEPS REQUIRED
+        dump,         ! OUTPUT EVERY dump TIMESTEPS
+        narm          ! NUMBER OF SPIRAL ARMS
real     tstep,        ! SIMULATION TIME STEP
+        a0,           ! TURBULENT GAS VELOCITY
+        elas,        ! ELASTICITY OF CLOUD-CLOUD INTERACTIONS
+        vmax,        ! MAX SPEED GAIN FROM CLOUD-SNR INTERACTIONS
+        mst,         ! CRITICAL MASS FOR STIMULATED SF
+        msp,         ! CRITICAL MASS FOR SPONTANEOUS SF
+        eff,         ! CLOUD DISRUPTION FACTOR
+        omegap,      ! SPIRAL PATTERN SPEED
+        p,           ! POWER OF SPIRAL SWITCH-OVER
+        ang,         ! SPIRAL PITCH ANGLE
+        amp,         ! SPIRAL AMPLITUDE
+        r0           ! SPIRAL SWITCH-OVER RADIUS
character source*12 ! NAME OF SOURCE FILE

```

```

common /hdblkc/ tstep,a0,elas,vmax,mst,msp,eff,omegap,p,ang,amp,
+           r0,ncloud,nstar,itmax,narm,dump,source

c      06/11/93   jps18   ver 2.0
c
c      POTENTIAL.INC
c
c      Declarations for parameters describing potential

real a2,a3,a4,
+     b1,b2,
+     gm1,gm2,gm3,
+     a4sq,b1sq,b2sq,
+     a3_202,a3_102,
+     rtang

common /potblk/ a2,a3,a4,b1,b2,gm1,gm2,gm3,
+           a4sq,b1sq,b2sq,a3_202,a3_102,rtang

c      15/10/93   jps18   ver 2.1
c
c      NEIGHBLK.INC
c
c      Declarations for neighbour common blocks.
c      N.B. ncellx and ncellz MUST be even

integer neighmax,           ! MAX NO. POINTS IN ONE GRID CELL
+     ncellx,               ! NO. OF CELLS IN X/Y DIRECTION
+     ncellz                ! NO. OF CELLS IN Z DIRECTION
parameter (neighmax=50,ncellx=160,ncellz=30)

integer neigh(5*neighmax)  ! ARRAY OF NEIGHBOUR INDICES
integer*2 igrd(ncellx,ncellx,ncellz), ! POINT INDICES
+     ngrid(ncellx,ncellx,ncellz) ! NO. POINTS IN EACH CELL

real rneigh(5*neighmax), ! ARRAY OF NEIGHBOUR DISTANCES
+     halfx,              ! HALF SIZE OF GRID IN PLANE
+     halfz,              ! HALF SIZE OF GRID PERP. TO PLANE
+     gsize               ! GRID SPACING

common /nblk1/ neigh
common /nblk2/ igrd,ngrid
common /nblk3/ rneigh,halfx,halfz,gsize

```



makefile for entire program.

```
# 13/09/94   jps18   ver 1.3

# Makefile for program galaxy.  This version replaces the
# earlier makfile, and will hopefully be easier to update
# as the program evolves.  Simply update the macro lists with
# the new subroutines, compiler options etc.
#
# 13/09/94   ver 2.0   SOLARIS

PROGRAM= galaxy
SOURCES= model.f init.f rotate.f data_read.f output.f \
propagate.f collisions.f neighbour.f entropy.f
INCLUDE= common.inc header.inc neighblk.inc potential.inc
FFLAGS=-u -C -O4 -dalign -cg92 -libmil
ULIBS=  /home/jps18/library/libfp.a /home/jps18/library/libnr.a
SLIBS= -lnag `iolink`

# From here onwards nothing should need to be changed.

OBJECTS= $(SOURCES:.f=.o)
.SUFFIXES: .prj
.KEEP_STATE:

$(PROGRAM) : $(OBJECTS) $(INCLUDE) $(ULIBS)
$(LINK.f) $(OBJECTS) $(ULIBS) $(SLIBS) -o $@

$(ULIBS) : FORCE
cd $(@D) ; $(MAKE) $(@F) "FFLAGS=$(FFLAGS)"

FORCE :

PRJS=$(SOURCES:.f=.prj)
check : $(PRJS)
ftnchek $(PRJS)
.f.prj :
ftnchek -project -noextern -library $<
```

References

Numerical Algorithms Group Limited, 1993, *NAG Fortran Library Manual*, Mark 16
 Press W. H., Teukolsky S. A., Vetterling W. T., Flannery B. P., 1992, *Numerical Recipes in FORTRAN*, Cambridge University Press, Cambridge, 2nd edn.

Appendix C

Classification of galaxies

There are many classification schemes in common usage. I will not attempt here to discuss the relative merits of each scheme – Mihalas & Binney (1981) give a review in their book to which I refer the reader for further information. Instead I will give only an outline of each scheme and how to convert between them.

The most widely used scheme is that due to Hubble (1936), and is illustrated below in Fig. C.1. The ellipticals (early-type) are classed according to their sphericity, and this system has not been subsequently modified by other authors. Spiral galaxies (late-type) are divided according to the relative size of the bulge and the resolution and pitch angle of the arms. This approach to spiral galaxies, with their far greater range of morphologies is somewhat limited and has attracted a number of attempts to improve upon it.

De Vaucouleurs (1959) in his Revised system introduced several new features: (i) additional stages (e.g. Sd, Im) to supplement the Hubble scheme, (ii) a redesignation of normal galaxies as ‘SA’, with ‘SB’ used for clearly barred galaxies, and ‘SAB’ for those which are somewhat ambiguous and (iii) additional labels r and s for spiral and lenticular galaxies which are either ring- or s-shaped. The classification is completed by one or two lower case letters defining the tightness

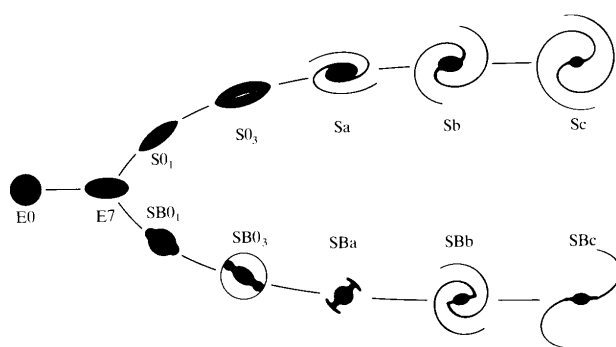


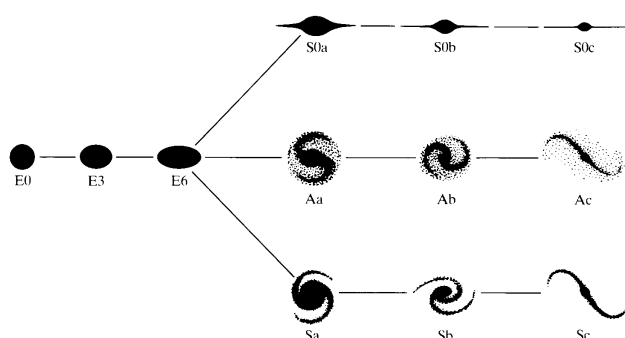
Figure C.1

The Hubble sequence of galactic morphologies. The diagram differs slightly from Hubble's original since it shows various stages of lenticular galaxies between the ellipticals and spirals. Illustration reproduced from Mihalas & Binney (1981).



Table C.1. The Revised Hubble sequence. Table reproduced from de Vaucouleurs *et al.* (1991).

Classes	Families	Varieties	Stages	T	Type	
Ellipticals		Compact		-6	cE	
			Elliptical (0–6)	-5	E0	
			Intermediate	-5	E0–1	
		“cD”	-4	E ⁺		
Lenticulars				-2	S0	
	Ordinary				SA0	
	Barred				SB0	
	Mixed				SAB0	
		Inner ring			S(r)0	
		S-shaped			S(s)0	
		Mixed			S(rs)0	
			Early	-3	S0 ⁻	
			Intermediate	-2	S0 ^o	
			Late	-1	S0 ⁺	
Spirals	Ordinary				SA	
					SB	
					SAB	
		Mixed				SAB
			Inner ring			S(r)
			S-shaped			S(s)
			Mixed			S(rs)
				0/a	0	S0/a
				a	1	Sa
				ab	2	Sab
				b	3	Sb
				bc	4	Sbc
				c	5	Sc
			cd	6	Scd	
			d	7	Sd	
			dm	8	Sdm	
			m	9	Sm	
Irregulars	Ordinary				IA	
					IB	
					IAB	
			S-shaped			I(s)
				Non-Magellanic	90	I0
				Magellanic	10	Im
		Compact		11	cI	

**Figure C.2**

The DDO system of galaxy classification. Illustration reproduced from Mihalas & Binney (1981).

of the spiral arms, similar to the original Hubble system. Table C.1 illustrates the extended system, and Table C.2 provides a correspondence between the the Revised and Hubble schemes. The T-types are simply a numeric scale corresponding to the Revised classification.

The Yerkes system (Morgan 1970) classifies galaxies according to their degree of central concentration only, in an attempt to clarify an overlapping of Hubble classes when considering the integrated spectra of the nuclear region. The Yerkes classification runs $k \rightarrow a$ with k representing the most centrally concentrated galaxies. This is followed by a capital letter representing the galaxy type (Spiral, Barred spiral, Elliptical, Irregular, Rotationally symmetric but without obvious spiral or elliptical form and finally those with an elliptical-like nucleus and a Diffuse envelope) together with a number indicating the sphericity in the range 1–7 (1 = spherical).

The DDO system, developed by van den Bergh (1976) at the David Dunlap Observatory, combines features of both the Hubble and Yerkes schemes. This time a three-pronged ‘tuning fork’ arrangement is adopted (Fig. C.2) with a new ‘anaemic spiral’ (i.e. gas poor) type introduced in parallel to the lenticulars and normal spirals. Bars are indicated by ‘B’, and within a sequence a

Hubble	Revised	T
E	E	-5
E-S0	L ⁻	-3
S0	L	-2
Irr II	IO	0
S0/a	S0/a	0
Sa	Sa	1
Sa-b	Sab	2
Sb	Sb	3
Sb-c	Sbc	4
Sc	Scd	6
Sc-Irr	Sdm	8
Irr I	Im	10

Table C.2

Conversion of Hubble types to Revised System. Table reproduced from de Vaucouleurs *et al.* (1976).



galaxy is categorised (using the letters a–c) by its degree of central concentration only (the arm pitch angle is not relevant). By combining this classification with a luminosity class for spirals (both normal and anaemic) we have the Revised DDO system. The luminosity class is assigned according to the development of the spiral arms and is denoted by roman numerals I–V, with I representing the most well-developed spiral structure.

The various schemes described in brief above refer principally to normal galaxies. Other classifications for peculiar, interacting and active galaxies also exist – I again refer the interested reader to Mihalas & Binney (1981) for a review.

References

- de Vaucouleurs G., 1959, in *Handbuch der Physik*, ed. Flügge S., vol. 53, p. 275, Springer–Verlag, Berlin
- de Vaucouleurs G., de Vaucouleurs A., Corwin Jr. H. G., 1976, *Second Reference Catalogue of Bright Galaxies*, University of Texas Press, Austin
- de Vaucouleurs G., de Vaucouleurs A., Corwin Jr. H. G., Buta R. J., Paturel G., Fouqué P., 1991, *Third Reference Catalogue of Bright Galaxies*, Springer–Verlag, New York
- Hubble E. P., 1936, *The Realm of the Nebulae*, Yale University Press, New Haven
- Mihalas D., Binney J., 1981, *Galactic Astronomy*, W. H. Freeman, San Francisco, 2nd edn.
- Morgan W. W., 1970, in *Spiral Structure of Our Galaxy*, eds Becker W., Contopoulos G., Reidel, Dordrecht
- van den Bergh S., 1976, *ApJ*, 206, 883

Abbreviations used in the text

A&A	Astronomy and Astrophysics
A&AS	Astronomy and Astrophysics Supplement
AJ	Astronomical Journal
ApJ	Astrophysical Journal
ApJS	Astrophysical Journal Supplement
CFR	Cluster Formation Rate
CPU	Central Processing Unit
CR	Co-rotation Resonance
DDO	David Dunlap Observatory (galaxy classification scheme)
DSS	Digitized Sky Survey – see page (ii)
GMC	Giant Molecular Cloud
FFT	Fast Fourier Transform
FIR	Far Infra-Red
IAP	Institut d’Astrophysique de Paris
IC	Index Catalogue
ILR	Inner Lindblad Resonance
IMF	Initial Mass Function
IR	Infra-Red
IRAS	Infra-Red Astronomical Satellite
ISM	Interstellar Medium
JCMT	James Clerk Maxwell Telescope
KS	Kolmogorov–Smirnov (statistical test)
LMC	Large Magellanic Cloud
MB	Megabyte
MNRAS	Monthly Notices of the Royal Astronomical Society
MST	Minimal Spanning Tree
NGC	New General Catalogue
OLR	Outer Lindblad Resonance



PA	Position Angle
PASP	Proceedings of the Astronomical Society of the Pacific
PM	Particle–Mesh method (N-body simulation)
PP	Particle–Particle method (N-body simulation)
P ³ M	Particle–Particle–Particle–Mesh method (N-body simulation)
PSF	Propagating Star Formation
RC3	Third Reference Catalogue of Bright Galaxies (de Vaucouleurs <i>et al.</i> 1991)
SDW	Spiral Density Wave
SF	Star Formation
SFR	Star Formation Rate
SI	Système International d’unités
SNe	Supernovae
SNR	Supernova Remnant
SPH	Smoothed Particle Hydrodynamics
SPSF	Self-Propagating Star Formation
SSPSF	Stochastic Self-Propagating Star Formation
UV	Ultra-Violet

Symbols used in the text

A	spiral density wave amplitude; Fourier transform of point distribution
B	magnetic field strength
B_{eq}	galactic magnetic field estimated using minimum-energy condition
C	cumulative distribution functions
d_{col}	cloud diameter
D	galactic diameter; Kuiper statistic
D_H	Hausdorff fractal dimension
$D(q)$	generalised Hausdorff multifractal dimensions
D_q	generalised Rényi multifractal dimensions
G	gravitational constant = $6.672 \times 10^{-11} \text{ N m}^2 \text{ kg}^{-2}$
h	integration step size
H I	atomic hydrogen
H II	ionised hydrogen
H α	radiation from ionised hydrogen corresponding to electron transition between $n=3$ and $n=2$ levels
H ₂	molecular hydrogen
i_0	pitch angle of imposed spiral density wave
i_*	pitch angle of pattern traced by young stellar clusters
K	Kolmogorov–Smirnov statistic
l	edge-lengths of minimal spanning tree
\bar{l}	mean value of l
L_{FIR}	far infra-red luminosity
L_{\odot}	Solar bolometric luminosity = $3.90 \times 10^{26} \text{ W}$
M	molecular cloud mass
M_{mag}	critical mass for collapse of a magnetised cloud
M_{med}	median cloud mass
M_{sp}	scaling mass for spontaneous star formation
M_{st}	scaling mass for stimulated star formation



M_{tot}	total cloud mass
M_{\odot}	Solar mass = 1.989×10^{30} kg
n	number density; number of spiral arms; Schmidt Law index
N	number of points
P	probability
P_c	critical probability (percolation theory)
P_{sp}	probability of spontaneous star formation
P_{st}	probability of stimulated star formation
q	Fourier transform conjugate variable, $q = -n \cot(i_0)$; density scaling regime for multifractals
r	radial coordinate
$r_{\text{min}}, r_{\text{max}}$	scaling range used with correlation–sum multifractal technique
u	$\ln(r)$
v, \mathbf{v}	general speed/velocity
v_{disp}	cloud velocity dispersion
v_{max}	maximum speed impulse that can be given to a cloud by a collision with a supershell
v_{rms}	root mean square velocity dispersion of clouds
v_s	speed of sound
V	volume of galaxy
W	kernel function used in smoothed particle hydrodynamics
z	axial coordinate
ε	fraction of cloud remaining after star formation event
η	‘elasticity’ of cloud–cloud collisions
θ	azimuthal coordinate
κ	epicyclic frequency
ρ	general density
ρ_{gas}	volume density of total gas (atomic plus molecular)
$\rho_{\text{H I}}$	volume density of atomic hydrogen
$\dot{\rho}_*$	star formation rate (volume density)
σ_{gas}	surface density of total gas (atomic plus molecular)
$\sigma_{\text{H I}}$	surface density of atomic hydrogen
σ_{H_2}	surface density of molecular hydrogen
$\dot{\sigma}_*$	star formation rate (surface density)
Σ_i	cloud cross-section
τ	refractory time; cloud regrowth time; multifractal function
ψ	cluster formation rate (number per unit time)
Ω	Keplerian angular velocity
Ω_p	spiral pattern speed

List of publications

- “A new model of the structure of spiral galaxies based on propagating star formation – I. The Galactic star formation rate and Schmidt Law.”
Sleath J. P., Alexander P., 1995a, *MNRAS*, 275, 507
- “A new model of the structure of spiral galaxies based on propagating star formation – II. The effect of a spiral density wave”
Sleath J. P., Alexander P., 1995b, *MNRAS*, submitted
- “A new model of the structure of spiral galaxies based on propagating star formation – III. Multifractal analysis of galactic structure.”
Sleath J. P., Alexander P., 1995c, *MNRAS*, in prep.
- “Analysis of H II distribution in spiral galaxies using the multifractal formalism and its estimators.”
Wu K. K. S., Sleath J. P., Alexander P., 1995, *MNRAS*, in prep.
- “A new model for star formation and galactic structure in spiral galaxies based on propagating star formation.”
Sleath J. P., Alexander P., 1996, in *The interplay between massive star formation, the ISM and galaxy evolution*, eds Kunth D., Guiderdoni B., Heydari-Malayeri M., Thuan T. X., Trân Thanh Vân J., Editions Frontières, Paris, in press Proceedings of 11th IAP meeting, Paris, 3–8 July, 1995
- “Limitations of detecting faint broad lines: low-level instrumental ripples.”
Röttgering H., Miley G., Jenness T., Sleath J. P., van Ojik R., van der Werf P., 1995, *The JCMT newsletter*, p. 32



Bibliography



- Aarseth S. J., 1993, lecture notes from EADN Astrophysics School VI, Thessaloniki, unpublished
- Aarseth S. J., 1994, in *Galactic Dynamics and N-body Simulations*, eds Contopoulos G., Spyrou N. K., Vlahos L., Springer-Verlag, Berlin
- Allen C., Martos M. A., 1986, *Rev. Mex. Astron. Astrofís.*, 13, 137
- Allen C., Santillán A., 1991, *Rev. Mex. Astron. Astrofís.*, 22, 255
- Arimoto N., Yoshii Y., Takahara F., 1992, *A&A*, 253, 21
- Arneodo A., Grasseau G., Kostelich E. J., 1987, *Phys. Lett. A*, 124, 426
- Avedisova V. S., 1988, in *Evolution of Galaxies, Proc. Eur. Reg. Meet. Astron. no. 10*, ed. Palouš J., p. 171, Publ. Inst. Czech Acad. Sci.



- Baade W., 1963, in *Evolution of Stars and Galaxies*, ed. Payne-Gaposchkin C., chap. 16, Harvard University Press
- Barnes J., Hut P., 1986, *Nature*, 324, 446
- Barrow J. D., Bhavsar S. P., Sonoda D. H., 1985, *MNRAS*, 216, 17
- Baugh C. M., Efstathiou G., 1994, *MNRAS*, 270, 183
- Belfort P., Crovisier J., 1984, *A&A*, 136, 368
- Bicay M. D., Kojoian G., Seal J., Dickinson D. F., Malkan M. A., 1995, *ApJS*, 98, 369
- Binney J., Tremaine S., 1987, *Galactic Dynamics*, Princeton University Press, New Jersey
- Blaauw A., 1984, *Irish Astron. J.*, 16, 141
- Bodenheimer P., 1992, in *Star Formation in Stellar Systems*, eds Tenorio-Tagle G., Prieto M., Sánchez F., p. 16, Cambridge University Press
- Borgani S., Plionis M., Valdarnini R., 1993, *ApJ*, 404, 21
- Bothun G. D., Lonsdale C. J., Rice W., 1989, *ApJ*, 341, 129
- Bowers R. L., Deeming T., 1984, *Astrophysics II: Interstellar matter and galaxies*, Jones and Bartlett Publishers Inc., Boston
- Broadbent S. R., Hammersley J. M., 1957, *Proc. Cambridge Phil. Soc.*, 53, 629
- Buat V., Deharveng J. M., Donas J., 1989, *A&A*, 223, 42



Burton W. B., 1988, in *Galactic and Extragalactic Radio Astronomy*, eds Verschuur G. L., Kellermann K. I., p. 332, Springer-Verlag, New York, 2nd edn.



Caimmi R., 1995, *A&A*, 295, 335
 Carranza G., Crillon R., Monnet G., 1969, *A&A*, 1, 479
 Chakrabarti S. K., Molteni D., 1995, *MNRAS*, 272, 80
 Condon J. J., 1992, *Ann. Rev. Ast. Astrophys.*, 30, 575
 Condon J. J., Yin Q. F., 1990, *ApJ*, 357, 97
 Considère S., Athanassoula E., 1982, *A&A*, 111, 28
 Contopoulos G., Grosbøl P., 1986, *A&A*, 155, 11
 Cox M. J., Eales S. A. E., Alexander P., Fitt A. J., 1988, *MNRAS*, 235, 1227
 Cox P., Krugel E., Mezger P. G., 1986, *A&A*, 155, 380



Danver C.-G., 1942, *Lund Obs. Ann.*, 10
 Davies M. B., Benz W., Piran T., Thieleman F. K., 1994, *ApJ*, 431, 742
 Davies R. D., 1994, in *Cosmical Magnetism*, ed. Lynden-Bell D., vol. 422 of *NATO ASI Series C*, p. 131, Kluwer, Dordrecht
 de Vaucouleurs G., 1959, in *Handbuch der Physik*, ed. Flügge S., vol. 53, p. 275, Springer-Verlag, Berlin
 de Vaucouleurs G., de Vaucouleurs A., Corwin Jr. H. G., 1976, *Second Reference Catalogue of Bright Galaxies*, University of Texas Press, Austin
 de Vaucouleurs G., de Vaucouleurs A., Corwin Jr. H. G., Buta R. J., Paturel G., Fouqué P., 1991, *Third Reference Catalogue of Bright Galaxies*, Springer-Verlag, New York
 Devereux N. A., Young J. S., 1990, *ApJ*, 350, L25
 Devereux N. A., Young J. S., 1991, *ApJ*, 371, 515
 Dopita M. A., 1985, *ApJ*, 295, L5
 Dopita M. A., 1990, in *The Interstellar Medium in Extnal Galaxies*, eds Thronson H. A., Shull J. M., p. 437, Dordrecht, Kluwer
 Dopita M. A., Ryder S. D., 1994, *ApJ*, 430, 163



Eales S. A., Wyn-Williams C. G., Duncan W. D., 1989, *ApJ*, 339, 859
 Edmunds M. G., 1990, *MNRAS*, 246, 678
 Efstathiou G., Davis M., Frenk C. S., White S. D. M., 1985, *ApJS*, 57, 241
 Elmegreen B. G., 1985, in *Birth and Evolution of Massive Stars and Stellar Groups*, eds Boland W., van Woerden H., p. 227, D. Reidel Publishing Company
 Elmegreen B. G., 1985, in *Birth and Infancy of Stars*, eds Lucas R., Omont A., Stora R., p. 215, Elsevier Science Publishers B.V., Amsterdam

- Elmegreen B. G., 1991, in *Evolution of Interstellar Matter and Dynamics of Galaxies*, eds Palouš J., Burton W. B., Lindblad P. O., Cambridge University Press
- Elmegreen B. G., 1992, in *Star Formation in Stellar Systems*, eds Tenorio-Tagle G., Prieto M., Sánchez F., p. 381, Cambridge University Press
- Elmegreen B. G., Clemens C., 1985, *ApJ*, 294, 523
- Elmegreen B. G., Elmegreen D. M., 1987, *ApJ*, 320, 182
- Elmegreen B. G., Wang M., 1988, in *Molecular Clouds in the Milky Way and External Galaxies*, eds Dickman R. L., Snell R. L., Young J. S., Springer-Verlag, Berlin
- Elmegreen B. G., Elmegreen D. M., Montenegro L., 1992, *ApJS*, 79, 37
- Elmegreen D. M., 1993, in *Star Formation, Galaxies and the Interstellar Medium*, eds Franco J., Ferrini F., Tenorio-Tagle G., p. 108, Cambridge University Press
- Elmegreen D. M., Elmegreen B. G., 1986, *ApJ*, 311, 554
- Elmegreen D. M., Elmegreen B. G., 1995, *ApJ*, 445, 591



- Falconer K. J., 1990, *Fractal Geometry: mathematical foundations and applications*, John Wiley & Sons Ltd., Chichester
- Feder J., 1988, *Fractals*, Plenum Press, New York
- Firmani C., Tutukov A., 1992, *A&A*, 264, 37
- Fitt A. J., Alexander P., 1992, *MNRAS*, 258, 241
- Fitt A. J., Alexander P., 1993, *MNRAS*, 261, 445
- Frisby J. P., 1979, *Seeing: illusion, brain and mind*, Oxford University Press



- García Gómez C., Athanassoula E., 1991, *A&AS*, 89, 159
- García Gómez C., Athanassoula E., 1993, *A&AS*, 100, 431
- Gerola H., Seiden P. E., 1978, *ApJ*, 223, 129
- Gerola H., Seiden P. E., Schulman L. S., 1980, *ApJ*, 242, 517
- Gingold R. A., Monaghan J. J., 1977, *MNRAS*, 181, 375
- Gordon M. A., 1995, *A&A*, in press
- Gragg W., 1965, *J. SIAM Numer. Anal. Ser. B*, 2, 384
- Grassberger P., Procaccia I., 1983, *Phys. Rev. Lett.*, 50, 346
- Grimmett G., 1989, *Percolation*, Springer-Verlag, NY



- Habe A., Ohta K., 1992, *Proc. Ast. Soc. Japan*, 44, 203
- Heiles C., 1990, in *IAU Symposium 140, Galactic and Intergalactic Magnetic Fields*, eds Beck R., Kronberg P. P., Wielebinski R., p. 35, Reidel, Dordrecht
- Hénon M., 1976, *Commun. Math. Phys.*, 50, 69



- Hernquist L., 1987, *ApJS*, 64, 715
 Hernquist L., 1993, *ApJ*, 404, 717
 Hernquist L., Katz N., 1989, *ApJS*, 70, 419
 Hernquist L., Weil M. L., 1993, *MNRAS*, 261, 804
 Heydari-Malayeri M., Testor G., 1983, *A&A*, 118, 116
 Heydari-Malayeri M., Niemala V. S., Testor G., 1987, *A&A*, 184, 300
 Heydari-Malayeri M., Magain P., Remy M., 1988, *A&A*, 201, L41
 Hobson M. P., 1994, private communication
 Hobson M. P., Padman R., Scott P. F., Prestage R. M., Ward-Thomson D., 1993, *MNRAS*, 264, 1025
 Hockney R. W., Eastwood J. W., 1981, *Computer Simulation Using Particles*, McGraw-Hill
 Hodge P. W., 1976, *ApJ*, 205, 728
 Hodge P. W., Kennicutt Jr. R. C., 1983, *AJ*, 88, 296
 Hubble E. P., 1936, *The Realm of the Nebulae*, Yale University Press, New Haven



- James R. A., Weeks T., 1986, in *The Use of Supercomputers in Stellar Dynamics*, eds Hut P., McMillan S., Springer-Verlag, Berlin
 Jungwiert B., Palouš J., 1994, *A&A*, 287, 55



- Katz N., 1992, *ApJ*, 391, 502
 Katz N., Gunn J. E., 1991, *ApJ*, 377, 365
 Kennicutt R. C., 1981, *AJ*, 86, 1847
 Kennicutt R. C., 1983, *ApJ*, 272, 54
 Kennicutt R. C., 1989, *ApJ*, 344, 685
 Knapen J. H., Arnth-Jensen N., Cepa J., Beckman J. E., 1993, *AJ*, 106, 56
 Kuiper N. H., 1962, *Proc. Koninklijke Nederlandse Akademie van Wetenschappen, ser. A*, 63, 38
 Kwan J., Valdes F., 1987, *ApJ*, 315, 92



- Lada E., Strom K., Myers P., 1992, in *Protostars and Planets III*, eds Levy E. H., Lunine J., Matthews M. S., University of Arizona Press
 Li J. G., Seaquist E. R., Wrobel J. M., Wang Z., Sage L. J., 1993, *ApJ*, 413, 150
 Lin C. C., Shu F. H., 1964, *ApJ*, 140, 646
 Lin C. C., Shu F. H., 1966, *Proc. Nat. Acad. Sci.*, 229, 55
 Liszt H. S., Burton W. B., Xiang D., 1984, *A&A*, 140, 303
 Longair M. S., 1994, *High Energy Astrophysics*, vol. 2, Cambridge University Press, 2nd edn.
 Lonsdale Persson C. J., Helou G., 1987, *ApJ*, 314, 513
 Lucy L., 1977, *AJ*, 82, 1013

Lyne A., 1990, in *IAU Symposium 140, Galactic and Intergalactic Magnetic Fields*, eds Beck R., Kronberg P. P., Wielebinski R., p. 41, Reidel, Dordrecht



- MacKay G., Jan N., 1984, *J. Phys. A: Math. Gen.*, 17, L757
 Magnani L., Blitz L., Mundy L., 1985, *ApJ*, 295, 402
 Mandelbrot B. B., 1982, *The Fractal Geometry of Nature*, W. H. Freeman & Co., San Francisco
 Martínez V. J., Jones B. J. T., Domínguez-Tenreiro R., van de Weygaert R., 1990, *ApJ*, 357, 50
 Martínez V. J., Domínguez-Tenreiro R., Roy L. J., 1993, *Phys. Rev. E*, 47, 735
 McMillan S. L. W., Aarseth S. J., 1993, *ApJ*, 414, 200
 Meaburn J., Solomos N., Laspias V., Goudis C., 1989, *A&A*, 225, 497
 Metzler C. A., Evrard A. E., 1994, *ApJ*, 437, 564
 Mihalas D., Binney J., 1981, *Galactic Astronomy*, W. H. Freeman, San Francisco, 2nd edn.
 Mihos J. C., Hernquist L., 1994a, *ApJ*, 425, L13
 Mihos J. C., Hernquist L., 1994b, *ApJ*, 437, 611
 Mihos J. C., Richstone D. O., Bothun G. D., 1991, *ApJ*, 377, 72
 Miller G. E., Scalo J. M., 1978, *PASP*, 90, 506
 Miller G. E., Scalo J. M., 1979, *ApJS*, 41, 513
 Monaghan J. J., 1992, *Ann. Rev. Astron. Astrophys.*, 30, 543
 Monaghan J. J., Lattanzio J. C., 1985, *A&A*, 149, 135
 Morgan W. W., 1970, in *Spiral Structure of Our Galaxy*, eds Becker W., Contopoulos G., Reidel, Dordrecht
 Mouschovias T. C., Spitzer L., 1976, *ApJ*, 210, 326
 Mueller M. W., Arnett W. D., 1976, *ApJ*, 210, 670



- Navarro J. V., White S. D. M., 1993, *MNRAS*, 265, 271
 Neukirch T., Feitzinger J. V., 1988, *MNRAS*, 235, 1343
 Nezlin M. V., Polyachenko V. L., Snezhkin E. N., Trubnikov A. S., Fridman A. M., 1986, *Pis'ma Astron. Zh.*, 12, 504
 Noh H.-R., Scalo J., 1990, *ApJ*, 352, 605
 Numerical Algorithms Group Limited, 1993, *NAG Fortran Library Manual*, Mark 16



- Ohtsuki T., Keyes T., 1986, *J. Phys. A: Math. Gen.*, 19, L281
 Ollongren A., 1962, *Bulletin of the Astronomical Institutes of the Netherlands*, 16, 241
 Olson K. M., Kwan J., 1986, *ApJ*, 349, 480
 Öpik E. J., 1953, *Irish Astron. J.*, 2, 219





- Patsis P. A., Hiotelis N., Contopoulos G., Grosbøl P., 1994, *A&A*, 286, 46
 Press W. H., Teukolsky S. A., Vetterling W. T., Flannery B. P., 1992, *Numerical Recipes in FORTRAN*, Cambridge University Press, Cambridge, 2nd edn.
 Puerari I., Dottori H. A., 1992, *A&AS*, 93, 469



- Rana N. C., Wilkinson D. A., 1986, *MNRAS*, 218, 497
 Rényi A., 1970, *Probability Theory*, North-Holland, Amsterdam
 Roberts W. W., Hausman M. A., 1984, *ApJ*, 277, 744
 Roberts Jr. W. W., Roberts M. S., Shu F. H., 1975, *ApJ*, 196, 381
 Röttgering H., Miley G., Jenness T., Sleath J. P., van Ojik R., van der Werf P., 1995, *The JCMT newsletter*, p. 32



- Sanders D. B., Solomon P. M., Scoville N. Z., 1984, *ApJ*, 276, 182
 Sanders D. B., Scoville N. Z., Solomon P. M., 1985, *ApJ*, 289, 373
 Schmidt M., 1959, *ApJ*, 129, 736
 Schmidt M., 1963, *ApJ*, 137, 758
 Schroeder M., 1991, *Fractals, Chaos, Power Laws. Minutes from an infinite paradise*, W. H. Freeman & Co., New York, Chpt. 9
 Schulman L. S., Seiden P. E., 1983, *Ann. Israel Phys. Soc.*, 5, 251
 Scoville N. Z., Good J. C., 1989, *ApJ*, 339, 149
 Seiden P. E., 1983, *ApJ*, 266, 555
 Seiden P. E., Gerola H., 1982, *Fundam. Cosmic Phys.*, 7, 241
 Seiden P. E., Schulman L. S., 1990, *Advances in Physics*, 39, 1
 Sellwood J. A., 1987, *Ann. Rev. Astron. Astrophys.*, 25, 151
 Shu F. H., 1992, *The Physics of Astrophysics – volume II: Gas Dynamics*, University Science Books
 Sleath J. P., 1992, Dissertation submitted towards BA Natural Sciences (Physics and Theoretical Physics), University of Cambridge, not published
 Sleath J. P., Alexander P., 1995a, *MNRAS*, 275, 507
 Sleath J. P., Alexander P., 1995b, *MNRAS*, submitted
 Sleath J. P., Alexander P., 1995c, *MNRAS*, in prep.
 Sleath J. P., Alexander P., 1996, in *The interplay between massive star formation, the ISM and galaxy evolution*, eds Kunth D., Guiderdoni B., Heydari-Malayeri M., Thuan T. X., Trân Thanh Vân J., Editions Frontières, Paris, in press
 Stark A. A., Brand J., 1989, *ApJ*, 339, 763
 Stiefel E. L., Scheifele G., 1971, *Linear and Regular Celestial Mechanics*, Springer-Verlag, New York
 Stoer J., Bulirsch R., 1980, *Introduction to Numerical Analysis*, Springer-Verlag, New York, §7.2.14



- Takata T., Okeefe J. D., Ahrens T. J., Orton G. S., 1994, *Icarus*, 109, 3
 Taylor J. H., Cordes J. M., 1993, *ApJ*, 411, 674
 Tenjes P., Haud U., 1991, *A&A*, 251, 11
 Tenorio-Tagle G., Bodenheimer P., 1988, *Ann. Rev. Astron. Astrophys.*, 26, 145
 Thomasson M., Elmegreen B. G., Donner K. J., Sundelius B., 1990, *ApJ*, 356, L9
 Thronson H. A., Telesco C. M., 1986, *ApJ*, 311, 98
 Tosi M., Díaz A. I., 1990, *MNRAS*, 246, 616
 Tsujimoto T., Nomoto K., Shigeyama T., Ishimaru Y., 1993, in *IAU Symposium 153*, p. 395, Kluwer, Dordrecht
 Turner B. E., 1984, *Vistas Astron.*, 27, 303
 Turner B. E., 1988, in *Galactic and Extragalactic Radio Astronomy*, eds Verschuur G. L., Kellermann K. I., Springer-Verlag, New York, 2nd edn.



- Valentijn E. A., 1990, *Nature*, 346, 153
 Vallée J. P., 1995, *ApJ*, in press
 van de Weygaert R., Jones B. J. T., Martínez V. J., 1992, *Phys. Lett. A*, 169, 145
 van den Bergh S., 1976, *ApJ*, 206, 883
 von Niessen W., Blumen A., 1986, *J. Phys. A: Math. Gen.*, 19, L289



- Wannier P. G., Lichten S. M., Morris M., 1983, *ApJ*, 268, 727
 Whitney V. K. M., 1972, *Commun. ACM*, 15, 273
 Wilding T., Alexander P., Crane P., Pooley G., 1993, in *Star Formation, Galaxies and the Interstellar Medium*, eds Franco J., Ferrini F., Tenorio-Tagle G., p. 301, Cambridge University Press
 Wu K. K. S., Sleath J. P., Alexander P., 1995, *MNRAS*, in prep.
 Wynn-Williams C. G., 1986, in *IAU Symposium 115*
 Wyse R. F. G., Silk J., 1989, *ApJ*, 339, 700



- Xu C., Lisenfeld U., Völk H. J., Wunderlich E., 1994a, *A&A*, 282, 19
 Xu C., Lisenfeld U., Völk H. J., 1994b, *A&A*, 285, 19
 Young J. S., Xie S., Kenney J. D. P., Rice W. L., 1989, *ApJS*, 70, 699
 Zallen R., 1983, *Ann. Israel Phys. Soc.*, 5, 3
 Zinneker H., 1996, in *The interplay between massive star formation, the ISM and galaxy evolution*, eds Kunth D., Guiderdoni B., Heydari-Malayeri M., Thuan T. X., Trân Thanh Vân J., Editions Frontières, Paris, in press



Vulgo enim dicitur: Icundi acti labores.

For it is commonly said: completed labours are pleasant.

Cicero, De Finibus book 2, ch. 105